Dirk Manske

Theory of Unconventional Superconductors

Cooper-Pairing Mediated by Spin Excitations

With 84 Figures

Springer

Dirk Manske
Max-Planck-Institut für Festkörperforschung
Heisenbergstr. 1
70569 Stuttgart, Germany
E-mail:d.manske@fkf.mpg.de

Library of Congress Control Number: 2004104588

Physics and Astronomy Classification Scheme (PACS):
74.20.Mn, 74.25.-q, 74.70.Pq

ISSN print edition: 0081-3869
ISSN electronic edition: 1615-0430
ISBN 3-540-21229-9 Springer-Verlag Berlin Heidelberg New York

Typesetting: by the author using a Springer LaTeX macro package
Cover concept: eStudio Calamar Steinen
Cover production: *design &production* GmbH, Heidelberg

Printed on acid-free paper SPIN: 10947487 56/3141/jl 5 4 3 2 1 0

To Claudia, Philipp, and Isabell

Preface

Superconductivity remains one of the most interesting research areas in physics and complementary theoretical and experimental studies have advanced our understanding of it. In unconventional superconductors, the symmetry of the superconducting order parameter is different from the usual s-wave form found in BCS-like superconductors. For the investigation of these new material systems, well-known experimental tools have been improved and new experimental techniques have been developed.

This book is written for advanced students and researchers in the field of unconventional superconductivity. It contains results I obtained over the last years with various coworkers. The state of the art of research on high-T_c cuprates and on Sr_2RuO_4 obtained from a generalized Eliashberg theory is presented. Using the Hubbard Hamiltonian and a self-consistent treatment of spin excitations and quasiparticles, we study the interplay between magnetism and superconductivity in various unconventional superconductors. The obtained results are then contrasted to those of other approaches. In particular, a theory of Cooper pairing due to exchange of spin fluctuations is formulated for the case of singlet pairing in hole- and electron-doped cuprate superconductors, and for the case of triplet pairing in Sr_2RuO_4. We calculate both many normal and superconducting properties of these materials, their elementary excitations, and their phase diagrams, which reflect the interplay between magnetism and superconductivity.

In the case of high-T_c superconductors, we emphasize the similarities of the phase diagrams of hole- and electron-doped cuprates and give general arguments for a $d_{x^2-y^2}$-wave superconducting order parameter. A comparison with the results of angle-resolved photoemission and inelastic neutron scattering experiments, and also Raman scattering data, is given. We find that key experimental results can be explained.

For triplet Cooper pairing in Sr_2RuO_4, we focus on the important role of spin–orbit coupling in the normal state and compare the theoretical results with nuclear magnetic resonance data. For the superconducting state, results and general arguments related to the symmetry of the order parameter are provided. It turns out that the magnetic anisotropy of the normal state plays an important role in superconductivity.

Stuttgart, May 2004 *Dirk Manske*

D. Manske: Theory of Unconventional Superconductors, STMP 202, VII–XI (2004)

Contents

1 Introduction

One of the most exciting and fascinating fields in condensed matter physics is high-temperature and unconventional superconductivity, for example in hole- and electron-doped cuprates, in Sr_2RuO_4, in organic superconductors, in MgB_2, and in C_{60} compounds. In cuprates, the highest transition temperature (without application of pressure) $T_c \simeq 134$ K has been measured in $HgBa_2Ca_2Cu_3O_{8+\delta}$, followed by – to name just a few – $Bi_2Sr_2CaCu_2O_{8+\delta}$ ($\delta = 0.15 \leftrightarrow T_c \simeq 95$ K), $YBa_2Cu_3O_{6+x}$ ($x = 0.93 \leftrightarrow T_c \simeq 93$ K), $Nd_{2-x}Ce_xCuO_4$ ($x = 0.15 \leftrightarrow T_c \simeq 24$ K), and $La_{2-x}Sr_xCuO_4$, where, for an optimum doping concentration $x = 0.15$, a maximum value of $T_c \simeq 39$ K occurs. Since 77 K is the boiling temperature of nitrogen, it is now possible that new technologies, based for example on SQUIDs (superconducting quantum interference devices) or Josephson integrated circuits [1], might be developed. However, at present, the critical current densities are still not high enough for most technology applications. A recent overview an account of the possible prospects can be found in [2] and references therein.

Throughout this book, we shall focus mainly on Cooper pairing in cuprates and in Sr_2RuO_4. All members of the cuprate family discovered so far contain one or more CuO_2 planes and various metallic elements. As we shall discuss in the next section, their structure resembles that of the perovskites [3]. It is now fairly well established that the important physics related to superconductivity occurs in the CuO_2 planes and that the other layers simply act as charge reservoirs. Thus, the coupling in the c direction provides a three–dimensional superconducting state, but the main pairing interaction acts between carriers within a CuO_2 plane. The undoped parent compounds are antiferromagnetic insulators, but if one dopes the copper–oxygen plane with carriers (electrons or holes), the long-range order is destroyed. Note that even without strict long-range order, the spin correlation length can be large enough to produce a local arrangement of magnetic moments that differs only little from that observed below the Néel temperature in the insulating state. In the doped state the cuprates become metallic or, below T_c, superconducting.

As mentioned above, in hole–doped cuprates T_c is of the order of 100 K and in electron–doped cuprates one finds $T_c \simeq 25$K (as will be explained later), and thus much larger values of T_c are obtained than in conventional

D. Manske: Theory of Unconventional Superconductors, STMP 202, 1–32 (2004)

strong–coupling superconductors such as lead ($T_c = 7.2$ K) or niobium ($T_c = 9.25$ K). Therefore, the phenomenon of high–T_c superconductivity in cuprates that occurs in the vicinity of an antiferromagnetic phase transition suggests a purely electronic or magnetic mechanism, in contrast to the conventional picture of electrons paired through the exchange of phonons. For example, the simplest idea to explain such high critical temperatures might be to introduce a higher cutoff energy ω_c due to electronic correlations in the system instead of integrating over an energy shell corresponding to ω_D (the Debye frequency), i.e.

$$T_c \propto \omega_c \exp\left(-\frac{1}{\lambda}\right) \quad , \tag{1.1}$$

where λ denotes the usual coupling strength for a given symmetry of the gap function. In the BCS theory [4], λ is equal to $N(0)V$, where $N(0)$ is the density of states (per spin) at the Fermi level and $V = \text{const}$ is the attractive pairing potential acting between electrons, leading to the superconducting instability of the normal state. If the relevant energy cutoff ω_c of the problem is of the order of *electronic* degrees of freedom, e.g. $\omega_c \simeq 0.3\,\text{eV} \approx 250$ K [5], one can easily obtain a transition temperature of the order of 100 K. However, as we shall discuss below, in a more realistic treatment the relation between T_c and λ is not as simple as in (1.1).

Superconductivity in strontium ruthenate (Sr_2RuO_4) is also very exciting because its structure is similar to that of the high–T_c cuprate $La_{2-x}Sr_xCuO_4$ (RuO_2 planes instead of CuO_2 planes), but its superconducting properties resemble those of ^{3}He. As will be discussed later in detail, Sr_2RuO_4 is in the vicinity of a ferromagnetic transition and thus is a triplet superconductor. It has a $T_c \simeq 1.5$ K. Furthermore, in contrast to cuprates, its normal–state behavior follows the standard Fermi liquid theory. All this makes the theoretical investigation of Sr_2RuO_4 very interesting.

In this book, we present a general theory of the elementary excitations and singlet Cooper pairing in hole– and electron–doped high–T_c cuprates and compare our results with experiment. Then, we apply our theory also to the novel superconductor Sr_2RuO_4, where triplet pairing is present. We shall present the structures and electronic properties of the most important compounds and their possible theoretical descriptions, and then use those descriptions in the rest of the book. We shall point out some general features of many unconventional superconductors and give the main ideas and concepts used to describe Cooper pairing in these materials. Although it is known that organic superconductors, heavy–fermion superconductors, and some other materials cannot be described by the BCS model [4], we consider the theory of BCS–like pairing (or its strong–coupling extension, i.e. the Eliashberg theory) as a broader and still valid concept in many–body theory. However, the source of the corresponding pairing interaction has to be calculated from a microscopic theory. This is one important goal of this book.

This Introduction is organized as follows: first, we present the most relevant materials, and their crystal and electronic structures. Then, in Sect. 1.2, we ask the most important questions in connection with the phase diagram and the elementary excitations of cuprate high–T_c superconductors, which will be answered in Chap. 3. In Sect. 1.3, we introduce Sr_2RuO_4. In Sect. 1.4, we describe how to find an appropriate Hamiltonian for both cuprates and ruthenates and give some general arguments about the expected symmetry of the superconducting order parameter.

1.1 Layered Materials and Their Electronic Structure

Before deriving an electronic theory for Cooper pairing in cuprates, one has to analyze and understand the underlying crystal structure and corresponding electronic properties. In general, all high–T_c cuprates are basically tetragonal with a lattice constant of about 3.8 Å and consist of one or more CuO_2 planes in their structure, which are separated by layers of other atoms (Ba, La, O, ...). The in–plane oxygen bond length is about 1.9 Å. As mentioned above, most researchers in this field believe that superconductivity is related to processes occurring in the CuO_2 planes, whereas the other layers simply provide the carriers. All cuprates have such charge reservoirs. The superconducting transition temperature T_c seems to depend on the number of CuO_2 planes per unit cell; for example, the three–layer Hg and Tl compounds have a T_c of 134 K and 127 K, respectively. The fact that T_c increases with the number of layers has led to speculation about increasing T_c up to room temperature which, however, has not been not realized up to now [6].

In Tables 1.1and 1.2, we present some materials and their corresponding T_c. For comparison, we also list some "cold" superconductors such as the heavy–fermion compound UPt_3, the BCS–Eliashberg–like superconductors Nb and Pb, and Nb_3Ge, which had the highest T_c before the discovery of cuprates by Bednorz and Müller in 1986 [7].

We present also the recently discovered (phonon-induced) "high–T_c" superconductor MgB_2 and the C_{60} compounds. Very recently it has been demonstrated that even iron becomes superconducting at $T_c \simeq 2$ K, but

Table 1.1. Superconducting transition temperatures of cuprate materials.

Material	T_c (K)
$HgBa_2Ca_2Cu_3O_{8+\delta}$	134
$Tl_2Ca_2Ba_2Cu_3O_{10}$	127
$YBa_2Cu_3O_7$	92
$Bi_2Sr_2CaCu_2O_8$	89
$La_{1.85}Sr_{0.15}CuO_4$	39

Table 1.2. Superconducting transition temperatures of some "cold" superconductors, of Sr_2RuO_4, and of other compounds.

Material	T_c (K)
hole–doped C_{60}	52
MgB_2	39
$Nd_{1.85}Ce_{0.15}CuO_4$	24
C_{60} crystal	18
electron–doped C_{60}	12
Nb	9.25
Pb	7.20
Sr_2RuO_4	1.5
UPt_3	0.54

only in its nonmagnetic phase, i.e. when high pressure is applied [8]. For a more complete list of superconducting materials, see [9, 10].

It is well established that the so–called undoped parent cuprate compounds are insulators and that their Cu spins are ordered antiferromagnetically below a Néel temperature T_N. However, this contradicts a simple band-structure point of view. For example, the formal valencies of La^{3+}, O^{2-}, and Cu^{2+} in the parent compound La_2SrCuO_4 lead to an [Ar] $3d^9$ state, which contains a single d–hole located within the planar $3d_{x^2-y^2}$ orbital. Thus, a naive argument would suggest that the undoped parent compounds are simple metals, which was also concluded from by early local–density approximation (LDA) calculations. This is not restricted to La_2SrCuO_4; in fact, the LDA behaves similarly for other parent compounds. As we shall discuss later, the inconsistency of LDA calculations is a direct consequence of an improper treatment of the strong local Coulomb correlations. On the other hand, it is obvious that the localized copper spins provide the magnetic moments for the antiferromagnetic order. The in–plane exchange coupling $J_{||}$ is generated by Cu-spin superexchange and can be well described by a two-dimensional spin–1/2 Heisenberg model. Inelastic neutron scattering (INS) experiments [11, 12] and Raman scattering [13] have measured $J_{||} \sim 100$ meV and a large anisotropy with respect to the next unit cell, $J_\perp/J_{||} \sim 10^{-5}$ [14, 15]. Therefore, above T_N, the spin correlations are essentially two–dimensional.

1.1.1 $La_{2-x}Sr_xCuO_4$

This compound, usually abbreviated to LSCO, crystallizes in a body–centered tetragonal structure (similar to K_2NiF_4) and is shown in Fig. 1.1. The CuO_2 planes are approximately 6.6 Å are apart and separated by two LaO planes, which form the charge reservoir. Each copper atom in the conducting planes has a bond to oxygen atoms above and below in the c direction, which are

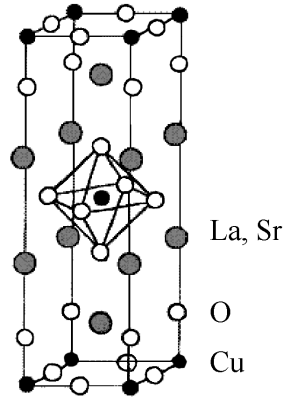

Fig. 1.1. Structure of the hole-doped high-T_c cuprate $La_{2-x}Sr_xCuO_2$ (LSCO), which has a perovskite-like structure with one CuO_2 plane per unit cell. It is believed that the main physics related to Cooper-pairing occurs within the CuO_2 planes.

called apical oxygens. This is typical for all hole–doped high–T_c cuprate materials. Furthermore, the Cu ions are surrounded by octahedra of oxygens as in a perovskite structure. The Cu–O bond in the c direction is much weaker than in the ab plane because its length is considerably larger (~ 2.4 Å) than the Cu–O distance in the CuO_2 planes (~ 1.9 Å). Thus the dominant bonds are those in the planes, and the importance of the apical oxygens is still under discussion.

1.1.2 $YBa_2Cu_3O_{6+x}$

In YBCO, there are two CuO_2 planes per unit cell, approximately 3.2 Å apart and separated by yttrium ions. The tetragonal structure of this compound is shown in Fig. 1.2. The pairs of CuO_2 planes are themselves separated by atoms of barium, oxygen, and copper forming the charge reservoir. The distance between adjacent pairs of these conducting planes is ~ 8.2 Å. As is the case for LSCO, the number of carriers in the CuO_2 planes is controlled by the amount of charge transferred between the conducting layers and charge reservoir layers. Note that in YBCO there are Cu atoms in the charge reservoir, in contrast to LSCO. In combination with oxygen, they form Cu–O chains along the b direction, which leads to an orthorhombic distortion. The Cu–O distance is about 1.9 Å, as in the planes. For $YBa_2Cu_3O_7$, i.e. $x = 1$, the chains are well defined, but they are absent for the undoped parent compound $YBa_2Cu_3O_6$. It is usually believed that adding oxygen to the chains is equivalent to adding holes to the CuO_2 planes. For more details, see [9]. Because of the nonlinear increase of the in–plane hole density with the doping x, YBCO has a so–called 60 K plateau in its $T_c(x)$ curve, which will be discussed later.

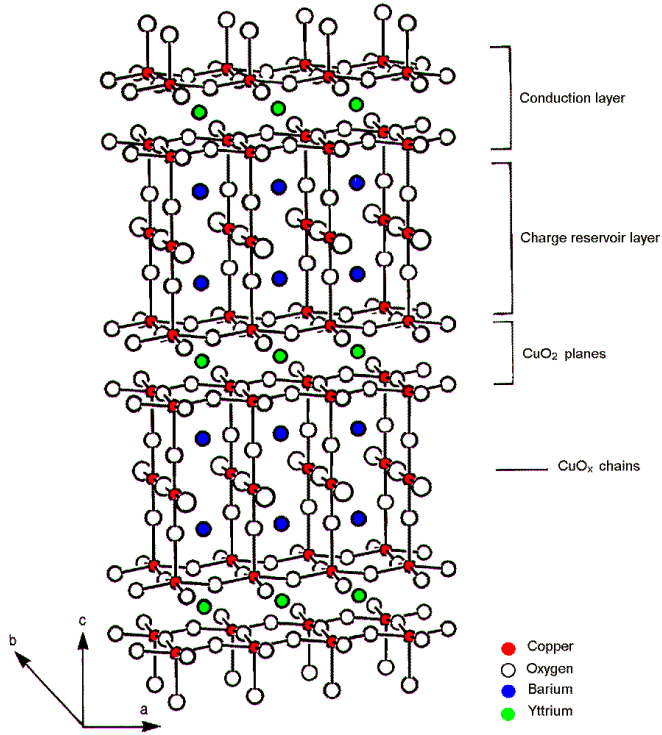

Fig. 1.2. Structure of the hole–doped high–T_c superconductor $YBa_2Cu_3O_{6+x}$ (YBCO). It consists of two CuO_2 planes per unit cell and charge reservoirs. In contrast to LSCO, YBCO has Cu–O chains, which are formed along the b direction.

1.1.3 $Nd_{2-x}Ce_xCuO_4$

The structure of this compound, usually abbreviated to NCCO, is body–centered tetragonal like LSCO and is shown in Fig. 1.3. The difference between NCCO and LSCO lies in the position of the oxygen atoms of the charge reservoir. It is interesting to note that LSCO can be easily doped with holes, while NCCO can be easily doped with electrons. In the NCCO crystal, copper becomes Cu^{2+}, oxygen becomes O^{2-}, and neodymium is in the Nd^{3+} state. After doping with Ce^{4+}, which replaces Nd ions, the CuO_2 planes gain an excess of electrons. It is believed that an additional electron occupies a hole of the d shell of Cu (producing a closed–shell configuration) and does not move to an oxygen site as is the case for hole–doped cuprates. Thus, different bands are doped by holes and electrons, and one expects, on general grounds, that the phase diagram of hole– and electron–doped cuprates will not be symmetric with respect to the carrier concentration x.

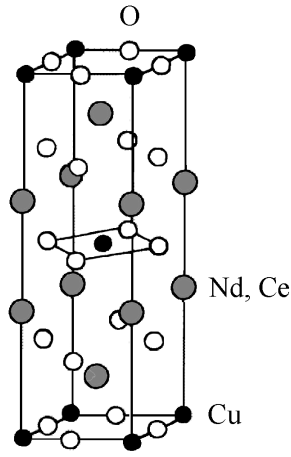

Fig. 1.3. Structure of the electron–doped high–T_c cuprate $Nd_{2-x}Ce_xCuO_2$ (NCCO). This structure is similar to that of LSCO, but no apical oxygen is present.

To briefly summarize this section, we have demonstrated that the main ingredient of the strong electronic correlations that yield high–T_c superconductivity is the CuO_2 planes. In the following we shall assume that the main physics and most important properties of cuprates are intimately related to the electronic correlations within *one* CuO_2 plane. The regions between the CuO_2 planes are believed to act mainly as a charge reservoir. Bilayer effects are treated elsewhere [16]. Thus the general phase diagram, the pairing mechanism, the important transport and optical properties, etc. should be independent of the number of CuO_2 layers per unit cell, in principle. These general questions, motivated by experiment, will be asked in the next section.

1.2 General Phase Diagram of Cuprates and Main Questions

One fundamental problem which one has to solve is the theoretical description and understanding of the general phase diagrams of both hole–doped and electron–doped cuprates, which are shown in Figs. 1.4 and 1.5, respectively. Although details of the $T(x)$ diagram may differ from material to material, for practical purposes Fig. 1.4 describes all of the main features of hole–doped cuprates. As already mentioned, high–T_c superconductivity in hole–doped cuprates always occurs in the vicinity of an antiferromagnetic (AF) phase transition, and has its highest T_c for an optimum doping concentration of around $x_{opt} \simeq 0.16$. The regions in the phase diagram where $x < x_{opt}$ and $x > x_{opt}$ are called "underdoped" and "overdoped", respectively. In Fig. 1.5, we compare the phase diagram of electron–doped NCCO with that

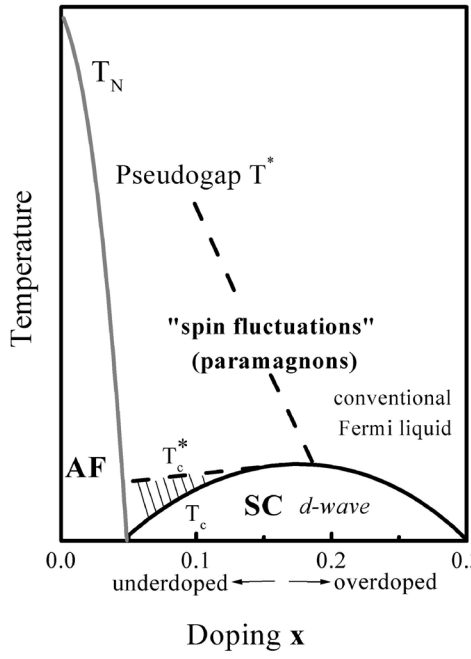

Fig. 1.4. Schematic generic phase diagram of hole–doped cuprates. High-T_c superconductivity always occurs in the vicinity of an antiferromagnetic (AF) phase transition, and the superconducting transition temperature as a function of the hole concentration, $T_c(x)$, has a characteristic (nearly parabola–like) shape [17]. Below T_c, the corresponding superconducting order parameter is of d–wave symmetry. The normal state can be separated into two parts. In the overdoped region, i.e. $x > 0.15$, the system behaves like a conventional Fermi liquid, whereas in the underdoped regime, below the pseudogap temperature T^*, one find strong antiferromagnetic correlations. As is discussed in the text, Cooper pairing can be mainly described by the exchange of AF spin fluctuations (often called paramagnons), which are present everywhere in the system. In the doping region between T_c and T_c^* (*shaded region*) local Cooper pair formation occurs. Below T_c these pairs become phase–coherent and the Meissner effect is observed.

of hole–doped LSCO. The similarities between the two phase diagrams are remarkable. In particular, both cases reveal an antiferromagnetic phase with a similar Néel temperature and a superconducting phase in its vicinity. In the following, we shall describe these phase diagrams in more detail.

1.2.1 Normal–State Properties

It is widely believed that understanding the normal–state properties of high-T_c cuprates will also shed some light on the mechanism of superconduc-

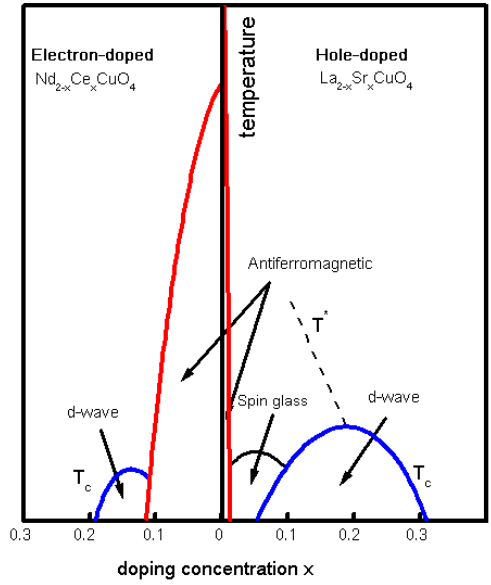

Fig. 1.5. Phase diagrams of the electron–doped superconductor NCCO and of hole–doped LSCO. Superconductivity in the electron–doped cuprates occurs only in a narrow doping range and has a smaller T_c.

tivity. One important fact which we shall analyze is the asymmetry of the cuprate phase diagram with respect to hole and electron doping. In the case of electron–doped cuprates, the antiferromagnetic phase persists up to higher doping values and superconductivity occurs only in a narrow doping region. Also, T_c in the electron–doped case is usually smaller than in hole–doped cuprates, namely approximately 25 K.

Let us start with the analysis of the elementary excitations. Important data are provided by angle–resolved photoemission (ARPES) studies, which provide detailed information about the spectral function $A(\mathbf{k}, \omega)$ (i.e. the local density of states) of the quasiparticles. Owing to recent developments in ARPES, $A(\mathbf{k}, \omega)$ can be studied with high accuracy versus frequency for a fixed momentum (energy distribution curve, EDC) and as a function of momentum at a fixed frequency (momentum distribution curve, MDC). One of the most important results that one obtains by analyzing MDCs and EDCs is the renormalized energy dispersion $\omega_{\mathbf{k}}$, which is shown in Fig. 1.6. These experiments reveal a so–called "kink feature", which reflects a change of the quasiparticle velocity below k_F due to strong correlation effects. The kink is seen in various hole–doped cuprates, but not in electron–doped ones [18, 19, 20]. It has been argued in [18] that the kink is seen along all directions in the Brillouin zone. However, in most of the studies the kink feature has

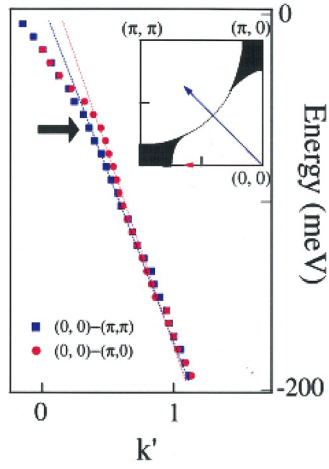

Fig. 1.6. ARPES results for the renormalized energy dispersion $\omega_{\mathbf{k}}$ along different directions in the first Brillouin zone, as shown in the *inset*. Taken from [18].

been investigated only along the $(0,0) \rightarrow (\pi,\pi)$ direction. This is connected to the fact that along the $(0,0) \rightarrow (\pi,0)$ direction there are additional effects such as matrix elements and bilayer splitting which complicate the analysis of experimental data. Originally, the kink feature was attributed to a coupling of itinerant quasiparticles to phonons, in particular to a longitudinal phonon mode at 70 meV which behaves anomalously in several experiments [21]. However, this interpretation has several difficulties. The first relates to the fact that the in–plane resistivity ρ_{ab} in hole–doped cuprates (at the optimal doping) is linear with frequency or temperature (whichever dependence gives the larger value), which is hard to explain within conventional electron–phonon coupling, which predicts $\rho_{ab} \propto T^2$ or $\rho_{ab} \propto \omega^2$. At the same time, in electron–doped cuprates no kink is observed [18], and the resistivity is quadratic in temperature. Thus, it is not clear whether both sets of results can be explained assuming the same electron–phonon coupling. In this book we shall study the spectrum of the elementary excitations, and thus the kink feature due to coupling of holes or electrons to spin fluctuations. Spin excitations result in a frequency and momentum dependence of the quasiparticle self–energy which differs from the phonon case. We shall demonstrate that the kink feature is one of the key facts that can be explained by coupling of holes to spin fluctuations. Furthermore, the anisotropy in $\mathbf{k}$–space and the doping dependence of the kink might be seen as a fingerprint of the coupling to spin fluctuations, too. This will be discussed in detail later.

In general, the normal state can be separated into two parts. In the overdoped region the system behaves mainly like a conventional Fermi liquid, whereas in the underdoped case, in particular below the pseudogap temper-

ature T^*, the system reveals some unusual properties. For example, a gap is present in the elementary excitations, strong anisotropies are observed (caused mainly by the 2D nature of the system), and local magnetic phases exist. To be more precise, important examples are provided by the ^{63}Cu spin–lattice relaxation rate and the inelastic neutron scattering intensity in hole–doped cuprates: while in the overdoped regime the spin–lattice relaxation rate $1/T_1T$ increases monotonically as T decreases to T_c, one finds in the underdoped case that $1/T_1T$ passes through a maximum at the spin gap temperature T^* with decreasing T (see [22] for a review). These results are confirmed by INS data, where in the underdoped regime, $\mathrm{Im}\,\chi(\mathbf{Q},\omega)$ at fixed small ω ($\simeq$ 10–15 meV) also passes through a maximum at T^* with decreasing T [23]. Thus, one of the main theoretical questions for hole–doped cuprates is to explain the origin of this spin gap temperature in the normal state and its relation to the underlying mechanism of Cooper pairing. In addition, ARPES experiments on underdoped $Bi_2Sr_2CaCu_2O_{8+\delta}$ show the presence of a gap with $d_{x^2-y^2}$–wave symmetry well above T_c in the charge excitation spectrum [24, 25]. This gap also opens below the temperature T^* and thus seems to coincide with the spin gap temperature. Furthermore, recently several experiments, including measurements of heat capacity [26], transport [27], and Raman scattering [28], and, in particular, scanning tunneling spectroscopy [29, 30] have confirmed the existence of a gap in the elementary excitations below T^*. Thus T^* is usually called the pseudogap temperature. Whether a pseudogap is present in electron-doped cuprates is still a subject of debate. While measurements of the optical conductivity report a pseudogap similarly to the hole–doped case [31], tunneling data reveal a pseudogap (i.e. a reduction of the spectral weight at the Fermi level) only below T_c and when a high magnetic field ($> H_{c2}$) is applied [32, 33].

The existence and origin of the pseudogap are another fundamental question which we shall address in this book. So far, a few phenomenological models, such as marginal–Fermi liquid (MFL) [34], nested–Fermi liquid (NFL) [35, 36], and nearly–antiferromagnetic–liquid (NAFL) [37] models, have been developed in order to understand the unusual Fermi liquid properties in the normal state. At the moment it is not clear whether these concepts can also be applied to electron-doped superconductors.

Another important energy scale is the temperature T_c^*, which is only present in the underdoped region and close to T_c. Below T_c^*, local Cooper pairs without long-range phase coherence are found [40, 41, 42] ("preformed pairs"), which become phase–coherent only for temperatures $T < T_c$ where the Meissner effect is observed. T_c^* and T^* seem to be crossover temperatures rather than true phase transitions (although this is a subject of debate [38, 39]). As we shall discuss later, T_c^* is connected with the fact that, in the doping behavior of the superconducting transition temperature $T_c(x)$, a maximum around $x = 0.15$ is found. It has to be clarified whether T_c^* exists also in the case of electron–doped cuprates.

Let us briefly summarize the main questions for the normal state of cuprates:

- How can we understand the phase diagrams of both for hole– and electron–doped cuprates, in particular the doping dependence of the characteristic temperatures $T^*(x)$, $T_c^*(x)$, and $T_c(x)$? What is the origin of the pseudogap? Do T^* and T_c^* exist for electron-doped cuprates?
- What is the origin of the asymmetry of the cuprate phase diagram with respect to hole and electron doping? Why does superconductivity occur only within a small doping region, and why does it have a smaller T_c in the case of electron-doped cuprates?
- How can we describe and understand the elementary excitations in cuprates, for example the kink feature in hole–doped cuprates and its absence in electron–doped cuprates?

Finally Fig. 1.4 illustrates that (mainly AF) spin fluctuations are present in the normal state of hole–doped cuprates; these can be measured by INS experiments, for example [43]. Spin fluctuations have also been measured in electron-doped cuprates [44]; however, they are weaker than in hole–doped cuprates. As already mentioned, their occurrence is related to the quasi–2D character of the spin correlations within a CuO_2 plane, which are more robust against doping than is the 3D Néel state. The origin of these excitations in hole–doped cuprates is the copper spins, which are surrounded by itinerant holes which have destroyed the 3D long-range order. Consequently, the underlying idea for the Cooper-pairing mechanism in high-T_c cuprates is the exchange of these spin fluctuations between (dressed) holes or electrons in a generalized Eliashberg-like theory. This will be discussed in detail in Chap. 2. These ideas are similar to the exchange of "paramagnons" in the case of triplet pairing in ^{3}He, where the system is close to a ferromagnetic instability [45, 46]. Later in this book we shall use a similar approach to describe the interesting properties of the novel triplet superconductor Sr_2RuO_4.

1.2.2 Superconducting State: Symmetry of the Order Parameter

In Fig. 1.4, we also show the $T_c(x)$ curve, which has a characteristic shape $T_c(x) = 1 - (x - 0.16)^2$, as pointed out in [17, 47]. Below T_c, superconductivity occurs and it is believed that the order parameter has $d_{x^2-y^2}$–wave symmetry, i.e. $\Delta_k = \Delta_0 [\cos k_x - \cos k_y]/2$. The evidence for d–wave pairing in hole–doped cuprates comes from several sources, in particular phase–sensitive measurements, NMR studies, penetration depth measurements, ARPES, and polarization-dependent Raman scattering experiments:

1. Phase sensitive experiments by Wollmann *et al.* [48] and Kirtley and Tsuei [49, 50, 51], measuring the phase coherence of YBCO–Pb dc SQUIDs, have reported a $d_{x^2-y^2}$-wave order parameter.

2. Bourges, Regnault, Keimer, and others have demonstrated that INS experiments reveal a feedback effect of superconductivity on the neutron scattering intensity. In particular, a strong rearrangement of the spectral weight, a so–called resonance peak, is observed below T_c (see Fig. 1.7) [52, 53, 54, 55, 56].[1] On general grounds, one expect this peak at a resonance frequency $\omega_{res} \approx 2\Delta$ where Δ is the (average) superconducting gap. INS experiments show intensity below this threshold frequency (i.e. $0 < \omega < \omega_{res}$) also supporting a d–wave gap in the superconducting state.
3. NMR measurements probe the local magnetic field around an atom and allow the determination of the Cu relaxation rate. Below T_c this relaxation rate varies as T^3, in agreement with several predictions for a $d_{x^2-y^2}$–wave order parameter.
4. It follows from simple statistical arguments that the penetration depth λ of an external magnetic field varies exponentially with T at small temperatures. However, when nodes are present in the superconducting order parameter, and thus Cooper pairs can be broken very easily along the corresponding directions in the Brillouin zone (BZ), λ should vary linearly with temperature (or $\lambda \propto T^2$ in the dirty limit). Bonn, Hardy, and coworkers have reported such behavior in YBCO [57, 58].
5. Shen *et al.* and Campuzano *et al.* have reported strong anisotropy of the superconducting gap using ARPES techniques [59]. Their interpretation is consistent with a $d_{x^2-y^2}$–wave order parameter.
6. Polarization-dependent Raman scattering below T_c measures a pair-breaking peak and thus (via the Tsuneto function) [60, 61]) the anisotropy of Δ_k. So far, the interpretations of several groups are compatible with an order parameter that has nodes along the diagonal of the BZ [62, 63, 64, 65]. Further analytical results for small transferred energies, i.e. power laws for the observed intensity, support this interpretation.

Obviously, only method 1 reveals clearly a sign change in the superconducting order parameter; the other techniques can determine only the existence of nodes. Strictly speaking, some of the results of these experiments would also be consistent with an extended s–wave gap, i.e. $\Delta_k = \Delta_0 [\cos k_x + \cos k_y]/2$. In addition, another phase–sensitive measurement along the c direction by Li *et al.*, which was suggested by R. Klemm, seems to be inconsistent with a $d_{x^2-y^2}$–wave gap [66, 67]. Very recently, this experiment has been repeated and improved and a d–wave gap has been observed [68]. However, there is still controversy over the interpretation [69]. Furthermore, we show throughout this book that a d–wave order parameter occurs naturally if singlet pairing is mediated by AF spin fluctuations. This is related to general arguments about a *repulsive* pairing interaction and will be discussed in Sect. 1.4.3.

[1] A closer inspection for the normal-state data of underdoped $YBa_2Cu_3O_{6+x}$ [55] shows that this peak is qualitatively different from the resonance peak [56].

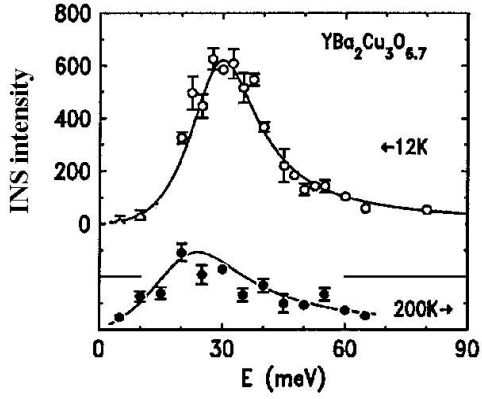

Fig. 1.7. Neutron scattering intensity versus transferred energy for underdoped YBCO in the normal state ($T = 200$ K) and superconducting state ($T = 12$ K). In the normal state, an Ornstein–Zernicke behavior is observed. Below T_c, a strong rearrangement of spectral weight takes place and a resonance peak develops.

New phase–sensitive measurements by Kirtley and Tsuei show strong evidence that the superconducting order parameter of electron–doped cuprates also has $d_{x^2-y^2}$–wave symmetry [51, 70]. This is further supported by measurements of the in–plane penetration depth λ, and ARPES experiments [71, 72]. This is interesting because it was believed for more than one decade that NCCO and other electron–doped superconductors were s–wave superconductors. In particular, early experiments by Anlage *et al.* reported that λ follows an exponential behavior at low temperatures [73], Raman scattering experiments saw no variation of the scattered intensity as a function of the applied polarization [74], and no zero–bias peak has been observed [75]. However, after the recent experiments by Kirtley and Tsuei mentioned above, it seems clear now that d–wave pairing is present in electron–doped cuprates. We consider this as an important step towards a unified phase diagram of hole– and electron–doped cuprates.

We can briefly summarize the questions as follows:

- Why, *theoretically*, should a $d_{x^2-y^2}$–wave gap appear in the case of singlet pairing due to (repulsive) spin excitations for both hole– and electron–doped cuprates? Can we exclude a d_{xy} symmetry, for example? How is this related to the underlying band structure or the character of the quasiparticles (copper d states versus oxygen p states)?
- Why did earlier experiments on electron–doped cuprates report an s–wave symmetry of the superconducting order parameter?
- In general, if the order parameter has $d_{x^2-y^2}$–wave symmetry, why are deviations from the simple basis function $\propto [\cos k_x - \cos k_y]$ still possible?

Are there such deviations and, if so, what is their physical origin and interpretation?

– How can we describe and understand the "resonance peak" in INS experiments which reflects the interdependence of the elementary excitations and spin fluctuations? Does this provide information about the pairing interaction?

Another remarkable feature of the superconducting state of high–T_c cuprates is that they differ from conventional superconductors by having a small coherence length ξ. This length is usually associated with the average size of a Cooper pair, which for conventional superconductors is about 500 Å–10^4 Å. Therefore the size of a Cooper pair is larger than the average distance between pairs, resulting in a strong overlap of the corresponding wave functions. On the other hand, the cuprate superconductors have $\xi \sim 12$ Å–15 Å; these values have been obtained mainly from measurements of the upper critical field H_{c2}. All high–T_c cuprates are type II superconductors and are believed to be in the "clean limit" since the mean free path of the carriers ($\sim$ 150 Å) is much larger than ξ. Note that the coherence length in the c direction ξ_c, is only 2 Å–5 Å, i.e. even smaller than the interplanar distance, while ξ in the planes is about three to four lattice spacings.

1.3 Triplet Pairing in Strontium Ruthenate (Sr_2RuO_4): Main Facts and Main Questions

The discovery of high–T_c superconductivity in the cuprates led to extensive searches for other superconducting transition metal oxides. One important example is the novel superconductor strontium ruthenate (Sr_2RuO_4) which was discovered by Maeno and coworkers in 1994 [76]. Its crystal structure is isostructural to that of $(La,Sr)_2CuO_4$ (shown in Fig. 1.8), but it has $T_c \simeq 1.5$ K, and, more importantly, is believed to be a triplet superconductor. This makes a theoretical investigation of Sr_2RuO_4 very interesting.

The formal valence of the ruthenium ion is Ru^{4+}, i.e. there are four remaining electrons within the $4d$ shell. Similarly to LSCO, the Ru ion sits at the center of a RuO_6 octahedron, and the crystal field of the O^{2-} ions splits the five $4d$ states into threefold t_{2g} and fourfold e_g subshells. The negative charge of O^{2-} causes the t_{2g} states to lie lower in energy, and the corresponding xy, xz, and yz orbitals form the Fermi surface. Owing to the large interplanar separation of the RuO_6 octahedra, Sr_2RuO_4 has only a small energy dispersion along the c direction. Its highly planar structure leads also to very weak hybridization between xy orbitals and the xz and yz orbitals. Band structure calculations confirm these considerations and distribute the four electrons equally among all three orbitals [78]. The detailed shape of the Fermi surface has been determined from de Haas–van Alphen oscillations of

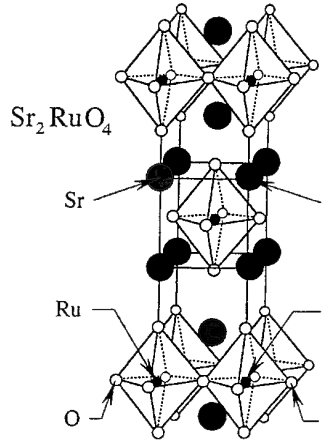

Fig. 1.8. Structure of Sr_2RuO_4, which is similar to that of the high–T_c cuprate family $La_{2-x}Ba_xCuO_4$. However, its normal and superconducting properties are quite different from those of cuprates: they resemble more the properties of superfluid ^{3}He, as described in the text. This is discussed in [77].

the magnetization in response to an external field and confirms the sheets of the Fermi surface predicted by band structure calculations.

Recent studies by means of INS [79] and nuclear magnetic resonance (NMR) [80] of the spin dynamics in Sr_2RuO_4 reveal the presence of strong incommensurate fluctuations in the RuO_2 planes at the antiferromagnetic wave vector $\mathbf{Q}_i = (2\pi/3, 2\pi/3)$. It was found from band structure calculations [81] that these fluctuations result from the nesting properties of the quasi-one-dimensional d_{xz} and d_{yz} bands. The two–dimensional d_{xy} band contains only weak ferromagnetic fluctuations. In general, owing to spin–orbit coupling or hybridization, one expects strong spin fluctuations between the RuO_2 planes in the z direction also [82, 83]. However, inelastic neutron scattering [84] shows that the magnetic fluctuations are purely two-dimensional and originate from the RuO_2 planes. Both behaviors could result as a consequence of the magnetic anisotropy within the RuO_2 planes as indeed was observed in recent NMR experiments by Ishida *et al.* [85]. In particular, by analyzing the temperature dependence of the nuclear spin–lattice relaxation rate for ^{17}O in the RuO_2 planes at low temperatures, these authors have demonstrated that the out–of–plane component of the spin susceptibility can become almost three times larger than the in–plane component. This strong and unexpected anisotropy disappears at approximately room temperature [85].

Superconductivity occurs in Sr_2RuO_4 only at low temperatures and in samples with a low residual resistivity, and it occurs out of a normal state that can be described well within Landau's Fermi liquid theory. This is in contrast to high–T_c cuprates. On the other hand, one may argue that $T_c \simeq 1.5$ K is

a relatively large transition temperature because the superconducting T_c for triplet pairing in ^{3}He is about 1 mK and thus three orders of magnitude smaller. An important result of Landau's Fermi liquid theory is that the resistivity ρ at low temperatures T should follow a $\rho \propto T^2$ law, which is a consequence of electron–electron collisions. The observation of this power law both within the RuO_2 planes and perpendicular to them (but with different prefactors, of course) clearly indicates that Fermi liquid theory is applicable. Furthermore, measurements of the Fermi velocity by de Haas–van Alphen experiments show that the effective mass is enhanced by a factor of 3 to 5, which agrees with values deduced from the specific heat coefficient, which is linear in T. This is also consistent with Landau's Fermi liquid theory [77].

In short, many experiments have confirmed that the dominant interactions in Sr_2RuO_4 are electron–electron interactions rather than the weaker interactions of the electron–phonon kind. Thus, on general grounds, one would expect that the superconductivity would turn out to be unconventional. In general, owing to Pauli's principle, (pairs of) fermions must have antisymmetric wave functions under particle interchange. For a Cooper pair this implies a relationship between the orbital and the spin character: orbital wave functions with even values for the orbital number ($l = 0, 2, \dots$), as in cuprates, are even under particle interchange and thus are spin singlets; on the other hand, odd values ($l = 1, 3, \dots$) require spin triplets. However, specifying the complete symmetry of the superconducting state requires more than just the angular–momentum channel and the spin state. The possible internal motion of the electrons (or holes) forming a Cooper pair has to be specified with respect to their center–of–mass coordinate, which must be in accordance with the underlying point group symmetry of the crystal. Note that the highly two-dimensional character of Sr_2RuO_4 (and its tetragonal symmetry) suggests pairing states that are mainly intraplanar rather than interplanar. This will be discussed later in detail.

Finally, we would like to mention the main experimental evidence for spin-triplet pairing in Sr_2RuO_4. The main proof comes from NMR experiments which measure the small change of the resonance line frequency caused by weak spin polarization of the electrons in an external applied field. In contrast to cuprates, where Cooper pairs are not polarized at all (because they are in a singlet state) and thus the Knight shift vanishes at low temperatures, in Sr_2RuO_4 *no* change (within the *ab* plane) has been observed [87]. This is expected for a triplet superconductor with parallel spins, where the application of a magnetic field changes only the relative numbers of spins parallel and antiparallel to the field. Thus the Knight shift is unchanged from its value in the normal state. Of course, these conclusions are only true for small spin–orbit coupling, i.e. $\mathbf{L} \cdot \mathbf{S}$ coupling, which seems to be the case for Sr_2RuO_4. More evidence for triplet pairing comes from the fact that the phase diagram of the Ruddlesen–Popper series (Fig. 1.9) suggests that Sr_2RuO_4 is indeed in the vicinity of a ferromagnetic transition. This, in analogy to ^{3}He, should

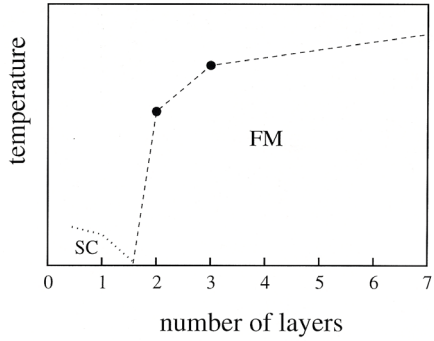

Fig. 1.9. Schematic phase diagram $T(n)$ of the Ruddlesen–Popper series $Sr_{n+1}Ru_nO_{3n+1}$ (after Sigrist *et al.* [86]). The number of layers is the parameter that determines the transition from a superconducting (SC) to a ferromagnetic (FM) state.

lead to a triplet state due to parallel spins already present in the normal state, and to p–wave pairing [45]. However, by fitting the specific heat and the ultrasound attenuation, Dahm *et al.* found reason to doubt the presence of p–wave superconductivity [88] and have proposed an f–wave symmetry of the superconducting order parameter. A similar conclusion has been drawn in [89]. Recently it has been reported that thermal–conductivity measurements are also most consistent with f–wave symmetry or with p–wave pairing within the planes and with nodes between the planes [90]. We shall therefore discuss later why the simple picture of p–wave pairing has to be modified strongly.

To summarize, the main questions in connection with Cooper pairing in Sr_2RuO_4 are:

- How can we explain the elementary excitations in the normal state, in particular the strong magnetic anisotropy observed in NMR experiments? What is the role of spin–orbit coupling and hybridization between the bands?
- How can we formulate an electronic theory for Cooper pairing in triplet superconductors, taking into account an interplay between ferromagnetic and strong *antiferromagnetic* spin fluctuations (resulting from nesting properties)?
- What symmetry of the superconducting order parameter is present in Sr_2RuO_4, if Cooper pairing due to spin excitations occurs mainly in–plane or mainly between RuO_2 planes?

1.4 From the Crystal Structure to Electronic Properties

After we have discussed the structure and the phase diagram of high-T_c cuprates and the main facts about triplet pairing in Sr_2RuO_4, the next step is to write down a Hamiltonian and to describe the elementary excitations with an electronic theory. Owing to the complexity of their structure, this is difficult. Instead, we need some reasonable simplifying approximations, for example we may construct a Hamiltonian for only a CuO_2 plane or RuO_2 plane. The very strong and important Cu-O–bonds in the conducting planes of cuprates and Ru-O–bonds in ruthenates justify this approximation.

1.4.1 Comparison of Cuprates and Sr_2RuO_4: Three–Band Approach

Many researchers believe that the general phase diagram for hole–doped cuprates presented in Fig. 1.4 (and also the phase diagram for electron–doped cuprates) can be explained within an approximation that focuses only on *one* CuO_2 plane. Why this is the case? As already mentioned, in the absence of doping the cuprates can be described well by mainly localized spin-1/2 states, which give these materials their antiferromagnetic character. The corresponding Cu and O orbitals are schematically shown in Fig. 1.10. The simplest microscopic model which can account for the calculated LDA band structure consists of two filled oxygen $p_{x,y}$ orbitals and one half–filled $d_{x^2-y^2}$ copper orbital. The bond lengths in the x and y directions are assumed to be identical. The corresponding tight–binding Hamiltonian reads

$$H_0^{3-band} = \epsilon_d \sum_{i,\sigma} d_{i\sigma}^\dagger d_{i\sigma} + \epsilon_p \sum_{i,\sigma} p_{i\sigma}^\dagger p_{i\sigma} + \sum_{\langle i,j\rangle\sigma} t_{pd}^{ij} \left(d_{i\sigma}^{(\dagger)} p_{j\sigma} + \text{h.c.} \right) + \sum_{\langle i,j\rangle\sigma} t_{pp}^{ij} \left(p_{i\sigma}^\dagger p_{j\sigma} + \text{h.c.} \right) . \quad (1.2)$$

Here, t_{pd}^{ij} and t_{pp}^{ij} are the corresponding hopping integrals between the orbitals shown in Fig. 1.10, and the sums are performed over copper and oxygen lattice positions labeled by i, where $\langle i, j\rangle$ denotes nearest–neighbor pairs, and σ is the spin index. Note that in the hole representation, the so–called charge–transfer gap $\Delta = \epsilon_p - \epsilon_d$ is positive.

However, the key ingredient missing in (1.2) is the strong Coulomb interaction in the Cu $3d$ wave functions. Thus, double occupancy is less energetically favored. A resultant Mott–Hubbard insulator was suggested early by Emery and coworkers [91, 92], which may be treated by a three-band version of the Hubbard Hamiltonian

$$H^{3-band} = H_0^{3-band} + U_d \sum_i n_{i\downarrow}^d n_{i\uparrow}^d + U_p \sum_i n_{i\downarrow}^p n_{i\uparrow}^p + U_{pd} \sum_{<i,j>} n_i^p n_j^d \quad , \quad (1.3)$$

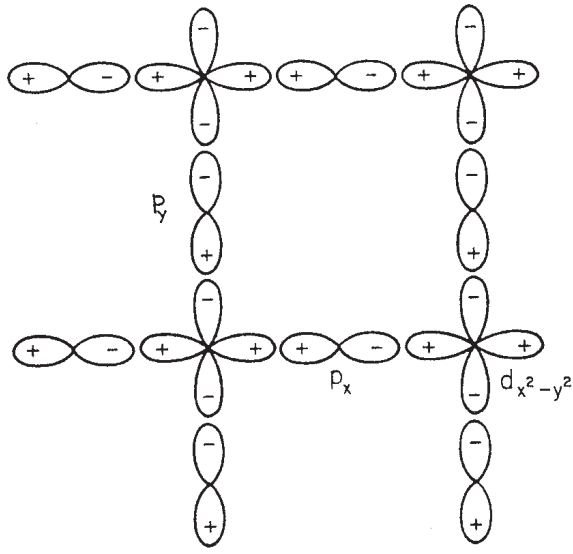

Fig. 1.10. Cu d- and oxygen p-orbitals within a CuO_2-plane. In the case of hole doping one has Zhang-Rice-like quasiparticles distributed on four oxygen sites around an Cu-atom. In electron-doped cuprates the doped electrons are more localized directly at the copper sites. Thus, in the electron-doped case, one finds a dilute antiferromagnet rather than frustrated spins.

where $n^d_{i\sigma} = d^\dagger_{i\sigma} d_{i\sigma}$ and $n^p_{i\sigma} = p^\dagger_{i\sigma} p_{i\sigma}$ are the Cu $3d$ and O $2p$ hole densities for site i and spin σ, and $n^{p,d}_i = \sum_\sigma n^{p,d}_{i\sigma}$. U_d and U_p denote the effective on–site copper and oxygen Hubbard repulsions, and U_{pd} refers to copper–oxygen interactions. H_0^{3-band} is defined in (1.2). Owing to the relatively small extent of the Cu $3d$ shell, U_d is the dominant correlation in (1.3). It can be derived from (1.2) that, in the case of $\Delta = \epsilon_p - \epsilon_d > 0$, the first hole added to the system will energetically prefer to occupy the d orbital of copper, while the next hole added will mainly occupy oxygen orbitals if $U_d > \Delta$. This is in agreement with electron energy loss spectroscopy (EELS) experiments by Nücker *et al.* [93]. Note that the values of the parameters in the Hamiltonian (1.3) can be estimated and are found to be in reasonable agreement with experiment [94, 95].

We would also like to mention that this three–band Hubbard Hamiltonian describing a single Cu–hole per unit cell in the regime t_{pp}, $t_{dp} \ll \Delta \ll U_d$ (charge–transfer insulator, CTI), can be mapped onto a 2D Heisenberg model,

$$H = J \sum_{\langle i,j \rangle} \mathbf{S}_i \cdot \mathbf{S}_j - \frac{1}{4} n^d_i n^d_j \quad , \tag{1.4}$$

where $\mathbf{S}_i$ refers to the copper spin, $\langle i, j \rangle$ again runs over pairs of nearest-neighbor copper sites, and J denotes the exchange coupling constant. J is

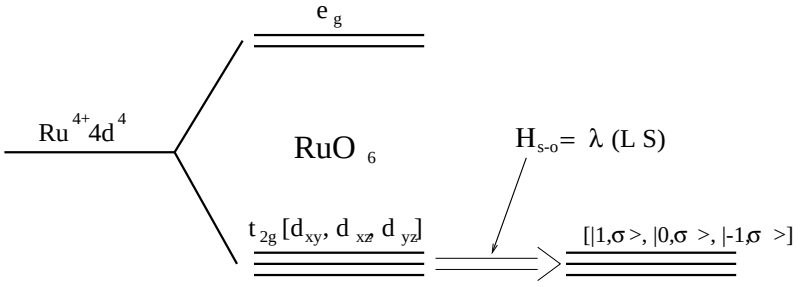

Fig. 1.11. Electronic structure of Sr_2RuO_4. The Ru ion is in the oxidation state Ru^{4+}, which corresponds to a $4d^4$ level. In addition, the 4d level is split in the RuO_6 crystal field into the e_g and t_{2g} subshells. The latter subshell, which consists of d_{xy}, d_{xz}, and d_{yz}, crosses the Fermi level. In addition, the spin–orbit coupling seems to play an important role and provides the mixing of the spin and orbital degrees of freedom.

of the order of 150 meV and can be determined by two–magnon Raman scattering, for example [13].

In the case of Sr_2RuO_4, it is also necessary to employ a three–band Hubbard Hamiltonian because three bands cross the Fermi level; see the electronic structure of Sr_2RuO_4 in Fig. 1.11. Thus we start from

$$H = H_t + H_U = \sum_{\mathbf{k},\sigma} \sum_{l} t_{\mathbf{k}l} a^{+}_{\mathbf{k},l\sigma} a_{\mathbf{k},l\sigma} + \sum_{i,l} U_l n_{il\uparrow} n_{il\downarrow} \quad , \tag{1.5}$$

where $a_{\mathbf{k},l\sigma}$ is the Fourier-transformed annihilation operator for the d_l orbital electrons ($l = xy, yz, zx$) and U_l is the corresponding on–site Coulomb repulsion. $t_{\mathbf{k}l}$ denotes the energy dispersions of the tight–binding bands, calculated as follows: $t_{\mathbf{k}l} = -\epsilon_0 - 2t_x \cos k_x - 2t_y \cos k_y + 4t' \cos k_x \cos k_y$. For our calculations, we chose the values for the parameter set $(\epsilon_0, t_x, t_y, t')$ as (0.5, 0.42, 0.44, 0.14), (0.23, 0.31, 0.055, 0.01), and (0.24, 0.045, 0.31, 0.01) eV for the d_{xy}, d_{zx}, and d_{yz} orbitals, respectively, in accordance with band structure calculations [78]. The electronic properties of this model applied to Sr_2RuO_4 were studied recently and were we found to be able to explain some features of the spin excitation spectrum of Sr_2RuO_4 [81, 96, 97]. However, this model fails to explain the observed magnetic anisotropy at low temperatures [85] and the possible line nodes in the superconducting order parameter below T_c. In contrast to cuprates, it is known that the spin–orbit coupling plays an important role in the superconducting state of Sr_2RuO_4 [96]. This is further confirmed by the recent observation of a large spin–orbit coupling in the insulator Ca_2RuO_4 [98]. Therefore, we shall include in our theory the spin–orbit coupling

$$H_{so} = \lambda \sum_{i} \mathbf{L}_i \mathbf{S}_i \quad , \tag{1.6}$$

where the angular momentum $\mathbf{L}_i$ operates on the three t_{2g} orbitals on the site i. Similarly to an earlier approach [96], we shall restrict ourselves to these three orbitals, ignoring e_{2g} orbitals, and choose the coupling constant λ such that the t_{2g} states behave like an $l = 1$ angular–momentum representation.

To summarize, a three–band Hubbard Hamiltonian provides a reasonable description of a CuO_2 plane in cuprates and of an RuO_2 plane in Sr_2RuO_4. In both cases the local Coulomb correlations play an important role in describing the electronic properties. This is because both classes of materials are in the vicinity of a magnetic transition (as described earlier). It turns out that for Sr_2RuO_4 no effective one–band approach can be applied, because all three bands cross the Fermi level and show signs of hybridization and strong spin–orbit coupling. On the other hand, for cuprate superconductors, an effective one-band theory is possible.

1.4.2 Effective Theory for Cuprates: One–Band Approach

Because a three-band Hamiltonian is difficult to solve, it is desirable to reduce it to a simpler model. It is generally believed that this is indeed possible for cuprate superconductors. Zhang and Rice [99] analyzed hole-doped cuprates and made progress in this direction by combining a Cu hole with an added hole (nearly on oxygen sites) to form a new spin singlet state and have shown that it is possible to work within this singlet subspace without changing the physics of the problem. In their description, the hole originally located at the oxygen has been replaced by a new (spin singlet) state at the copper. Thus, in this analysis, oxygen atoms are no longer present in an effective theory. Note this is *not* equivalent to simply removing one Cu spin–1/2 state, because frustration of spins is also induced owing to doping of holes on oxygen sites. A removal of one Cu spin–1/2 state takes place only in the case of electron–doped cuprates, where the additional electron goes directly on the copper site, yielding a dilute antiferromagnet.

The analysis of Zhang and Rice leads to the so–called t–J model (originally introduced by Anderson [100]),

$$H = J \sum_{\langle i,j \rangle} \left[\mathbf{S}_i \cdot \mathbf{S}_j - \frac{1}{4} n_i^d n_j^d \right] - t \sum_{\langle i,j \rangle \sigma} \left[c_{i\sigma}^\dagger \left(1 - n_{i-\sigma}\right) \left(1 - n_{j-\sigma}\right) c_{j\sigma} + \text{h.c.} \right] \quad , \tag{1.7}$$

or to an effective one–band Hubbard model,

$$H = -t \sum_{\langle i,j \rangle \sigma}^{nn} \left(c_{i\sigma}^\dagger c_{j\sigma} + \text{h.c.} \right) - t' \sum_{\langle i,j \rangle \sigma}^{nnn} \left(c_{j\sigma} + \text{h.c.} \right) + U \sum_i n_{i\uparrow} n_{i\downarrow} \quad , \tag{1.8}$$

which is the main model that we shall use for cuprates in this book. Here, as usual, $c_{i\sigma}^\dagger$ is a fermionic operator that creates an electron or hole at site i with

spin σ on a square lattice, and U denotes the effective Coulomb repulsion. $n_{i\sigma} = c^{\dagger}_{i\sigma} c_{i\sigma}$ is the density for spin σ. In addition to the usual hopping integral t describing nearest neighbors, we add also a second–nearest–neighbor hopping integral t'. The sums $\langle i, j \rangle$ are performed taking second–nearest–neighbors into account in this way.

Simply speaking, the one–band Hubbard model tries to mimic the presence of the charge-transfer gap Δ by means of an effective value of the Coulomb repulsion U. Thus, in the case of hole doping, the oxygen band becomes the lower band of the model. Note that in the strong–coupling limit it can be shown that the Hubbard model reduces to the t–J model. However, during this procedure, additional terms such as $-(1/4) n_i^d n_j^d$ appear spontaneously, which have not received much attention, and their importance is unclear. Usually, they are excluded from numerical studies.

In short, we believe that the one–band Hubbard model is more than just an appropriate starting point for building up an electronic theory of Cooper pairing within a CuO_2 plane. The main ingredients are present in this model: kinetic energy vs. potential energy, a strong repulsive (mainly on-site) interaction describing the physics in the vicinity of a Mott–Hubbard transition, and also itinerant carriers, which are experimentally observed in the CuO_2 planes and which can easily condense into Cooper pairs below T_c.

In order to obtain a unified theory for both hole–doped and electron–doped cuprates, it is tempting to use the same Hubbard Hamiltonian, taking into account, of course the different dispersions for the carriers [101]. As mentioned above, in the case of electron doping the electrons occupy copper d–like states of the upper Hubbard band, while the holes are related to oxygen–like p states, yielding different energy dispersions, which we shall use in our calculations. Then, assuming similar itinerancy of the electrons and holes, the mapping onto an effective one–band model seems to be justified. We consider U as an effective Coulomb interaction. Throughout this article we shall work within the grand canonical limit, with a chemical potential μ describing the band filling. The parameters t and t' will be employed to describe the normal–state energy dispersion measured in ARPES experiments, and a rigid–band approximation for all doping concentrations is assumed. This will be discussed in Chap. 2.

1.4.3 Spin Fluctuation Mechanism for Superconductivity

Before we illustrate how singlet pairing in high-T_c cuprates and triplet pairing in Sr_2RuO_4 are possible, let us remind the reader of some generalities. In connection with the general phase diagram for hole–doped cuprates, Fig. 1.4, we have discussed the occurrence of (mainly antiferromagnetic) spin fluctuations in the paramagnetic metallic state above T_c. These excitations can be measured in INS experiments, for example [43]. However, they do not appear as an additional excitation in the Hubbard Hamiltonian. Instead, these spin excitations are generated by itinerant carriers in the system and are mainly

of two–dimensional character, and thus are more robust than the long-range 3D Néel state. To study fluctuations in the paramagnetic state beyond the mean-field level it is convenient to employ the random–phase approximation (RPA). In particular, the spin-wave-like excitations can be obtained from the retarded transverse spin susceptibility

$$\chi^{+-}(\mathbf{q},\mathbf{q}',t) = i\Theta(t)\,\left\langle\left[S^{+}_{\mathbf{q}}(t), S^{-}_{\mathbf{q}'}(0)\right]\right\rangle \quad . \tag{1.9}$$

A similar expression holds for the longitudinal spin susceptibility χ^{zz}. The RPA result for the transverse spin susceptibility then reads [102]

$$\chi^{+-}_{RPA}(\mathbf{q},\mathbf{q}',z) = \sum_{q''} \chi_0(\mathbf{q},\mathbf{q}'',z)\,\left[1 - U\chi_0(\mathbf{q}'',\mathbf{q}',z)\right] \quad , \tag{1.10}$$

where χ_0 refers to the Lindhard function and has to be calculated from the single-particle Green's function G (and thus from the elementary excitations) of the system using the Hubbard Hamiltonian. z denotes a complex frequency. Note that G can also be simply related to the sublattice magnetization. Thus, we shall assume in the following that an effective perturbation series for the description of spin fluctuations is valid, and we shall sum the corresponding ladder and bubble diagrams up to infinite order at the RPA level. This procedure, for both singlet and triplet Cooper pairing, will be discussed in detail in the next chapter.

Next, we want to define the term "unconventional" and to investigate how a transition temperature T_c of the order of 100 K for hole–doped cuprates might occur as a result of a purely electronic (i.e. repulsive) mechanism. For this purpose, let us consider the simplified weak–coupling gap equation for singlet pairing ($T = 0$),

$$\Delta(\mathbf{k}) = -\sum_{\mathbf{k}'} \frac{V_s^{eff}(\mathbf{k}-\mathbf{k}')}{2E(\mathbf{k}')}\,\Delta(\mathbf{k}') \quad , \tag{1.11}$$

which is a self–consistency equation for the superconducting order parameter $\Delta(\mathbf{k})$ in momentum space, where $\mathbf{k}$ is defined in the first Brillouin zone. $V_s^{eff}(\mathbf{k}-\mathbf{k}')$ represents the effective two–particle pairing interaction in the singlet channel and is, to a good approximation, proportional to χ_{RPA} if Cooper pairing due to spin fluctuations is present. The energy $E(\mathbf{k}) = \sqrt{\Delta^2(\mathbf{k}) + \epsilon^2(\mathbf{k})}$ corresponds to the dispersion relation of the Bogoliubov quasiparticles (i.e. the Cooper pairs), where $\epsilon(\mathbf{k})$ denotes the dispersion of the electrons in the normal state. In the BCS theory, $V_s^{eff} < 0$ is taken as a constant and therefore one obtains a solution for $\Delta(\mathbf{k})$ of (1.11) which is structureless in momentum space.[2]

[2] Of course, owing to retardation effects, the summation in (1.11) runs over an energy shell of order ω_D; however, the arguments given above remain valid if one integrates over the whole Brillouin zone.

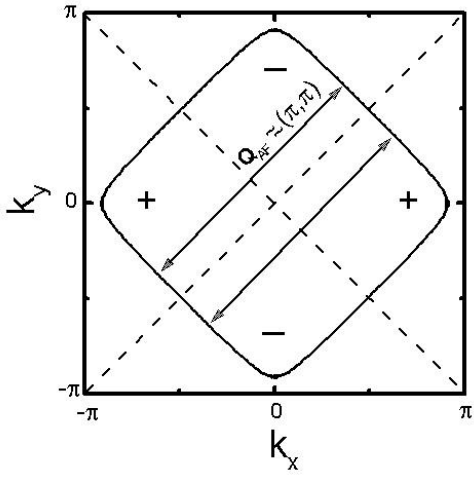

Fig. 1.12. Fermi surface of the one-band Hubbard model close to half-filling, for a square Brillouin zone. The nesting vector $\mathbf{Q}$ connects different parts of the Fermi surface where the $d_{x^2-y^2}$-wave order parameter has opposite sign. Thus the gap equation can be solved for a repulsive pairing potential. Along the diagonal lines, the corresponding gap has nodes (i.e. $\Delta(\mathbf{k})$ vanishes).

Let us now investigate the case of singlet pairing and how it is possible to solve (1.11) with a *repulsive* pairing potential. Owing to the fact that $V_s^{eff} > 0$, one might naively think that there exists no solution; however, this is wrong. If one takes into account that $V_s^{eff}(\mathbf{k} - \mathbf{k}')$ might have a strong momentum dependence, it is easily seen that indeed the gap equation has a solution. This can be recognized from Fig. 1.12, where we show the first Brillouin zone and a Fermi surface which corresponds to the half–filled case of the two-dimensional one–band Hubbard model. This Fermi surface in fact resembles the measured Fermi surface for the high–T_c superconductor $La_{2-x}Sr_xCuO_4$. For simplicity, we assume also an underlying tetragonal symmetry of the crystal. In order to illustrate the following argument, a possible superconducting order parameter ($d_{x^2-y^2}$–wave symmetry, with positive and negative signs) is also displayed. If one now assumes that the effective pairing interaction has a strong momentum dependence, for example a large peak at the antiferromagnetic wave vector $\mathbf{q}_{AF} = \mathbf{Q} = (\pi, \pi)$, $V_s^{eff}(\mathbf{k} - \mathbf{k}')$ connects different parts of the Fermi surface where the order parameter has opposite signs! Thus, one indeed finds a solution of equation (1.11). The simplest solution is the $d_{x^2-y^2}$–wave gap ($\Delta(\mathbf{k}) = \Delta_0 \left[\cos k_x - \cos k_y\right]/2$), which has nodes along the diagonals. Note, however, that for an effective pairing interaction which was structureless in momentum space, such a solution of the gap equation for a d–wave order parameter would not be possible. In fact, an order parameter which belonged to an anisotropic s–wave representation (possi-

bly with nodes) would not satisfy the pairing condition mentioned above either. In order to solve (1.11) for a pairing interaction which is peaked at (π, π), one definitely needs an order parameter that changes sign. Therefore, we see that the superconducting gap has less symmetry than the underlying Fermi surface. In such a situation where, in addition to a broken gauge ($U(1)$) invariance due to the occurrence of superconductivity, a further symmetry is broken (in our case invariance under a rotation of 90 degrees), we define the situation as "unconventional". Notice that this definition implies neither an electronic pairing mechanism nor a correspondingly large value of T_c. Finally, let us briefly mention that the arguments, given above are weak-coupling arguments which may be reformulated in the strong–coupling limit of the pairing process. However, it will turn out that, although lifetime effects of the electrons will lead to a renormalization of the quasiparticles, the weak-coupling arguments given above remain valid.

In the case of triplet pairing, one has to solve the corresponding gap equation

$$\Delta(\mathbf{k}) = -\sum_{\mathbf{k}'} \frac{V_t^{eff}(\mathbf{k}-\mathbf{k}')}{2E(\mathbf{k}')}\,\Delta(\mathbf{k}') \quad , \tag{1.12}$$

where $V_t^{eff}(\mathbf{k}-\mathbf{k}')$ denotes the effective two–particle pairing interaction in the triplet channel. Most importantly, Pauli's principle requires that $V_t^{eff} < 0$, i.e. an *attractive* pairing interaction in momentum space. This is in analogy to phonons, where the minus sign in front of the right-hand side of (1.12) is also canceled, which makes a solution of the gap equation relatively easy. In particular, if the transferred momentum $q = k - k'$ is small, one obtains a p–wave symmetry of the superconducting order parameter, for example

$$\Delta_p(\mathbf{k}) = \Delta_0(\sin k_x + i \sin k_y) \quad . \tag{1.13}$$

Note that the condition $q \approx 0$ is indeed fulfilled in the case of superfluid ^{3}He, which it is close to a ferromagnetic transition. Simply speaking, a similar situation is present in the case of Sr_2RuO_4 (see its phase diagram in Fig. 1.9), which makes p–wave symmetry the most probable candidate for the order parameter.

In order to investigate triplet pairing in Sr_2RuO_4 in more detail, we show in Fig. 1.13 its corresponding Fermi surface topology, obtained using the three–band Hubbard Hamiltonian discussed earlier in this chapter. However, for simplicity, we discuss here only the γ–band (which has a high density of states). Of course, the other bands (α and β) and their consequences will be analyzed in detail later. For the moment and for simplicity, let us discuss only the γ-band in order to discriminate between Sr_2RuO_4 and cuprates. A closer inspection of (1.13) shows that $|\Delta_p|^2$ has no nodes; however, $\mathrm{Re}\,\Delta_p$ (and also $\mathrm{Im}\,\Delta_p$) has a nodal line also displayed in Fig. 1.13. This has important consequences if nesting is present: the summation over $\mathbf{k}'$ in the first BZ is dominated by the contributions due to $\mathbf{Q}_{pair}$ and those due to a smaller

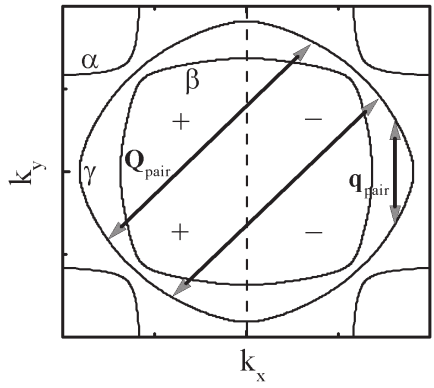

Fig. 1.13. Calculated Fermi surface (FS) topology for Sr_2RuO_4 and symmetry analysis of the superconducting order parameter Δ. The real part of the p–wave order parameter has a node along $k_x = 0$. The plus and minus signs and the *dashed lines* refer to the sign of the momentum dependence of Δ. α, β, and γ denote the FS of the corresponding (hybridized) bands.

wave vector $\mathbf{q}_{pair}$. Thus, we obtain approximately the following for the γ–band contribution ($l = f$ or p):

$$\Delta_l(\mathbf{k}) \approx \sum_i \frac{V_t^{eff}(\mathbf{Q}_i)}{2\epsilon^{\gamma}_{\mathbf{k}+\mathbf{Q}_i}} \Delta_l(\mathbf{k}+\mathbf{Q}_i) + \sum_i \frac{V_t^{eff}(\mathbf{q}_i)}{2\epsilon^{\gamma}_{\mathbf{k}+\mathbf{q}_i}} \Delta_l(\mathbf{k}+\mathbf{q}_i) \quad , \tag{1.14}$$

where the sum is over all contributions due to $\mathbf{Q}_i$ and $\mathbf{q}_{pair}$. The wave vectors $\mathbf{Q}_{pair}$ bridge portions of the FS where $\mathrm{Re}\,\Delta_p$ has opposite signs. Because the smaller wave vector $\mathbf{q}_{pair}$ bridges areas on the Fermi surface with both the same sign *and* opposite signs, its total contribution is almost zero, i.e.

$$\sum_i \frac{V_t^{eff}(\mathbf{q}_i)}{2\epsilon^{\gamma}_{\mathbf{k}+\mathbf{q}_i}} \Delta_l(\mathbf{k}+\mathbf{q}_i) \approx 0 \quad . \tag{1.15}$$

Thus, we find a gap equation where Δ_l is expected to change its sign for an attractive interaction. This is not possible! In other words, if the corresponding pairing interaction were to have nesting properties similar to those of cuprates, i.e. a peak of χ_{RPA} at $q \approx \mathbf{Q}_{pair}$, Cooper pairing and a solution of (1.13) would not be possible, because $V_t^{eff} < 0$. In this case, the nesting properties would suppress a p–wave and favor an f–wave, i.e.

$$\Delta_f(\mathbf{k}) = \Delta_0(\cos k_x - \cos k_y)(\sin k_x + i \sin k_y) \quad . \tag{1.16}$$

Like the $d_{x^2-y^2}$–wave order parameter in cuprates, the f–wave symmetry also has nodes along the diagonals.

To summarize this subsection, we have demonstrated on general grounds that, if Cooper pairing via spin fluctuations is present, the underlying Fermi

surface topology plays an important role. In particular, for singlet pairing one expects a $d_{x^2-y^2}$-wave order parameter if nesting properties are present. Without nesting, one expects no solution for a repulsive pairing interaction. In the case of (attractive) triplet pairing, no nesting properties are needed and p–wave symmetry of the superconducting order parameter occurs naturally if the pairing is dominated by nearly ferromagnetic spin fluctuations. However, if strong nesting is present, p–wave symmetry is suppressed and an order parameter with f–wave symmetry is possible. We shall see later in this book that the symmetry of the superconducting order parameter calculated from a microscopic electronic theory indeed follows these general arguments.

References

1. R. Simon, Phys. Today **44**, 64 (1991). 1
2. F. Siching and J. Frölingsdorf, Phys. Bl. **57**, 57 (2001). 1
3. J. D. Jorgensen, Phys. Today **44**, 34 (1991). 1
4. J. Bardeen, L. N. Cooper, and J. R. Schrieffer, Phys. Rev. B **108**, 1175 (1957). 2
5. J. Ruvalds, C. T. Rieck, S. Tewari, J. Thoma, and A. Virosztek, Phys. Rev. B **51**, 3797 (1995). 2
6. M. Lagues, *Proceedings of the NATO Advanced Research Workshop on New Trends in Superconductivity*, Yalta, Ukraine, edited by S. Kruchinin and J. Annett, Kluwer, Dordrecht (2001). 3
7. J. G. Bednorz and K. A. Müller, Z. Phys. B **64**, 189 (1986). 3
8. K. Shimizu, T. Kimura, S. Furomoto, K. Takeda, K. Kontani, Y. Onuki, and K. Amaya, Nature **412**, 316 (2001). 4
9. G. Burns, *High-Temperature Superconductivity*, Academic Press, New York (1992). 4, 5
10. D. R. Harshman and A. P. Mills Jr., Phys. Rev. B **45**, 10684 (1992). 4
11. R. J. Birgenau and G. Shirane, in *Physical Properties of High-Temperature Superconductors*, edited by D. M. Ginsberg, World Scientific, Singapore, page 151 (1989). 4
12. J. Rossat-Mignod, L. P. Regnault, C. Vettier, P. Burlet, J. Y. Henry, and G. Lapertot, Physica B **169**, 58 (1991). 4
13. K. B. Lyons, P. A. Fleury, R. R. Singh, and P. E. Sulewski, in *NATO Advanced Workshop on Dynamics and Magnetic Fluctuations in High-Temperature Superconductors*, edited by G. Reiter, P. Horsch, and G. Psaltakis, Plenum, New York, page 159 (1991). 4, 21
14. S.-W. Cheong, Z. Fisk, J. O: Willis, S. E. Brown, J. D. Thompson, J. P. Remeika, A. S. Cooper, R. M. Aikin, D. Schiferl, and G. Gruner, Solid State Commun. **65**, 111 (1988). 4
15. T. Thio, T. R. Thurston, N W. Preyer, P. J. Picone, M. A. Kastner, H. P. Jenssen, D. R. Gabbe, C. Y. Chen, R. J. Birgeneau, and A. Aharony, Phys. Rev. B **38**, 905 (1988). 4
16. D. Manske, *Phonons, Electronic Correlations, and Self-Energy Effects in High-T_c Superconductors*, Dissertation, Shaker Verlag, Aachen (1997). 7

17. J. L. Tallon, C. Bernhard, H. Shaked, R. L. Hittermann, and J. D. Jorgensen, Phys. Rev. B **51**, 12911 (1995). 8, 12
18. A. Lanzara, P. V. Bogdanov, X. J. Zhou, S. A. Kellar, W. J. Zheng, E. D. Lu, Y. Yoshida, H. Elsaki, A. Fijimori, K. Kishio, J.-I. Shimoyama,, T. Noda, S. Uchida, Z. Hussain, and Z.-X. Shen, Nature **412**, 510 (2001). 9, 10
19. P. D. Johnson, T. Valla, A. V. Fedorov, Z. Yusof, B. O. Wells, Q. Li, A. R. Moodenbaugh, G. D. Gu, N. Koshizuka,, C. Kendziora, S. Jian, and D. G. Hinks, Phys. Rev. Lett. **87**, 177007 (2001). 9
20. A. Kaminski, M. Randeria, J. C. Campuzano, M. R. Norman, H. Fretwell, J. Mesot, T. Sato, T. Takahashi, and K. Kadowaki, Phys. Rev. Lett. **86**, 1070 (2001). 9
21. R. J. McQueeney, Y. Petrov, T. Egami, M. Yethiraj, G. Shirane, and Y. Endoh, Phys. Rev. Lett. **82**, 628 (1999). 10
22. C. P. Slichter in *Strongly Correlated Electronic Systems*, edited by K. S. Bedell, Addison Wesley, Reading, MA (1994). 11
23. L. P. Regnault, P. Bourges, P. Burlet, J. Y. Henry, J. Rossat-Mignod, Y. Sidis, and C. Vettier, Physica B **213–214**, 48 (1995). 11
24. D. S. Marshall, D. S. Dessau, A. G. Loeser, C.-H. Park, A. Y. Matsuura, J. N. Eckstein, I. Bozovic, P. Fournier, A. Kapitulnik, W. E. Spicer, and Z.-X. Shen, Phys. Rev. Lett. **76**, 4841 (1996). 11
25. P. J. White, Z.-X. Shen, C. Kim, J. M. Harris, A. G. Loeser, P. Fournier, and A. Kapitulnik, Phys. Rev. B **54**, R15669 (1996). 11
26. J. Loram, K. A. Mirza, J. R. Cooper, and W. Y. Liang, Phys. Rev. Lett. **71**, 1740 (1993); J. W. Loram, J. Supercond. **7**, 234 (1994). 11
27. B. Batlogg, H. Y. Hwang, H. Takagi, R. J. Cava, H. L. Kao, and J. Kwo, Physica C **235–240**, 130 (1994). 11
28. R. Nemetschek, M. Opel, C. Hoffmann, P. F. Müller, R. Hackl, H. Berger, L. Forro, A. Erb, and E. Walker, Phys. Rev. Lett. **78**, 4837 (1997). 11
29. C. Renner, B. Revaz, J.-Y. Genoud, K. Kadowaki, and Ø. Fischer, Phys. Rev. Lett. **80**, 149 (1998). 11
30. A. K. Gupta and K.-W. Ng, Phys. Rev. B **58**, R8901 (1998). 11
31. Y. Onose, Y. Taguchi, K. Ishizaka, and Y. Tokura, Phys. Rev. Lett. **87**, 217001 (2001). 11
32. A. Biswas, P. Furnier, V. N. Smolyaninova, R. C. Budhani, J. S. Higgins, and R. L. Greene, Phys. Rev. B **64**, 104519 (2001). 11
33. S. Kleefisch, B. Welter, A. Marx, L. Alff, R. Gross, and M. Naito, Phys. Rev. B **63**, R100507 (2001). 11
34. C. M. Varma, P. B. Littlewood, S. Schmitt-Rink, E. Abrahams, and A. E. Ruckenstein, Phys. Rev. Lett. **63**, 1996 (1989). 11
35. A. Virosztek and J. Ruvalds, Phys. Rev. B **42**, 4064 (1990). 11
36. J. Ruvalds, C. T. Rieck, J. Zhang, and A. Virosztek, Science **256**, 1664 (1992). 11
37. A. J. Millis, H. Monien, and D. Pines, Phys. Rev. B **42**, 167 (1990). 11
38. A. Kaminski, S. Rosenkranz, H. M. Fretwell, J. C. Campuzano, Z. Li, H. Raffy, W. G. Cullen, H. You, C. G. Olson, C. V. Varma, and H. Höchst, Nature **416**, 610 (2002). 11
39. R. Zeyher and A. Greco, Phys. Rev. Lett. **89**, 177004 (2002). 11
40. Z. A. Xu, N. P. Ong, Y. Wang, T. Kakeshita, S. Uchida, Nature **406**, 486 (2000) 11

41. C. Meingast, V. Pasler, P. Nagel, A. Gykov, S. Tajima, and P. Olsson, Phys. Rev. Lett. **86**, 1606 (2001). 11
42. I. Iguchi, T. Yamaguchi, and A. Sugimoto, Nature **412**, 420 (2001). 11
43. L. P. Regnault, P. Bourges, and P. Burlet, in *Neutron Scattering in Layered Copper-Oxide Superconductors*, edited by A. Furrer, Kluwer Academic, London (1998). 12, 23
44. K. Yamada, K. Kurahashi, Y. Endoh, R. J. Birgeneau, and G. Sirane, J. Phys. Chem. Solids **60**, 1025 (1999). 12
45. A. J. Layzer and D. Fay in *Proceedngs of the International Low Temperature Conference*, St. Andrews (LT-11), Academic Press, London (1968); P. W. Anderson and W. F. Brinkmann, in *The Physics of Liquid and Solid Helium*, Vol. 2, edited. by K. H. Bennemann and J. B. Ketterson, Wiley-Interscience (1978). 12, 18
46. N. F. Berk and J. R. Schrieffer, Phys. Rev. Lett. **17**, 433 (1966). 12
47. M. R. Presland, J. L. Tallon, R. G. Buckley, R. S. Liu, and N. E. Flower, Physica C **176**, 95 (1991); J. R. Cooper and J. W. Loram, J. Phys. I **6**, 1 (1996); J. L. Tallon and J. W. Loram, Physica C **349**, 53 (2001). 12
48. D. A. Wollmann, D. J. van Harlingen, W. C. Lee, D. M. Ginsberg, and A. J. Leggett, Phys. Rev. Lett. **71**, 2134 (1993). 12
49. J. R. Kirtley, C. C. Tsuei, J. Z. Sun, C. C. Chi, L. S. Yu-Jahnes, A. Gupta, M. Rupp, and M. B. Ketchen, Nature **373**, 225 (1995). 12
50. C. C. Tsuei, J. R. Kirtley, M. Rupp, J. Z. Sun, A. Gupta, M. B. Ketchen, C. A. Wang, Z. F. Ren, J. H. Wang, and M. Bhushan, Science **272**, 329 (1996). 12
51. C. C. Tsuei, J. R. Kirtley, Rev. Mod. Phys. **72**, 969 (2000). 12, 14
52. H. F. Fong, B. Keimer, D. Reznik, D. L. Milius, and I. A. Aksay, Phys. Rev. B **54**, 6708 (1996). 13
53. H. He, Y. Sidis, P. Bourges, G. D. Gu, A. Ivanov, N. Koshizuka, B. Liang, C. T. Lin, L. P. Regnault, E. Schoenherr, and B. Keimer, Phys. Rev. Lett. **86**, 1610 (2001). 13
54. H. He, P. Bourges, Y. Sidis, C. Ulrich, L. P. Regnault, S. Pailhes, N. S. Berzigiarova, N. N. Kolesnikov, and B. Keimer, Science **285**, 1045 (2002). 13
55. P. Dai, H. A. Mook, S. M. Hayden, G. Aeppli, T. G. Perring, R. D. Hunt, F. Dogan, Science **284**, 1344 (1999). 13
56. P. Bourges, B. Keimer, L. P. Regnault, and Y. Sidis, Science **288**, 1234 (2000). 13
57. W. N. Hardy, D. A. Bonn, D. C. Morgan, R. Liang, and K. Zhang, Phys. Rev. Lett. **70**, 3999 (1994). 13
58. S. Kamal, R. Liang, A. Hosseini, D. A. Bonn, and W. N. Hardy, Phys. Rev. B **58**, R8933 (1998); S, Kamal, D. A. Bonn, N. Goldenfeld, P. J. Hirschfeld, R. Liang, and W. N. Hardy, Phys. Rev. Lett. **73**, 1845 (1994). 13
59. Z. X. Shen, D. S. Dessau, B. O. Wells, D. M. King, W. E. Spicer, A. J. Arko, D. Marshall, L. W. Lombardo, A. Kapitulnik, P. Dickinson, S. Doniach, J. DiCarlo, T. Loeser, and C. H. Park, Phys. Rev. Lett. **70**, 1553 (1993). 13
60. A. A. Abrikosov and L. A. Fal'kovskii, Zh. Eksp. Teor. Fiz. **40**, 262 (1961) [Sov. Phys. JETP **13**, 67 (1961)]. 13
61. T. P. Devereaux, D. Einzel, B. Stadlober, R. Hackl, D. H. Leach, and J. J. Neumeier, Phys. Rev. Lett. **72**, 396 (1994). 13

62. M. C. Krantz and M. Cardona, J. Low Temp. Phys. **99**, 205 (1995). 13
63. D. Einzel and R. Hackl, J. Raman Spectrosc. **27**, 307 (1996). 13
64. T. P. Devereaux and D. Einzel, Phys. Rev. B **51**, 16336 (1995); Phys. Rev. B **54**, 15547 (1996). 13
65. D. Manske, C. T. Rieck, R. Das Sharma, A. Bock, and D. Fay, Phys. Rev. B **56**, R2940 (1997). 13
66. Q. Li, Y. N. Tsay, M. Suenaga, R. A. Klemm, G. D. Gu, and N. Koshizuka, Phys. Rev. Lett. **83**, 4160 (1999). 13
67. A. Bille, R. A. Klemm, and K. Scharnberg, Phys. Rev. B **64**, 174507 (2001). 13
68. Y. Takano, T. Hatano, A. Fukuyo, A. Ishii, M. Ohmori, S. Arisawa, K. Togano, and M. Tachiki, Phys. Rev. B **65**, 140513 (2002). 13
69. R. A. Klemm, Physica B **329–333**, 1325 (2003). 13
70. C. C. Tsuei and J. R. Kirtley, Phys. Rev. Lett. **85**, 182 (2000). 14
71. N. P. Armitage, D. H. Lu, D. L. Feng, C. Kim, A. Damascelli, K. M. Shen, F. Ronning, Z. X. Shen, Y. Onose, Y. Taguchi, and Y. Tokura, Phys. Rev. Lett. **86**, 1126 (2001). 14
72. T. Sato, T. Kamiyama, T. Takahashi, K. Kurahashi, and K. Yamada, Science **291**, 1517 (2001). 14
73. S. M. Anlage, D.-H. Wu, S. N. Mao, X. X. Xi, T. Venkatesan, J. L. Peng, and R. L. Greene, Phys. Rev. B. **50**, 523 (1994). 14
74. B. Stadlober, G. Krug. R. Nemetschek, R. Hackl, J. L. Cobb, and J. T. Markert, Phys. Rev. Lett. **74**, 4911 (1995). 14
75. L. Alff, A. Beck, R. Gross, A. Marx, S. Kleefisch, T. Bauch, H. Sato, M. Naito, and G. Koren, Phys. Rev. B. **58**, 11197 (1998). 14
76. Y. Maeno, H. Hashimoto, K. Yoshida, S. Nishizaki, T. Fujita, J. G. Bednorz, and F. Lichtenberg, Nature **372**, 532 (1994). 15
77. Y. Maeno, T. M. Rice, and M. Sigrist, Phys. Today **54**, 42 (2001). 16, 17
78. A. Liebsch and A. Lichtenstein, Phys. Rev. Lett. **84**, 1591 (2000). 15, 21
79. Y. Sidis, M. Braden, P. Bourges, B. Hennion, S. NishiZaki, Y. Maeno, and Y. Mori, Phys. Rev. Lett. **83**, 3320 (1999). 16
80. H. Mukuda, K. Ishida, Y. Kitaoka, K. Asayama, Z. Mao, Y. Mori, and Y. Maeno, J. Phys. Soc. Jpn. **67**, 3945 (1998); H. Mukuda, K. Ishida, Y. Kitaoka, K. Asayama, R. Kanno, and M. Takano, Phys. Rev. B. **60**, 12279 (1999). 16
81. I. I. Mazin and D. J. Singh, Phys. Rev. Lett. **82**, 4324 (1999); D. J. Singh, Phys. Rev. B. **52**, 1358 (1995). 16, 21
82. M. E. Zhitomirsky and T. M. Rice, Phys. Rev. Lett. **87**, 057001 (2001). 16
83. J. F. Annett, G. Litak, B. L. Gyorffy, and K. I. Wysokinsi, preprint cond-mat/0109023 (unpublished). 16
84. F. Servant, S. Raymond, B. Fak, P. Lejay, and J. Flouquet, Solid State Commun. **116**, 489 (2000). 16
85. K. Ishida, H. Mukuda, Y. Minami, Y. Kitaoka, Z. Q. Mao, H. Fukazawa, and Y. Maeno, Phys. Rev. B **64**, 100501(R) (2001). 16, 21
86. M. Sigrist, D. Agterberg, A. Furusaki, C. Honerkamp, K. K. Ng, T. M. Rice, and M. E. Zhitomirsky, Physica C **317–318**, 134 (1999). 18
87. K. Ishida, H. Mukuda, Y. Kitaoka, K. Asayama, Z. Q. Mao, Y. Mori, and Y. Maeno, Nature **396**, 658 (1998). 17
88. H. Won and K. Maki, Europhys. Lett. **52**, 427 (2000); T. Dahm, H. Won, and K. Maki, preprint cond-mat/0006301 (unpublished). 18

89. Y. Hasegawa, K. Machida, and M. Ozaki, J. Phys. Soc. Jpn. **69**, 336 (2000). 18
90. K. Izawa, H. Takahashi, H. Yamaguchi, Y. Matsuda, M. Suzuki, T. Sasaki, T. Fukase, Y. Yoshida, R. Settai, and Y. Onuki, Phys. Rev. Lett. **86**, 2653 (2001). 18
91. V. J. Emery, Phys. Rev. Lett. **58**, 2794 (1987). 19
92. V. J. Emery and G. Reiter, Phys. Rev. B **38**, 4547 (1988). 19
93. N. Nücker, Z. Phys. B **67**, 9 (1987). 20
94. M. S. Hybertsen, M. Schlüter, and N. E. Christensen, Phys. Rev. B **39**, 9028 (1989). 20
95. F. Mila, Phys. Rev. B **38**, 11358 (1988). 20
96. K. K. Ng and M. Sigrist, Europhys. Lett. **49**, 473 (2000). 21, 22
97. D. K. Morr, P. F. Trautmann, and M. J. Graf, Phys. Rev. Lett. **86**, 5978 (2001). 21
98. T. Mizokawa, L. H. Tjeng, G. A. Sawatzky, G. Ghiringhelli, O. Tjernberg, N. B. Brookes, H. Fukazawa, S. Nakatsuji, and Y. Maeno, Phys. Rev. Lett. **87**, 077202 (2001). 21
99. F. C. Zhang and T. M. Rice, Phys. Rev. B **37**, 3759 (1988). 22
100. P. W. Anderson, Science **235**, 1196 (1987). 22
101. D. M. King, Z.-X. Shen, D. S. Dessau, B. O. Wells, W. E. Spicer, A. J. Arko, D. S. Marshall, J. DiCarlo, A. G. Loeser, C. H. Park, E. R. Ratner, J. L. Peng, Z. Y. Li, and R. L. Greene, Phys. Rev. Lett. **70**, 3159 (1993). 23
102. J. R. Schrieffer, X. G. Wen, and S. C. Zhang, Phys. Rev. B **39**, 11663 (1989); J. R. Schrieffer, X. G. Wen, and S. C. Zhang, Phys. Rev. Lett. **60**, 944 (1988). 24

2 Theory of Cooper Pairing Due to Exchange of Spin Fluctuations

2.1 Generalized Eliashberg Equations for Cuprates and Strontium Ruthenate

It is of general interest whether singlet high-T_c superconductivity in the hole- and electron-doped cuprates and triplet pairing in strontium ruthenate (Sr_2RuO_4) can be explained by use of generalized Eliashberg equations describing the exchange of magnetic degrees of freedom as the relevant pairing mechanism. As pointed out in the preceding chapter, for the description of superconductivity in cuprates, the two-dimensional (one-band) Hubbard model should be an appropriate starting point because superconductivity occurs in the vicinity of an antiferromagnetic phase transition. The Hubbard model reads, on a tetragonal lattice and in second quantization,

$$H = -\sum_{\langle ij\rangle\sigma} t_{ij}\left(c^{\dagger}_{i\sigma}c_{j\sigma} + c^{\dagger}_{j\sigma}c_{i\sigma}\right) + U\sum_{i} n_{i\uparrow}n_{i\downarrow} - \mu t\sum_{i\sigma} n_{i\sigma}. \tag{2.1}$$

Here, $c^{\dagger}_{i\sigma}$ and $c_{i\sigma}$ create and annihilate an electron or hole on site i with spin σ, t_{ij} denotes the hopping matrix element, and the sum $\langle ij\rangle$ is performed over nearest neighbors. In this case, t_{ij} is equal to t. U corresponds to the intra-orbital (i.e. on-site) effective Coulomb repulsion, $n_{i\sigma} = c^{\dagger}_{i\sigma}c_{i\sigma}$, and μ denotes the chemical potential. Thus the model can be characterized by two dimensionless parameters, U/t and μ.

Using Bloch wave functions, one arrives at

$$H = \sum_{\mathbf{k}\sigma}\epsilon_{\mathbf{k}}c^{\dagger}_{\mathbf{k}\sigma}c_{\mathbf{k}\sigma} + \frac{U}{2N}\sum_{\mathbf{k}\mathbf{k}'\mathbf{q}\sigma} c^{\dagger}_{\mathbf{k}\sigma}c^{\dagger}_{\mathbf{k}',-\sigma}c_{\mathbf{k}'+\mathbf{q},-\sigma}c_{\mathbf{k}-\mathbf{q},\sigma}, \tag{2.2}$$

where the one-band electron (or hole) energy is

$$\epsilon_{\mathbf{k}} = -2t\left[\cos(k_x) + \cos(k_y) + \frac{\mu}{2}\right] \tag{2.3}$$

or

$$\epsilon_{\mathbf{k}} = -2t\left[\cos(k_x) + \cos(k_y) - 2t'\cos(k_x)\cos(k_y) + \frac{\mu}{2}\right], \tag{2.4}$$

for nearest-neighbor or next-nearest-neighbor hopping (described by tt'), respectively. N denotes the number of lattice points. Here and in the following, we set the lattice constant to unity. In order to obtain a unified theory

D. Manske: Theory of Unconventional Superconductors, STMP 202, 33–97 (2004)

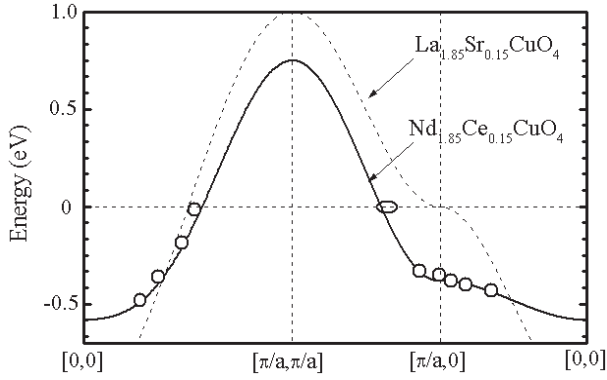

Fig. 2.1. Results for the energy dispersion ϵ_k of optimally hole-doped $La_{1.85}Sr_{0.15}CuO_4$ (LSCO, *dashed curve*) and of optimally electron-doped $Nd_{1.85}Ce_{0.15}CuO_4$ (NCCO). The dashed curve corresponds to using $t = 250$ meV and $t' = 0$, and is typical of hole-doped cuprates. The *solid curve* refers to our tight-binding calculation, choosing $t = 138$ meV and $t' = 0.3$. Data (*open circles*) are taken from [5].

for both hole-doped and electron-doped cuprates, we use the same Hubbard Hamiltonian, taking into account the different dispersions of the carriers. Experiments have shown that in the case of electron doping the electrons occupy the copper d-like states of the upper Hubbard band, while the holes are related to oxygen-like p states, yielding different energy dispersions. For an improved view, one should employ a three-band p–d model [1, 2] and use a generalized tight-binding method for determining the hopping parameters [3]. However, it turns out, for a wide range of doping that it is sufficient to use effective parameters for the band dispersion [4].

As an example, we show in Fig. 2.1 the energy dispersions for optimally hole-doped $La_{2-x}Sr_xCuO_4$ (LSCO) and electron-doped $Nd_{1.85}Ce_{0.15}CuO_4$ (NCCO). Using $t = 250$ meV, (2.3) describes the Fermi surface of LSCO, whereas $t = 138$ meV and $t' = 0.3$ in (2.4) correspond to NCCO. One immediately sees the important difference: in the case of NCCO, the flat part of the quasiparticle band is approximately 300 meV *below* the Fermi level, whereas for the hole-doped case the flat band lies very close to the Fermi level. Thus, as will be discussed later, by using the resulting ϵ_k in a theory of spin-fluctuation-induced pairing, we obtain a smaller T_c for electron-doped cuprates than for the hole-doped ones.

With the help of the Heisenberg picture, i.e.

$$c_{\mathbf{k}\sigma}(\tau) \equiv e^{\tau H}\, c_{\mathbf{k}\sigma}\, e^{-\tau H} \tag{2.5}$$

and

$$\bar{c}_{\mathbf{k}\sigma}(\tau) \equiv e^{\tau H}\, c^{\dagger}_{\mathbf{k}\sigma}\, e^{-\tau H} \quad , \tag{2.6}$$

where τ corresponds to an imaginary time, we define the one-particle Green's functions as

$$\begin{aligned} G_{\alpha\beta}(\mathbf{k},\tau) &= -\langle T_\tau\, c_{\mathbf{k}\alpha}(\tau) c^\dagger_{\mathbf{k}\beta}\rangle \\ \bar{G}_{\alpha\beta}(\mathbf{k},\tau) &= -\langle T_\tau\, \bar{c}_{-\mathbf{k}\alpha}(\tau) c_{-\mathbf{k}\beta}\rangle \\ F_{\alpha\beta}(\mathbf{k},\tau) &= -\langle T_\tau\, c_{\mathbf{k}\alpha}(\tau) c_{-\mathbf{k}\beta}\rangle \\ \bar{F}_{\alpha\beta}(\mathbf{k},\tau) &= -\langle T_\tau\, \bar{c}_{-\mathbf{k}\alpha}(\tau) c^\dagger_{\mathbf{k}\beta}\rangle \quad . \end{aligned} \tag{2.7}$$

Here, T_τ is the time-ordering operator:

$$\begin{aligned} T_\tau\, \psi(\tau_1)\phi(\tau_2) &= \psi(\tau_1)\phi(\tau_2) \qquad \text{for} \qquad \tau_1 > \tau_2 \quad , \\ T_\tau\, \psi(\tau_1)\phi(\tau_2) &= \pm\, \phi(\tau_2)\phi(\psi_1) \qquad \text{for} \qquad \tau_1 < \tau_2 \quad , \end{aligned} \tag{2.8}$$

and

$$\langle A\rangle = \frac{\mathrm{Tr}\left[e^{-\beta H} A\right]}{\mathrm{Tr}\left[e^{-\beta H}\right]} \quad . \tag{2.9}$$

The plus and minus signs apply for boson and fermion operators, respectively, Tr denotes the trace, and $\beta = (k_B T)^{-1}$ is the inverse temperature.

Throughout this book we use mainly the FLuctuatuation EXchange (FLEX) [6, 7, 8, 9, 10, 11, 12, 13] or T-matrix [14] approximation for the dressed one-particle Green's functions which will solve the generalized Eliashberg equations. The physical idea is that these dressed Green's functions are used to calculate the charge and spin susceptibilities in the paramagnetic (metallic) regime, where superconductivity occurs in the cuprates. These susceptibilities are used to construct a Berk Schrieffer-like [15] pairing interaction describing the exchange of charge and spin fluctuations. In particular, within this approach, the itinerant character of the quasiparticles is taken into account. Perturbation theory graphs for the exchange of longitudinal and transverse spin fluctuations are shown in Fig. 2.2. This gives rise to an effective electron electron interaction [15]

$$\Gamma_1 = V^{eff} = \frac{U^2\chi_0(q'+q)}{1-U\chi_0(q'+q)} + \frac{U^3\chi_0^2(q'-q)}{1-U^2\chi_0^2(q'-q)} \quad . \tag{2.10}$$

Note that a self-consistent treatment of the quasiparticles and the pairing interaction is essential and is required because the electrons or holes not only condense into Cooper pairs but also provide the pairing interaction. This is in contrast to a phonon-mediated pairing interaction within standard BCS and Eliashberg theory, where the feedback of the pairing interaction on the spectral function of the electrons is, according to Migdal's theorem [16, 17], very small. Details of the numerical procedure can be found in Appendix A.

In the case of high-T_c cuprates, the corresponding self-energy reads

$$\begin{aligned} \Sigma^G(\mathbf{k}, i\omega_n) = \frac{1}{\beta N}\sum_{\mathbf{k}' i\omega'_n} \Bigg[&\frac{1}{2}U^2 \frac{\chi_{c0}(\mathbf{q}, i\nu_m)}{1+U\chi_{c0}(\mathbf{q}, i\nu_m)} + \frac{3}{2}U^2 \frac{\chi_{s0}(\mathbf{q}, i\nu_m)}{1-U\chi_{s0}(\mathbf{q}, i\nu_m)} \\ &+ U^2\chi_G(\mathbf{q}, i\nu_m)\Bigg] G(\mathbf{k}', i\omega'_n) \end{aligned} \tag{2.11}$$

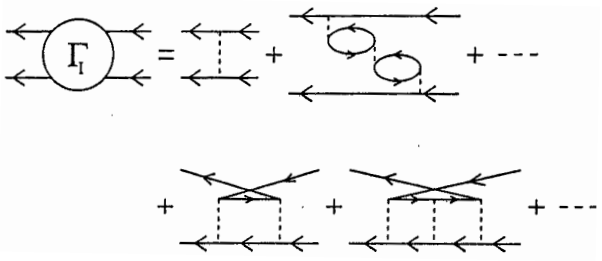

Fig. 2.2. Particle particle channel of the Bethe Salpeter equation for superconductivity, containing RPA diagrams for the effective pairing interaction V^{eff} for singlet pairing in cuprates consisting of the exchange of longitudinal and transverse spin fluctuations. The *solid lines* refer to G and the *dashed lines* denote the effective Coulomb interaction U. Vertex corrections that would yield a renormalized coupling strength $U_{\rm eff}$ are neglected. The summation of the corresponding bubble and ladder diagrams is performed up to infinity. While in principle it is possible to treat $V_{\rm eff}\{\chi\}$ and $G(\mathbf{k},\omega)$ on different levels, we assume that both quantities are generated by the *same* itinerant quasiparticles.

and

$$\Sigma^F(\mathbf{k},i\omega_n) = -\frac{1}{\beta N}\sum_{\mathbf{k}'i\omega_n'}\left[\frac{1}{2}U^2\frac{\chi_{c0}(\mathbf{q},i\nu_m)}{1+U\chi_{c0}(\mathbf{q},i\nu_m)} - \frac{3}{2}U^2\frac{\chi_{s0}(\mathbf{q},i\nu_m)}{1-U\chi_{s0}(\mathbf{q},i\nu_m)} - U^2\chi_F(\mathbf{q},i\nu_m)\right]G(\mathbf{k}',i\omega_n') \tag{2.12}$$

where $i\nu_m = i\omega_n - i\omega_n'$. The term $U^2\chi_{G,F}$ on the right-hand side compensates double counting that occurs in the second order. Σ^G and Σ^F denote the normal and superconducting parts, respectively, of the self-energy [14]. χ_{c0} and χ_{s0} correspond to the irreducible charge and spin susceptibilities, respectively, and are given by

$$\begin{aligned}\chi_{c0}(\mathbf{q},i\nu_m) &= -\frac{1}{\beta N}\sum_{\mathbf{k}i\omega_n}\left[G(\mathbf{k}+\mathbf{q},i\omega_n+i\nu_m)G(\mathbf{k},i\omega_n)\right.\\ &\quad\left. - F(\mathbf{k}+\mathbf{q},i\omega_n+i\nu_m)F^\dagger(-\mathbf{k},i\omega_n)\right]\\ &\equiv \chi_G(\mathbf{q},i\nu_m) - \chi_F(\mathbf{q},i\nu_m)\end{aligned} \tag{2.13}$$

and

$$\chi_{s0}(\mathbf{q},i\nu_m) \equiv \chi_G(\mathbf{q},i\nu_m) + \chi_F(\mathbf{q},i\nu_m) \quad . \tag{2.14}$$

In the Nambu notation [18], the one-particle Green's function is a 2×2-matrix

$$\hat{G}(\mathbf{k},i\omega_n) = \int_0^\beta d\tau\, e^{i\omega_n\tau}\hat{G}(\mathbf{k},\tau) \quad , \tag{2.15}$$

where

$$\hat{G}(\mathbf{k},\tau) = -\langle T_\tau\, \psi_{\mathbf{k}}(\tau)\psi^\dagger_{\mathbf{k}}(0)\rangle \tag{2.16}$$

and

$$\psi_{\mathbf{k}}(\tau) = \begin{pmatrix} c_{\mathbf{k}\uparrow}(\tau) \\ c^\dagger_{-\mathbf{k}\downarrow}(\tau) \end{pmatrix} \quad . \tag{2.17}$$

In order to obtain the renormalized single-particle Green's function, we solve the Dyson equation

$$\hat{G}^{-1} = \hat{G}_0^{-1} - \hat{\Sigma} \quad , \tag{2.18}$$

which relates the matrix representing the bare propagator $\hat{G}_0$ and its renormalization due to the sum of all irreducible self-energy diagrams $\hat{\Sigma}$ to the dressed propagator $\hat{G}$. The Dyson equation reads in Nambu space

$$\hat{G}^{-1} = \begin{pmatrix} G_0^{-1} - \Sigma^G & -\Sigma^F \\ -\bar{\Sigma}^F & \bar{G}_0^{-1} - \bar{\Sigma}^G \end{pmatrix} \quad , \tag{2.19}$$

where the inverse bare propagator is given by $\hat{G}_0^{-1} = i\omega_n - \epsilon_{\mathbf{k}}$. Because $\mathrm{Re}\,\Sigma$ is symmetric and $\mathrm{Im}\,\Sigma$ is antisymmetric with respect to $i\omega_n$, it is possible to make the following ansatz:

$$\Sigma^G(\mathbf{k}, i\omega_n) = i\omega_n\,[1 - Z(\mathbf{k}, i\omega_n)] + \xi(\mathbf{k}, i\omega_n) \tag{2.20}$$

$$\Sigma^F(\mathbf{k}, i\omega_n) = \phi(\mathbf{k}, i\omega_n) \quad , \tag{2.21}$$

where Z and ξ are real and also symmetric with respect to $i\omega_n$. Z describes the renormalization of the quasiparticle mass and ξ corresponds to the renormalization of the bare band energy $\epsilon_{\mathbf{k}}$. This will be discussed later in detail. $\phi(\mathbf{k}, i\omega_n) = Z(\mathbf{k}, i\omega_n)\Delta(\mathbf{k}, i\omega_n)$ denotes the strong-coupling superconducting gap function. Note that if one chooses the phase α between the anomalous Green's functions in

$$F(\mathbf{k}, i\omega_n) = e^{2i\alpha} F^*(\mathbf{k}, -i\omega_n) \tag{2.22}$$

to be equal to zero, no equation for $\bar{\phi}(\mathbf{k}, i\omega_n)$ occurs. With the help of (2.20) and (2.21), we are now able to write down the diagonal and off-diagonal parts of the one-particle Green's function [19]:

$$G(\mathbf{k}, i\omega_n) = \frac{i\omega_n Z(\mathbf{k}, i\omega_n) + \epsilon_{\mathbf{k}} + \xi(\mathbf{k}, i\omega_n)}{\left(i\omega_n Z(\mathbf{k}, i\omega_n)\right)^2 - \left(\epsilon_{\mathbf{k}} + \xi(\mathbf{k}, i\omega_n)\right)^2 - \phi^2(\mathbf{k}, i\omega_n)} \tag{2.23}$$

and

$$F(\mathbf{k}, i\omega_n) = \frac{\phi(\mathbf{k}, i\omega_n)}{\left(i\omega_n Z(\mathbf{k}, i\omega_n)\right)^2 - \left(\epsilon_{\mathbf{k}} + \xi(\mathbf{k}, i\omega_n)\right)^2 - \phi^2(\mathbf{k}, i\omega_n)} \quad . \tag{2.24}$$

Because we want to solve the generalized Eliashberg equations on the real ω axis rather than on the Matsubara points on the imaginary axis, we use now the spectral representation of the one-particle Green's function

$$G(\mathbf{k}, i\omega_n) = \int_{-\infty}^{\infty} d\omega \, \frac{N(\mathbf{k}, \omega)}{i\omega_n - \omega} \tag{2.25}$$

and

$$F(\mathbf{k}, i\omega_n) = \int_{-\infty}^{\infty} d\omega \, \frac{A_1(\mathbf{k}, \omega)}{i\omega_n - \omega} \quad . \tag{2.26}$$

Inserting (2.25) and (2.26) into (2.13) and (2.14), and performing the sum over the Matsubara frequencies [20], we arrive at

$$\begin{aligned} \mathrm{Im}\, \chi_{s0,c0}(\mathbf{q}, \omega) &= \frac{\pi}{N} \int_{-\infty}^{\infty} d\omega' \, [f(\omega') - f(\omega' + \omega)] \\ &\times \sum_{\mathbf{k}} [N(\mathbf{k} + \mathbf{q}, \omega' + \omega) N(\mathbf{k}, \omega') \pm A_1(\mathbf{k} + \mathbf{q}, \omega' + \omega) A_1(\mathbf{k}, \omega')] \,, \end{aligned} \tag{2.27}$$

where f denotes the Fermi distribution function. Thus we arrive at the following set of equations for the quasiparticle self-energy components X_ν ($\nu = 0$, 3, 1) with respect to the Pauli matrices τ_ν in the Nambu representation, which are usually called *generalized Eliashberg equations*, which one has to solve self-consistently:

$$\begin{aligned} X_\nu(\mathbf{k}, \omega) = \sum_{\mathbf{k}'} \int_0^\infty \mathrm{d}\Omega \, [P_s(\mathbf{k} - \mathbf{k}', \Omega) + (\delta_{\nu 0} + \delta_{\nu 3} - \delta_{\nu 1}) \, P_c(\mathbf{k} - \mathbf{k}', \Omega)] \\ \times \int_{-\infty}^{\infty} \mathrm{d}\omega' \, I(\omega, \Omega, \omega') A_\nu(\mathbf{k}', \omega') \quad , \end{aligned} \tag{2.28}$$

where $X_0 = \omega(1 - Z)$ (renormalization), $X_3 = \xi$ (energy shift), and $X_1 = \phi$ (gap parameter). The kernel I and the spectral functions A_ν are given by

$$I(\omega, \Omega, \omega') = \frac{f(-\omega') + b(\Omega)}{\omega + i\delta - \Omega - \omega'} + \frac{f(\omega') + b(\Omega)}{\omega + i\delta + \Omega - \omega'} \quad , \tag{2.29}$$

$$A_\nu(\mathbf{k}, \omega) = -\pi^{-1} \, \mathrm{Im} \, [a_\nu(\mathbf{k}, \omega)/D(\mathbf{k}, \omega)] \quad ,$$

and

$$\begin{aligned} D &= [\omega Z]^2 - [\epsilon(\mathbf{k}) + \xi]^2 - \phi^2 \quad , \\ a_0 &= \omega Z, \quad a_3 = \epsilon(\mathbf{k}) + \xi, \quad a_1 = \phi \quad . \end{aligned} \tag{2.30}$$

Here, b denotes the Bose distribution function. The band filling $n = \sum_{\mathbf{k}} n_{\mathbf{k}}$ is determined with the help of the $\mathbf{k}$-dependent occupation number $n_{\mathbf{k}} = 2 \int_{-\infty}^{\infty} \mathrm{d}\omega f(\omega) A(\mathbf{k}, \omega)$, which is calculated self-consistently. $n = 1$ corresponds to half filling. The spin and charge fluctuation interactions are given by

$$P_s = (2\pi)^{-1} U^2 \, \mathrm{Im} \, (3\chi_s - \chi_{s0}) \qquad , \qquad \chi_s = \chi_{s0} \, (1 - U\chi_{s0})^{-1} \tag{2.31}$$

and

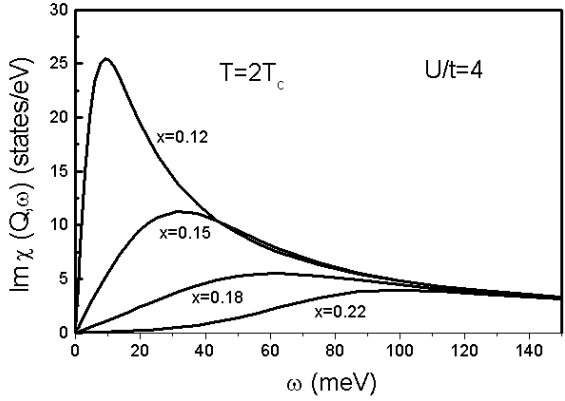

Fig. 2.3. Calculated dynamical spin susceptibility $\mathrm{Im}\,\chi(\mathbf{Q},\omega)$ at a temperature $T = 2T_c$ for different doping concentrations: $x = 0.12$ (underdoped), $x = 0.15$ (optimal doping), $x = 0.18$, and $x = 0.22$ (overdoped).

$$P_c = (2\pi)^{-1} U^2 \,\mathrm{Im}\,(3\chi_c - \chi_{c0})\,, \qquad , \qquad \chi_s = \chi_{c0}\,(1 + U\chi_{c0})^{-1} \quad . \tag{2.32}$$

Here, we use $N(\mathbf{k},\omega) = A(\mathbf{k},\omega) = A_0(\mathbf{k},\omega) + A_3(\mathbf{k},\omega)$. For an illustration, we show in Fig. 2.3 the calculated dynamical spin susceptibility for various doping concentrations. The real parts were calculated with the help of the Kramers–Kronig relation. Note that the subtracted terms in (2.31) and (2.32) remove a double counting that occurs in the second order. The method of solution of (2.28)–(2.32) is described in Appendix A.

Before we extend our theory to include effects of Cooper pairs and amplitude fluctuations, let us briefly discuss the solutions of the generalized Eliashberg equations (2.28)–(2.32) derived so far. For this purpose it is instructive to calculate all characteristic temperature scales (i.e. $T_c(x)$, $T^*(x)$, and $T_c^*(x)$) for hole-doped cuprates as a function of the doping concentration x.

In Fig. 2.4, we present our results for the mean-field (i.e. without Cooper pair phase and amplitude fluctuations) phase diagram $T(x)$ obtained by solving (2.28)–(2.32) self-consistently on the real frequency axis. A bandwidth of $W = 8t = 2$ eV was assumed. Below a characteristic temperature T^*, the so-called weak pseudogap temperature, we find a reduction of spectral weight in the density of states $N(\omega = 0)$, which is shown in the inset for $x = 0.15$. Such a behavior is seen experimentally in various superconductor–insulator–superconductor (SIS) and superdonductor–insulator–normal metal (SIN) tunneling data, in reflectivity measurements and in the two-magnon response in Raman scattering [22, 23]. Physically speaking, below T^* the electrons at the Fermi level scatter inelastically from antiferromagnetic spin fluctuations. However, the calculated size of the pseudogap is too small in comparison with experiment. Furthermore, there exists no pseudogap in the calculated $\mathbf{k}$-dependent spectral function $N(\mathbf{k},\omega)$. In order to solve this prob-

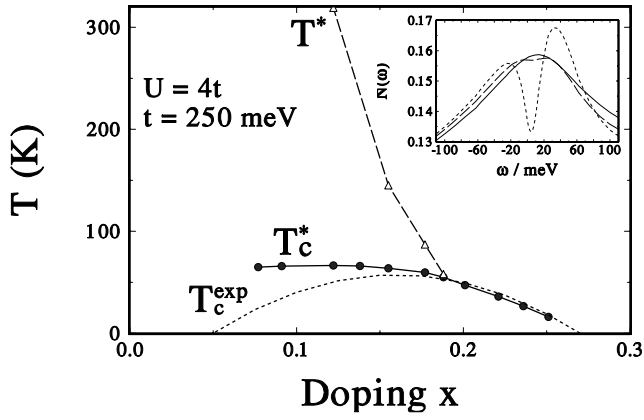

Fig. 2.4. Results for the 2D one-band Hubbard model for hole-doped cuprates *without* Cooper pair phase and amplitude fluctuations, for various hole doping concentrations $x = 1 - n$ and with an on-site Coulomb repulsion $U = 4t$, where t is the nearest neighbor hopping integral. Below the weak pseudogap temperature T^* (*dashed line*) one finds a reduction of spectral weight in the density of states at $\omega = 0$ (see *inset*). T_c^* (*solid line*) denotes the superconducting transition temperature, neglecting Cooper pair phase fluctuations. The *dotted line* corresponds to a phenomenological fit to experimental data [21]. *Inset:* density of states $N(\omega)$ in units of $1/t$ for doping $x = 0.15$ at temperatures $T = 4.5T_c^*$ (*solid line*), $T = 2.3T_c^* \equiv T^*$ (*dashed line*), and $T = 1.01T_c^*$ (*dotted line*).

lem one has to extend the FLEX approximation by the inclusion of a d-wave pseudogap, which is observed experimentally. The resulting equations will be presented in the next section. However, the origin of the pseudogap is still unknown.

At T_c^* the largest eigenvalue of the linearized gap equation reaches unity; in other words, we find an off-diagonal self-energy contribution due to the formation of Cooper pairs. A similar behavior of this instability was found in [8, 11]. Below T_c^*, we find a $d_{x^2-y^2}$-wave order parameter. Note that in an isotropic system, the 2D long-range order would be destroyed owing to phase fluctuations [24, 25]. Therefore, this temperature T_c^* is a mean-field transition temperature in the sense that Cooper pair phase fluctuations have been neglected. However, the antiferromagnetic fluctuations are treated well beyond the mean-field level. Owing to our self-consistent treatment of the self-energy described in Appendix A, we never reach the antiferromagnetic phase transition in our calculations, where perturbation theory would no longer be valid.

In Fig. 2.4, we also compare our results for T_c^* with the generalized experimental phase diagram $T_c^{exp}(x)$ that describes many hole-doped high-T_c superconductors, as pointed out by Tallon [21] and discussed in the previous chapter. One can clearly see that T_c^* agrees with experiment in the overdoped

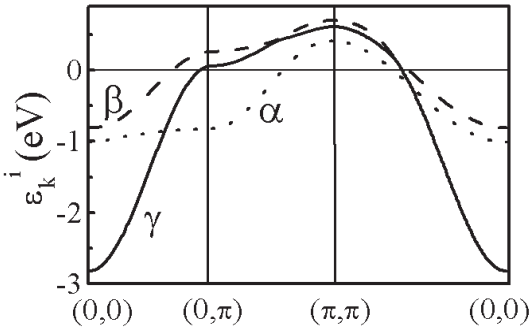

Fig. 2.5. Results for the energies ϵ_k^i of the hybridized bands ($i = \alpha,\ \beta,\ \gamma$) in Sr_2RuO_4.

region, whereas in the underdoped region T_c^* and T_c^{exp} obviously disagree. We shall see in the next subsection that this discrepancy can be resolved if phase fluctuations of the Cooper pairs are taken into account. Finally, we would like to mention that T^* and T_c^* coincide at $x = x^* = 0.19$. This suggests that for $x > x^*$, magnetic degrees of freedom do not play a dominant role in the one-particle spectral function, yielding Fermi-liquid-like properties although spin fluctuations still mediate the pairing interaction.

Let us now turn to the case of triplet Cooper pairing in Sr_2RuO_4. As mentioned in the Introduction, Sr_2RuO_4 is a layered system and there are three Ru^{4+} t_{2g} bands that cross the Fermi level, with approximately two-thirds filling of every band. Thus, in contrast to the situation for cuprates, this makes it difficult to employ an effective one-band Hamiltonian. Therefore we start from the two-dimensional three-band Hubbard Hamiltonian

$$H = \sum_{\mathbf{k},\sigma} \sum_{\alpha} t_{\mathbf{k}\alpha} a^{+}_{\mathbf{k},\alpha\sigma} a_{\mathbf{k},\alpha\sigma} + \sum_{i,\alpha} U_\alpha \, n_{i\alpha\uparrow} n_{i\alpha\downarrow} \quad , \tag{2.33}$$

where $a_{\mathbf{k},\alpha\sigma}$ is the Fourier transform of the annihilation operator for the d_α orbital electrons ($\alpha = xy,\ yz,\ zx$) and U_α is an effective on-site Coulomb repulsion. $t_{\mathbf{k}\alpha}$ denotes the energy dispersions of the tight-binding bands,

$$t_{\mathbf{k}\alpha} = -\epsilon_0 - 2t_x \cos k_x - 2t_y \cos k_y + 4t' \cos k_x \cos k_y \quad . \tag{2.34}$$

In accordance with experimental measurements of the Fermi surface and energy dispersions, we have choosen the values for the parameter set $(\epsilon_0, t_x, t_y, t')$ as (0.5, 0.42, 0.44, 0.14), (0.23, 0.31, 0.055, 0.01), and (0.24, 0.045, 0.31, 0.01) eV for d_{xy}, d_{zx}, and d_{yz} orbitals [26]. An analysis of de Haas–van Alphen experiments [27] shows a substantial hybridization (or spin–orbit coupling) between xz- and yz- orbitals of about $t_\perp = 0.1$ eV, but not with the xy-orbital [28]. However, the observation of a single T_c implies a coupling between all three bands. Therefore, we have choosen a weak hybridization $t_{hyb} = 0.01$ eV (hybridization between xy orbitals and xz, yz) $\ll t_\perp$. Note that even such

a weak hybridization transfers the nesting properties to the xy orbital. This will be discussed later in detail.

For a comparison with cuprates, we show in Fig. 2.5 the resultant energy dispersions of the hole-like α-band and electron-like β- and γ-bands obtained after hybridization. Owing to the small value of the hybridization between the xy orbitals and the yz and xz orbitals, the dispersion curves and resulting Fermi surface look quite similar to the nonhybridized ones [29]. However, the hybridization between these orbitals is important for the spin susceptibility $\chi(\mathbf{q},\omega)$. This susceptibility is given by

$$\chi_0^{ij}(\mathbf{q},\omega) = \frac{1}{N}\sum_{\mathbf{k}} \frac{f(\epsilon^i_{\mathbf{k},\gamma}) - f(\epsilon^j_{\mathbf{k}+\mathbf{q},\gamma})}{\epsilon^i_{\mathbf{k}+\mathbf{q},\gamma} - \epsilon^j_{\mathbf{k},\gamma} + \omega + i0^+} \quad , \tag{2.35}$$

where $f(\epsilon)$ is the Fermi function and ϵ^i_k is the energy dispersion of the α, β, and γ band.[1]

In order to obtain an effective spin response of Sr_2RuO_4, we employ the random-phase approximation and diagonalize the matrix $[\chi_0^{ij}]$, which leads to

$$\chi(\mathbf{q},\omega) = \frac{\chi_0(\mathbf{q},\omega)}{1 - U(\mathbf{q})\chi_0(\mathbf{q},\omega)} \quad , \tag{2.36}$$

where now

$$\chi_0(\mathbf{q},\omega) = \sum_{i'} \chi_0^{i'}(\mathbf{q},\omega) \quad . \tag{2.37}$$

Here, $\chi_0^{i'}(\mathbf{q},\omega)$ ($i' = \alpha'$, β', γ') are the diagonal elements of the diagonalized matrix $[\chi_0^{ij}]$ and $U(\mathbf{q})$ is an effective Coulomb interaction. The effective susceptibility $\chi(\mathbf{q},\omega)$ obtained characterizes the normal–state magnetic properties of Sr_2RuO_4. As we shall discuss later, the spin fluctuations of this material have peaks at wave vectors $\mathbf{Q}_i$ and $\mathbf{q}_i$, which are important for determining the symmetry of the superconducting order parameter.

The electronic properties of this model applied to Sr_2RuO_4 were studied recently and can explain some features of the spin excitation spectrum in Sr_2RuO_4 [30, 31, 28]. However, this model fails to explain the observed magnetic anisotropy at low temperatures measured in NMR experiments [32]. On the other hand, it is known that the spin–orbit coupling plays an important role in the superconducting state of Sr_2RuO_4 [31]. This is further confirmed by the recent observation of a large spin–orbit coupling in the insulator Ca_2RuO_4 [33]. Therefore, we include in our theory spin–orbit coupling:

$$H_{so} = \lambda \sum_i \mathbf{L}_i \cdot \mathbf{S}_i \quad , \tag{2.38}$$

[1] We include also the matrix element for the spin susceptibility χ_0^{ij}, taken to be 1 between two states which have the same maximal character and 0 otherwise, in accordance with [30].

where the angular momentum $\mathbf{L}_i$ operates on the three t_{2g} orbitals on the site i. Similarly to an earlier approach [31], we restrict ourselves to these three orbitals, ignoring e_{2g} orbitals, and choose the coupling constant λ such that the t_{2g} states behave like an $l = 1$ angular–momentum representation. Moreover, it is known that the quasi-two-dimensional xy band is separated from the quasi-one-dimensional xz and yz bands. In this case, one expects that the effect of spin–orbit coupling will be small and it be excluded for simplicity. Therefore, we consider the effect of the spin–orbit coupling on xz and yz bands only. The kinetic part of the Hamiltonian $H_t + H_{so}$ can then be diagonalized, and the new energy dispersions are

$$\begin{aligned} \epsilon^{\sigma}_{\mathbf{k},yz} &= (t_{\mathbf{k},yz} + t_{\mathbf{k},xz} + A_{\mathbf{k}})/2 \quad , \\ \epsilon^{\sigma}_{\mathbf{k},xz} &= (t_{\mathbf{k},yz} + t_{\mathbf{k},xz} - A_{\mathbf{k}})/2 \quad , \end{aligned} \tag{2.39}$$

where $A_{\mathbf{k}} = \sqrt{(t_{\mathbf{k},yz} - t_{\mathbf{k},xz})^2 + \lambda^2}$, and σ refers to spin projection. One can clearly see that the spin–orbit coupling does not remove the Kramers degeneracy of the spins. Therefore, the resultant Fermi surface consists of three sheets, as observed in the experiments. Most importantly, spin–orbit coupling together with (2.33) leads to a new quasiparticle, which we label by pseudo-spin and pseudo-orbital indices. The unitary transformation $\tilde{U}_{\mathbf{k}}$ connecting theold and new quasiparticles is defined for each wave vector and leads to the following relations:

$$\begin{aligned} c^{+}_{\mathbf{k},yz+} &= u_{1\mathbf{k}} a^{+}_{\mathbf{k},yz+} - i v_{1\mathbf{k}} a^{+}_{\mathbf{k},xz+} \quad , \\ c^{+}_{\mathbf{k},xz+} &= u_{2\mathbf{k}} a^{+}_{\mathbf{k},yz+} - i v_{2\mathbf{k}} a^{+}_{\mathbf{k},xz+} \quad , \\ c^{+}_{\mathbf{k},yz-} &= u_{1\mathbf{k}} a^{+}_{\mathbf{k},yz-} + i v_{1\mathbf{k}} a^{+}_{\mathbf{k},xz-} \quad , \\ c^{+}_{\mathbf{k},xz-} &= u_{2\mathbf{k}} a^{+}_{\mathbf{k},yz-} + i v_{2\mathbf{k}} a^{+}_{\mathbf{k},xz-} \quad , \end{aligned} \tag{2.40}$$

where

$$u_{m\mathbf{k}} = \frac{\lambda}{\sqrt{(t_{\mathbf{k},yz} - t_{\mathbf{k},xz} \mp A_{\mathbf{k}})^2 + \lambda^2}} \tag{2.41}$$

and

$$v_{m\mathbf{k}} = \frac{t_{\mathbf{k},yz} - t_{\mathbf{k},xz} \mp A_{\mathbf{k}}}{\sqrt{(t_{\mathbf{k},yz} - t_{\mathbf{k},xz} \mp A_{\mathbf{k}})^2 + \lambda^2}} \quad . \tag{2.42}$$

The minus and plus signs refer to $m = 1$ and $m = 2$, respectively.

In Fig. 2.6 we show the resultant Fermi surfaces for $t_{hyb} = 0$ for each band obtained, where we have chosen $\lambda = 100$ meV in agreement with earlier estimations [31, 33]. One can immediately see that xz and yz bands split around the nested parts, in good agreement with experiment [26]. Thus, spin–orbit coupling acts like a hybridization between these bands. However, in contrast to a simple hybridization as described above, spin–orbit coupling also introduces an anisotropy for the states with pseudo-spins $\uparrow$ and $\downarrow$. This will be reflected in the magnetic susceptibility. Since the spin and orbital

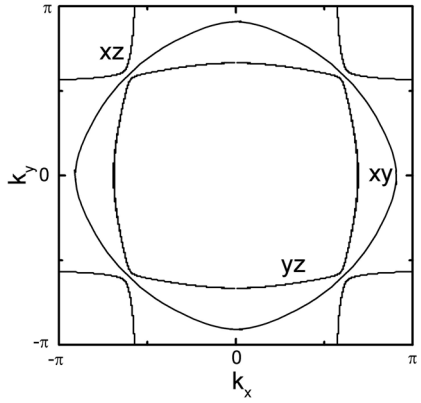

Fig. 2.6. Calculated Fermi surface for an RuO_2 plane in Sr_2RuO_4 for $t_{hyb} = 0$ taking into account spin–orbit coupling.

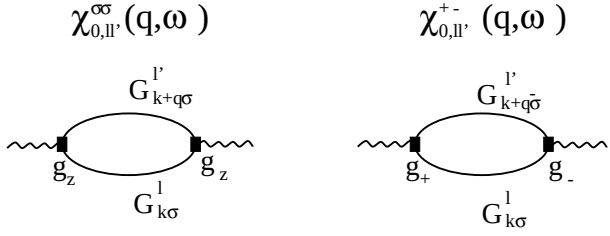

Fig. 2.7. Diagrammatic representation of the transverse and longitudinal components of the magnetic susceptibility. The *full lines* represent the electron Green's function, with pseudospin indices σ and pseudo-orbital indexes l; g_+ and g_z denote the vertices as described in the text.

degrees of freedom are now mixed, resulting in a "spin–orbital" liquid, the magnetic susceptibility involves also the orbital magnetism, which is very anisotropic.

For the calculation of the transverse and longitudinal components, χ_l^{+-} and χ_l^{zz}, respectively, of the spin susceptibility of each band l, we use the diagrammatic representation shown in Fig. 2.7. Since the Kramers degeneracy is not removed by the spin–orbit coupling, the main anisotropy arises from the calculations of the anisotropic vertices $g_z = \tilde{l}_z + 2s_z$ and $g_+ = \tilde{l}_+ + 2s_+$ calculated on the basis of the new quasiparticle states. In addition, owing to the hybridization between the xz and yz bands, we have also calculate the transverse and longitudinal components of the the interband susceptibility $\chi_{ll'}$. For example,

$$\chi^{+-}_{0,xz}(\mathbf{q},\omega) = -\frac{4}{N}\sum_{\mathbf{k}}(u_{2\mathbf{k}}u_{2\mathbf{k}+\mathbf{q}} - v_{2\mathbf{k}}v_{2\mathbf{k}+\mathbf{q}})^2\,\frac{f(\epsilon^+_{\mathbf{k}xz}) - f(\epsilon^-_{\mathbf{k}+\mathbf{q}xz})}{\epsilon^+_{\mathbf{k}xz} - \epsilon^-_{\mathbf{k}+\mathbf{q}xz} + \omega + iO^+} \tag{2.43}$$

and

$$\chi^{zz}_{0,xz}(\mathbf{q},\omega) = \chi^{\uparrow}_{xz}(\mathbf{q},\omega) + \chi^{\downarrow}_{xz}(\mathbf{q},\omega)$$
$$= -\frac{2}{N}\sum_{\mathbf{k}}\left[u_{2\mathbf{k}}u_{2\mathbf{k}+\mathbf{q}} + v_{2\mathbf{k}}v_{2\mathbf{k}+\mathbf{q}} + \sqrt{2}(u_{2\mathbf{k}}v_{2\mathbf{k}+\mathbf{q}} + v_{2\mathbf{k}}u_{2\mathbf{k}+\mathbf{q}})\right]^2$$
$$\times \frac{f(\epsilon^{+}_{\mathbf{k}xz}) - f(\epsilon^{+}_{\mathbf{k}+\mathbf{q}xz})}{\epsilon^{+}_{\mathbf{k}xz} - \epsilon^{+}_{\mathbf{k}+\mathbf{q}xz} + \omega + iO^{+}} \quad , \tag{2.44}$$

where $f(x)$ is again the Fermi function and $u^2_{\mathbf{k}}$ and $v^2_{\mathbf{k}}$ are the corresponding coherence factors, which we have calculated through the corresponding vertices using (2.40). For all other orbitals, the calculations are straightforward. Note that the magnetic response of the xy band remains isotropic.

One can clearly see the difference between the longitudinal and transverse components which results from the calculated matrix elements. Moreover, the longitudinal component contains an extra term due to $\tilde{l}_z$, while the transverse component does not contain contributions from $\tilde{l}_+$ or $\tilde{l}_-$. The latter occurs because xz and yz states are a combination of the real orbital states $|2,+1\rangle$ and $|2,-1\rangle$. Thus a transition between these two states is not possible with $\tilde{l}_+$ or $\tilde{l}_-$ operators. Therefore, each component of the longitudinal susceptibility has an extra term in the matrix element that significantly enhances their absolute values.

Assuming $U_{ij} = \delta_{ij}U$, one obtains the following expression for the transverse susceptibility within the RPA:

$$\chi^{+-}_{RPA,l}(\mathbf{q},\omega) = \frac{\chi^{+-}_{0,l}(\mathbf{q},\omega)}{1 - U\chi^{+-}_{0,l}(\mathbf{q},\omega)} \quad . \tag{2.45}$$

For the longitudinal susceptibility, one obtains

$$\chi^{zz}_{RPA,l}(\mathbf{q},\omega) = \frac{\chi^{\uparrow}_{0,l}(\mathbf{q},\omega) + \chi^{\downarrow}_{0,l}(\mathbf{q},\omega) + 2U\chi^{\uparrow}_{0,l}(\mathbf{q},\omega)\chi^{\downarrow}_{0,l}(\mathbf{q},\omega)}{1 - U^2\chi^{\downarrow}_{0,l}(\mathbf{q},\omega)\chi^{\uparrow}_{0,l}(\mathbf{q},\omega)} \quad . \tag{2.46}$$

For the construction of a pairing theory, we follow the analysis by Anderson and Brinkmann for ^{3}He [34] and use the calculated Fermi surface and spin susceptibility for Sr_2RuO_4 including spin–orbit coupling. In order to discriminate between cuprates and Sr_2RuO_4, we remind the reader that the effective Berk–Schrieffer–like interaction reads as follows for singlet pairing in the weak-coupling limit (i.e. $\omega, \omega' \to 0$), neglecting double counting in the second order:

$$V^{eff}_0(\mathbf{k},\mathbf{k}') = \frac{U^2\chi_0(\mathbf{k}-\mathbf{k}',0)}{1 - U\chi_0(\mathbf{k}-\mathbf{k}',0)} + \frac{U^3\chi^2_0(\mathbf{k}-\mathbf{k}',0)}{1 - U^2\chi^2_0(\mathbf{k}-\mathbf{k}',0)} \quad . \tag{2.47}$$

Remember that the first term arises from the contributions from the ladder diagrams, whereas the second term corresponds to infinite series of bubble diagrams of the Bethe–Salpeter equation. We abbreviate the effective Coulomb

interaction to $U \equiv U(\mathbf{Q}_i)$. In (2.47) we have also assumed that no self-consistent calculation of $\chi(\mathbf{q} = \mathbf{k} - \mathbf{k}', \omega = 0)$ is required. Thus we work with χ_0, which enters (2.36). Of course, for a description of cuprates this would not be enough. On the other hand, for triplet pairing in Sr_2RuO_4, it turns out that a nonself-consistent treatment and the weak-coupling limit of the generalized Eliashberg equations seem to provide a reasonable approximation. For triplet pairing, the effective pairing interaction due to spin fluctuations is given by

$$V_1^{eff}(\mathbf{k}, \mathbf{k}') = -\frac{U^2 \chi_0(\mathbf{k} - \mathbf{k}', 0)}{1 - U^2 \chi_0^2(\mathbf{k} - \mathbf{k}', 0)}$$
$$= -\frac{U^2}{2}\left(\frac{\chi_0(\mathbf{k} - \mathbf{k}', 0)}{1 - U\chi_0(\mathbf{k} - \mathbf{k}', 0)} + \frac{\chi_0(\mathbf{k} - \mathbf{k}', 0)}{1 + U\chi_0(\mathbf{k} - \mathbf{k}', 0)}\right) \quad . \tag{2.48}$$

Note that the sign of the bubble contribution has changed with respect to singlet pairing and that there exists no contribution from the ladder diagrams. The spin susceptibility χ_0 includes spin–orbit coupling, of course.

For a given pairing interaction, we solve now the weak-coupling gap equation, which reads in matrix form (owing to the three important bands)

$$\Delta_{\mathbf{k}}^i = -\sum_{\mathbf{k}', j} [V_\sigma^{eff}(\mathbf{k}, \mathbf{k}')]^{ij} \frac{\Delta_{\mathbf{k}'}^j}{2E_{\mathbf{k}'}^j} \tanh\left(\frac{E_{\mathbf{k}'}^j}{2k_B T}\right) \quad , \tag{2.49}$$

where $E_{\mathbf{k}}^i = \sqrt{\epsilon_{\mathbf{k}}^{i\,2} + \Delta_{\mathbf{k}}^2}$ are the energy dispersions of the bands, and the pairing potential $V_\sigma^{eff}(\mathbf{k}, \mathbf{k}')$ is different for singlet ($\sigma = 0$) and triplet ($\sigma = 1$) Cooper pairing. In general, an eigenvalue analysis of (2.49) will yield the symmetry with lowest energy. Since the γ-band contains a high density of states, it is tempting to solve the gap equation only for the γ-band (i.e. $E_{\mathbf{k}'}^j \to E_{\mathbf{k}'}^\gamma$), but still taking into account the full pairing potential obtained from diagonalizing the $[\chi^{ij}]$ matrix. To a good approximation we can also linearize (2.49) in Δ_l, i.e. $E_{\mathbf{k}'}^{\gamma'} \to \epsilon_{\mathbf{k}'}^\gamma$, because the main contribution to the pairing comes from the Fermi level. Note that the minus sign in (2.49) is canceled for triplet pairing (see (2.48)). We would like to remark that for $E_F \gg \Delta_l$ the gap function can be expanded into spherical harmonics corresponding to the angular momenta $l = 1, 2, 3, \ldots$ and that no mixture of Δ_l belonging to different symmetry representations can be present if a single T_c is observed. Therefore, we can immediately exclude a $(p + d)$-wave superconducting state, for example.

2.2 Theory for Underdoped Cuprates

As mentioned in the Introduction, in the underdoped regime for hole-doped high-T_c cuprates, a "pseudogap" behavior for temperatures $T < T^*$ in both

the spin and the charge degrees of freedom has been widely observed in experiments such as nuclear magnetic resonance (NMR), Knight shift, and specific heat measurements [35]; angular-resolved photoemission spectroscopy (ARPES) [36, 37, 38]; scanning tunneling (STS) spectroscopy, and optical measuremenst *ab* plane and *c* axis conductivity [39, 22]. Many theoretical proposals about the origin of this pseudogap in the normal state have been invoked; however, no consensus has been reached yet. For example, Williams *et al.* [35] have shown that a phenomenological model for the pseudogap having *d*-wave symmetry can account well for thermodynamic quantities of underdoped cuprates. We shall follow their idea in the next subsection and combine this phenomenological model with the self-consistent FLEX approximation for the exchange of spin fluctuations.

Recently, Chakravarty *et al.* [40] and Varma [41] have proposed that a "hidden order" is present in the pseudogap state, which will be present only below the temperature T^* and should even coexist with superconductivity below T_c. To do this, they extended earlier ideas of Zhang [42] and Marston and Affleck [43]. As a consequence, T^* is no longer a crossover temperature; it becomes a true phase transition. So far, there seems to be experimental evidences (a) from neutron scattering data on YBCO, which show a magnetic moment below T^* [44], (b) from muon spin relaxation measurements, again on YBCO, that are consistent with a small spontaneous (static) magnetic field [45], and (c) from the observed dichroism in ARPES experiments on BISSCO for $T < T^*$ [46], that such a pseudogap state might indeed exist. The corresponding order parameter of *d*-wave type that breaks time-reversal symmetry is called the *d*-density wave (DDW) state [40]. At present, the calculated consequences of a DDW order parameter for Raman scattering [47], and the electrical and thermal transport [48] and their dependence on a magnetic field [49] are consistent with experiment; however, the doping dependence of the superfluid density $n_s(x)$ seems to disagree with the available experimental data [50]. In addition, the state proposed by Chakravarty *et al.* breaks also translational symmetry which is *not* observed. Further investigations are necessary. Although we shall formulate the theory in this section for the competition of a charge-density-wave (CDW) state, not a DDW state, with superconductivity, the resulting equations are much more general, describing two competing order parameters. For example, it turns out that the gap equation for the superconducting order parameter and the new quasiparticle spectrum, in the pseudogap phase and below T_c are identical to those which would have been obtained if we had considered a DDW state. This is due to the symmetry of the corresponding order parameter.

In the following subsection, we turn to the analysis of the "strong" pseudogap regime, i.e. the behavior of hole-doped cuprates for temperatures $T_c < T < T_c^*$. In this connection we study two interesting possible explanations for the pseudogap behavior which involve a discussion of precursors of the possible Cooper pair formation above T_c. Among these kinds of the-

ories, several different scenarios have been investigated: precursors based on "preformed pairs" (i.e. local Cooper pairs without long-range phase coherence) which are related to a fluctuating phase [51, 52, 53], and precursors based on fluctuations of the amplitude of the superconducting order parameter [54, 55, 56, 57, 58]. In Sect. 2.2.2 we shall formulate the corresponding theoretical background.

2.2.1 Extensions for the Inclusion of a *d*-Wave Pseudogap

In this subsection we develop the strong-coupling theory of a coexisting d-wave pseudogap and superconductivity within the framework of the generalized Eliashberg equations using the FLEX (fluctuation exchange) approximation for the two-dimensional Hubbard model. We follow here the idea of competing charge-density-wave and superconductivity gaps which are caused by the same interaction [59]. However, the equations which will be presented are more general; for example, the gap equation for the resulting superconducting order parameter and the corresponding spectrum will be the same as for the DDW state [40]. These equations are also valid for other mechanisms causing a d-wave pseudogap in underdoped cuprates. We shall show that that at distinct points of the 2D Fermi line for YBCO where the nesting condition is satisfied (the "hot spots"), these equations reduce to the previous FLEX equations for superconductivity. However, the squared superconductivity gap ϕ_s^2 occurring in the denominator of the Green's function is replaced by $(\phi_s^2 + \phi_c^2)$, where ϕ_c is the CDW gap. The difference with respect to the earlier phenomenological approaches of [60] and [61] is that we calculate self-consistently the momentum and frequency dependence of the dynamical spin susceptibility $\chi_s(\mathbf{q}, \omega)$, the quasiparticle spectral function $N(\mathbf{k}, \omega)$, and the superconducting gap $\phi_s(\mathbf{k}, \omega)$. In our calculation we take into account the renormalization by the normal self-energy, in particular the quasiparticle damping, due to interaction with antiferromagnetic spin fluctuations.

We start with the definition of the 4×4 matrix Green's function:

$$G(\mathbf{k}, \tau) = -\langle T\alpha_{\mathbf{k}}(\tau)\alpha_{\mathbf{k}}^{\dagger}(0)\rangle \text{ , where } \quad \alpha_{\mathbf{k}}^{\dagger} = (c_{\mathbf{k}\sigma}^{\dagger}, c_{\mathbf{k}+\mathbf{Q},\sigma}^{\dagger}, c_{-\mathbf{k},-\sigma}, c_{-\mathbf{k}-\mathbf{Q},-\sigma}) \,, \tag{2.50}$$

and $c_{k\sigma}$ and $c_{k\sigma}^{\dagger}$ are the annihilation and creation operators, respectively, for electrons or holes and $\mathbf{Q} = (\pi, \pi)$. In the generalized Eliashberg equations for the two-dimensional Hubbard Hamiltonian with on-site Coulomb repulsion U, the self-energy components Σ_{ij} are determined by the equations

$$\Sigma_{ij}(k) = \sum_{k'} P_s(k - k')G_{ij}(k') \,, \quad (k \equiv (\mathbf{k}, i\omega_n)) \,, \tag{2.51}$$

where P_s is the spin fluctuation interaction (for simplicity, we omit the charge fluctuation interaction) and G_{ij} are the components of the dressed 4×4

matrix Green's function. The normal self-energy components are defined as follows:

$$\Sigma_{11} = (\omega - \omega_1) + \xi_1 \quad , \quad \Sigma_{22} = (\omega - \omega_2) + \xi_2 \quad ,$$
$$\Sigma_{33} = (\omega - \omega_1) - \xi_1 \quad , \quad \Sigma_{44} = (\omega - \omega_2) - \xi_2 \quad ,$$

$$\omega \equiv i\omega_n \quad , \quad \omega_1 \equiv i\omega_n Z(\mathbf{k}, i\omega_n) \quad , \quad \omega_2 \equiv i\omega_n Z(\mathbf{k}+\mathbf{Q}, i\omega_n) \quad ,$$
$$\xi_1 \equiv \xi(\mathbf{k}, i\omega_n) \quad , \quad \xi_2 \equiv \xi(\mathbf{k}+\mathbf{Q}, i\omega_n) \quad . \tag{2.52}$$

Here again, Z is the effective–mass function and ξ is the shift of the energy band $\epsilon(\mathbf{k})$. The anomalous self-energy components for the charge density wave and superconducting order parameter ϕ_c and ϕ_s are defined by

$$\Sigma_{12} = \Sigma_{21} = \phi_c(\mathbf{k}, i\omega_n) \propto \langle c^{\dagger}_{k+Q,\sigma} c_{k\sigma} \rangle \quad , \tag{2.53}$$
$$\Sigma_{13} = \Sigma_{31} = \phi_s(\mathbf{k}, i\omega_n) \propto \langle c_{-k-\sigma} c_{k\sigma} \rangle \quad . \tag{2.54}$$

With the help of the equations of motion of $c_{k\sigma}(\tau)$ for the 2D Hubbard Hamiltonian and the Dyson equation $G^{-1} = G_0^{-1} - \Sigma$, we obtain the following components of the 4×4 matrix Green's function:

$$G_{11} = \left[\left(\omega_2^2 - \epsilon_2^2\right)(\omega_1 + \epsilon_1) - \phi_c^2 (\omega_2 - \epsilon_2) - \phi_s^2 (\omega_1 + \epsilon_1) \right] D^{-1} \quad , \tag{2.55}$$

$$G_{22} = \left[\left(\omega_1^2 - \epsilon_1^2\right)(\omega_2 + \epsilon_2) - \phi_c^2 (\omega_1 - \epsilon_1) - \phi_s^2 (\omega_2 + \epsilon_2) \right] D^{-1} \quad , \tag{2.56}$$

$$G_{12} = G_{21} = \phi_c \left[(\omega_1 + \epsilon_1)(\omega_2 + \epsilon_2) - \phi_c^2 - \phi_s^2 \right] D^{-1} \quad , \tag{2.57}$$

$$G_{13} = G_{31} = \phi_s \left[\left(\omega_2^2 - \epsilon_2^2\right) - \phi_c^2 - \phi_s^2 \right] D^{-1} \quad , \tag{2.58}$$

with the denominator

$$D = \left(\omega_1^2 - \epsilon_1^2\right)\left(\omega_2^2 - \epsilon_2^2\right) - \phi_c^2 \left[(\omega_1 - \epsilon_1)(\omega_2 - \epsilon_2) + (\omega_1 + \epsilon_1)(\omega_2 + \epsilon_2) \right]$$
$$-\phi_s^2 \left[\left(\omega_1^2 - \epsilon_1^2\right) + \left(\omega_2^2 - \epsilon_2^2\right) \right] + \left[\phi_c^2 + \phi_s^2 \right]^2 \quad , \tag{2.59}$$

$$\epsilon_1 \equiv \epsilon(\mathbf{k}) + \xi_1 \quad , \quad \epsilon_2 \equiv \epsilon(\mathbf{k}+\mathbf{Q}) + \xi_2 \quad . \tag{2.60}$$

Here, $\epsilon(\mathbf{k})$ is the dispersion relation of the quasiparticles discussed earlier. Note that the off-diagonal components $G_{14} = G_{41}$ and $G_{23} = G_{32}$ are proportional to $\phi_c \phi_s$.

With the Green's functions defined above, the effective spin and charge fluctuation interactions are given by the RPA expressions

$$\frac{3}{2} U^2 \frac{\chi_{s0}}{1 - U\chi_{s0}} \qquad \text{and} \qquad \frac{1}{2} U^2 \frac{\chi_{c0}}{1 + U\chi_{c0}} \quad , \tag{2.61}$$

where the bubble spin susceptibility χ_{s0} is calculated self-consistently from the expression

$$\mathrm{Im}\chi_{s0}(\mathbf{q},\omega) = \pi \int_{-\infty}^{\infty} d\omega' \left[f(\omega') - f(\omega'+\omega)\right] \sum_{\mathbf{k}} \left[N(\mathbf{k}+\mathbf{q},\omega'+\omega)N(\mathbf{k},\omega')\right.$$
$$\left. + A_1(\mathbf{k}+\mathbf{q},\omega'+\omega)A_1(\mathbf{k},\omega') + A_g(\mathbf{k}+\mathbf{q},\omega'+\omega)A_g(\mathbf{k},\omega')\right] \qquad (2.62)$$

and thus depends on the pseudogap via the spectral functions. Note that the charge susceptibility χ_{c0} has the opposite sign in front of the anomalous terms in (2.62). The components of the Hubbard model interaction with respect to the particle–hole and spin space have been obtained by an expansion in terms of the 2×2 unit matrix and the Pauli matrices. N denotes the normal spectral function, and A_1 and A_g are the anomalous spectral functions with respect to the superconducting gap and the pseudogap, respectively. These spectral functions have been obtained from a self-consistent solution of the generalized Eliashberg equations in the presence of the pseudogap and are given by

$$N(\mathbf{k},\omega) = -\frac{1}{\pi}\,\mathrm{Im}\frac{\omega Z + \epsilon_k + \xi}{(\omega Z)^2 - (\epsilon_k+\xi)^2 - E_g^2 - \phi^2} \quad , \qquad (2.63)$$

$$A_1(\mathbf{k},\omega) = -\frac{1}{\pi}\,\mathrm{Im}\frac{\phi}{(\omega Z)^2 - (\epsilon_k+\xi)^2 - E_g^2 - \phi^2} \quad , \qquad (2.64)$$

$$A_g(\mathbf{k},\omega) = -\frac{1}{\pi}\,\mathrm{Im}\frac{E_g}{(\omega Z)^2 - (\epsilon_k+\xi)^2 - E_g^2 - \phi^2} \quad , \qquad (2.65)$$

where

$$\phi^2 = \phi_s^2 + \phi_c^2 \quad . \qquad (2.66)$$

We want to emphasize that it is necessary to include the bubble contribution due to A_g in the conductivities and susceptibilities. Neglecting this term leads to severe disagreement with experimental data. Following [61], for the pseudogap we assume the simple form

$$E_g\,(\mathbf{k},T,x) = E_g(T,x)\,[\cos k_x - \cos k_y] \quad , \qquad (2.67)$$

where E_g is temperature–dependent and increases with decreasing doping level below the optimal doping level. Here, the consideration of an imaginary order parameter as in the case of a DDW state [40] is also possible. The generalized Eliashberg equations are then solved self-consistently in the presence of this pseudogap (as described in Appendix A) and yield the quasiparticle self-energy components $Z(\mathbf{k},\omega)$ and $\xi(\mathbf{k},\omega)$ and the superconducting gap $\phi(\mathbf{k},\omega)$. For simplicity, we have neglected in (2.51) the interaction P_c due to exchange of charge fluctuations. The interaction P_c is proportional to χ_c which is obtained from χ_s by changing the signs of U and of the anomalous terms due to ϕ_c and ϕ_s in the irreducible susceptibility χ_0. We want to emphasize that the charge-fluctuation interaction in the underdoped regime is much smaller than the spin-fluctuation interaction P_s. The set of coupled equations (2.51)–(2.67) has to be solved self-consistently. Obviously, for $\phi_c \equiv 0$ these equations reduce to the FLEX equations for Z, ξ, and the superconducting gap ϕ_s. In

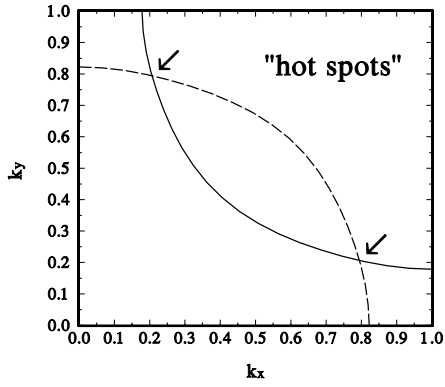

Fig. 2.8. Fermi lines $\epsilon(\mathbf{k}) = 0$ (*solid line*) and $\epsilon(\mathbf{k}+\mathbf{Q}) = 0$ (*dashed line*) in the first quadrant of the Brillouin zone for hole-doped YBCO and Bi 2212. The crossing points are the "hot spots".

the weak-coupling limit (i.e. $Z \equiv 1$, $\xi \equiv 0$), these equations reduce to the gap equations for the CDW gap $\phi_c(\mathbf{k})$ and the superconducting gap $\phi_s(\mathbf{k})$ of earlier approaches [59].

In most cases, we consider a tight-binding band $\epsilon(\mathbf{k})$ whose Fermi line approximates those of the hole-doped YBCO and Bi 2212 compounds. The "hot spots" where the Fermi lines $\epsilon(\mathbf{k})+\xi(\mathbf{k}) = 0$ and $\epsilon(\mathbf{k}+\mathbf{Q})+\xi(\mathbf{k}+\mathbf{Q}) = 0$ in the first quadrant of the square Brillouin zone cross each other then lie in the vicinity of the corners $\mathbf{k} = (\pi, 0)$ and $\mathbf{k} = (0, \pi)$ (see Fig. 2.8). One can recognize from (2.20)–(2.60) that at the hot spots ($\epsilon_2 + \xi_2 = -\epsilon_1 - \xi_1$, $Z_2 = Z_1$), the Green's functions reduce to those for superconductivity apart from the fact that in the denominators of the G_{ij}, ϕ_s^2 is replaced by $\phi_s^2 + \phi_c^2$. For example, within the weak-coupling approximation the gap equation reads (here Δ_s denotes the superconducting gap and Δ_c corresponds to the CDW gap):

$$\begin{aligned}
&\Delta_s(\mathbf{k}) \\
&= -\sum_{\mathbf{k}'} P_s(\mathbf{k}-\mathbf{k}')\Delta_s(\mathbf{k}')\,\frac{1}{2}\left[\frac{1-2f(E'_+)}{2E'_+} + \frac{1-2f(E'_-)}{2E'_-}\right. \\
&\left. +\ (\epsilon'_1-\epsilon'_2)\left[(\epsilon'_1-\epsilon'_2)^2 + 4\Delta_c^2\right]^{-1/2}\left(\frac{1-2f(E'_+)}{2E'_+} - \frac{1-2f(E'_-)}{2E'_-}\right)\right],
\end{aligned} \tag{2.68}$$

where

$$E_\pm^2 = \left[\frac{1}{2}(\epsilon_1+\epsilon_2) \pm \frac{1}{2}\left[(\epsilon_1-\epsilon_2)^2 + 4\Delta_c^2\right]^{1/2}\right]^2 + \Delta_s^2 \tag{2.69}$$

and

$$\epsilon_1 = \epsilon_1(\mathbf{k})\,, \qquad \epsilon_2 = \epsilon_2(\mathbf{k}+\mathbf{Q})\,, \qquad \Delta_s = \Delta_s(\mathbf{k})\,, \qquad \Delta_c = \Delta_c(\mathbf{k}+\mathbf{Q})\,. \tag{2.70}$$

Note that (2.68) and (2.69) remain the same for the DDW state proposed by Chakravarty *et al.* [40]. It is also interesting to remark that at the hot spots with $\epsilon_1 + \epsilon_2 = 0$, the quasiparticle energy $E_\pm$ in (2.69) takes the BCS form with a total squared energy equal to $\Delta_s^2(\mathbf{k}) + \Delta_c^2(\mathbf{k})$. Since the repulsive spin fluctuation interaction $P_s(\mathbf{k}-\mathbf{k}')$, as well as the superconducting gap, has a large peak at $\mathbf{k}-\mathbf{k}' = \mathbf{Q}' = (-\pi, \pi)$, the effective pseudogap also has $d_{x^2-y^2}$-wave symmetry. The form of $E_\pm$ at the hot spots with $\epsilon_1 + \epsilon_2 = 0$ in (2.69) may also justify the expressions for the quasiparticle energy used earlier by Loram *et al.* [60] and Williams *et al.* [61] in order to describe heat capacity and Knight shift data in both the normal and the superconducting state for underdoped cuprates. Of course, in our calculations the full momentum and frequency dependence of the quasiparticle self-energy is taken into account.

2.2.2 Fluctuation Effects

In this subsection we shall to analyze the region where preformed pairs might occur, the region of so-called strong pseudogap behavior of the quasiparticles, close to the superconducting transition, i.e. for temperatures $T_c < T < T_c^*$. In the following we formulate a theoretical description of the effects due to fluctuations of the phase and amplitude of the Cooper pairs. Let us start with a microscopic theory in real space on a square lattice in order to investigate the role of Cooper pair phase fluctuations. If one considers the Fourier transform of the spectral density of the pairing interaction P_s, it turns out that the effective pairing potential V_{eff} is *attractive* on nearest–neighbor sites in real space [8]. Following the work by Schäfer *et al.*, we employ a Hamiltonian ($V_{eff} < 0$) [62]

$$H = -t \sum_{\langle ij \rangle \sigma} c_{i\sigma}^\dagger c_{j\sigma} + V_{eff} \sum_{\langle ij \rangle} c_{i\uparrow}^\dagger c_{i\uparrow} c_{j\downarrow}^\dagger c_{j\downarrow} \tag{2.71}$$

in analogy to (2.1). In order to evaluate the free energy and correlation functions of the system one has to evaluate the partition function

$$\mathcal{Z} = \int \mathcal{D}(\Phi, \Phi^*)\, \mathrm{e}^{-\mathcal{S}_{eff}[\Phi^*, \Phi]} \quad , \tag{2.72}$$

where Φ, $\Phi^* =$ are Grassmann variables and the effective action is given by

$$\mathcal{S}_{eff}[\Phi^*, \Phi] = \int_0^\beta \mathrm{d}\tau \left\{ \sum_{i\sigma} \Phi_{i\sigma}^* (\partial_\tau - \mu) \Phi_{i\sigma} - t \sum_{\langle ij \rangle \sigma} \Phi_{i\sigma}^* \Phi_{j\sigma} \right. \tag{2.73}$$

$$\left. + V_{eff} \sum_{\langle ij \rangle} \Phi_{i\uparrow}^* \Phi_{j\downarrow}^* \Phi_{j\downarrow} \Phi_{i\uparrow} \right\} \quad , \tag{2.74}$$

or, after performing a Hubbard–Stratonovich transformation,

$$\mathcal{Z} = \int \mathcal{D}(\Phi,\Phi^*)\,\mathcal{D}(\Delta,\Delta^*)\,\mathrm{e}^{-\mathcal{S}_{eff}[\Phi^*,\Phi;\Delta^*,\Delta]} \quad , \tag{2.75}$$

where

$$\mathcal{S}_{eff}[\Phi^*,\Phi;\Delta^*,\Delta] = \int_0^\beta \mathrm{d}\tau \left\{ \sum_{i\sigma} \Phi^*_{i\sigma}(\partial_\tau - \mu)\Phi_{i\sigma} + t \sum_{\langle ij\rangle\sigma} \Phi^*_{i\sigma}\Phi_{j\sigma} + \sum_{\langle ij\rangle} \left[\Delta_{ij}\ \Phi^*_{i\uparrow}\ \Phi^*_{j\downarrow} + \Delta^*_{ij}\ \Phi_{j\downarrow}\ \Phi_{i\uparrow} + \frac{|\Delta_{ij}|^2}{|V_{eff}|} \right] \right\} \quad . \tag{2.76}$$

For simplicity, we first neglect fluctuations of the amplitude of the superconducting order parameter and derive, with the help of

$$\Delta_{ij} \ = \Delta^0_{ij}\ \mathrm{e}^{+\frac{i}{2}[\varphi_i(\tau)+\varphi_j(\tau)]} \quad , \tag{2.77}$$

$$\psi_{i\sigma} = \Phi_{i\sigma}\ \mathrm{e}^{-\frac{i}{2}\varphi_i(\tau)} \tag{2.78}$$

(as used in [62, 63]), the following effective action:

$$\mathcal{S}_{eff}[\psi^*,\psi;\varphi] = \int_0^\beta \mathrm{d}\tau \left\{ \sum_{i\sigma} \psi^*_{i\sigma} \left[\partial_\tau + \frac{i}{2}\,\partial_\tau\varphi_i(\tau) - \mu \right] \psi_{i\sigma} + \ t \sum_{\langle ij\rangle\sigma} \psi^*_{i\sigma}\psi_{j\sigma}\ \mathrm{e}^{-\frac{i}{2}[\varphi_i(\tau)-\varphi_j(\tau)]} + \sum_{\langle ij\rangle} \left[\Delta^0_{ij}\ \left(\psi^*_{i\uparrow}\psi^*_{j\downarrow} + \psi_{j\downarrow}\psi_{i\uparrow} \right) + \frac{(\Delta^0_{ij})^2}{|V_{eff}|} \right] \right\} \quad . \tag{2.79}$$

After a straightforward calculation, $\mathcal{S}_{eff}$ reads, Nambu space using Matsubara frequencies,

$$\mathcal{S}_{eff}[\psi^*,\psi;\varphi] = \mathcal{S}_{\Delta^0}[\psi^*,\psi] + \mathcal{S}_{\varphi}[\psi^*,\psi;\varphi] \quad , \tag{2.80}$$

where

$$\mathcal{S}_{\Delta^0}[\psi^*,\psi] = -\frac{1}{\beta} \sum_{\substack{kk'\\ nn'}} \Psi^\dagger(k,i\omega_n)\ \hat{\mathcal{G}}_0^{-1}(k,i\omega_n;k',i\omega_{n'})\ \Psi(k',i\omega_{n'}) + \beta N\ \frac{|\Delta^0|^2}{|V_{eff}|} \quad , \tag{2.81}$$

$$\mathcal{S}_{\varphi}[\psi^*,\psi;\varphi] = -\frac{1}{\beta} \sum_{\substack{k,k'\\ n,n'}} \Psi^\dagger(k,i\omega_n)\ \frac{1}{\beta\sqrt{N}} \times \hat{\Gamma}^1_0(k,i\omega_n;k',i\omega_{n'})\varphi(k-k',i\omega_n - i\omega_{n'})\ \Psi(k',i\omega_{n'})$$

$$- \frac{1}{\beta} \sum_{\substack{k,k' \\ n,n'}} \Psi^{\dagger}(k, i\omega_n) \left\{ \frac{1}{\beta^2 N} \sum_{k'',n''} \hat{\Gamma}_0^2(k;k';k'')\, \varphi(k'', i\nu_{n''}) \right.$$

$$\left. \times\ \varphi(k-k'-k'', i\omega_n - i\omega_{n'} - i\nu_{n''}) \right\} \Psi(k', i\omega_{n'}) \quad , \quad (2.82)$$

and

$$\Psi(k, i\omega_n) = \begin{pmatrix} \Psi_{k\uparrow}(i\omega_n) \\ \Psi^{\dagger}_{-k\downarrow}(-i\omega_n) \end{pmatrix} \quad . \quad (2.83)$$

Here, the Green's function (in the weak-coupling limit), and the vertices which couple the quasiparticles (holes) and the phases are given by

$$\hat{\mathcal{G}}_0(k, i\omega_n, k', i\omega_{n'}) = \begin{pmatrix} i\omega_n - \epsilon_k + \mu & -\Delta_k^0 \\ -\Delta_k^0 & i\omega_n + \epsilon_k - \mu \end{pmatrix}^{-1} \delta_{k,k'} \delta_{n,n'} \quad , \quad (2.84)$$

$$\hat{\Gamma}_0^1(k,k') = \frac{i}{2} \left[(ik_0 - ik_0')\hat{\tau}_3 - (\epsilon_{\mathbf{k}} - \epsilon_{\mathbf{k}'})\hat{\tau}_0 \right] =$$

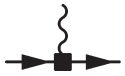

, (2.85)

$$\hat{\Gamma}_0^2(k,k',k'') = \frac{1}{8} \left[\epsilon_{\mathbf{k}} - \epsilon_{\mathbf{k}-\mathbf{k}''} - \epsilon_{\mathbf{k}''+\mathbf{k}'} + \epsilon_{\mathbf{k}'} \right] \hat{\tau}_3 =$$

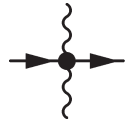

; (2.86)

$\hat{\tau}_i$ are the corresponding Pauli matrices.

In analogy to the previous subsection, we shall now derive the propagator of Cooper pair phase fluctuations and thus their corresponding self-energy equations. For this purpose we have to integrate out the electronic degrees of freedom. This leads to

$$\mathcal{S}_{eff}[\varphi] = \mathcal{S}_{eff}^{BCS}(\Delta^0) + \frac{1}{\beta} \sum_{qn} \varphi(q, i\nu_n) \left[\mathcal{D}_{\varphi}(q, i\nu_n) \right]^{-1} \varphi(-q, -i\nu_n) \quad (2.87)$$

or, diagrammatically,

$\mathcal{S}_{\text{eff}}[\varphi] =$

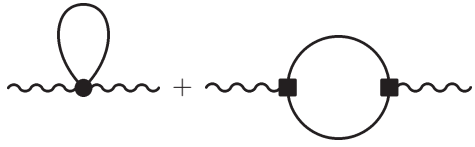

. (2.88)

Here, the BCS part is given by

$$\mathcal{S}_{eff}^{BCS}(\Delta^0) = -\mathrm{Tr} \ln \left[-\hat{\mathcal{G}}_0^{-1} \right] + \beta N \frac{|\Delta^0|^2}{|V_{eff}|} \quad . \quad (2.89)$$

$\mathcal{D}_{\varphi}(q, i\nu_n) = \langle\langle \varphi(q, i\nu_n)\, \varphi(-q, -i\nu_n) \rangle\rangle$ denotes the propagator of the corresponding phase of a Cooper pair and reads [62]

$$\mathcal{D}_{\varphi}(q,i\nu_n) = 8\,\Big[-\chi^{\rho\rho}(q,i\nu_n)\,(i\nu_n)^2 - (i\nu_n)\sum_{\alpha}\big[\Pi^{\alpha\rho}(q,i\nu_n) + \Pi^{\rho\alpha}(q,i\nu_n)\big]\,2\sin\frac{q_\alpha}{2} + \sum_{\alpha\beta}\rho^{\alpha\beta}(q,i\nu_n)\,\Big(2\sin\frac{q_\alpha}{2}\Big)\,\Big(2\sin\frac{q_\beta}{2}\Big)\Big]^{-1}\,, \quad (2.90)$$

where the phase stiffness is $\rho^{\alpha\beta}(q,i\nu_n) = \mathrm{T}^{\alpha\beta} + \Pi^{\alpha\beta}$. Here Π and T are the current–current correlation function and the mass operator, respectively [20], i.e.

$$\chi^{\rho\rho}(q,\tau) = \frac{1}{\beta N}\sum_{kn'} v^{\alpha}_{k+\frac{q}{2}}\,\mathrm{Tr}\big[\hat{\mathcal{G}}_0(k+q,i\omega_{n'}+i\nu_n)\,\hat{\tau}_3\,\hat{\mathcal{G}}_0(k,i\omega_{n'})\,\hat{\tau}_3\big]\quad, \quad (2.91)$$

$$\Pi^{\alpha\rho}(q,i\nu_n) = \frac{1}{\beta N}\sum_{kn'} v^{\alpha}_{k-\frac{q}{2}}\mathrm{Tr}\big[\hat{\mathcal{G}}_0(k,i\omega_{n'})\,\hat{\tau}_3\,\hat{\mathcal{G}}_0(k-q,i\omega_{n'}-i\nu_n)\big] \quad (2.92)$$

$$= \Pi^{\rho\alpha}(-q,-i\nu_n)\quad, \quad (2.93)$$

$$\rho^{\alpha\beta}(q,i\nu_n) = \frac{1}{\beta N}\sum_{kn'} v^{\alpha}_{k-\frac{q}{2}}\,v^{\beta}_{k-\frac{q}{2}} \times \mathrm{Tr}\big[\hat{\mathcal{G}}_0(k,i\omega_{n'})\,\hat{\mathcal{G}}_0(k-q,i\omega_{n'}-i\nu_n)\big]\quad, \quad (2.94)$$

$$\mathrm{T}^{\alpha\beta} = \frac{1}{N}\sum_{k} t^{\alpha\beta}_{k}\,(n_{k\uparrow}+n_{k\downarrow})\quad. \quad (2.95)$$

In analogy to the treatment by Kadanoff and Baym [64, 65], we are now able to calculate the dressed Green's functions and their corresponding self-energies. In general, one has to start with the generating function

$$\mathcal{S}[\psi^*,\psi;\eta] = \mathcal{S}[\psi^*,\psi] + \mathcal{S}_{source}[\psi^*,\psi;\eta]\quad, \quad (2.96)$$

with a source term

$$\mathcal{S}_{source}[\psi^*,\psi;\eta] = -\frac{1}{\beta}\sum_{\substack{kn\\k'n'}}\Psi^{\dagger}(k,i\omega_n)\,\hat{\eta}(k,i\omega_n;k',i\omega_{\prime})\,\Psi(k',i\omega_{n'})\quad, \quad (2.97)$$

where

$$\hat{\eta}(k,i\omega_n;k',i\omega_{\prime}) = \begin{pmatrix}\eta(k,i\omega_n) & \bar{\eta}^*(k,i\omega_n)\\ \bar{\eta}(k,i\omega_n) & \tilde{\eta}(k,i\omega_n)\end{pmatrix}\quad. \quad (2.98)$$

The corresponding Green's functions are given by

$$\mathcal{G}(k,i\omega_n) = -\left.\frac{\delta\ln\mathcal{Z}[\eta]}{\delta\eta(k,i\omega_n)}\right|_{\eta=0}\quad, \quad \tilde{\mathcal{G}}(k,i\omega_n) = -\left.\frac{\delta\ln\mathcal{Z}[\eta]}{\delta\tilde{\eta}(k,i\omega_n)}\right|_{\eta=0}\quad, \quad (2.99)$$

$$\mathcal{F}(k,i\omega_n) = -\left.\frac{\delta\ln\mathcal{Z}[\eta]}{\delta\bar{\eta}(k,i\omega_n)}\right|_{\eta=0}\quad, \quad \bar{\mathcal{F}}(k,i\omega_n) = -\left.\frac{\delta\ln\mathcal{Z}[\eta]}{\delta\bar{\eta}^*(k,i\omega_n)}\right|_{\eta=0}\quad. \quad (2.100)$$

Thus, if we consider Cooper pair phase fluctuations and treat them up to second order, we arrive at [62]

$$\begin{aligned}\hat{\mathcal{G}}(k,i\omega_n) &= \hat{\mathcal{G}}_0(k,i\omega_n) \\ &\quad - \hat{\mathcal{G}}_0(k,i\omega_n)\left[\frac{1}{\beta N}\sum_{q,n'} \hat{\Gamma}_0^2(k,k,q)\; \Pi^{\varphi\varphi}(q,i\nu_n)\right] \hat{\mathcal{G}}_0(k,i\omega_n) \\ &+ \hat{\mathcal{G}}_0(k,i\omega_n)\left[\frac{1}{\beta N}\sum_{q,n'} \hat{\Gamma}_0^1(k,i\omega_n;k-q,i\omega_n-i\nu_{n'})\; \hat{\mathcal{G}}_0(k-q,i\omega_n-i\nu_{n'})\right. \\ &\quad \left.\times\; \hat{\Gamma}_0^1(k-q,i\omega_n-i\nu_{n'};k,i\omega_n)\; \Pi^{\varphi\varphi}(q,i\nu_n)\right] \hat{\mathcal{G}}_0(k,i\omega_n) \qquad (2.101) \\ &= \hat{\mathcal{G}}_0(k,i\omega_n) - \hat{\mathcal{G}}_0(k,i\omega_n)\; \hat{\Sigma}^{\varphi\varphi}(k,i\omega_n)\; \hat{\mathcal{G}}_0(k,i\omega_n) \qquad (2.102)\end{aligned}$$

or, diagrammatically,

(2.103)

Thus, the normal and anomalous parts of the self-energy due to Cooper pair phase fluctuations are given by

$$\begin{aligned}\Sigma^{\mathcal{G}}(k,i\omega_n) &= \frac{1}{4\beta N}\sum_{q,n'}[(i\nu_{n'})^2 - 2i\nu_{n'}(\epsilon_k-\epsilon_{k-q}) + (\epsilon_k-\epsilon_{k-q})^2] \\ &\quad\times\; \mathcal{G}_0(k-q,i\omega_n-i\nu_{n'})\; \Pi^{\varphi\varphi}(q,i\nu_n) \quad , \qquad (2.104) \\ \Sigma^{\mathcal{F}}(k,i\omega_n) &= \frac{1}{4\beta N}\sum_{q,n'}[(i\nu_{n'})^2 + (\epsilon_k-\epsilon_{k-q})^2] \\ &\quad\times\; \mathcal{F}_0(k-q,i\omega_n-i\nu_{n'})\; \Pi^{\varphi\varphi}(q,i\nu_n) \quad . \qquad (2.105)\end{aligned}$$

These self-energy corrections are the main result of this subsection and must be added to their counterparts Σ^G and Σ^F given by the exchange of spin fluctuations alone in (2.19). One can then perform an analytical continuation to the real ω axis and solve the corresponding equations as described in Appendix A. Of course, the current–current correlation function Π has to be calculated self-consistently using (2.90), which describes the propagation of Cooper pair phase fluctuations.

As done in the previous subsection, we close our analysis with a discussion of a few limiting cases of our theory. First, the BCS gap equation can be recovered if one neglects all fluctuations of the order parameter, i.e. $\Delta_{ij}(x,\tau) = \Delta_{ij}^0$. Then the partition function reads ($|V_{eff}| = |V|$)

$$\mathcal{Z} = \int \mathcal{D}(\Phi^*,\Phi)\; \mathrm{e}^{-\mathcal{S}[\Phi^*,\Phi]} \quad , \qquad (2.106)$$

where

$$\mathcal{S}[\Psi^\dagger,\Psi] = -\frac{1}{\beta}\sum_{\substack{kk'\\nn'}} \Psi^\dagger(k,i\omega_n)\,\hat{\mathcal{G}}_0^{-1}(k,i\omega_n;k',i\omega_{n'})\,\Psi(k',i\omega_{n'}) + \beta N\,\frac{|\Delta^0|^2}{|V|} \quad , \tag{2.107}$$

and we use the standard definitions [19]

$$\Psi(k,i\omega_n) = \begin{pmatrix} \Phi_{k\uparrow}(i\omega_n) \\ \Phi^*_{-k\downarrow}(-i\omega_n) \end{pmatrix} , \tag{2.108}$$

$$\hat{\mathcal{G}}_0(k,i\omega_n;k',i\omega_{n'}) = \begin{pmatrix} i\omega_n - \epsilon_k + \mu & -\Delta_k^{0\,*} \\ -\Delta_k^0 & i\omega_n + \epsilon_{-k} - \mu \end{pmatrix}^{-1} \delta_{k,k'}\delta_{n,n'} \quad . \tag{2.109}$$

Hence,

$$\begin{aligned} \mathcal{Z} &= \mathrm{e}^{-\beta N\,\frac{|\Delta^0|^2}{|V|}}\,\left[\det(-\hat{\mathcal{G}}_0)\right]^{-1} \\ &= \mathrm{e}^{-\beta N\,\frac{|\Delta^0|^2}{|V|}\,+\sum_{kn}\left[\ln(i\omega_n - E_k+\mu)+\ln(i\omega_n+E_k-\mu)\right]} \quad , \end{aligned} \tag{2.110}$$

where the Cooper pair dispersion is $E_k = \sqrt{\epsilon_k^2 + \Delta_k^2}$. Thus, the free energy reads

$$\begin{aligned} \mathcal{F} &= -\beta^{-1}\,\ln Z \\ &= N\,\frac{|\Delta^0|^2}{|V|} - \beta^{-1}\sum_{kn}\left[\ln(i\omega_n - E_k+\mu)+\ln(i\omega_n+E_k-\mu)\right] \quad , \end{aligned} \tag{2.111}$$

which leads, with $\frac{\partial \mathcal{F}}{\partial \Delta^0} = 0$, to the BCS gap equation:

$$1 = \sum_k \frac{|V|}{2E_k}\,\big(1 - 2f(E_k)\big) \quad . \tag{2.112}$$

The second limiting case that we want to consider here is the connection with Ginzburg–Landau theory. If we evaluate all correlation functions in the limit $\mathbf{q} \to 0$ and $i\nu_m \to 0$ and change from our lattice representation to the continuum, the approximate propagator reads

$$\mathcal{D}_\varphi(q,i\nu_n) = \frac{8}{-\chi(i\nu_n)^2 + \rho q^2} \quad , \tag{2.113}$$

which describes a Goldstone mode with velocity $v_s = \sqrt{\rho/\chi}$ and dispersion $\omega = v_s|q|$. The phase stiffness ρ is given by the ratio of the superfluid velocity to the effective mass, n_s/m^*. Thus, in the case of cuprate high-T_c superconductors, the coherence length of Cooper pair phase fluctuations,

$\xi_s = \pi/(\Delta v_s)$, can be estimated to be of the order of 30 lattice constants. Moreover, with the above approximations, the effective action can be rewritten as

$$\mathcal{S}_{eff}[\varphi] = \frac{Na^2}{32\pi^2\beta}\int d^2q \sum_n \Big\{ -\chi(i\nu_n)^2 + \rho q^2 \Big\}\, \varphi(q, i\nu_n)\, \varphi(-q, -i\nu_n)$$

or, after Fourier transformations,

$$\mathcal{S}_{eff}[\varphi] = \frac{Na^2}{32\pi^2}\int dr \int_0^\beta d\tau \Big\{ \chi\, (\partial_\tau \varphi(r,\tau))^2 + \rho\, (\nabla_r \varphi(r,\tau))^2 \Big\} \quad . \quad (2.114)$$

This corresponds to a quantum Ginzburg–Landau theory for the phase of a superconductor [25]. In this case the partition function reads

$$\mathcal{Z}_\varphi = \int \mathcal{D}(\varphi)\, \mathrm{e}^{-\mathcal{S}_{eff.}[\varphi]} = \frac{1}{2}\prod_{\substack{q>0\\ n}} \frac{8}{-\chi(i\nu_n)^2 + \rho q^2} \quad , \quad (2.115)$$

and thus

$$\mathcal{F}_\varphi = -\frac{1}{\beta}\ln \mathcal{Z}_\varphi = \frac{1}{\beta}\sum_{\substack{q>0\\ n}} \ln\left(\frac{-\chi(i\nu_n)^2 + \rho q^2}{4}\right) = \zeta(3)\frac{Na^2}{2\pi}\frac{\chi}{\rho\beta^3} \quad . \quad (2.116)$$

As already pointed out by Rice, Cooper pair phase fluctuations do not contribute to the free energy at $T = 0$ and scale in proportion to T^3 at finite temperatures [25]. Furthermore, we see from (2.116) that these fluctuations diverge if the superfluid velocity vanishes.

Next we consider the extension of the generalized Eliashberg equations to take account of amplitude fluctuations of the superconducting order parameter within the FLEX approximation. To do this, one has to solve the Bethe–Salpeter equation for the particle–particle scattering matrix T', which reads in the strong-coupling limit [55]

$$\begin{aligned} &T'(k_1, k_3; q = k_1 + k_4) \\ &= P_s(k_1 - k_3) - T\sum_{k_1'} P_s(k_1 - k_1')G(k_1')G(q - k_1')T'(k_1', k_3; q) \quad . \quad (2.117) \end{aligned}$$

A diagrammatic representation of (2.117) is shown in Fig. 2.9. The main reason for employing the conventional pair fluctuation theory is that the pair fluctuation propagator $T' = [|(T - T_c)/T_c| + \xi_0^2 q^2 - i\omega\tau]^{-1}$ is relatively large for the high-T_c superconductors, because the pair coherence length $\xi_0 \approx v_F/\pi T_c$ (where v_F denotes the Fermi velocity) and the pair lifetime $\tau \approx \pi/8T_c$ are rather small due to the high superconducting transition temperature T_c. Another reason is that the propagator T' might account for the observed momentum dependence of the strong pseudogap in photoemission (ARPES)

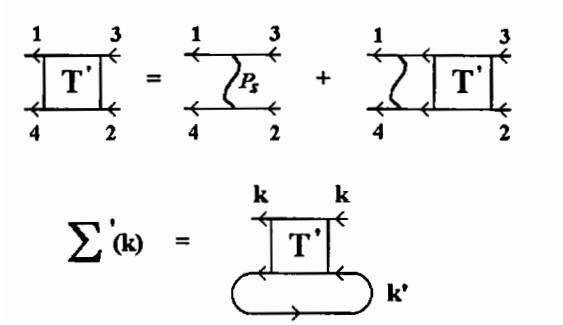

Fig. 2.9. Bethe–Salpeter equation for the particle–particle scattering matrix T' in the ladder approximation with the full pairing interaction P_s and the self-energy contributions Σ' arising from T'. The *solid lines* denote the dressed particle propagators.

experiments, because T' is proportional to $(\cos k_x - \cos k_y)^2$ if the preformed pairs above T_c have d-wave symmetry [55]. It has been shown in [54] that this theory leads to a suppression of T_c with increasing pair fluctuation strength and to a maximum of $1/T_1T$ (where $1/T_1$ is the NMR spin–lattice relaxation rate) with decreasing temperature T, in agreement with experiments.

For further calculations, we have generalized the wave function of the preformed state in the pair fluctuation propagator T', i.e. $\psi_d(\mathbf{k}) = [\cos k_x - \cos k_y]$, to the superconducting order parameter *above* T_c, $\phi_d(\mathbf{k},\omega)$, and shall later approximate $\ln(T/T_c)$ by $(1-\lambda_d)$ in (2.120), where λ_d is the corresponding eigenvalue for $d_{x^2-y^2}$-wave superconductivity in the normal state. Thus, the self-energy contribution $\Sigma'(k)$ due to the particle–particle scattering matrix T' (also shown in Fig. 2.9) is simply given by

$$\Sigma'(k,i\omega_n) = T\sum_{\omega_n'}\sum_{\mathbf{k}'} T'(k,\mathbf{q}=\mathbf{k}+\mathbf{k}',i\nu_m = i\omega_n + i\omega_n')\, G(\mathbf{k}',i\omega_n') \quad . \tag{2.118}$$

We continue to a real-frequency formulation in the usual way described earlier. The odd-ω part of the quasiparticle self-energy due to exchange of spin and pairing fluctuations is obtained as [54, 55]

$$\omega\,[1-Z(\mathbf{k},\omega)] = \sum_{\mathbf{k}'}\int_0^\infty \mathrm{d}\Omega\,\left[|\psi_d(\mathbf{k},\omega)|^2 K(\mathbf{k}-\mathbf{k}',\Omega) + P_s(\mathbf{k}-\mathbf{k}',\Omega)\right] \times \int_{-\infty}^{\infty}\mathrm{d}\omega'\, I(\omega,\Omega,\omega')\, A_0(\mathbf{k}',\omega') \quad , \tag{2.119}$$

where the pair fluctuation propagator is

$$K(\mathbf{q},\omega) = \frac{g}{\pi\bar{N}}\,\frac{\omega\tau}{\left[\ln(T/T_c) + \xi_0^2 q^2 + b\,(\omega/4T)^2\right]^2 + [\omega\tau]^2} \tag{2.120}$$

and the abbreviations

$$\omega\tau = (\pi/2)\tanh(\omega/4T)\,, \quad b = 7\xi(3)/\pi^2\,, \quad \xi_0^2 = (7\xi(3)/48)(v_F/\pi T)^2 \tag{2.121}$$

have been used. Equations (2.119)–(2.121) now enter the equation for the quasiparticle self-energy, i.e. (2.28), and are solved self-consistently. The equation for the even-ω part $\xi(\mathbf{k},\omega)$ of the self-energy is obtained from (2.119) by changing the sign in front of the term $|\psi_d|^2 K$ and replacing the spectral function A_0 of the Green's function proportional to τ_0 by the spectral function A_3 that refers to the τ_3 component. The spin fluctuation interaction $P_s = (3/2)U^2 \mathrm{Im}\,\chi_0(1 - U\chi_0)^{-1}$, the spectral functions A_0 and A_3, and the kernel I are defined in (2.29) and are calculated self-consistently as described in Appendix A. It should be pointed out that our pair propagator K is related to the T-matrix Γ calculated earlier by Hotta *et al.* [58] by the equation $\pi K = -\mathrm{Im}\,\Gamma_0 = \mathrm{Im}\,\phi_0[(V^{-1} - \mathrm{Re}\,\phi_0)^2 + (\mathrm{Im}\,\phi_0)^2]^{-1}$, where Γ_0 and ϕ_0 are the undressed particle-particle T-matrix and susceptibility, respectively, and V is the BCS pairing constant for a d-wave. It has been pointed out in [58] that the equation $1 = V\mathrm{Re}\,\phi_0(0,\Omega)$ agrees with that for the binding energy Ω of a Cooper pair. In calculating K from the expression given above we have subtracted $1/V$ from $\mathrm{Re}\,\phi_0$ utilizing the gap equation and expanding the rest in terms of $\xi_0^2 q^2$ and $\tau\omega$ (see (9) and (10) in [54] for ξ_0^2 and τ). Thus, our contribution from K to the self-energy in (2.119) and the corresponding contribution for ξ agrees with those obtained in [58] if the dressed particle–particle T-matrix Γ is replaced by the undressed one. Of course, we have solved (2.119) for the self-energy component $\omega\,[1 - Z(\mathbf{k},\omega)]$ and the corresponding equation for $\xi(\mathbf{k},\omega)$ self-consistently by employing a tight-binding energy $\epsilon(\mathbf{k})$ with nearest and next-nearest neighbor hopping, whose 2D Fermi line has been adjusted to that of underdoped hole-doped cuprates. For example, in (2.4) the chemical potential has been taken to be $\mu = -1.1$, yielding a doping concentration $x = 0.08$. For the effective Coulomb repulsion we employed $U(\mathbf{q})$ introduced in [54], with a maximum value $U(\mathbf{Q}) = U = 3.2t$. In that case, in accordance with our calculated phase diagram for hole-doped cuprates (see Fig. 2.4), the value of T_c in the absence of order parameter fluctuations, i.e. $K = 0$, becomes about $0.03t$.

2.3 Derivation of Important Formulae and Quantities

2.3.1 Elementary Excitations

For understanding the high-T_c cuprates, their elementary excitations are of central significance. Their theoretical analysis is based on the Green's functions for the elementary excitations, which are given in Nambu space [18, 19]. After continuation to the real ω axis, the corresponding spectral density for a fixed temperature is given by

$$A(\mathbf{k},\omega) = -\frac{1}{\pi}\frac{\Sigma''(\mathbf{k},\omega)}{\left[\omega - \epsilon_{\mathbf{k}} - \Sigma'(\mathbf{k},\omega)\right]^2 + \left[\Sigma''(\mathbf{k},\omega)\right]^2} \quad . \tag{2.122}$$

Here, $\epsilon_{\mathbf{k}}$ is the tight-binding energy dispersion on a square lattice introduced in (2.4) and $\Sigma'(\mathbf{k},\omega)$ and $\Sigma''(\mathbf{k},\omega)$ are the real and imaginary parts, respectively, of the self-energy described earlier in this chapter. We have performed our calculations for the elementary excitations

$$\omega(\mathbf{k},T) = \epsilon(\mathbf{k}) + \Sigma(\mathbf{k},\omega(\mathbf{k},T),T) \tag{2.123}$$

for various doping concentrations x, where Σ was calculated self-consistently using the 2D one-band Hubbard Hamiltonian for a CuO_2 plane and the FLEX approximation. Below T_c the superconducting gap function $\phi(\mathbf{k},\omega)$ has also been calculated self-consistently. As described earlier the full momentum and frequency dependence of the quantities has been kept and no further parameter has been introduced.

These equations are standard; however, it is important to realize that, owing to the combined effects of Fermi surface topology and $\chi(\mathbf{q}=\mathbf{Q},\omega)$ at the antiferromagnetic wave vector $\mathbf{Q}_{AF} = (\pi,\pi)$, the $\mathbf{k}$ and ω dependences of $\Sigma(\mathbf{k},\omega)$ become very pronounced and change the dispersion $\omega(\mathbf{k})$. It is known that the strong scattering of quasiparticles by antiferromagnetic spin fluctuations results in a non-Fermi liquid behavior of the quasiparticle self-energy for low-lying energy excitations; in particular, in $\mathrm{Im}\,\Sigma \sim \omega$ [66, 67]. Clearly, it follows from (2.123) that the expected doping and momentum dependence resulting from the crossover from $\Sigma \propto \omega^2$ to $\Sigma \propto \omega$, *i.e.* to a non-Fermi liquid behavior, can be reflected in $\omega(\mathbf{k})$ and $A(\mathbf{k},\omega)$. Physically speaking, the change in the ω dependence of the self-energy $\Sigma(\mathbf{k},\omega)$ changes the velocity of the elementary excitations. Thus, as mentioned in the Introduction and as will be discussed later, for a given $\mathbf{k}$-vector, the momentum distribution curve in ARPES experiments shows a "kink" at some characteristic frequency controlled by the spin fluctuation energy ω_{sf}. Regarding the superconducting state, the $\mathbf{k}$ and ω dependence of the order parameter $\Delta(\mathbf{k},\omega)$ is important and yields the feedback of the superconducting state on the elementary excitations.

From the elementary excitations of the quasiparticles mentioned above, we have calculated the spin excitations of the cuprates mainly via the expression

$$\mathrm{Im}\ \chi_{s0,c0}(\mathbf{q},\omega) = \frac{\pi}{N}\int_{-\infty}^{\infty} \mathrm{d}\omega'\ [f(\omega') - f(\omega'+\omega)]$$
$$\times \sum_{\mathbf{k}} [A(\mathbf{k}+\mathbf{q},\omega'+\omega)A(\mathbf{k},\omega') \pm A_1(\mathbf{k}+\mathbf{q},\omega'+\omega)A_1(\mathbf{k},\omega')] \ , \tag{2.124}$$

where f denotes the Fermi distribution function and A_1 is the spectral function of the anomalous Green's function defined in (2.26). The corresponding procedure is described in Appendix A. In order to compare the results with inelastic neutron scattering experiments, we have calculated the imaginary part of the renormalized (RPA) susceptibility, i.e.

$$\mathrm{Im}\,\chi_s(\mathbf{Q},\omega) = \frac{\mathrm{Im}\,\chi_{s0}(\mathbf{Q},\omega)}{(1 - U\,\mathrm{Re}\,\chi_{s0}(\mathbf{Q},\omega))^2 + U^2\,(\mathrm{Im}\,\chi_{s0}(\mathbf{Q},\omega))^2} \quad . \tag{2.125}$$

Here, U denotes an effective Coulomb interaction using the Hubbard Hamiltonian ((2.1)). We have choosen $t' = 0.2$ in order to describe the Fermi surface topology of both YBCO and LSCO. In general, one finds that the structure of $\mathrm{Im}\,\chi$ is determined by $\mathrm{Im}\,\chi_0$ if $(U\mathrm{Re}\,\chi_0) \neq 1$ and by $(U\mathrm{Re}\;\chi_0) = 1$ if this latter condition can be fulfilled. This will be discussed later in connection with the resonance peak.

2.3.2 Superfluid Density and Transition Temperature for Underdoped Cuprates

In order to calculate the generic phase diagram for hole-doped cuprates (see Fig. 1.4), we have assumed that a rigid-band approximation is valid and have varied only the chemical potential μ in (2.1) in order to change the carrier concentration. The band filling $n = 1/N \sum_{\mathbf{k}} n_{\mathbf{k}}$ was determined with the help of the $\mathbf{k}$-dependent occupation number $n_{\mathbf{k}} = 2\int_{-\infty}^{\infty} \mathrm{d}\omega f(\omega) A(\mathbf{k},\omega)$ which was calculated self-consistently. The spectral function $A(\mathbf{k},\omega) = N(\mathbf{k},\omega)$ corresponds to the local density of states and has been defined in sect. 2.1. f denotes the Fermi distribution function. $n = 1$ corresponds to half filling. In order to simplify the discussion, we have also fixed the effective Coulomb interaction U as $U = 4t \approx 1$ eV in accordance with the tight-binding energy dispersion $\epsilon_{\mathbf{k}}$ measured in ARPES [68]. No further parameter is introduced.

The bulk transition temperature T_c at which phase coherence of the Cooper pairs occurs was determined by the Ginzburg–Landau free–energy functional $\Delta F\{n_s, \Delta\}$, where the superfluid density $n_s(x,T)/m$ was calculated self-consistently from the current–current correlation function and from

$$\frac{n_s}{m} = \frac{2t}{\hbar^2}\,(S_N - S_S) \quad , \tag{2.126}$$

where we have introduced for convenience the oscillator strength

$$S_N = \frac{\hbar^2 c}{2\pi e^2 t} \int_{0^+}^{\infty} \sigma_1(\omega)\,\mathrm{d}\omega \quad ; \tag{2.127}$$

S_S is the value of (2.127) in the superconducting state. Here, we utilize the f-sum rule for the real part of the conductivity $\sigma_1(\omega)$, i.e. $\int_0^{\infty} \sigma_1(\omega)\,\mathrm{d}\omega = \pi e^2 n/2m$, where n is the 3D electron density and m denotes the effective band mass for the tight-binding band considered. $\sigma(\omega)$ was calculated in the normal and superconducting states using the Kubo formula [20, 69]

$$\sigma(\omega) = \frac{2e^2}{\hbar c}\frac{\pi}{\omega}\int_{-\infty}^{\infty} d\omega' \left[f(\omega') - f(\omega'+\omega)\right] \sum_{\mathbf{k}} \left[v_{k,x}^2 + v_{k,y}^2\right] \times \left[A(\mathbf{k},\omega'+\omega)A(\mathbf{k},\omega')A_1(\mathbf{k},\omega'+\omega)A_1(\mathbf{k},\omega')\right] \quad , \tag{2.128}$$

where $v_{k,i} = \partial\epsilon_k/\partial k_i$ are the calculated band velocities within the CuO_2 plane and c is the c-axis lattice constant. The spectral function A_1 was defined in (2.26). Vertex corrections have been neglected. Physically speaking, we are looking for a loss of spectral weight of the Drude peak at $\omega = 0$ that corresponds to excited quasiparticles above the superconducting condensate for temperatures $T < T_c^*$. The penetration depth $\lambda(x,T)$ was calculated within the London theory through $\lambda^{-2} \propto n_s$ [70] and will be discussed later.

Most importantly, using our results for $n_s(x,T)$, we have calculated the doping dependence of the Ginzburg–Landau-like free-energy change $\Delta F \equiv F_S - F_N$, [10, 11],

$$\Delta F = \Delta F_{cond} + \Delta F_{phase} \quad , \tag{2.129}$$

where $\Delta F_{cond} \simeq \alpha\{n_s/m\}\Delta_0(x)$ is the condensation energy due to Cooper pairing and $\Delta F_{phase} \simeq \hbar^2 n_s/2m$ is the loss in energy due to phase incoherence of the Cooper pairs. α describes the available phase space for Cooper pairs (normalized per unit volume) and can be estimated in the strongly overdoped regime. In the BCS limit one finds $\alpha \simeq 1/400$. Δ_0 is the superconducting order parameter at $T = 0$. Within standard (time-dependent) Ginzburg–Landau theory[2], the superfluid density n_s can be calculated via $n_s^0/n_s = \langle\nabla\phi(\mathbf{r},t)\nabla\phi(0)\rangle$, where $\nabla\phi(\mathbf{r},t)$ reflects the changes of the spatial and time dependence of the Cooper pair wave function. n_s^0 is the static mean-field value of the superfluid density for a given temperature, calculated with our extended FLEX approximation for the generalized Eliashberg equations.

Owing to the layered structure of the cuprates, in the underdoped case they should behave in accordance with the 2D XY model except in a narrow critical range around T_c where the 3D XY model is more appropriate [71, 72]. The standard theory for the 2D XY model, the Berezinskii–Kosterlitz–Thouless (BKT) renormalization group theory, should thus be a reasonable starting point [73, 74, 75, 76]. The superconducting transition predicted by the BKT theory is due to unbinding of fluctuating vortex–antivortex pairs in the superconducting order parameter. Gaussian phase fluctuations are not important, since they do not shift T_c.[3] Furthermore, if one takes the coupling of the phase to the electromagnetic field into account, they become gapped at the plasma frequency (of the order of 1 eV) owing to the Higgs mechanism [77].

[2] In analogy to a ferromagnet, we expect $n_s^0/n_s = \langle\nabla\Phi(\mathbf{r},t)\nabla\Phi(0)\rangle$. Note that it is straightforward to map our electronic theory onto a lattice (Wannier–type representation) and then to derive from the product of the anomalous Green's functions, $\{\mathcal{F}\cdot\mathcal{F}^*\}$, a contribution to the free energy of the form $n_s\cos\Theta_{ij}$ as used by Chakraverty *et al.* [51]. Here, Θ_{ij} is the angle between the phases of neighboring Cooper-pairs. Approximately, one has $n_s = n_s^0\bar{\Theta}_{ij}$, with $\bar{\Theta}_{ij} = 1$ for $T < T_c$ and $\bar{\Theta}_{ij} = 0$ for $T > T_c$.

[3] This is true in three dimensions. Of course, in the 2D case Gaussian fluctuations destroy the long-range order, yielding $T_c = 0$, but the mean-field transition is still unchanged.

Let us now turn to a second possibility for the determination of T_c, namely with the help of the BKT theory. It turns out that the relevant parameters for the unbinding of thermally created vortex–antivortex pairs are the dimensionless stiffness K and the vortex core energy E_{core}. The stiffness is related to n_s by

$$K(T) = \beta\hbar^2 \frac{n_s(T)}{m} \frac{d}{4} \quad , \tag{2.130}$$

where β again denotes the inverse temperature and m the effective mass. d is the average spacing between CuO_2 layers. In our calculations we set d to half the height of the unit cell of $YBa_2Cu_3O_{6+x}$. One then has to solve the Kosterlitz recursion relations

$$\frac{dy}{dl} = (2 - \pi K)\, y \tag{2.131}$$

$$\frac{dK}{dl} = -4\pi^3 y^2 K^2 \quad . \tag{2.132}$$

Here $y = e^{-\beta E_c}$ denotes the vortex fugacity. For the vortex core energy, we have used the approximate result of Blatter *et al.*, i.e.

$$E_{core} = \pi k_B T K \ln \kappa \quad , \tag{2.133}$$

where κ is the Ginzburg parameter, and $l = (r/r_0)$ is a logarithmic length scale which relates K to the strength of the vortex–antivortex interaction. For $T > T_c$, K tends to zero for $l \to \infty$, so that the interaction at large distances is screened and the largest vortex–antivortex pairs unbind. This destroys the Meissner effect and leads to dissipation. On the other hand, bound Cooper pairs reduce K and thus n_s, but do not destroy superconductivity. After (2.131) and (2.133) have been solved, it turns out that that the renormalization of K is very small [78]. Thus, to a good approximation, one can obtain $T_c(x)$ from the simple criterion [62, 78, 79, 80][4]

$$K(T_c) = \frac{2}{\pi} \qquad \text{or} \qquad \frac{n_s(T_c, x)}{m} = \frac{2}{\pi} \frac{4k_B T_c}{\hbar^2 d} \quad . \tag{2.134}$$

In order to investigate the dynamical phase stiffness, one has to calculate $n_s(\omega)$. A dynamical generalization of the BKT theory was developed by Ambegeokar *et al.* [81, 75]. It turns out that the critical size for a vortex–antivortex pair is given by

$$r_\omega = \sqrt{\frac{D_\nu}{2\pi\omega}} \quad , \tag{2.135}$$

[4] In our FLEX theory, the fluctuations of the ordered antiferromagnetic state in the paramagnetic metallic regime are treated *beyond* the mean-field level, however, the fluctuations of the superconducting condensate were neglected in earlier treatments. A detailed comparison between $n_s(\omega)$ in the XY model and in the FLEX approximation is given in [78, 80].

where D_ν denotes the corresponding diffusion constant. Only pairs with size $r \leq r_\omega$ contribute to the screening. Unfortunately, D_ν is not easy to calculate. In the absence of pinning, the theory of Bardeen and Stephen yields [82]

$$D_\nu^0 = \frac{2\pi c^2 \xi_{ab}^2 \rho_n T}{\phi_0^2 \tilde{d}} \quad , \tag{2.136}$$

where c is the speed of light, $\xi_{ab} \sim r_0/2$ corresponds to the coherence length, ρ_n denotes the normal-state resistivity, $\phi_0 = hc/2e$ is the elementary superconducting flux quantum, and $\tilde{d}$ corresponds to an effective layer thickness. However, in cuprate superconductors, pinning becomes important. Thus we have assumed a simple Arrhenius law

$$D_\nu = D_\nu^0 \exp\left(\frac{-E_p}{T}\right) \quad , \tag{2.137}$$

where E_p denotes the corresponding pinning energy barrier. We insert (2.137) and (2.136) into (2.135), yielding a new length scale l in (2.131) and (2.132), namely a new upper limit $l = \ln(r_\omega/r_0)$. Then, with the help of (2.135)–(2.137) and (2.131) and (2.132), we calculate the dynamical conductivity $\sigma(\omega)$ via [20]

$$\frac{n_s(\omega)}{m} = \frac{1}{e^2}\,\omega\,\mathrm{Im}\;\sigma(\omega) \quad , \tag{2.138}$$

where e is the elementary charge, and $\mathrm{Im}\,\sigma(\omega)$ has been obtained from the current–current correlation function and the Kubo formula using the FLEX approximation (see (2.128)).

2.3.3 Raman Scattering Intensity Including Vertex Corrections

In general, the differential cross section in a Raman scattering experiment is proportional to the imaginary part of the Raman response function $\chi_{\Gamma\gamma}$, which is given by the analytic continuation of

$$\begin{aligned}&\chi_{\Gamma\gamma}(\mathbf{q}, i\nu_m)\\ &= -T \sum_{\mathbf{k}, i\omega_n} \mathrm{Tr}\left[\hat{G}(\mathbf{k}+\mathbf{q}, i\omega_n + i\nu_m)\hat{\Gamma}(\mathbf{k}, \mathbf{k}+\mathbf{q}, i\nu_m)\hat{G}(\mathbf{k}, i\omega_n)\hat{\tau}_3\right]\gamma(\mathbf{k}) \quad ,\end{aligned} \tag{2.139}$$

where $\hat{G}$ is the Green's function in Nambu space and $\hat{\tau}_i$ are the Pauli matrices. Since the momentum transfer from the scattered photon to the electronic system $\mathbf{q}$ is much smaller than the extension of the Brillouin zone, we put $\mathbf{q} = 0$. $\gamma_\mathbf{k}$ is the bare vertex that describes the coupling of light to effective density fluctuations, and Γ denotes the dressed vertex, which includes renormalization effects due to the pairing interaction and elastic electron–electron

scattering [83]. $\gamma(\mathbf{k})$ can be parameterized by the so-called effective–mass approximation, i.e.

$$\gamma(\mathbf{k}) = m \sum_{\alpha,\beta} \hat{e}^S_\alpha \frac{\partial^2 \epsilon_k}{\partial k_\alpha \, \partial k_\beta} \hat{e}^I_\beta \quad . \tag{2.140}$$

Here, $\hat{e}^I$ and $\hat{e}^S$ are the polarization vectors of the incoming and scattered light, respectively, and ϵ_k is the normal-state dispersion for which a two-dimensional tight-binding band structure

$$\epsilon_k = -2t \left[\cos(k_x) + \cos(k_y) - 2B \cos(k_x)\cos(k_y) + \mu/2\right]$$

introduced earlier in (2.4), is assumed. This approach is often used and is believed to be valid in the nonresonant limit (i.e. neglecting interband transitions). Analytic continuation from imaginary to real frequencies leads to the following expression for the Raman response function:

$$\begin{aligned} \mathrm{Im}\, \chi_{\Gamma\gamma}(\mathbf{q}=0,\omega) = \pi \int_{-\infty}^{\infty} \mathrm{d}\omega' \left[f(\omega') - f(\omega'+\omega)\right] \sum_{\mathbf{k}} \Gamma(\mathbf{k},\omega',\omega) \\ \times \left[N(\mathbf{k},\omega'+\omega)N(\mathbf{k},\omega') + A_1(\mathbf{k},\omega'+\omega)A_1(\mathbf{k},\omega')\right] \gamma(\mathbf{k}) \quad . \end{aligned} \tag{2.141}$$

Here, $N(\mathbf{k},\omega) = A_0(\mathbf{k},\omega) + A_3(\mathbf{k},\omega)$ and $A_1(\mathbf{k},\omega)$ are the spectral densities of the Green's functions G and F. The bare Raman vertices for the different polarization symmetries B_{1g}, B_{2g}, and A_{1g} are the following [83]:

$$\begin{aligned} \gamma_{B_{1g}} &= t\left[\cos(k_x) - \cos(k_y)\right] \quad , \\ \gamma_{B_{2g}} &= 4tB \sin(k_x)\sin(k_y) \quad , \\ \gamma_{A_{1g}} &= t\left[\cos(k_x) + \cos(k_y) - 4B\cos(k_x)\cos(k_y)\right] \quad . \end{aligned} \tag{2.142}$$

Here, t is the nearest–neighbor hopping energy and $t' = -Bt$ (with $B = 0.45$) is the next–nearest–neighbor hopping energy in the tight-binding band [84]. It should be pointed out that we have subtracted from the vertex for $A^{x'x'}$ symmetry given in [83] the vertex for B_{2g} symmetry in order to obtain an A_{1g} component which is fully symmetric with respect to the D_{4h} point group.

In order to derive the vertex corrections and thus the equation $\Gamma(\gamma)$, let us first show that Ward's identity for the electromagnetic kernel holds also for the FLEX approximation. The general expression for the current–charge correlation function in the 2×2 Nambu matrix formalism is given by [19] $(\mu, \nu = 1, 2, 3, 0)$

$$P_{\mu\nu} = -e^2 \sum_k \frac{1}{2} \mathrm{Tr}\left[\gamma_\mu(k, k+q) G(k+q) \Gamma_\nu(k+q, k) G(k)\right] \quad , \tag{2.143}$$

where

$$q \equiv \mathbf{q}, i\nu_m \quad , \qquad k \equiv \mathbf{k}, i\omega_n \quad , \qquad \sum_k = T \sum_{i\omega_n} \sum_{\mathbf{k}} \quad .$$

Again, here Γ_ν is the dressed vertex function, and γ_μ is the bare current–charge vertex ($\mu = 1, 2, 3$):

$$\begin{aligned} \gamma_\mu(k, k+q) &= v_\mu(\mathbf{k} + \mathbf{q}/2)\tau_0 \quad , \\ \gamma_0 &= \tau_3 \quad . \end{aligned} \tag{2.144}$$

Note that $P_{00}(q) = e^2\chi_{c0}(q)$, where χ_{c0} is the irreducible charge susceptibility. The Dyson equation yields the dressed 2×2 matrix Green's function G in terms of the bare Green's function G_0 and the self-energy Σ:

$$G^{-1}(k) = G_0^{-1}(k) - \Sigma(k)i\omega_n Z(k)\tau_0 - [\epsilon(k) + \xi(k)]\,\tau_3 - \phi(k)\tau_1 \quad . \tag{2.145}$$

As discussed earlier in this chapter, the self-energy Σ in the FLEX approximation for the Hubbard Hamiltonian is determined by the following generalized Eliashberg equations:

$$\Sigma(k) = \sum_{k'} [P_s(k-k')\tau_0 G(k')\tau_0 + P_c(k-k')\tau_3 G(k')\tau_3] \quad ,$$

where $P_s(q)$ and $P_c(q)$ are defined in (2.31) and (2.32), respectively. The ladder approximation to the vertex function Γ_μ corresponding to the FLEX approximation to Σ then yields the following linear equation:

$$\begin{aligned} \Gamma_\mu(k+q, k) = \gamma_\mu(k+q, k) \\ + \sum_{k'} [\tau_0 G(k'+q)\Gamma_\mu(k'+q, k')G(k')\tau_0 P_s(k-k') \\ + \tau_3 G(k'+q)\Gamma_\mu(k'+q, k')G(k')\tau_3 P_c(k-k')] \, . \end{aligned} \tag{2.146}$$

Gauge invariance of the electromagnetic kernel requires that Γ_μ satisfy Ward's identity [19]:

$$\sum_\mu q_\mu \Gamma_\mu(k+q, k) = \tau_3 G^{-1}(k) - G^{-1}(k+q)\tau_3 \quad . \tag{2.147}$$

One can derive Ward's identity (2.147) from (2.146) by inserting (2.147) on the right–hand side in (2.145) and then making use of the self-energy equations. For $\mathbf{q} = 0$, the important relationship $P_{00}(\mathbf{q} = 0, i\nu_m) = e^2\chi_{c0}(\mathbf{q} = 0, i\nu_m) = 0$ follows from (2.147). Furthermore, we obtain from Ward's identity in (2.147) for $\mathbf{q} = 0$ the following expression for the vertex Γ_0:

$$\begin{aligned} \Gamma_0(\mathbf{k}, \omega+\nu, \omega) = Z(\mathbf{k}, \omega+\nu)\tau_3 + \omega\,[Z(\mathbf{k}, \omega+\nu) - Z(\mathbf{k}, \omega)]\,\nu^{-1}\tau_3 \\ - [\xi(\mathbf{k}, \omega+\nu) - \xi(\mathbf{k}, \omega)]\,\nu^{-1}\tau_0 \\ + [\phi(\mathbf{k}, \omega+\nu) + \phi(\mathbf{k}, \omega)]\,\nu^{-1}\tau_3\tau_1 \quad . \end{aligned} \tag{2.148}$$

The last term, proportional to $\tau_3\tau_1 = i\tau_2$, in (2.148) diverges for $\nu \to 0$ and corresponds to the collective gauge mode [19, 85]. This is renormalized by the Coulomb interaction to the 2D plasmon.

We turn now to the Raman response function χ_γ for the polarization symmetry γ. This is derived from $P_{00}(q)$ in (2.143) by replacing γ_0 and Γ_0 by the bare and full Raman vertices $\gamma\tau_3$ and $\Gamma\tau_3$:

$$\chi_\gamma(Q) = -\sum_k \frac{1}{2}\mathrm{Tr}\left[\Gamma(k+Q,k)\tau_3 G(k+Q)\gamma(\mathbf{k})\tau_3 G(k)\right] \quad . \tag{2.149}$$

The full Raman vertex Γ satisfies the following integral equation:

$$\Gamma(k+Q,k) = \gamma(\mathbf{k}) + \sum_q \left[P_s(q)+P_c(q)\right]\frac{1}{2}\mathrm{Tr}\left[\tau_3 G(k+q+Q)\tau_3 G(k+q)\right] \times \Gamma(k+q+Q,k+q) \quad . \tag{2.150}$$

After analytic continuation, we obtain approximately the following integral equation for the vertex function $\Gamma(\mathbf{k},\omega',\omega)$ occurring in (2.141):

$$\Gamma(\mathbf{k},\omega',\omega) = \gamma(\mathbf{k}) + \pi^2 \sum_{\mathbf{q}} \int_{-\infty}^{\infty} \mathrm{d}\nu\, P_s(\mathbf{q},\nu)\left[f(\nu-\omega'-\omega)+b(\nu)\right] \times \left[N(\mathbf{k}+\mathbf{q},\omega'-\nu+\omega)N(\mathbf{k}+\mathbf{q},\omega'-\nu) - A_1(\mathbf{k}+\mathbf{q},\omega'-\nu+\omega)A_1(\mathbf{k}+\mathbf{q},\omega'-\nu)\right]\Gamma(\mathbf{k}+\mathbf{q},\omega'-\nu,\omega) \quad . \tag{2.151}$$

Here, $P_s(\mathbf{q},\nu) = (3/2)U^2\mathrm{Im}\,\chi_s(\mathbf{q},\nu)$ is the pairing interaction due to exchange of spin fluctuations (we have left out the interaction due to charge fluctuations because this is much smaller). We now approximate this vertex equation in the following way: first, we consider only the lowest–order term by inserting on the right–hand side the bare vertex $\gamma(\mathbf{k}+\mathbf{q})$; secondly, we replace $\gamma(\mathbf{k}+\mathbf{q})$ by $\gamma(\mathbf{k}+\mathbf{Q})$ with $\mathbf{Q}=(\pi,\pi)$ because $P_s(\mathbf{q},\nu)$ is strongly peaked at $\mathbf{Q}$ and the equivalent vectors $(\pm\pi,\pm\pi)$. In this way we obtain approximately the following vertex corrections for the three different symmetries of interest:

$$\Gamma_{B_{1g}}(\mathbf{k},\omega',\omega) = t\left[\cos(k_x)-\cos(k_y)\right]\left[1-J(\mathbf{k},\omega',\omega)\right] \quad , \tag{2.152}$$

$$\Gamma_{B_{2g}}(\mathbf{k},\omega',\omega) = 4tB\sin(k_x)\sin(k_y)\left[1+J(\mathbf{k},\omega',\omega)\right] \quad , \tag{2.153}$$

and

$$\Gamma_{A_{1g}}(\mathbf{k},\omega',\omega) = t\left[\cos(k_x)+\cos(k_y)\right]\left[1-J(\mathbf{k},\omega',\omega)\right] - 4tB\cos(k_x)\cos(k_y)\left[1+J(\mathbf{k},\omega',\omega)\right] \quad , \tag{2.154}$$

where

$$J(\mathbf{k},\omega',\omega) = \pi^2\int_{-\infty}^{\infty}\mathrm{d}\nu\left[f(\nu-\omega'-\omega)+b(\nu)\right]\sum_{\mathbf{q}} P_s(\mathbf{q},\nu) \times \left[N(\mathbf{k}+\mathbf{q},\omega'+\omega-\nu)N(\mathbf{k}+\mathbf{q},\omega'-\nu) - A_1(\mathbf{k}+\mathbf{q},\omega'+\omega-\nu)A_1(\mathbf{k}+\mathbf{q},\omega'-\nu)\right] \quad . \tag{2.155}$$

The functions f and b in (2.151) and (2.155) are again the Fermi and Bose functions.

In the weak-coupling limit, where the gap function $\Delta(\mathbf{k})$ is independent of ω, Manske *et al.* have shown that the Raman response functions for the three relevant polarization geometries including vertex corrections, are approximately given by the following (assuming particle–hole symmetry and $T = 0$) [83]:

$$\chi_{A_{1g}}(\omega) = 2\left[\langle\gamma_{A_{1g}}^2\Delta_k^2\rangle - \frac{\langle\gamma_{A_{1g}}\Delta_k^2\rangle^2}{\langle\Delta_k^2\rangle}\right] \quad , \tag{2.156}$$

$$\chi_{B_{1g}}(\omega) = 2\left[\langle\gamma_{B_{1g}}^2\Delta_k^2\rangle + \frac{\langle\gamma_{B_{1g}}\Delta_k^3\rangle^2}{\left(\frac{\omega}{2}\right)^2\langle\Delta_k^2\rangle - (\langle\epsilon_k^2\Delta_k^2\rangle + 2\langle\Delta_k^4\rangle)}\right] \quad , \tag{2.157}$$

and

$$\chi_{B_{2g}}(\omega) = 2\langle\gamma_{B_{2g}}^2\Delta_k^2\rangle \quad . \tag{2.158}$$

Here, the averages $\langle f(\mathbf{k})\rangle$ are defined in terms of the Tsuneto function (see (10) in [83]). Let us emphasize that the second term in (2.157) is present only for a d-wave gap, and vanishes for an s-wave symmetry of Δ.

We come now to the theoretical description of order parameter collective modes in Raman scattering experiments. These modes can be calculated analogously to those in p-wave–pairing superconductors [86]. In general, it can be said that the $d_{x^2-y^2}$-wave pairing component in weak-coupling theory gives rise to a phase fluctuation mode which is renormalized into a 2D plasmon [87], and to an amplitude fluctuation mode of the d-wave gap. For each additional (weaker) pairing component, such as an extended s-wave component, one obtains an amplitude (real) and a phase (imaginary) fluctuation mode. Let us consider first the amplitude fluctuation mode of the $d_{x^2-y^2}$-wave gap. We have calculated the mode frequency ω_0 from the weak-coupling expression in [88] for $\mathbf{q} = 0$ and find

$$\mathrm{Re}\left[\sum_k(\omega^2 - 4\Delta_k^2)\left[\cos(k_x) - \cos(k_y)\right]^2\left[4E_k^2 - (\omega + i\Gamma)^2\right]^{-1}\frac{\tanh(E_k/2T)}{E_k}\right] = 0 \quad . \tag{2.159}$$

The effect of quasiparticle damping is taken into account by carrying out an analytical continuation of this result from $i\omega_m$ to $\omega + i\Gamma$. For a gap $\Delta(\mathbf{k}) = (\Delta_0/2)(\cos k_x - \cos k_y)$ and a band $\epsilon(\mathbf{k})$ with $t' = 0$ and chemical potential μ, the summation over $\mathbf{k}$ in the square Brillouin zone has been carried out numerically for the following expression for $T = 0$:

$$\chi_{s0}(\mathbf{Q},\omega) = \sum_k \frac{E_kE_{k+Q} - \epsilon_k\epsilon_{k+Q} - \Delta_k\Delta_{k+Q}}{(E_k + E_{k+Q})^2 - (\omega + i\Gamma)^2}\,\frac{E_k + E_{k+Q}}{2E_kE_{k+Q}} \quad . \tag{2.160}$$

Here, $E_k^2 = \epsilon^2(\mathbf{k}) + \Delta^2(\mathbf{k})$. We obtain a peak in the function of ω, $\mathrm{Re}\,\chi_{s0}(\mathbf{Q},\omega)$ at the kinematical gap $\omega = 2|\mu|$ [89], whose height decreases with increasing Γ. The approximate analytic result for $T = 0$ is given by

$$\chi_{s0}(\mathbf{Q},\omega) = V_0^{-1} - N_F(z/1+z)^{1/2}\log\left[4\,(1+z)^{1/2}\right] \quad , \tag{2.161}$$

where N_F is the density of states at the Fermi energy,

$$z = \left[4\mu^2 - (\omega + i\Gamma)^2\right]/\,(2\Delta_0)^2 \quad \text{and} \quad , \quad V_0^{-1} = N_F \log\,(2W/\Delta_0)\ . \tag{2.162}$$

Here, $W = 4t$ is the half bandwidth. The function $\mathrm{Re}\,\chi_{s0}(\mathbf{Q},\omega)$ in (2.162) first rises with ω^2 and then exhibits a peak at the kinematical gap $2|\mu|$, whose height is about $V_0^{-1} - (\pi/2)N_F(\Gamma/2\Delta_0)$. A low-frequency mode, i.e. a zero of the equation $\mathrm{Re}\,\chi_{s0}(\mathbf{Q},\omega) = 1/U$, is obtained only for a finite range of U values which decreases with increasing Γ. For $t' = -0.45t$, a kinematical gap no longer exists and the effective $|\mu|$ is nearly zero. The approximate analytical result for the expression in (2.161) becomes then equal to

$$\chi_{s0}(\mathbf{Q},\omega) = V_0^{-1} + \frac{1}{2}N_F i\frac{\bar{\omega}^2}{(\bar{\omega}+i\gamma)}K(\bar{\omega}+i\gamma) \quad , \tag{2.163}$$

where

$$\bar{\omega} = \omega/2\Delta_0 \qquad \text{and} \qquad \gamma = \Gamma/2\Delta_0 \quad .$$

Here, K is the first elliptic integral. By summing numerically over $\mathbf{k}$ in the square Brillouin zone, we obtain, for $t' = 0$ in $\epsilon(\mathbf{k})$ and $T = 0$, two solutions of (2.159) with frequencies $\omega_0 \simeq \sqrt{3}\Delta_0$ provided that the damping Γ is sufficiently large, namely, $\omega_0 < 3.5\Gamma$. For $t' = -0.45t$ and $T = 0$, we obtain two solutions whose frequencies are somewhat larger, $\omega_0 \simeq 2\Delta_0$, where again the condition $\omega_0 < 3.5\Gamma$ has to be satisfied. For a mode frequency $\omega_0 = 2\Delta_0 \simeq 0.2t$ at $T/T_c = 0.77$, we find a damping $\Gamma(\omega_0) \simeq 0.1t$ at the anti-node $\mathbf{k}_a$ which means that the condition $\omega_0 < 3.5\Gamma$ is satisfied. In [87], Wu and Griffin have obtained a frequency $\omega_0 = \sqrt{3}\Delta_0$ for the amplitude collective mode; however, the coupling of this mode to the charge fluctuations was neglected. We find that the coupling of this fluctuation in the particle–particle channel to the charge fluctuation in the particle-hole channel yields approximately the following contribution χ_{fl} to the charge susceptibility χ_{c0} at $T = 0$ (see [88] and [86]):

$$\chi_{fl}(\mathbf{q}=0,\omega) = 2\left(\frac{N_F'}{N_F}\frac{1}{V_0}\right)^2 \Delta_0^2\,\frac{1}{g(\omega)} \quad , \tag{2.164}$$

where

$$g(\omega) = N_F\left[\frac{2}{3}\bar{\omega}^2 + \frac{4}{3}\gamma^2 - 1 - \frac{8}{3}i\bar{\omega}\gamma \right.$$
$$\left. +\ \gamma\left(4\bar{\omega}^2 - 2\gamma^2 + 6i\bar{\omega}\gamma\right)\log\left(4\left[1-(\bar{\omega}+i\gamma)^2\right]^{-1/2}\right)\right] . \tag{2.165}$$

Here, N_F and $N_F' = \mathrm{d}N_F/d\omega$ are the density of states and its derivative at the Fermi energy $\omega = 0$. One notices from (2.165) that in the limit $\gamma \to 0$ one

obtains no valid solution of the equation $\mathrm{Re}\, g(\omega_0) = 0$ because the solution $\bar{\omega_0} = \sqrt{3/2}$ violates the condition that $\bar{\omega_0} \leq 1$. However, for suffiently large values of Γ ($\gamma \geq \bar{\omega}/2$), one obtains a solution of the equation $\mathrm{Re}\, g(\omega_0) = 0$ which satisfies the condition $\bar{\omega_0} \leq 1$.

We have also calculated the resonance frequency of the exciton-like s-wave mode of the order parameter which is caused by an additional s-wave pairing component $|g_0|$ smaller than the main d-wave pairing component $|\bar{g_2}|$ (see [87]). The method of Refs. [88] and [86] yields the following contribution χ_{exc} from this order parameter fluctuation mode to the charge susceptibility χ_{c0} at $T = 0$:

$$\chi_{exc}(\mathbf{q} = 0, \omega) = -\left(N_F \omega\right)^2 \left[g_{exc}(\omega)\right]^{-1} \quad , \tag{2.166}$$

where

$$g_{exc}(\omega) = \left(1 - \frac{\bar{g_2}}{g_0}\right) \sum_k \frac{1}{2E_k} + \frac{1}{2}\omega^2 \sum_k \frac{\tanh(E_k/2T)}{E_k \left[4E_k^2 - (\omega + i\Gamma)^2\right]} \quad . \tag{2.167}$$

From (2.167) we obtain the following approximate result:

$$g_{exc}(\omega) = \left(1 - \frac{\bar{g_2}}{g_0}\right) \frac{1}{V_0} + N_F i \frac{\bar{\omega}^2}{(\bar{\omega} + i\gamma)} K(\bar{\omega} + i\gamma) \quad , \tag{2.168}$$

where V_0^{-1} is given by (2.162) and $\bar{\omega}$ and γ by (2.163). We have carried out the summation over $\mathbf{k}$ in (2.167) numerically and find in agreement with Ref. [87], that a solution of the equation $\mathrm{Re}\, g_{exc}(\omega_0) = 0$ for given Δ_0 and Γ exists only for very small values of the parameter $(\bar{g_2}/g_0) - 1$ (≤ 0.1). This means that the s-wave pairing coupling has to be almost as strong as the d-wave pairing component, which is quite unrealistic. However, with increasing Γ the resonance frequency ω_0 decreases and becomes much smaller than the pair-breaking threshold $2\Delta_0$ for reasonably large scattering rates ($\Gamma/2\Delta_0 \sim 1/2$). This means that the contribution $\mathrm{Im}\, \chi_{exc}(\omega)$ of the exciton-like mode to the Raman scattering intensity with the B_{1g} polarization shows up as a small peak below the pair-breaking threshold. Since the damping Γ in the direction of the momentum of the antinode of the order parameter rises rapidly with ω, it may be that this peak becomes observable for smaller values of the ratio $g_0/\bar{g_2}$ of the s-wave and d-wave pairing couplings than those obtained from weak-coupling theory [87]. This will be discussed in the next chapter.

2.3.4 Optical Conductivity

Similarly to the Raman response, the optical conductivity $\sigma(\omega)$ is calculated here with the help of the current–current correlation function using the spectral densities which solve the generalized Eliashberg equations. For underdoped cuprates, in the presence of a pseudogap, the in-plane conductivity $\sigma_{ab}(\omega)$, neglecting vertex corrections, is given by

$$\sigma_{ab}(\omega) = \frac{2e^2}{\hbar c_0}\frac{\pi}{\omega}\int_{-\infty}^{\infty} \mathrm{d}\omega' \left[f(\omega') - f(\omega'+\omega)\right] \times \sum_{\mathbf{k}} \left[v_{k,x}^2 + v_{k,y}^2\right] \left[N(\mathbf{k},\omega'+\omega)N(\mathbf{k},\omega') + A_1(\mathbf{k},\omega'+\omega)A_1(\mathbf{k},\omega') + A_g(\mathbf{k},\omega'+\omega)A_g(\mathbf{k},\omega')\right] \quad , (2.169)$$

where $v_{k,i} = \partial\epsilon_k/\partial k_i$ are the band velocities within the ab plane and are calculated for the corresponding tight-binding energy dispersion of the quasiparticles. Again, N is the normal spectral function, and A_1 and A_g are the anomalous spectral functions with respect to the superconducting gap and the pseudogap, respectively. These spectral functions have been taken from a self-consistent solution of the generalized Eliashberg equations in the presence of the pseudogap, as already descibed in (2.63)–(2.65):

$$N(\mathbf{k},\omega) = -\frac{1}{\pi}\mathrm{Im}\frac{\omega Z + \epsilon_k + \xi}{(\omega Z)^2 - (\epsilon_k+\xi)^2 - E_g^2 - \phi^2} \quad ,$$

$$A_1(\mathbf{k},\omega) = -\frac{1}{\pi}\mathrm{Im}\frac{\phi}{(\omega Z)^2 - (\epsilon_k+\xi)^2 - E_g^2 - \phi^2} \quad ,$$

$$A_g(\mathbf{k},\omega) = -\frac{1}{\pi}\mathrm{Im}\frac{E_g}{(\omega Z)^2 - (\epsilon_k+\xi)^2 - E_g^2 - \phi^2} \quad .$$

We again want to emphasize that it is necessary to include the bubble contribution due to A_g in the conductivities and susceptibilities. Although Ward's identities are satisfied, neglect of this term leads to disagreement with experimental data. In the optimally and overdoped cases where no pseudogap is present, we take $A_g \equiv 0$.

It is interesting to remark that for high-T_c cuprates the transport properties *perpendicular* to the CuO_2 planes are also of significant interest. For example, measurements of the c-axis conductivity suggest that the conductance in c direction is coherent in the overdoped regime [90] and successively becomes incoherent in the underdoped regime [91, 92]. In this work we shall therefore study the two limits of coherent and incoherent c-axis conductivity. The coherent conductivity along the interplane c direction is given, to lowest order in the interlayer hopping parameter $t_\perp$ [93], by

$$\sigma_c(\omega) = \frac{e^2 t_\perp^2 c_0}{\hbar a_0^2}\frac{\pi}{\omega}\int_{-\infty}^{\infty} \mathrm{d}\omega' \left[f(\omega') - f(\omega'+\omega)\right] \sum_{\mathbf{k}} \left[N(\mathbf{k},\omega'+\omega)N(\mathbf{k},\omega') + A_1(\mathbf{k},\omega'+\omega)A_1(\mathbf{k},\omega') + A_g(\mathbf{k},\omega'+\omega)A_g(\mathbf{k},\omega')\right] \quad , \qquad (2.170)$$

where c_0 and a_0 are the c-axis and ab-plane lattice constants taken from experiment. On the other hand, incoherent conductivity corresponds to diffuse c-axis transmission and amounts to taking the averages of the spectral functions $N(\mathbf{k},\omega)$, $A_1(\mathbf{k},\omega)$, and $A_g(\mathbf{k},\omega)$ over all momenta (see the discussion in [94]). This means that $N(\mathbf{k},\omega)$ is replaced by the density of states

$$N(\omega) = \sum_k N(\mathbf{k}, \omega) \quad , \tag{2.171}$$

while the averages of A_1 and A_g vanish owing to the d-wave symmetry of the superconducting gap and pseudogap [94]. We find

$$\sigma_c^{\text{incoh}}(\omega) = \frac{e^2 t_\perp^2 c_0}{\hbar a_0^2} \frac{\pi}{\omega} \int_{-\infty}^{\infty} \mathrm{d}\omega' \left[f(\omega') - f(\omega' + \omega) \right] N(\omega' + \omega) N(\omega') \quad . \tag{2.172}$$

In the next chapter we shall discuss our results within these different approximations. In all cases the corresponding resistivity is given by $\rho = \sigma^{-1}(\omega \to 0)$. The frequency-dependent scattering rate $\tau^{-1}(\omega)$, which is a two-particle property, is obtained with the help of Drude's theory. As will be discussed later, determining $\tau^{-1}(\omega)$ from the Raman response yields approximately the same results.

2.4 Comparison with Similar Approaches for Cuprates

In this subsection we compare our electronic theory for Cooper pairing in high-T_c cuprates with similar approaches that also use the exchange of spin fluctuations as the relevant pairing mechanism. Let us emphasize that, obviously, the mechanism of Cooper pairing cannot be measured directly; therefore it is important to search for fingerprints of the pairing interaction in the superconducting gap function $\Delta(\mathbf{k}, \omega)$ in various experiments. In this connection, ARPES experiments that measure the spectral density directly and inelastic neutron scattering experiments that study the interplay between the quasiparticles and the spin excitations ("resonance peak"), are two key experiments in which fingerprints of the Cooper pairing can be seen directly.

In view of the well-known strong-coupling theory for phonons of Scalapino, Schrieffer, and Wilkins [95], it is therefore important to calculate $\Delta(\mathbf{k}, \omega)$ self-consistently. As mentioned earlier, the method for doing this is the FLEX approximation proposed by Bickers, Scalapino, and White [6]. In the past, the solution of the corresponding FLEX equations was done on the imaginary axis (or slightly above the real axis [11]), while in our theory, similarly to Dahm and Tewordt [10], we solve the generalized Eliashberg equations directly on the real frequency axis.

Thus, in short, we would like to stress that we do not want to focus on limiting solutions of the FLEX approach for $T \to 0$, doping $x \to 0$, and very large U (as was done by Serene, Hess, and others [96, 97, 98]). In our approach, for the cuprates and ruthenates we use a Berk–Schrieffer-type theory for the behavior of the quasiparticles in relation to spin excitations,

$$G = G\{\chi\} \quad , \quad \chi = \chi\{G\} \quad , \tag{2.173}$$

and determine χ from an electronic theory within the RPA. Obviously, the calculation demands a high degree of self-consistency in determining G, the

resultant elementary excitations, the spin susceptibility, and the superconducting properties. Although we are not fully reviewing the most closely related theories, we shall point out the main differences of those theories from our approach.

2.4.1 The Spin Bag Mechanism

In an early theory of Schrieffer and coworkers it was argued that the local suppression of the electronic gap in the antiferromagnetic phase can lead to an attractive interaction between quasiparticles [99]. Schrieffer *et al.* performed detailed calculations of the pairing potential mediated by the collective modes of the spin-density-wave (SDW) background. Thus, the main difference from the idea of conventional paramagnon theory that we use in our approach is that the spin bag theory takes into account explicitly the effect of the local antiferromagnetic order on the self-energy of the quasiparticles. On the other hand, however, simple model susceptibilities were used and, most importantly, the topology of the Fermi surface was neglected yielding nodeless p- or d-wave pairing in disagreement with experiment.

What is a simple physical picture for the spin bag mechanism? If the effective Coulomb interaction U is less than W (where W is the bandwidth), a hole injected into an SDW system depresses the staggered magnetization M surrounding a hole, in a region whose size L and shape depend on the nature of the Fermi surface and on the mean SDW amplitude [100]. The region of depressed M provides a bag, inside of which the hole is trapped self-consistently. As a result, the bag containing the hole moves as an entity and acts as a quasiparticle of spin $1/2$ and charge e. In a detailed analysis, Schrieffer and coworkers showed that two holes attract each other by sharing a common bag [99]. In the opposite limit, i.e. $U > W$, it was shown by several authors that a similar result occurs if finite-range antiferromagnetic order exists. In essence, an added hole always leads to a reduction of the local staggered order parameter by disordering the spins in the vicinity of the hole.

What is the main difference between the spin bag mechanism and our self-consistent theory? Although the effective pairing potential arising from the one-spin fluctuation exchange processes in the singlet channel is the well-known antiparamagnon result, i.e.

$$V_{APM} = U + \frac{U^3\chi_0^2(\mathbf{k}' - \mathbf{k})}{1 - U^2\chi_0^2(\mathbf{k}' - \mathbf{k})} + \frac{U^2\chi_0(\mathbf{k}' - \mathbf{k})}{1 - U\chi_0(\mathbf{k}' - \mathbf{k})} \quad , \tag{2.174}$$

the existence of the electronic gap provides a new mechanism for an attractive spin bag pairing potential. It arises from Pauli's exclusion principle because a fermionic line inside a bubble diagram is equal to the momentum of the injected particle. This leads to a compensation by its exchange counterpart or corresponding crossing diagrams. As a result, the corresponding self-energy due to the above spin fluctuations is positive near the SDW instability and

leads to a pseudogap. A second particle added to the system suppresses these fluctuations through Pauli's principle, reducing the phase space for electron–hole excitations and hence reducing χ. This leads to an effective interaction

$$V_{\mathbf{k}\mathbf{k}'}^{SB}(w,\omega') = i\sum_{\mathbf{q}}\int \frac{\mathrm{d}\nu}{2\pi}\, G_0(\omega-\nu,\mathbf{k}-\mathbf{q})\, G_0(-\omega'-\nu,-\mathbf{k}'-\mathbf{q}) \times U^2\chi(\mathbf{q},\nu)\, U^2\chi(\mathbf{q}+\mathbf{k}'-\mathbf{k},\nu+\omega'-\omega) \tag{2.175}$$

(for an illustration see, for example, Fig. 10 in [101]), where χ refers to an RPA series containing χ_0 that is calculated using a model susceptibility. In general, if the frequency scale associated with the fluctuations of the antiferromagnetically ordered domain is small compared with the (Hubbard) energy gap and if the length scale of the local antiferromagnetic order is large compared with the SDW coherence length $\xi_{SDW} \equiv \hbar v_F/\Delta$, where v_F is the Fermi velocity in the absence of the SDW, the above starting point is qualitatively correct. To some extent this is similar to our approach, in which a hole generates a local spin density wave that interacts with a second hole, finally yielding a Cooper pair. However, our corresponding interaction is purely repulsive in momentum space. It is interesting to remark that the attractive part of the spin bag pairing potential is indeed helpful for $d_{x^2-y^2}$-wave pairing, as pointed out by Scharnberg and coworkers [102]. This can be easily seen from the general arguments made in connection with Fig. 1.12. In contrast to the spin bag mechanism, in our self-consistent theory a stabilization of the $d_{x^2-y^2}$-wave order parameter occurs in frequency space owing to the feedback effect of $\Delta(\mathbf{k},\omega)$ on χ, yielding a resonance peak at ω_{res} as described above.

Finally, Kampf and Schrieffer extended the spin bag approach in order to study the spectral density in antiferromagnetically correlated metals [103]. They showed that in the spectral function, weight is shifted from the single–quasiparticle peak to the incoherent background, which evolves into upper and lower Hubbard bands of the antiferromagnetic insulator. Kampf and Schrieffer argued that precursors of these split bands should show up as *shadow bands* in ARPES measurements, which have indeed been observed [104]. For sufficiently strong antiferromagnetic correlations a coupling of states $\mathbf{k}$ and $\mathbf{k}'$ under the condition

$$|\mathbf{k}-\mathbf{k}'-\mathbf{Q}| < \xi^{-1} \quad , \tag{2.176}$$

where again $\mathbf{Q} = (\pi,\pi)$ and ξ is the antiferromagnetic correlation length, leads to distinct states in ARPES experiments. This happens because the energy eigenstates $|\Phi_{\mathbf{k}s}\rangle$ no longer have a sharp momentum; that is,

$$|\Phi_{\mathbf{k}s}\rangle = u_{\mathbf{k}}\,|\mathbf{k}\rangle + s v_{\mathbf{k}}\,|\mathbf{k}+\mathbf{Q}\rangle \quad , \tag{2.177}$$

where

$$u_{\mathbf{k}}^2 + v_{\mathbf{k}}^2 = 1 \quad , \tag{2.178}$$

owing to Bragg scattering. Therefore, if one creates a hole with energy $E(\mathbf{k})$ in a lower band by photoemission, one will observe the corresponding emitted electron with momentum $\mathbf{k}$ with a probability $u_{\mathbf{k}}^2$, but a momentum $\mathbf{k}+\mathbf{Q}$ also occurs with probability $1-u_{\mathbf{k}}^2$. Thus, quite generally, Bragg scattering with strong antiferromagnetic correlations leads to shadow states. This picture was supported by early FLEX and QMC calculations [11, 105] and is also contained in our approach, of course.

2.4.2 The Theory of a Nearly Antiferromagnetic Fermi Liquid (NAFL)

In 1992, Monthoux and Pines pointed out that for the theoretical description of spin-fluctuation-induced superconductivity in cuprates it is extremely important to take full account of the momentum and frequency dependence of the pairing interaction [106, 107]. Similarly to our theory described in Chap. 2, Monthoux and Pines used a Hamiltonian H for the in-plane quasiparticles that reads

$$H = H_0 + H_{int} \quad , \tag{2.179}$$

where

$$H_0 = \sum_{\mathbf{p},\sigma} \epsilon_{\mathbf{p}}\, \psi^{\dagger}_{\mathbf{p},\sigma} \psi_{\mathbf{p},\sigma} \tag{2.180}$$

and $\epsilon_{\mathbf{p}}$ describes the bare quasiparticles with a simple tight-binding dispersion relation. The interaction part H_{int} models an effective interaction between the quasiparticles and the spin fluctuations and is given by

$$H_{int} = \sum_{\mathbf{q}} g(\mathbf{q})\, \mathbf{s}(\mathbf{q}) \cdot \mathbf{S}(-\mathbf{q}) \quad , \tag{2.181}$$

where

$$\mathbf{s}(\mathbf{q}) = \frac{1}{2} \sum_{\alpha,\beta,\mathbf{k}} \psi^{\dagger}_{\mathbf{k}+\mathbf{q},\alpha}\, \sigma_{\alpha\beta}\, \psi_{\mathbf{k},\beta} \tag{2.182}$$

and $\mathbf{S}$ is the spin-fluctuation propagator. Its properties are determined by the spin–spin correlation function $\chi_{ij}(\mathbf{q},\omega) = \delta_{ij}\chi(\mathbf{q},\omega)$. Later, the momentum dependence of g is neglected. An important step was taken by Millis, Monien, and Pines [108], who proposed for $\chi(\mathbf{q},\omega)$ the form

$$\chi(\mathbf{q},\omega) = \chi_{MMP}(\mathbf{q},\omega) = \frac{\chi_Q}{1+\xi^2(\mathbf{q}-\mathbf{Q}) - i\omega/\omega_{sf}} \quad , \tag{2.183}$$

where the parameter χ_Q denotes the static spin susceptibility at the wave vector $\mathbf{Q} = (\pi,\pi)$, ξ is a temperature-dependent antiferromagnetic correlation length, and ω_{sf} reflects the characteristic spin-fluctuation (i.e. paramagnon) mode energy of the system considered. All these parameters have been determined by fitting NMR data.

Physically speaking, since the dynamical spin susceptibility $\chi(\mathbf{q},\omega)$ peaks at wave vectors close to (π,π), two different kinds of quasiparticle emerge: (a) "hot" quasiparticles that are located not far from those momentum points on the Fermi surface that can be connected by $\mathbf{Q}$ (see Fig. 2.8, the "hot spots") and (b) "cold" (or nodal) quasiparticles that are located not far from the diagonals and feel a "normal" interaction. Pines and coworkers argued, by a detailed analysis, that the cold quasiparticles may be characterized by Landau's Fermi liquid theory, whereas the hot quasiparticles have many highly anomalous properties.

Using the above assumptions, Monthoux and Pines performed strong-coupling calculations using the Eliashberg formalism and concluded that the normal state of hole-doped cuprates might be described by "nearly antiferromagnetic Fermi liquid" (NAFL) model [107]. Monthoux and Pines found, depending on the parameters, a high T_c and also $d_{x^2-y^2}$ pairing. This can be easily understood in view of the general remarks made in sect. 1.4.3. The main difference from our work arises from the fact that the pairing interaction in the NAFL model is

$$V_{eff}^{\mathrm{NAFL}}(\mathbf{q},\omega) = g^2 \chi_{MMP}(\mathbf{q},\omega) \tag{2.184}$$

and thus is a parameterization mainly in terms of measured NMR data. In our theory, the effective pairing interaction is determined the Feynman diagrams shown in Fig. 2.2 and is calculated self-consistently, taking into account the scattering processes of the in-plane quasiparticles from spin fluctuations that are also generated by the quasiparticles. This was first done by Bickers, Scalapino, and White [6]. Thus, the antiferromagnetic correlation length ξ and the characteristic frequency of the spin fluctuations, ω_{sf}, are results of a microscopic calculation and no longer parameters. This is particularly important if doping-dependent quantities are considered. Furthermore, below T_c the feedback effect of the elementary excitations on the dynamical spin susceptibility is very strong, yielding a resonant-like peak in agreement with observations in INS experiments. This strong interdependence also supports our self-consistent procedure.

2.4.3 The Spin–Fermion Model

Because the NAFL approach is formulated in a phenomenological way and only applicable to the normal state. i.e. for temperatures $T \geq T_c$, one might ask how one can generalize this approach below T_c and find a microscopic basis for the NAFL picture. This has been done by Chubukov, Schmalian, and Pines in the so–called spin–fermion model [109]. They derive an effective low-energy model from a microscopic Hubbard–type Hamiltonian with a four–fermion interaction

$$H = \sum_{\mathbf{k},\alpha} \varepsilon_{\mathbf{k}} \psi^{\dagger}_{\mathbf{k},\alpha} \psi_{\mathbf{k},\alpha} + \sum_{\mathbf{k_i},\alpha_i} U^{\alpha_1,\alpha_2,\alpha_3,\alpha_4}_{\mathbf{k}_1,\mathbf{k}_2,\mathbf{k}_3,\mathbf{k}_4} \; \psi^{\dagger}_{\mathbf{k}_1,\alpha_1} \psi^{\dagger}_{\mathbf{k}_2,\alpha_2} \psi_{\mathbf{k}_3,\alpha_3} \psi_{\mathbf{k}_4,\alpha_4} \tag{2.185}$$

for fermions with spin α and momentum $\mathbf{k}$; $\epsilon_{\mathbf{k}}$ is again the band structure dispersion. Similarly to our approach, one then uses the one–band Hubbard model with local Coulomb interaction,

$$U^{\alpha_1,\alpha_2,\alpha_3,\alpha_4}_{\mathbf{k}_1,\mathbf{k}_2,\mathbf{k}_3,\mathbf{k}_4} = U\delta_{\mathbf{k_1}+\mathbf{k_2}-\mathbf{k_3}-\mathbf{k_4}} \times (\delta_{\alpha_1\alpha_4}\delta_{\alpha_2\alpha_3} - \delta_{\alpha_1\alpha_3}\delta_{\alpha_2\alpha_4}) \ . \quad (2.186)$$

The next step contains the assumption that Mott physics does not play a major role and therefore a separation of energy scales is possible. To project out the low-energy physics, one uses a strategy from field theory: introduce a characteristic energy cutoff Λ, and generate an effective low–energy model by eliminating all degrees of freedom above Λ in the hope that some of the system properties will be universally determined by the low-energy behavior and as such will not depend sensitively on the actual choice of Λ. The most straightforward way to obtain the corresponding low-energy action is to introduce a spin 1 bose field $\mathbf{S}$ and decouple the four–fermion interaction using the Hubbard–Stratonovich procedure. This yields [110]

$$\begin{aligned} H = &\sum_{\mathbf{k},\alpha} \varepsilon_{\mathbf{k}} \psi^{\dagger}_{\mathbf{k},\alpha}\psi_{\mathbf{k},\alpha} + \sum_{\mathbf{q}} U(\mathbf{q})\mathbf{S}_{\mathbf{q}} \cdot \mathbf{S}_{-\mathbf{q}} \\ &+ \sum_{\mathbf{k},\mathbf{q},\alpha,\beta} U(\mathbf{q})\psi^{\dagger}_{\mathbf{k}+\mathbf{q},\alpha}\sigma_{\alpha\beta}\psi_{\mathbf{k},\beta} \cdot \mathbf{S}_{-\mathbf{q}} \quad , \end{aligned} \quad (2.187)$$

where one assumes that the four–fermion interaction makes a contribution only in the spin channel with momentum transfer $\mathbf{q}$. Integrating formally over energies larger than Λ, one obtains an effective action in the form

$$\begin{aligned} \mathcal{S} = &-\int_k^{\Lambda} G_0^{-1}(k)\psi^{\dagger}_{k,\alpha}\psi_{k,\alpha} + \frac{1}{2}\int_q^{\Lambda} \chi_0^{-1}(q)\ \mathbf{S}_{\mathbf{q}} \cdot \mathbf{S}_{-\mathbf{q}} \\ &+ g\int_{k,q}^{\Lambda} \psi^{\dagger}_{k+q,\alpha}\sigma_{\alpha\beta}\psi_{k,\beta} \cdot \mathbf{S}_{-\mathbf{q}} \quad . \end{aligned} \quad (2.188)$$

The integration over k and q is over $2+1$ dimensional vectors $q = (\mathbf{q}, i\omega_m)$ with aMatsubara frequency ω_m. It reads

$$\int_q^{\Lambda} ... = \int_{|\mathbf{q}-\mathbf{Q}|<\Lambda} \frac{\mathrm{d}^d\mathbf{q}}{(2\pi)^d}\ T\sum_m ... \quad (2.189)$$

in the boson case, and

$$\int_k^{\Lambda} ... = \int_{|\mathbf{k}-\mathbf{k}_F|<\Lambda} \frac{\mathrm{d}^d\mathbf{k}}{(2\pi)^d} T\sum_m ... \quad (2.190)$$

in the fermion case. In (2.188), g is the effective coupling constant, $G_0\,(k)$ denotes the bare low–energy fermion propagator, and $\chi_0\,(q)$ is the bare low–energy collective spin boson propagator. If one further assumes that $G_0(k)$ and $\chi_0(q)$ should have a Fermi-liquid and Ornstein–Zernicke form, i.e.

$$G_0(k) = \frac{z_0}{i\omega_m - \epsilon_{\mathbf{k}}}\,, \tag{2.191}$$

$$\chi_0(q) = \frac{\alpha}{\xi_0^{-2} + (\mathbf{q}-\mathbf{Q})^2 + \omega_m^2/c^2}\,, \tag{2.192}$$

one is able to formulate Gorkov equations for the superconducting state. In (2.192), ξ_0 is the bare value of the spin correlation length. The actual ξ generally differs from the bare value because the low–energy fermions that damp the spin fluctuation modes might change their static properties as well. ξ acquires an additional temperature dependence owing to spin–spin interactions and is a parameter of the theory.

The corresponding Gor'kov expressions then read [109]

$$G_{\mathbf{k}}(i\omega) = \frac{i\omega + \Sigma_{\mathbf{k}}(i\omega) + \varepsilon_{\mathbf{k}}}{[i\omega + \Sigma_{\mathbf{k}}(i\omega)]^2 - \Phi_{\mathbf{k}}^2(i\omega) - \varepsilon_{\mathbf{k}}^2} \quad , \tag{2.193}$$

$$F_{\mathbf{k}}(i\omega) = -\frac{\Phi_{\mathbf{k}}(i\omega)}{[i\omega + \Sigma_{\mathbf{k}}(i\omega)]^2 - \Phi_{\mathbf{k}}^2(i\omega) - \varepsilon_{\mathbf{k}}^2} \quad , \tag{2.194}$$

$$\chi_{\mathbf{q}}(i\omega) = \frac{\alpha\xi^2}{1 + \xi^2(\mathbf{q}-\mathbf{Q})^2 - \Pi_{\mathbf{Q}}(i\omega)} \quad . \tag{2.195}$$

Here, $\Sigma_{\mathbf{k}}(i\omega)$ and $\Pi_{\mathbf{Q}}(i\omega)$ are fermionic and bosonic self–energies ($\mathbf{k}$ refers to the component along the Fermi surface), and $F_{\mathbf{k}}(i\omega)$ and $\Phi_{\mathbf{k}}(i\omega)$ are the anomalous Green's function and the anomalous self-energy, respectively. In the above equations, the relation to the NAFL approach becomes quite clear. However, it is interesting to remark that the spin–fermion model could also have been motivated by assuming that the influence of the other fermionic quasiparticles on a given quasiparticle can be described in terms of a set of molecular fields. In the present case the dominant molecular field is an exchange field produced by the Coulomb interaction $U(\mathbf{q})$. However, one has to consider this field as dynamic, not static. The corresponding part of the action reads

$$\mathcal{S} = -\int_k^\Lambda G_0^{-1}(k)\psi_{k,\alpha}^\dagger\psi_{k,\alpha} + \frac{1}{2}\int_q^\Lambda \mathbf{H}_q^{\rm int}\cdot\mathbf{s}_{-q} \quad , \tag{2.196}$$

with a fermionic spin density $\mathbf{s}_{-q} = \int_k^\Lambda \psi_{k+q,\alpha}^\dagger \sigma_{\alpha\beta}\psi_{k,\beta}$. One assumes further that the molecular field $\mathbf{H}_q^{\rm int}$ is given by the linear response function, i.e.

$$\mathbf{H}_q^{\rm int} = g^2\chi_0(q)\mathbf{s}_{-q} \quad . \tag{2.197}$$

This expression is valid as long as one is not in a region so close to a magnetic instability that nonlinear magnetic effects play an important role. Formally, this expression can be obtained from (2.188) by integrating out the collective degrees of freedom. A relation between this purely fermionic approach and

the bosonic spin susceptibility $\chi(\mathbf{q})$ of (2.195) can be seen by evaluating the reducible four–point vertex in the spin channel in the lowest order of perturbation theory. One finds

$$\Gamma_{\alpha\beta,\gamma\delta}(k,k',q) = -V_{\rm eff}(q)\sigma_{\alpha\beta}\sigma_{\gamma\delta} \quad , \tag{2.198}$$

where the effective quasiparticle interaction is proportional to the renormalized spin propagator of (2.195):

$$V_{\rm eff}(q) = g^2\chi(q) = \frac{g^2\alpha\xi^2}{1+\xi^2(\mathbf{q}-\mathbf{Q})^2 - \Pi_{\mathbf{Q}}(\omega)} \quad . \tag{2.199}$$

Thus, to summarize, what are the main differences from our self–consistent theory? From the above equations, we see that the input parameters in (2.188) are an effective coupling energy $\bar{g} = g^2 z_0^2 \alpha$, the typical quasiparticle energy $v_F\xi^{-1}$ (one assumes that the low-energy dispersion can be linearized), and the upper cutoff Λ. Note also that an additional parameter in the spin–fermion model is the angle ϕ_0 between the Fermi velocities at the two hot spots separated by $\mathbf{Q}$, but this angle does not enter the theory in any significant manner as long as it is different from 0 or π. This is the case when the hot spots are located near the $(0,\pi)$ and $(\pi,0)$ points as in optimally doped cuprates. In short, although the spin–fermion model has several advantages with respect to the simple NAFL approach (it contains important feedback effects from the superconducting gap function on χ and $V_{\rm eff}$, for example), it still needs the magnetic correlation length as an input parameter and is not calculated self–consistently. This is particularly important for the calculation of the dispersion of the resonance peak and its doping dependence, for example.

2.4.4 BCS–Like Model Calculations

Finally, we discuss BCS-like calculations based on standard many-body theory. They have the advantage that they can model experimental data without assuming a specific Hamiltonian, for example, but the disadvantage is that no microscopic insight into physical properties can be provided. An important example was the "preformed pair" model of Levin and coworkers [111], who investigated the role of Coulomb correlations [111, 112], resonant pair scattering [113], and residual pairing correlations below T_c [57] in the pseudogap and its consequences in underdoped hole–doped cuprates. The approach of Levin and coworkers is based on a conserving diagrammatic BCS Bose–Einstein crossover (the so-called "pairing approximation" of Kadanoff and Martin [114]) that is a generalization of the theory Legett [115]. How is this done? Levin and coworkers derived a complete set of equations that is typical for such an approach (here $K = (\mathbf{k}, i\omega_n)$):

$$\Sigma(K) = G_0^{-1}(K) - G^{-1}(K) = \sum_Q t(Q)\, G_0(Q-K)\, \varphi^2_{k-q/2} \quad , \tag{2.200}$$

$$g = [1 + g\chi(Q)]\, t(Q) \quad , \tag{2.201}$$

$$\chi(Q) = \sum_K G(K)\, G_0(Q-K)\, \varphi^2_{k-q/2} \quad , \tag{2.202}$$

which, together with the particle conservation condition $n = 2\sum_K G(K)$ and the pairing interaction $V_{\mathbf{k}\mathbf{k}'} = -|g|\varphi_{\mathbf{k}}\varphi_{\mathbf{k}'}$, determines self-consistently both the Green's function G and the T–matrix $t(Q)$. Again, $\Sigma(K)$ is the self–energy and $\chi(Q)$ denotes the pair susceptibility. Within this improved BCS–like approach, one can obtain the important result that pairing fluctuations necessarily persist below T_c down to the lowest temperatures. Only at $T = 0$ do these fluctuations vanish. Also, further predictions for other response functions are possible.

The difference from our approach for the pseudogap presented in sect. 2.2 is quite clear. In our self-consistent theory, fluctuations of the Cooper pair amplitude and phase are coupled and compete with each other. As we shall demonstrate in the next chapter, Cooper pair phase fluctuations drastically reduce T_c, and amplitude fluctuations can lead to a gap in various experiments measuring the spin and charge channel. Only if phase fluctuations are neglected, the amplitude fluctuations are assumed to be static, and the hot spots dominate the scattering processes (see, for example, (2.68)), is our theory similar to the one proposed by Levin and coworkers. We believe, however, that experiments show that Cooper pair phase fluctuations and their dynamics, including lifetime effects, are indeed important in underdoped hole–doped cuprates [116].

Although a large number of papers by various authors exist in the literature about BCS-like model calculations, here we shall focus on contributions concerned with the elementary excitations, i.e. work related to ARPES data and the resonance peak seen in INS experiments. Let us start with the description of the neutron data. An important initial step was taken by Radtke, Ullah, Levin, and Norman [117], who proposed a model susceptibility for modeling directly the neutron scattering data from $YBa_2Cu_3O_{6.9}$ (YBCO),

$$\begin{aligned}\chi(\mathbf{q},\omega) &= \chi_{RUNL}(\mathbf{q},\omega) \\ &= C\left[\frac{1}{1 + J_0\left[\cos(q_x a) + \cos(q_y a)\right]}\right]^2 \\ &\times \frac{3(T+5)\omega}{1.05\omega^2 - 60|\omega| + 900 + 3(T+5)^2}\,\Theta(\Omega_c - |\omega|) \quad ,\end{aligned}$$

where T and ω are measured in meV, and the parameters are $\Omega_c = 100$ meV (frequency cutoff), $J_0 = 0.3$, and $C = 0.19\,\mathrm{eV}^{-1}$. Similarly to the NAFL approach described above, the spin–fluctuation–mediated pairing potential is obtained by multiplying $\chi(\mathbf{q},\omega)$ by a coupling constant g^2,

$$V_{eff}^{\mathrm{RUNL}}(\mathbf{q},\omega) = g^2\chi_{RUNL}(\mathbf{q},\omega) = g^2\int_{-\infty}^{\infty}\frac{\mathrm{d}\omega'}{\pi}\,\frac{\mathrm{Im}\,\chi(\mathbf{q},\omega'+i0^+)}{\omega'-\omega} \tag{2.203}$$

for an electron and for a momentum transfer $(\mathbf{q}, \omega)$. However, a $d_{x^2-y^2}$–wave T_c of only 10 K was found. A critical comparison of the NAFL and RUNL approaches has been performed in [118], where Schüttler and Norman concluded that the big difference in the calculated T_c between the two models arises from the difference in the spectral weight distribution of the two model susceptibilities.

In order to overcome this problem, Levin and coworkers improved their theory and proposed [119] a dynamical susceptibility

$$\chi(\mathbf{q}, \omega) = \frac{\chi_0(\mathbf{q}, \omega)}{1 - J(\mathbf{q})\chi_0(\mathbf{q}, \omega)} \tag{2.204}$$

within the random phase approximation, in which the enhancement factor contains an additional tight–binding structure (where $a = b =$ lattice constant)

$$J(\mathbf{q}) = -J_0 \left[\cos(q_x a) + \cos(q_y a)\right] \quad . \tag{2.205}$$

Here χ_0 denotes the usual Lindhard function. Taking bilayer effects into account, one can rewrite (2.204) as

$$\chi(\mathbf{q}, \omega) = \frac{\chi^0 + 2(\chi^0_{22}\chi^0_{11} - \chi^0_{12}\chi^0_{21})(-J_{\perp 0}\cos q_z l - J)}{1 - J(\chi^0_{11} + \chi^0_{22}) - (J_{\perp 21}\chi^0_{12} + J_{\perp}\chi^0_{21}) + (\chi^0_{11}\chi^0_{22} - \chi^0_{21}\chi^0_{12})(J^2 - J^2_{\perp 0})} \quad . \tag{2.206}$$

Here, χ^0_{ij} $(i, j = 1, 2)$ is again the Lindhard function, using the layer indices of the bilayer system, and

$$J_{\perp 12}(\mathbf{q}) = J_{\perp 0}\, e^{iq_z l} = J^*_{\perp 21} \tag{2.207}$$

denotes the antiferromagnetic interlayer coupling that is included in the usual RPA procedure. l is the distance between the closest CuO_2 layers in YBCO. The corresponding hopping matrix element between the planes, $t_\perp$, is embedded in the band structure that enters χ^0:

$$\begin{aligned} \chi^0 &= \chi^0_{11} + \chi^0_{12} + \chi^0_{21} + \chi^0_{22} \\ &= \frac{1 + \cos q_z l}{2}\,(\chi^0_{++} + \chi^0_{--}) + \frac{1 - \cos q_z l}{2}\,(\chi^0_{+-} + \chi^0_{-+}) \quad , \end{aligned} \tag{2.208}$$

where $\chi^0_{\alpha\beta}$ $(\alpha, \beta = +, -)$ are the Lindhard functions for the bonding and the antibonding band, respectively. Assuming a constant superconducting gap of $\Delta_0 = 23$ meV, Levin and coworkers were able to find a description of the resonance peak at 41 meV in optimally doped YBCO. To some extent this approach is similar to our theory (see (2.125), for example), and to the theory proposed by Lee and coworkers [120]; however, we calculate the superconducting gap function $\Delta(\mathbf{q}, \omega)$ self–consistently, we do not need a $\mathbf{q}$–dependent coupling $J(\mathbf{q})$, and also bilayer coupling is not needed for obtaining

a resonance peak. Note that the resonance peak has recently also been found in a single–layer cuprate superconductor by Keimer and coworkers [121].

Inspired by the above RPA calculations and by a careful analysis by Shen and Schrieffer [122], Norman and coworkers took an important step towards a unified description of the elementary excitations in cuprates using a BCS–like model calculation: they described the sharp peak in INS experiments below T_c by a simple model of holes interacting with a collective mode, and were also able to explain the dramatic change of photoemission spectra for BISCCO below T_c within the same model [123]. ARPES data reveal a very broad normal–state spectrum that evolves quite rapidly below T_c into a resolution–limited quasiparticle peak, followed at higher binding energies by a dip and then a hump, after which the spectrum is equivalent to that for the normal state [68, 124, 125]. Norman *et al.* concluded that electron–electron scattering plays a dominant role in hole–doped cuprates, supporting an electronic mechanism for Cooper pairing in these systems. As we shall discuss in the next chapter, similar effects have also been seen in tunneling spectra, where it was found that all of these spectral features, i.e. the (coherence) peak, dip, and hump, scale with the superconducting gap [126, 127]. Of course, this implies that the electron self–energy reveals dramatic changes below T_c, which also might be described by a BCS–like model [128] using the Kramers–Kronig relation, as well as implying that

$$\mathrm{Im}\,\Sigma = \frac{\mathrm{Im}\,G}{(\mathrm{Re}\,G)^2 + (\mathrm{Im}\,G)^2} \quad , \tag{2.209}$$

and

$$\mathrm{Re}\,\Sigma = \omega - \epsilon_{\mathbf{k}} - \frac{\mathrm{Re}\,G}{(\mathrm{Re}\,G)^2 + (\mathrm{Im}\,G)^2} \quad . \tag{2.210}$$

Recently, Norman and coworkers were able to model ARPES data further, including the kink feature simultaneously with SIN and SIS tunneling data [129]. They were also able to study the dispersion of the collective mode considered here below T_c, i.e. $\omega_{res}(\mathbf{q})$, and to extend the model calculations by including a spin fluctuation continuum describing the normal state of high–T_c cuprates [130].

Thus, we believe, the main advantage of the BCS-like model calculations discussed above is the fact that they are simple and provide some physical insight without fixing a specific Hamiltonian. Furthermore, using response theory, a simultaneous description of different experiments is easily possible, allowing one to obtain a simple physical picture of the processes occurring in a CuO_2 plane. However, we prefer a microscopic but quite general picture starting from a specific Hamiltonian, yielding generalized Eliashberg equations. From these equations, we calculate and predict various physical properties for the cuprate and ruthenate family taking lifetime and renormalization effects into account self–consistently. One important example is the superconducting gap function $\Delta(\mathbf{k}, \omega)$, which also yields a peak–dip–hump

structure in our theory and, in addition, contains fingerprints of the pairing interaction.

2.5 Other Scenarios for Cuprates: Doping a Mott Insulator

Although our generalized Eliashberg theory is quite successful in describing the elementary excitations and their interdependence with spin excitations in hole- and electron-doped cuprates, it has a few weak points. The main problem of our approach is the fact that for $x \to 0$ (where x is the doping) one does not obtain a Mott insulator. Physically speaking, our theory profits from the vicinity to an antiferromagnetic phase (because paramagnons are present), but ignores the fact that cuprates are doped Mott insulators. Therefore, in this subsection, we shall sketch other theoretical scenarios based on doping a Mott insulator and contrast them with our theory. Note that the above criticism does not hold for Sr_2RuO_4 because it is a good Fermi liquid, i.e. a more weakly correlated material, and, as discussed in connection with Fig. 1.9, it is in the vicinity of a ferromagnetic metallic phase (except when Sr is replaced by Ca; Ca_2SrO_4 is a Mott–Hubbard insulator).

2.5.1 Local vs. Nonlocal Correlations

In 1989, Metzner and Vollhardt [131] showed in a pioneering work that the Hubbard model used in our theory undergoes significant simplifications in the limit of infinite dimensions, i.e. $d = \infty$. In this limit, provided that the kinetic energy is scaled as $1/\sqrt{d}$, the self-energy and vertex functions may be taken to be purely local in space, although they retain a nontrivial frequency dependence. This means that the Hubbard model can be mapped onto a self–consistently embedded Anderson impurity problem, which can then be solved by various many–body techniques [132, 133]. The resulting dynamical mean–field theory (DMFT) is exact in an infinite number of dimensions. Recently, Wölfle and coworkers extended the DMFT of the t–J model discussed below and also generalized the noncrossing approximation (NCA) [134, 135]. These authors have calculated the single–particle spectral density and other response functions and find good agreement with the properties of underdoped cuprates. Also back in 1989, Müller-Hartmann [136] proved the locality of many–body Green's function perturbation theory and used it in order to derive self-consistent equations for the self-energy in terms of the Luttinger–Ward functional, which he evaluated to various orders in weak-coupling perturbation theory. A similar self-consistent single site theory was developed by Jarrell and coworkers [137] who *assumed* a purely local self–energy and vertex function even in a finite number of dimensions. The resulting mean–field theory for correlated lattice systems is usually called the dynamical mean–field approximation (DMFA).

How can we approximate a complicated problem with correlated electrons on a lattice to a single–site effective problem with fewer degrees of freedom? Similarly to the well–known case of the Weiss mean–field theory for magnetism, in which the resultant mean–field equations become exact in the limit where the coordination number of the lattice becomes large, the mean–field description of the Hubbard model (see (2.1)) involves a generalized Weiss function which is a function of time instead of being a single number. Thus we are required to take local quantum fluctuations into account. The corresponding mean-field description involves

$$S_{eff} = -\int_0^\beta d\tau \int_0^\beta d\tau' \sum_\sigma c_{0\sigma}^\dagger(\tau)\, \mathcal{G}_0^{-1}(\tau-\tau')\, c_{0\sigma} + U\int_0^\beta d\tau\, n_{0\uparrow}(\tau) n_{0\downarrow}(\tau) \quad . \tag{2.211}$$

Here, the subscript 0 refers to the mean–field and $\mathcal{G}_0^{-1}(\tau-\tau')$ plays the role of the generalized Weiss effective field. Its physical content is an effective amplitude for a fermion to be created on an isolated site at time τ (coming from an "external bath") and to be destroyed at time τ' (going back to the bath). As shown by Kotliar and coworkers [133], a closed set of mean-field equations can be obtained from (2.211) and from expressions relating $\mathcal{G}_0$ to local quantities computable from S_{eff} itself. One obtains

$$\mathcal{G}_0^{-1}(i\omega_n) = i\omega_n + \mu + G(i\omega_n)^{-1} - R[G(i\omega_n)] \quad , \tag{2.212}$$

where $G(i\omega_n)$ is the on-site interacting Green's function and $R(G)$ denotes the reciprocal function of the Hilbert transform of the corresponding density of states. Hence, the DMFA approach provides a good possibility for a controlled treatment of the Mott–Hubbard transition. However, as shown by Hettler *et al.* [138], the DMFA is not a conserving approximation, with violations of the Ward identity associated with current conservation in the equation of continuity for any number of dimensions, including the limit $d = \infty$. Furthermore, the DMFA does not incorporate the important nonlocal correlations, and hence it is not possible to study $d_{x^2-y^2}$–wave Cooper pairing with it.

To overcome these problems, Jarrell and coworkers developed the so-called dynamical cluster approximation (DCA), which incorporates the nonlocal corrections to the DMFA by mapping the lattice problem onto an embedded cluster of size N_c, rather than onto an impurity problem [138]. These authors have shown further that the DCA is a fully causal approach and that it becomes exact in the limit of large N_c, while it reduces to the DMFA for $N_c = 1$. Thus N_c determines the order of the approximation in a simple way and provides also a systematic expansion parameter, $1/N_c$. Similarly to DMFA, the DCA solution remains in the thermodynamic limit, but the dynamical correlation length is restricted to the size of the embedded cluster, of course.

Within this approach, Maier *et al.* calculated the mean-field $d_{x^2-y^2}$–wave T_c for $N_c = 4$ by using the NCA to solve the cluster problem [139]. For $U = 12t$, they found that T_c has its maximum value of approximately $0.05t \simeq 150$ K for a doping concentration $x = 0.2$. It was also found that T_c increases for positive values of the next–nearest–neighbor hopping parameter t', and decreases for negative values of t'. Note that this is in agreement with density–matrix–renormalization–group (DMRG) calculations on the t–J model by White and Scalapino who find $d_{x^2-y^2}$–wave pairing for $t' > 0$ [140]. Recently, Jarrell and coworkers used the DCA approach with the Hubbard model in order to analyze ARPES spectra [141], the occurrence of a pseudogap [142], and the role of impurities in $d_{x^2-y^2}$-wave superconductors [141], and extended the DCA in such a way that the FLEX approximation rather than the NCA was employed for the cluster problem [143].

Thus, in short, the current DCA approach is an interesting method that incorporates causal nonlocal corrections to the DMFA in a transparent way. Importantly, at half-filling the DCA yields a $T = 0$ phase transition and a charge pseudogap accompanied by a non-Fermi-liquid behavior in the thermodynamic limit. For finite N_c, the DCA retains some mean-field character, which emulates the finite coupling of the two-dimensional model to the third dimension and hence emulates the Mermin–Wagner theorem [144, 145]. This is similar to our theory based on the two–dimensional generalized Eliashberg equations (see Appendix A), in which the self-consistent treatment prevents the system from becoming antiferromagnetic as required by the Mermin–Wagner theorem. On the other hand, in our theory fluctuations of the superconducting state are considered in a controlled way (see sect. 2.2.2) yielding a Kosterlitz–Thouless–like transition for T_c. Another advantage of the DCA with respect to our theory is the fact that its mean-field character can gradually be reduced as N_c tends to infinity. On the other hand, within the DCA the very small cluster size of $N_c = 4$ (which is the minimum for determining $d_{x^2-y^2}$–wave Cooper pairing) is the largest cluster that can be treated so far. Finally, we would like to stress that the DCA yields a crossover from a Fermi surface centered around the $(0, 0)$ point in the Brillouin zone for large doping to a Fermi surface centered around (π, π) for small doping which is in disagreement with ARPES experiments [141]. Thus, we can safely conclude that it would be difficult to find a consistent description of the elementary excitations (i.e. for the kink feature) and their interdependence with spin excitations below T_c (the resonance peak) using the DCA approach. This is one of the main advantages of our theory.

2.5.2 The Large-U Limit

As discussed in connection with Fig. 1.10, the electronic states of the cuprates can be described by a three-band version of the Hubbard model, where in each unit cell one has a Cu $d_{x^2-y^2}$ orbital and two oxygen p orbitals (see (1.3)). However, the largest energies in the problem are the correlation energies for

doubly occupying the copper or oxygen orbitals. In the hole picture, the Cu d^9 configuration is reflected by an energy level E_d occupied by a single hole with $S = 1/2$ and the oxygen p orbital is empty of holes and has an energy of E_p. The energy cost for doubly occupying E_d, yielding a d^8 configuration, is U_d, which is very large and often considered to be infinity. Thus, following this picture, the lowest–energy excitation is the charge transfer excitation where a hole hops from d to p with amplitude $-t_{pd}$. If the energy difference $E_p - E_d$ is sufficiently large compared with t_{pd}, the hole will form a local moment on Cu [146]. Essentially, $E_p - E_d$ plays the role of the Hubbard U in a one-band model of a Mott insulator.

In a one-band Mott–Hubbard insulator, in which virtual hopping to doubly occupied states leads to an exchange interaction $J\mathbf{S}_1 \cdot \mathbf{S}_2$ (with $J = 4t^2/U$), the local moments on nearest–neighbor Cu sites prefer to align antiferromagnetically because spins can virtually hop to an orbital with energy E_d. If one ignores the U_p for doubly occupying the p orbital with holes, the exchange integral is given by

$$J = \frac{t_{pd}^4}{(E_p - E_d)^3} \quad . \tag{2.213}$$

Early Raman scattering experiments on two–magnon excitations by Klein and coworkers found an exchange energy of $J \simeq 0.13$ eV ([147] and references therein), and this value has been confirmed by INS experiments, described with a spin wave theory in which additional exchange terms are found [148, 149].

As described in Chap. 1, by focusing on the low-lying singlet excitations, we can make the doped three–band Hubbard model simplifly into an effective one–band model, using an effective hopping integral t and an effective on–site Coulomb repulsion U, which is –within the above picture– of the order of $E_p - E_d$. In the large–U limit, the Hubbard model that we use in this work (see (2.1)) maps onto the t–J model,

$$H = \sum_{\langle ij \rangle \sigma} t\, \mathcal{P}(c_{i\sigma}^\dagger c_{j\sigma} + \text{h.c.})\mathcal{P} + J(\mathbf{S}_i \cdot \mathbf{S}_j - \frac{1}{4} n_i n_j) \quad , \tag{2.214}$$

where $n = c_{i\sigma}^\dagger c_{i\sigma}$, $\mathbf{S}_i = 1/2 c_{i\alpha}^\dagger \sigma_{\alpha\beta} c_{i\beta}$ ($\sigma_{\alpha\beta}$ is a vector of Pauli matrices), and $\mathcal{P}$ is a projection operator that restricts the Hilbert space by projecting out double occupation. Within the t–J model, the basic physics is seen to be the competition between the energy gain $\sim xt$ (where x denotes the doping concentration) due to mobile holes, and the cost of the exchange energy $\sim J$ resulting from the disruption of the antiferromagnetic order. If J was small, the cost of the exchange energy could be overcome by delocalization, yielding a conventional Fermi liquid. This seems to be the case for the doped Mott insulator $La_{1-x}Sr_xTiO_3$. However, in the case of cuprates J is large and one can expect different physics. One important idea is the following:

spins on nearby sites form into "resonating" singlet pairs to retain some exchange energy and have a sufficiently liquid–like character that the "holes" can propagate through them coherently, and, finally, superconduct at low temperatures. This is the main idea of a paper by Anderson *et al.* published early in 1987 on the resonating–valence–bond (RVB) theory of high–T_c superconductivity [150]. The antiferromagnetic order of the parent compound does not invalidate the essence of the argument; it is important that in the doped case mobile holes frustrate the tendency for the spins to order and stabilize the singlet liquid phase. One important consequence of the RVB theory is the so–called spin–charge separation. Note that this scenario points to a strong deviation from standard metallic behavior because the usual Fermi liquid is hard to reconcile with quasiparticles propagating with both spin and charge. On the other hand, in our theory the system remains a Fermi liquid for $T \to 0$; deviations from the Fermi liquid in the normal state above T_c (similar to the marginal–Fermi liquid (MFL) mentioned earlier) are the result of an anomalous behavior of the quasiparticle scattering rate τ^{-1} calculated self-consistently. This will be discussed in connection with Fig. 3.22.

2.5.3 Projected Trial Wave Functions and the RVB Picture

In [150] Anderson *et al.* proposed a trial wave function as a description of the RVB state mentioned above:

$$\Psi = P_G|\psi_0\rangle \quad , \tag{2.215}$$

where $P_G = \prod_i (1 - n_{i\uparrow} n_{i\downarrow})$ is the Gutzwiller projection operator. This operator has the effect of suppressing all amplitudes in $|\psi_0\rangle$ with double occupation of the sites i, thereby enforcing the constraint of the t–J model exactly. The unprojected wave function contains variational parameters and its choice is guided by mean–field theory. We discuss here mainly the projected wave function because the underlying concepts are quite simple. The projection operator is a relatively complicated object to treat analytically, but the properties of the trial wave function may be handled using Monte Carlo techniques.

Historically, the notation of a linear superposition of spin singlet pairs, called an RVB, was introduced by Anderson as a possible ground state for the $S = 1/2$ antiferromagnetic Heisenberg model on a triangular lattice [151]. This type of lattice is of special interest because an Ising–like ordering of the spins is frustrated. An important concept associated with the RVB picture is the notion of spinons and holons, and spin–charge separation: it was postulated that the spin excitations in an RVB state are $S = 1/2$ fermions which Anderson called spinons. Note that this is in contrast to the Néel state, in which excitations are $S = 1$ magnons or $S = 0$ singlet excitations. On the other hand, the concept of spinons is related to one–dimensional spin chains, where spinons act as domain walls and are well understood. In two dimensions, the concept is not well established, but if the singlet bonds are "liquid",

two $S = 1/2$ spins formed by breaking a single bond can drift, with the liquid of singlet bonds filling in the space between them. Thus they behave as free particles and are called spinons.

What happens in the half–filled case, in which the problem reduces to the Heisenberg model? It was soon found that the d–wave BCS state is a good candidate for a trial wave function ([152] and references therein) by using the Variational Monte Carlo method for Gutzwiller states [153]:

$$H_{d-wave} = \sum_{\langle ij\rangle\sigma} (-t_{ij} - \mu)\, f^\dagger_{i\sigma} f_{i\sigma} + \text{c.c.} + \Delta_{ij} \left(f^\dagger_{i\uparrow} f^\dagger_{j\downarrow} - f^\dagger_{i\downarrow} f^\dagger_{j\uparrow} \right) + \text{c.c.} \quad , \tag{2.216}$$

where $t_{ij} = t$ for nearest neighbors, and $\Delta_{ij} = \Delta_0$ for $j = i + \hat{x}$ and $-\Delta_0$ for $j = i + \hat{y}$. The corresponding spectrum consists of the well-known BCS result

$$E_{\mathbf{k}} = \sqrt{(\varepsilon_{\mathbf{k}} - \mu)^2 + \Delta^2_{\mathbf{k}}} \quad , \tag{2.217}$$

where $\varepsilon_{\mathbf{k}} = -2t(\cos k_x + \cos k_y)$ and $\Delta_{\mathbf{k}} = \Delta_0(\cos k_x - \cos k_y)$. At half filling ($\mu = 0$), $|\psi_0\rangle$ is the usual BCS wave function

$$|\psi_0\rangle = |\phi_0\rangle = \left(u_{\mathbf{k}} + v_{\mathbf{k}} f^\dagger_{\mathbf{k}\uparrow} f^\dagger_{-\mathbf{k}\downarrow} \right) |0\rangle \quad . \tag{2.218}$$

Since then, many mean–field wave functions have been discovered which yield an identical energy and dispersion. This can be explained as being to a certain local $SU(2)$ symmetry [154]. Among these wave functions is the important staggered–flux phase, in which the hopping parameter t_{ij} is complex, $t_{ij} = t_0 \exp(i(-1)^{i_x + i_y} \Phi_0)$, and the phase is arranged in such a way that it describes free fermion hopping with a flux $\pm 4\Phi_0$ [43]. One can show that if $\tan \Phi_0 = \Delta_0/t_0$, the eigenvalues are identical to those in (2.217). Note that the case $\Phi_0 = \pi/4$, the so–called π flux phase, is special in such a way that it does not break the lattice translational symmetry.

What are the properties of the projected wave function? First, the superfluid density vanishes linearly with the doping x. This is expected, since the projection operator is designed to yield an insulator at half–filling. Second, the momentum distribution has a jump near the noninteracting Fermi surface. This is interpreted as the quasiparticle weight z according to Fermi liquid theory. It vanishes smoothly as $x \to 0$. Third, using a sum rule and assuming Fermi liquid behavior for the nodal quasiparticles, one can estimate the corresponding Fermi velocity, which is found to be in reasonable agreement with experiment. Recently Lee and coworkers analyzed the question of whether there are signs of the orbital currents and the $SU(2)$ symmetry mentioned above in the projected d–wave superconductor. Since this state does not break time-reversal and translational symmetry, there is no static current, of course. However, Lee and coworkers found fluctuations of the orbital current that are entirely a consequence of the projection [155]. Physically speaking, this result is similar to a hole moving around a Cu–O plaquette

that experiences a Berry phase owing to the noncollinearity of the spin quantization axes of the (instantaneous) spin configurations. Thus the flux Φ_0 of the staggered–flux phase has its origin in the coupling between the kinetic energy of a hole and the corresponding spin chirality.

How can we realize mathematically the RVB picture? In the slave boson method, one can decompose the electron operator into a neutral spin–1/2 fermion operator and a charge-e spinless boson operator ($c^\dagger_{i\sigma} = f^\dagger_{i\sigma} b_i$), and enforce the non-double-occupancy constraint by a Lagrange multiplier. In other words, a "slave" boson operator that keeps track of a moving hole has been introduced. The t–J Hamiltonian then becomes

$$H = -t \sum_{\langle ij\rangle\sigma} (f^\dagger_{i\sigma} b_i b^\dagger_j f_{j\sigma}) + \frac{J}{4} \sum_{\langle ij\rangle} f^\dagger_{i\alpha} \tau_{\alpha\beta} f_{i\beta} \cdot f^\dagger_{j\alpha} \tau_{\alpha\beta} f_{i\beta} + \sum_i \lambda_i \left(f^\dagger_{i\sigma} f_{i\sigma} + b^\dagger_i b_i - 1\right) \quad . \tag{2.219}$$

Here λ_i is the Lagrange multiplier. Note that a crucial simplification is that the constraint enforces on average $\lambda_i \to \lambda = \text{const}\ \forall i$. At this point the situation seems to be more complicated, but now a mean-field analysis can be applied. Fukuyama and coworkers [156] and Kotliar and Liu [157] have obtained a phase diagram consisting of a superconducting phase with a d–wave order parameter ($\langle b\rangle \neq 0$, $\Delta_{i,i+x} = -\Delta_{i,i+y}$), a "spin-gap" phase ($\langle b\rangle = 0$, $\Delta_{ij} \neq 0$), the so–called uniform RVB (uRVB) phase ($\langle b\rangle = 0$, $\Delta_{ij} = 0$), and a Fermi liquid–like phase ($\langle b\rangle \neq 0$, $\Delta_{ij} = 0$). In the superconducting phase, the bosons are condensed and the fermions are paired. The spin–gap phase is a metallic phase, since the bosons have not yet condensed, but the fermions are paired, yielding a gap for magnetic excitations. Remarkably, this approach captures some rough qualitative features of the hole-doped cuprates (see Fig. 1.4). Note that the key feature of the mean–field theory is that the spin carrying fermions (spinons) and the charge–carrying bosons (holons) are decoupled. In other words, one has a full spin–charge separation of the kind mentioned above.

2.5.4 Current Research and Discussion

In order to compare the above approach with our theory, let us point out some problems of the RVB picture. (a) The mean–field theory does not capture all energy scales accurately. In particular, the Bose–Einstein temperature at which holons acquire macroscopic coherence, i.e. $\langle b\rangle \neq 0$, comes out too high. Thus the superconducting transition temperature T_c is too high. (b) There are fictitious phase transitions between certain mean field phases which should be just crossovers; for example, between the spin gap phase and the uniform RVB phase. (c) The mean–field theory can hardly explain why the normal state is a poor metal. (d) The mean–field theory loses most of the antiferromagnetic

correlations. These problems are related to current research in which the key is to include fluctuations around the RVB mean fields.

The gauge fields reflect the fact that the t–J model is invariant under the local transformation $f_i \rightarrow e^{i\Theta_i} f_i$, $b_i \rightarrow e^{i\Theta_i} b_i$, since $c_{i\sigma} = b_i^\dagger f_{i\sigma}$ is obviously a gauge singlet. With the inclusion of gauge fields, the RVB approach takes the following schematic form in the continuum limit:

$$Z = \int D\mathbf{a}\, Da_0\, Df^*\, Df\, Db^*\, Dbe^{-\int \mathrm{d}^2x \mathrm{d}\tau \mathcal{L}} \quad , \tag{2.220}$$

where

$$\mathcal{L} = \mathcal{L}_\mathcal{F} + \mathcal{L}_\mathcal{B} - i\mathbf{a}\cdot(\mathbf{j}_f + \mathbf{j}_b) - ia_0 \cdot (n_f + n_b - 1) \quad . \tag{2.221}$$

Here $\mathcal{L}_\mathcal{F}$ and $\mathcal{L}_\mathcal{B}$ are mean field spinon and holon Lagrangians, a_0 refers to λ_i in (2.219), and $\mathbf{a}$ denotes the spatial part of the local gauge transformation. Note that the main difference between this Lagrangian and the corresponding QED Lagrangians is that the "kinetic term" for the gauge fields, $F_{\mu\nu}^2$, is absent. Thus the apparent coupling is infinitely strong. This enforces the no–double–occupancy constraint and the constraint that the boson current is canceled by fermion backflow [158].

The gauge field acquires dynamics from the fermions and bosons. Integrating out the matter fields, one finds that the gauge propagator in the Coulomb gauge is given by

$$\begin{aligned} \langle a_i(q) a_j(q) \rangle &= (\delta_{ij} - q_i q_j / \mathbf{q}^2)(\Pi_F^\perp + \Pi_B^\perp) \quad , \\ \langle a_0(q) a_0(q) \rangle &= (\Pi_F^{00} + \Pi_F^{00})^{-1} \quad , \end{aligned} \tag{2.222}$$

where $\Pi_{F,B}^\perp$ and $\Pi_{F,B}^{00}$ are transverse and longitudinal polarization functions of fermions and bosons, respectively. Therefore, the dynamics of the gauge field depend on the mean–field ground states and excitations of spinons and holons, and, vice versa, the gauge field affects the dynamics of the matter fields. Moreover, because of the gauge field, the fermions and bosons are no longer decoupled, yielding only a "quasi" spin–charge separation. Within this picture, one can argue that the magnetic properties of cuprates are related to spinons interacting with a gauge field, while the transport properties should be calculated mainly in terms of holons interacting with a gauge field.

One important problem is related to the type of the dominant fluctuations. Lee and coworkers find that the staggered–flux fluctuations may yield new collective modes [159], a prediction that has to be tested experimentally. Another question is related to the degree and control of the "quasi"–spin–charge separation mentioned above. In this connection, Herbut *et al.* have argued that there should exist no gapless spinons, for example [160]. Finally, as long as gauge fluctuations are treated as Gaussian, the Ioffe–Larkin law holds which predicts that the superfluid density n_s behaves as $n_s \simeq ax - bx^2T$. The quadratic term, however, which arises from the Gaussian fluctuations

($\sim xv_F$), is in disagreement with experiment [161]. Thus, in short, the RVB picture allows us to connect d–wave superconductivity and some basic features of the cuprate phase diagram to the insulating Mott state in a smooth way and the corresponding mean field theory yields reasonable results. On the other hand, the RVB theory is difficult to handle owing to constraints, and the mean–field theory is difficult to control. Finally, we stress that in contrast to our perturbative paramagnon–like theory, there are only a few reliable results for excitations and *dynamical* properties using the RVB picture [162], because projected wave functions can only treat statics so far. We believe, in view of the detailed comparison with experiments in the next chapter for the elementary excitations (ARPES) and their interdependence with spin excitations (INS experiments), that this is probably the main advantage of our theory.

References

1. V. J. Emery, Phys. Rev. Lett. **58**, 2794 (1987). 34
2. C. M. Varma, S. Schmitt-Rink, and E. Abrahams, Solid State Commun. **62**, 681 (1987). 34
3. S. G. Ovchinnikov and I. S. Sandalov, Physica C **161**, 607 (1989). 34
4. M. M. Korshunov, V. A. Gavrichkov, D. Manske, and I. Eremin, Physica C **402**, 365 (2004). 34
5. D. M. King, Z.-X. Shen, D. S. Dessau, B. O. Wells, W. E. Spicer, A. J. Arko, D. S. Marshall, J. DiCarlo, A. G. Loeser, C. H. Park, E. R. Ratner, J. L. Peng, Z. Y. Li, and R. L. Greene, Phys. Rev. Lett. **70**, 3159 (1993). 34
6. N. E. Bickers, D. J. Scalapino, and S. R. White, Phys. Rev. Lett. **62**, 961 (1989); N. E. Bickers and D. J. Scalapino, Ann. Phys. (N.Y.) **193**, 206 (1989). 35, 73, 77
7. C.-H. Pao and N. E. Bickers, Phys. Rev. Lett. **72**, 1870 (1994); Phys. Rev. B **51**, 16310 (1995). 35
8. D. J. Scalapino, Phys. Rep. **250**, 329 (1995). 35, 40, 52
9. P. Monthoux and D. J. Scalapino, Phys. Rev. Lett. **72**, 1874 (1994). 35
10. T. Dahm and L. Tewordt, Phys. Rev. Lett. **74**, 793 (1995). 35, 63, 73
11. M. Langer, J. Schmalian, S. Grabowski, and K. H. Bennemann, Phys. Rev. Lett. **75**, 4508 (1995). 35, 40, 63, 73, 76
12. H.-B. Schüttler and C.-H. Pao, Phys. Rev. Lett. **75**, 4504 (1995). 35
13. J. Schmalian, S. Grabowski, and K. H. Bennemann, Phys. Rev. B **56**, R509 (1997). 35
14. L. Tewordt, J. Low Temp. Phys. **15**, 349 (1974). 35, 36
15. N. F. Berk and J. R. Schrieffer, Phys. Rev. Lett. **17**, 433 (1966). 35
16. A. B. Migdal, Zh. Eksp. Teor. Fiz. **34**, 1438 (1958) (Sov. Phys. JETP **34**, 996 (1958)). 35
17. G. Grimvall, *The Electron–Phonon Interaction in Metals*, North–Holland, Amsterdam (1981). 35
18. Y. Nambu, Phys. Rev. **117**, 648 (1960). 36, 60
19. J. R Schrieffer, *Theory of Superconductivity*, Addison-Wesley, Redwood City (1964). 37, 57, 60, 66, 67

20. G. D. Mahan, *Many-Particle Physics*, Plenum, New York, (1981). 38, 55, 62, 65
21. J. L. Tallon, C. Bernhard, H. Shaked, R. L. Hittermann, and J. D. Jorgensen, Phys. Rev. B **51**, 12911 (1995). 40
22. T. Timusk and B. Statt, Rep. Prog. Phys. **62**, 61 (1999). 39, 47
23. M. Rübhausen, J. Zasadzinski, N. Miyakawa, P. Guptasarma, H. L. Liu, and M. V. Klein, submitted to Nature. 39
24. P. C. Hohenberg, Phys. Rev. **158**, 383 (1967). 40
25. T. M. Rice, Phys. Rev. **140**, A1889 (1965). 40, 58
26. A. Damascelli, D. H. Lu, K. M. Shen, N. P. Armitage, F. Ronning, D. L. Feng, C. Kim, Z.-X. Shen, T. Kimura, Y. Tokura, Z. Q. Mao, and Y. Maeno, Phys. Rev. Lett. **85**, 5194 (2000); A. Liebsch, Phys. Rev. Lett. **87**, 239701 (2001); A. Damascelli, K. M. Shen, D. H. Lu, and Z.-X. Shen, Phys. Rev. Lett. **87**, 239702 (2001). 41, 43
27. A. P. Mackenzie, S. R. Julian, A. J. Diver, G. J. McMullan, M. P. Ray, G. G. Lonzarich, Y. Maeno, S. Nishizaki, and T. Fujita, Phys. Rev. Lett. **76**, 3786 (1996). 41
28. D. K. Morr, P. F. Trautmann, and M. J. Graf, Phys. Rev. Lett. **86**, 5978 (2001). 41, 42
29. T. Takimoto, Phys. Rev. B **62**, R14641 (2000). 42
30. I. I. Mazin and D. J. Singh, Phys. Rev. Lett. **82**, 4324 (1999); D. J. Singh, Phys. Rev. B. **52**, 1358 (1995). 42
31. K. K. Ng and M. Sigrist, Europhys. Lett. **49**, 473 (2000). 42, 43
32. K. Ishida, H. Mukuda, Y. Minami, Y. Kitaoka, Z. Q. Mao, H. Fukazawa, and Y. Maeno, Phys. Rev. B **64**, 100501(R) (2001). 42
33. T. Mizokawa, L. H. Tjeng, G. A. Sawatzky, G. Ghiringhelli, O. Tjernberg, N. B. Brookes, H. Fukazawa, S. Nakatsuji, and Y. Maeno, Phys. Rev. Lett. **87**, 077202 (2001). 42, 43
34. A. J. Layzer and D. Fay, *Proceedings of the International Low Temperature Conference*, St. Andrews (LT-11), Academic Press, London (1968); P. W. Anderson and W. F. Brinkmann, in *The physics of liquid and solid Helium*, edited by K. H. Bennemann and J. B. Ketterson, Vol. 2, Wiley-Interscience (1978). 45
35. G. V. M. Williams, J. L. Tallon, and J. W. Loram, Phys. Rev. B **58**, 15053 (1998). 47
36. A. G. Loeser, Z.-X. Shen, D. S. Dessau, D. S. Marshall, C. H. Park, P. Fournier, and A. Kapitulnik, Science **273**, 325 (1996). 47
37. A. Kaminski, J. Mesot. H. Fretwell, J. C. Campuzano, M. R. Norman, M. Randeria, H. Ding, T. Sato, T. Takahashi, T. Mochiku, K. Kadowaki, and H. Hoechst, Phys. Rev. Lett. **84**, 1788 (2000). 47
38. M. R. Norman, M. Randeria, H. Ding, and J. C. Campuzano, Phys. Rev. B **57**, R11093 (1998). 47
39. A. Puchkov, D. N. Basov, and T. Timusk, J. Phys.: Condens. Matter **8**, 10049 (1996). 47
40. S. Chakravarty, R. B. Laughlin, D. K. Morr, and C. Nayak, Phys. Rev. B **63**, 094503 (2001). 47, 48, 50, 52
41. M. E. Simon and C. M. Varma, preprint cond-mat/0201036 (unpublished). 47
42. F. C. Zhang, Phys. Rev. Lett. **64**, 974 (1990). 47

43. J. B. Marston and I. Affleck, Phys. Rev. B **39**, 11538 (1989). 47, 89
44. H. A. Mook, P. Dai, and F. Dogan, Phys. Rev. B **64**, 012502 (2001). 47
45. J. E. Sonier, J. H. Brewer, R. F. Kiefl, R. I. Miller, G. D. Morris, C. E. Stronach, J. S. Gardner, S. R. Dunsiger, D. A. Bonn, W. N. Hardy, R. Liang, and R. H. Heffner, Science **292**, 1692 (2001). 47
46. A. Kaminski, S. Rosenkranz, H. M. Fretwell, J. C. Campuzano, Z. Li, H. Raffy, W. G. Cullen, H. You, C. G. Olson, C. V. Varma, and H. Höchst, Nature **416**, 610 (2002). 47
47. R. Zeyher and A. Greco, Phys. Rev. Lett. **89**, 177004 (2002). 47
48. X. Yang and C. Nayak, Phys. Rev. B **65**, 064523 (2002). 47
49. H. K. Nguyen and S. Chakravarty, Phys. Rev. B **65**, 180519 (2002). 47
50. Q.-H. Wang, J. H. Han, and D.-H. Lee, Phys. Rev. Lett. **87**, 077004 (2001). 47
51. B. K. Chakraverty, A. Taraphder, and M. Avignon, Physica C **235–240**, 2323 (1994); B. K. Chakraverty and T. V. Ramakrishnan, Physica C **282–287**, 290 (1997). 48, 63
52. V. J. Emery and S. A. Kivelson, Nature **374**, 434 (1995). 48
53. M. Franz and A. J. Millis, Phys. Rev. B **58**, 14572 (1998). 48
54. T. Dahm, D. Manske, and L. Tewordt, Phys. Rev. B **55**, 15274 (1997). 48, 59, 60
55. L. Tewordt, D. Fay, and T. Wölkhausen, Solid State Commun. **67**, 301 (1988). 48, 58, 59
56. K. Maki and H. Won, Physica C **282–287**, 1839 (1997); Physica C **341–348**, 891 (2000). 48
57. B. Janko, J. Maly, and K. Levin, Phys. Rev. B **56**, 11407 (1997); I. Kosztin, Q. Chen, B. Janko, and K. Levin, Phys. Rev. B **58**, R5936 (1998). 48, 80
58. T. Hotta, M. Mayr, and E. Dagotto, Phys. Rev. B **60**, 13085 (1999). 48, 60
59. C. A. Balseiro and L. M. Falicov, Phys. Rev. B **20**, 4457 (1979). 48, 51
60. J. Loram, K. A. Mirza, J. R. Cooper, and W. Y. Liang, Phys. Rev. Lett. **71**, 1740 (1993); J. W. Loram, J. Superconductivity **7**, 234 (1994). 48, 52
61. G. V. M. Williams, J. L. Tallon, E. M. Haines, R. Michalak, and R. Dupree, Phys. Rev. Lett. **78**, 721 (1997); G. V. M. Williams, J. L. Tallon, and J. W. Loram, Phys. Rev. B **58**, 15053 (1998). 48, 50, 52
62. F. Schäfer, C. Timm, D. Manske, and K. H. Bennemann, J. Low Temp. Phys. **117**, 223 (1999). 52, 53, 54, 56, 64
63. H.-J. Kwon and A. T. Dorsey, Phys. Rev. B **59**, 6438 (1999). 53
64. G. Baym and L. P. Kadanoff, Phys. Rev. **124**, 287 (1961). 55
65. G. Baym, Phys. Rev. **127**, 1391 (1962). 55
66. C. M. Varma, P. B. Littlewood, S. Schmitt-Rink, E. Abrahams, and A. E. Ruckenstein, Phys. Rev. Lett. **63**, 1996 (1989). 61
67. J. Ruvalds, C. T. Rieck, S. Tewari, J. Thoma, and A. Virosztek, Phys. Rev. B **51**, 3797 (1995). 61
68. Z.-X. Shen and D. S Dessau, Phys. Rep. **253**, 1 (1995). 62, 83
69. S. Wermbter and L. Tewordt, Physica C **211**, 132 (1993). 62
70. F. London and H. London, Proc. Roy. Soc. (London) A **149**, 71 (1935). 63
71. M. V. Feigel'mann, Zh. Eksp. Teor. Fiz. **76**, 784 (1989) [Sov. Phys. JETP **49**, 395 (1989)]. 63
72. G. Blatter, M. V. Feigel'mann, V. B. Geshkenbein, A. I. Larkin, and V. M. Vinokur, Rev. Mod. Phys. **66**, 1125 (1994). 63

73. V. L. Berezinskii, Zh. Eksp. Teor. Fiz. **61**, 1144 (1971) [Sov. Phys. JETP **34**, 610 (1972)]; J. M. Kosterlitz and D. J. Thouless, J. Phys. C **6**, 1181 (1973); J. M. Kosterlitz, J. Phys. C **7**, 1046 (1974). 63
74. M. R. Beasley, J. E. Mooij, and T. P. Orlando, Phys. Rev. Lett. **42**, 1165 (1979); S. Doniach and B. A. Hubermann, Phys. Rev. Lett. **42**, 1169 (1979); B. I. Halperin and D. R. Nelson, J. Low Temp. Phys. **36**, 599 (1979); L. A. Turkevich, J. Phys. C **12**, L385 (1979). 63
75. P. Minnhagen, Rev. Mod. Phys. **59**, 1001 (1987). 63, 64
76. A. Kovner and B. Rosenstein, Phys. Rev. B **42**, 4748 (1990). 63
77. P. W. Anderson, Phys. Rev. **112**, 1900 (1958). 63
78. C. Timm, D. Manske, and K. H. Bennemann, Phys. Rev. B **66**, 094515 (2002). 64
79. J. M. Kosterlitz and D. J. Thouless, J. Phys. C **6**, 1181 (1973); J. M. Kosterlitz, J. Phys. C **7**, 1046 (1974). 64
80. D. Manske and K. H. Bennemann, Physica C **341–348**, 83 (2000); D. Manske, T. Dahm, and K. H. Bennemann, Phys. Rev. B **64**, 144520 (2001). 64
81. V. Ambegeokar, B. I. Halperin, D. R. Nelson, and E. D. Siggia, Phys. Rev. Lett. **40**, 783 (1978); V. Ambegeokar and D. Seitel, Phys. Rev. B **19**, 1667 (1979); V. Ambegeokar, B. I. Halperin, D. R. Nelson, and E. D. Siggia, Phys. Rev. Lett. **21**, 1806 (1980). 64
82. J. Bardeen and M. J. Stephen, Phys. Rev. **140**, 1197A (1965). 65
83. D. Manske, C. T. Rieck, R. Das Sharma, A. Bock, and D. Fay, Phys. Rev. B **56**, R2940 (1997). 66, 69
84. D. Manske, T. Dahm, and K. H. Bennemann, preprint cond-mat/9912062. 66
85. T. Dahm, D. Manske, and L. Tewordt, Phys. Rev. B **58**, 12454 (1998). 67
86. H. Monien, K. Scharnberg, N. Schopohl, and L. Tewordt, J. Low Temp. Phys. **65**, 13 (1986). 69, 70, 71
87. Wen-Chin Wu and A. Griffin, Phys. Rev. B **51**, 1190 (1995). 69, 70, 71
88. N. Schopohl and L. Tewordt, J. Low Temp. Phys. **45**, 67 (1981). 69, 70, 71
89. N. Bulut and D. J. Scalapino, Phys. Rev. B **53**, 5149 (1996). 69
90. C. Bernhard, R. Henn, A. Wittlin, M. Kläser, T. Wolf, G. Müller-Vogt, C. T. Lin, and M. Cardona, Phys. Rev. Lett. **80**, 1762 (1998). 72
91. C. C. Homes, T. Timusk, R. Liang, D. A. Bonn, and W. N. Hardy, Physica C **254**, 265 (1995). 72
92. S. Uchida, Physica C **282–287**, 12 (1997). 72
93. P. Prelovšek, A. Ramšak, and I. Sega, Phys. Rev. Lett. **81**, 3745 (1998). 72
94. P. J. Hirschfeld, S. M. Quinlan, and D. J. Scalapino, Phys. Rev. B **55**, 12742 (1997). 72, 73
95. D. J. Scalapino, J. R. Schrieffer, and J. W. Wilkins, Phys. Rev. **148**, 263 (1966). 73
96. J. W. Serene and D. W. Hess, Phys. Rev. B **44**, 3391 (1991). 73
97. J. J. Deisz, D. W. Hess, and J. W. Serene, Phys. Rev. Lett. **76**, 1312 (1996). 73
98. G. Esirgen and N. E. Bickers, Phys. Rev. B **55**, 2122 (1997). 73
99. J. R. Schrieffer, X. G. Wen, and S. C. Zhang, Phys. Rev. B **39**, 11663 (1989); J. R. Schrieffer, X. G. Wen, and S. C. Zhang, Phys. Rev. Lett. **60**, 944 (1988). 74
100. W. P. Su, Phys. Rev. B **37**, 9904 (1988). 74

101. A. Kampf and J. R. Schrieffer, Phys. Rev. B **41**, 6399 (1990). 75
102. T. Dahm, J. Erdmenger, K. Scharnberg, and C. T. Rieck, Phys. Rev. B **48**, 3896 (1993). 75
103. A. Kampf and J. R. Schrieffer, Phys. Rev. B **42**, 7967 (1990). 75
104. P. Aebi, J. Osterwalder, P. Schwaller, L. Schlapbach, M. Shinoda, T. Mochiku, and K. Kadowaki, Phys. Rev. Lett. **72**, 2757 (1994). 75
105. S. Haas, A. Moreo, and E. Dagotto, Phys. Rev. Lett. **74**, 4281 (1995). 76
106. P. Monthoux and D. Pines, Phys. Rev. Lett. **69**, 961 (1992). 76
107. P. Monthoux and D. Pines, Phys. Rev. B **47**, 6069 (1993). 76, 77
108. A. J. Millis, H. Monien, and D. Pines, Phys. Rev. B **42**, 167 (1990). 76
109. A. V. Chubukov, D. Pines, and J. Schmalian, in *The Physics of Superconductors*, Vol. 1, edited by K. H. Bennemann and J. B. Ketterson, Springer, Berlin, Heidelberg (2002), Chap. 7. 77, 79
110. Ar. Abanov and A. V. Chubukov, Phys. Rev. Lett. **84**, 5608 (2000). 78
111. J. Mali, K. Levin, and D. Z. Liu, Phys. Rev. B **54**, 15657 (1996). 80
112. Q. Chen, I. Kosztin, B. Janko, and K. Levin, Phys. Rev. B **59**, 7083 (1999). 80
113. B. Janko, J. Mali, and K. Levin, Phys. Rev. B **56**, 11407 (1997). 80
114. L. P. Kadanoff and P. C. Martin, Phys. Rev. **124**, 670 (1961). 80
115. A. J. Legett, J. Phys. (Paris) **41**, C7 (1980). 80
116. Z. A. Xu, N. P. Ong, Y. Wang, T. Kakeshita, S. Uchida, Nature **406**, 486 (2000) 81
117. R. J. Radtke, S. Ullah, K. Levin, and M. R. Norman, Phys. Rev. B **46**, 11975 (1992). 81
118. H.-B. Schüttler and M. R. Norman, Phys. Rev. B **54**, 13295 (1996). 82
119. D. Z. Liu, Y. Zha, and K. Levin, Phys. Rev. Lett. **75**, 4130 (1995). 82
120. J. Brinckmann and P. A. Lee, Phys. Rev. Lett. **82**, 2915 (1999). 82
121. H. He, P. Bourges, Y. Sidis, C. Ulrich, L. P. Regnault, S. Pailhes, N. S. Berzigiarova, N. N. Kolesnikov, and B. Keimer, Science **295**, 1045 (2002). 83
122. Z.-X. Shen and J. R. Schrieffer, Phys. Rev. Lett. **78**, 1771 (1997). 83
123. M. R. Norman and H. Ding, Phys. Rev. B **57**, 11089 (1998). 83
124. D. S. Dessau, B. O. Wells, Z.-X. Shen, W. E. Spicer, A. J. Arko, R. S. List, D. B. Mitzi, and A. Kapitulnik, Phys. Rev. Lett. **66**, 2160 (1991). 83
125. H. Ding, A. F. Bellmann, J. C. Campuzano, M. Randeria, M. R. Norman, T. Yokoya, T. Takahashi, H. Katayama-Yoshida, T. Mochiku, K. Kadowaki, G. Jennings, and G. P. Brivio, Phys. Rev. Lett. **76**, 1533 (1996). 83
126. J. Zasadzinski, in *The Physics of Superconductors*, Vol. 1, edited by K. H. Bennemann and J. B. Ketterson, Springer, Berlin, Heidelberg (2002), Chap. 8. 83
127. C. Renner and Ø. Fischer, Phys. Rev. B **51**, 9208 (1995). 83
128. M. R. Norman, H. Ding, H. Fretwell, M. Randeria, and J. C. Campuzano, Phys. Rev. B **60**, 7585 (1999). 83
129. M. Eschrig and M. R. Norman, Phys. Rev. Lett. **85**, 3261 (2000); M. R. Norman, Phys. Rev. B **63**, 092509 (2001). 83
130. M. Eschrig and M. R. Norman, Phys. Rev. B **67**, 144503 (2003). 83
131. W. Metzner and D. Vollhardt, Phys. Rev. Lett. **62**, 324 (1992). 84
132. T. Pruschke, M. Jarrell, and J. K. Freericks, Adv. Phys. **42**, 187 (1995). 84
133. A. Georges, G. Kotliar, W. Krauth, and M. J. Rozenberg, Rev. Mod. Phys. **68**, 13 (1996). 84, 85

134. K. Haule, A. Rosch, J. Kroha, and P. Wölfle, Phys. Rev. Lett. **89**, 236402 (2002). 84
135. K. Haule, A. Rosch, J. Kroha, and P. Wölfle, Phys. Rev. B **68**, 155119 (2003). 84
136. E. Müller-Hartmann, Z. Phys. B **74**, 507 (1989). 84
137. M. Jarrell, Phys. Rev. Lett. **69**, 168 (1992). 84
138. M. H. Hettler, M. Mukherjee, M. Jarrell, and H. R. Krishnamurthy, Phys. Rev. B **61**, 12739 (2000). 85
139. T. Maier, M. Jarrell, T. Pruschke, and J. Keller, Phys. Rev. Lett. **85**, 1524 (2000). 86
140. S. R. White and D. J. Scalapino, Phys. Rev. Lett. **80**, 1272 (1998), Phys. Rev. Lett. **81**, 3227 (1998). 86
141. T. Maier, T. Pruschke, and M. Jarrell, Phys. Rev. B **66**, 075102 (2002). 86
142. C. Huscroft, M. Jarrell, T. Maier, S. Moukouri, and A.N. Tahvildarzadeh, Phys. Rev. Lett. **86**, 139 (2001). 86
143. K. Aryanpour, M. H. Hettler, and M. Jarrell, Phys. Rev. B **67**, 085101 (2003). 86
144. G. Su, Phys. Rev. Lett. **86**, 3690 (2001). 86
145. T. Maier, M. Jarrell, and T. Pruschke, Phys. Rev. Lett. **86**, 3691 (2001). 86
146. J. Zaanen, G. A. Sawatzky, and J. W. Allen, Phys. Rev. Lett. **55**, 418 (1985). 87
147. G. Blumberg, R. Liu, M. V. Klein, W. C. Lee, D. M. Ginsberg, C. Gu, B. W. Veal, and B. Dabrowski, Phys. Rev. B **49**, 13295 (1994). 87
148. J. M. Tranquada, G. Shirane, B. Keimer, S. Shamoto, and M. Sato, Phys. Rev. B **40**, 4503 (1989). 87
149. R. Coldea, S. M. Hayden, G. Aeppli, T. G. Perring, C. D. Frost, T. E. Mason, S.-W. Cheong, and Z. Fisk, Phys. Rev. Lett. **86**, 5377 (2001). 87
150. P. W. Anderson, G. Baskaran, Z. Zou, and T. Hsu, Phys. Rev. Lett. **58**, 2790 (1987). 88
151. P. W. Anderson, Mater. Res. Bull. **8**, 153 (1973). 88
152. C. Gros, Ann. Phys. **189**, 53 (1989). 89
153. P. Horsch and T. A. Kaplan, J. Phys. C **16**, L1203 (1983). 89
154. I. Affleck, Z. Zou, T. Hsu, and P. W. Anderson, Phys. Rev. B **38**, 745 (1988). 89
155. D. A. Ivanov, P. A. Lee, and X.-G. Wen, Phys. Rev. Lett. **84**, 3958 (2000). 89
156. Y. Suzumura, Y. Hasegawa, and H. Fukuyama, J. Phys. Soc. Jpn. **57**, 2768 (1988). 90
157. G. Kotliar and J. Liu, Phys. Rev. B **38**, 5142 (1988). 90
158. N. Nagaosa, *Quantum Field Theory in Strongly Correlated Electronic Systems*, Chap. 5, Springer, Berlin, Heidelberg (1999). 91
159. P. A. Lee and N. Nagaosa, Phys. Rev. B **68**, 024516 (2003). 91
160. I. Herbut, B. H. Seradjeh, S. Sachdev, and G. Murthy, preprint cond-mat/0306537 (unpublished). 91
161. P. A. Lee and X.-G. Wen, Phys. Rev. Lett. **78**, 4111 (1997). 92
162. A. Paramekanti, M. Randeria, and N. Trivedi, Phys. Rev. Lett. **87**, 217002 (2001). 92

3 Results for High–T_c Cuprates Obtained from a Generalized Eliashberg Theory: Doping Dependence

3.1 The Phase Diagram for High–T_c Superconductors

One of the most interesting problems in the field of high–T_c superconductivity is the calculation of the generic phase diagram for both hole– and electron–doped cuprates, as was discussed in the Introduction. Even after more than ten years of research, no general consensus on this question has been achieved. This problem is related to the microscopic origin of the mechanism of high–T_c superconductivity because it would be highly desirable to explain the whole phase diagram for both hole– and electron–doped superconductors within a unified theory. In particular, many non–Fermi–liquid properties in the normal state in the underdoped region have to be understood. In this section we shall show that our microscopic electronic theory, which assumes the exchange of antiferromagnetic spin fluctuations as the relevant pairing mechanism, can account for the main features in the phase diagram of both hole– and electron–doped cuprate superconductors.

3.1.1 Hole–Doped Cuprates

In this subsection we focus on the hole-doped side of the phase diagram of high-T_c superconductors. Of particular interest is the underdoped regime, in which the doping in the CuO_2 planes is lower than that required for the maximum superconducting transition temperature T_c^{max}. This region can be experimentally characterized by a T_c which decreases with decreasing hole density x, and by a superfluid density $n_s \propto T_c$, i.e. the so–called Uemura scaling [1].[1] It was recognized early that a small n_s leads to a reduced stiffness against fluctuations of the phase of the superconducting order parameter [2, 3, 4]. Furthermore, cuprate superconductors consist of weakly-coupled 2D CuO_2 planes so that Cooper pair phase fluctuations are also enhanced by the reduced dimensionality, as discussed in Sect. 2.2.2. In conventional superconductors this mechanism is not relevant, since the large superfluid density leads to a typical energy scale of Cooper pair phase fluctuations much larger than the superconducting energy gap Δ, which governs the thermal breaking

[1] Note that $T_c \propto n_s$ has consequences for other thermodynamic quantities, such as the critical magnetic field [180].

D. Manske: Theory of Unconventional Superconductors, STMP 202, 99–176 (2004)

of a Cooper pair. Thus, in conventional superconductors, T_c is proportional to $\Delta(T=0)$ [5]. In contrast to this, the observation $T_c \propto n_s$ in underdoped (hole–doped) cuprates indicates that Cooper pair phase fluctuations drive the superconducting instability. The Cooper pairs break up only at a crossover temperature $T_c^* > T_c$, and between T_c and T_c^* local Cooper pairs exist, but without long–range phase coherence [2, 3, 4, 6, 7].

To remind the reader, there exists a third, even higher temperature scale T^*, below which a pseudogap starts to form, as seen in NMR, tunneling spectroscopy, electronic transport, and Hall effect measurements (to name just a few) [8, 9, 10, 11, 12, 13, 14]. The regions $T_c < T < T_c^*$ and $T_c^* < T < T^*$ are often called the strong and weak pseudogap regimes, respectively.

We shall demonstrate that our electronic theory that assumes the exchange of antiferromagnetic spin fluctuations as the relevant pairing mechanism for singlet pairing in cuprates can account for the main features in the phase diagram of hole–doped cuprates. In particular, we determine the doping dependence of the relevant temperatures of the phase diagram, namely $T_c^*(x)$, $T_c(x)$, and also T^*, at which a gap appears in the spectral density. Below T_c^* we indeed find incoherent Cooper pairs ("preformed pairs"), which become phase–coherent only below the critical temperature T_c of the bulk material. We show that phase fluctuations, contributing ΔF_{phase} to the free energy, lead to a decreasing critical temperature in the underdoped regime and thus to the appearance of an optimal doping x_{opt}. It is shown that this result is due to the small superfluid density $n_s(T)$ in the system. Most importantly, we calculate that $\Delta F_{cond} > \Delta F_{phase}$ (where ΔF_{cond} denotes the contribution to the free energy due to Cooper pair formation, where ΔF_{phase} denotes the contribution due to phase fluctuations of the Cooper pairs), for a doping $x < x_{opt}$, and $\Delta F_{cond} < \Delta F_{phase}$ for $x > x_{opt}$. We compare our results with the Berezinskii–Kosterlitz–Thouless (BKT) theory and with the XY model and find similar results for the resulting phase diagram. Finally, we also discuss the relaxation dynamics in pump–probe spectroscopy and find reasonable agreement with experiment. Of course, a detailed quantitative comparison for all classes of cuprate superconductors within the simple two–dimensional one–band Hubbard model is beyond the scope of this book. Nevertheless, we shall show that the key facts can be explained within our approach.

In Fig. 3.1, results are shown for $\Delta F(x)$. We find that ΔF_{cond} mainly follows the doping dependence of the mean–field transition temperature T_c^*. On the other hand, as discussed in the previous chapter, the doping dependence of $n_s(0)/m$ determines the doping dependence of ΔF_{phase}. Thus the energy cost due to phase fluctuations has the opposite behavior to the energy gain due to Cooper pair condensation with respect to the doping concentration x. It is remarkable that we obtain from our electronic theory a crossing of the two energy contributions ΔF_{cond} and ΔF_{phase} at $x \simeq 0.15$, where the largest T_c is observed. The consequence of this is that we find theoretically $T_c \propto n_s$

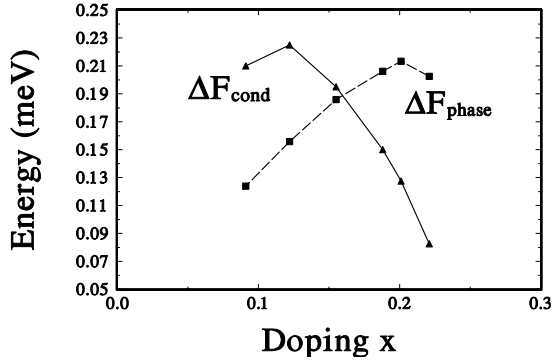

Fig. 3.1. Calculated crossover of the phase–stiffness energy. We find $\Delta F_{phase} \propto n_s/m^*$, whereas the condensation energy $\Delta F_{cond} \simeq \alpha\{n_s/m\}\Delta_0(x)$. Here, we estimate $\alpha \simeq 1/400$. Note that $\Delta F_{phase} < \Delta F_{cond}$ implies two characteristic temperatures: T_c^*, where Cooper pairs are formed at $T_c \sim \Delta_0$, and $T_c \approx \Delta F_{phase} \propto n_s$, where Cooper pairs become phase–coherent.

for underdoped cuprates (and thus the Uemura scaling), and a nonmonotonic doping dependence of $T_c(x)$ with an optimal doping at $x \simeq 0.15$. Physically speaking, in the overdoped regime we find a large ΔF_{phase} which means that Cooper pair phase fluctuations are associated with a large amount of energy. Thus the system will undergo a mean–field transition because of the small condensation energy ΔF_{cond}. In the underdoped regime of cuprate superconductors, the situation is the opposite: the energy gain due to the formation of Cooper pairs is not large enough to reach the Meissner state of the bulk material. This is only possible at a smaller temperature, where the Cooper pairs become phase–coherent; this temperature is determined by ΔF_{phase} and $\Delta F_{phase} < \Delta F_{cond}$.

Thus we can safely conclude that in the overdoped regime, T_c^* is identical to the bulk transition temperature T_c below which a Meissner effect is found experimentally. Further evidence for a mean-field superconducting transition comes from the fact that $T_c^* \propto \Delta(T \to 0)$, which we have calculated within our electronic theory. In contrast to this, in the underdoped regime the system behaves more two-dimensionally and thus, owing to the short coherence length of a Cooper pair in cuprates, another energy scale, namely the small superfluid density n_s, becomes important and leads to the fact that $T_c < T_c^*$. The temperature range $T_c < T < T_c^*$ may be viewed as the region where local Cooper pairs without long–range phase coherence ("preformed pairs") can exist. The occurrence of preformed pairs was postulated by Chakraverty and coworkers [3] and later by Emery and Kivelson [4]. Our calculations provide a microscopic justification for this scenario. However, no clear experimental proof of the existence of preformed pairs has been obtained so far.

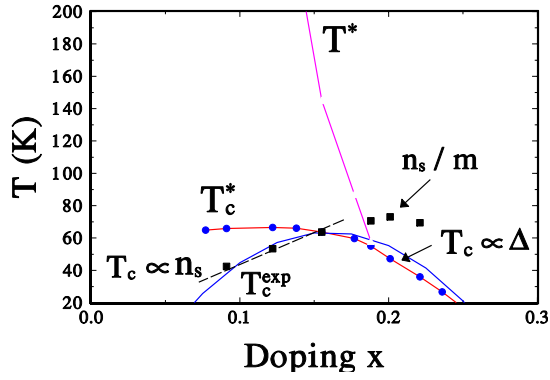

Fig. 3.2. Phase diagram for high–T_c superconductors resulting from considering a spin–fluctuation–induced Cooper pairing, including phase fluctuations. The calculated values for $n_s(0)/m$ are in good agreement with muon spin rotation experiments [15]. T_c^* denotes the temperature below which Cooper pairs are formed. The *dashed curve* gives the observed Uemura scaling $T_c \propto n_s(T=0,x)$ [1]. Below T^* we obtain a gap structure in the spectral density, as observed in tunneling spectroscopy [16, 17]. The *solid curve* T_c^{exp}, which describes many hole–doped superconductors, is taken from [18, 19].

In order to summarize our calculations, we now show our results for the resulting phase diagram for hole–doped cuprates in Fig. 3.2. Note that for illustration we have added the experimental $T_c(x)$ curve, which describes many hole-doped superconductors as pointed out by Tallon and coworkers [18, 19]. As mentioned earlier, the superconducting (mean–field) transition temperature T_c^*, below which one finds a finite gap function, has been determined from the linearized version of the gap equation (see (A.18)).

In order to illustrate the important behavior of n_s in more detail, we show in Fig. 3.3 the temperature dependence of $n_s(\omega = 0)/n$ (n denotes the normal–state band filling) below T_c^* for various doping concentrations. For this purpose we have calculated the current–current correlation function using standard many–body theory [20] and taken the corresponding Green's functions within the FLEX approximation. This has been described in the previous chapter. Note that according to London's theory [21], which states that $\lambda_L \propto n_s$, the ratio n_s/n can be related to measurements of the (in–plane) penetration depth, for example in microwave experiments.

As can also be seen from Fig. 3.3, qualitative agreement with the data of Bonn, Hardy and coworkers on $\lambda^2(T=0)/\lambda^2(T)$ concerning the slope of the curves in the vicinity of T_c^* and the linear behavior for $T \to 0$ is found [22]. In particular, the FLEX approximation to the generalized Eliashberg equations yields, close to T_c^*, a relation $\lambda^3(T=0)/\lambda^3(T) \propto (T_c^* - T)$. The same power law has been found by Kamal *et al.* and has been attributed to critical fluctuations starting about 10 K below T_c, since the slope coincides with the

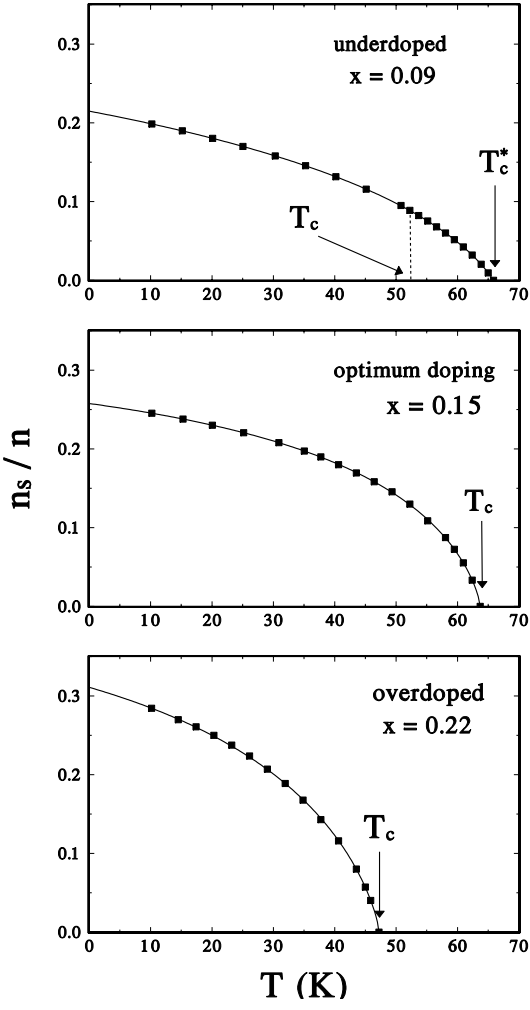

Fig. 3.3. Temperature dependence of the superfluid density $n_s(x,T)$ calculated with the help of (2.28) and (2.126)–(2.128) for various hole doping concentrations x. We have extrapolated the results to $T \to 0$. The *dashed curve* in the *top part* illustrates the effect of Cooper pair phase fluctuations according to the (static) Kosterlitz–Thouless theory. In Ginzburg–Landau theory the superfluid density can be described by $n_s^0/n_s = \langle \nabla\phi(r)\, \nabla\phi(0)\rangle$. Here, $\phi(r)$ denotes the spatial dependence of the Cooper pair wave function and n_s^0 the static mean-field value of the superfluid density for a given temperature calculated within our extended FLEX approximation. At $T_c < T < T_c^*$, where Cooper pairs become phase–incoherent, $n_s^0 \to 0$ (see Fig. 3.2). Our results are in fair agreement with measurements of the in-plane penetration depth by Bonn, Hardy and coworkers [22].

critical exponent for the 3D XY model [22]. Here, we obtain this power law from the generalized Eliashberg equations using the FLEX approximation, which is purely 2D and does not contain critical fluctuations. Instead, the rapid increase of n_s below T_c^* is due to the self-consistent treatment of the superconducting gap function $\Delta(\omega)$. Thus, we conclude that while 3D critical fluctuations are expected in a very narrow temperature range close to T_c, they are not the origin of the observed power law on the scale of 10 K.

Note that our calculations also show that roughly one–third of the holes become superconducting, even for $T \to 0$. This is typical of a strongly interacting system and is further support for the suggestion that preformed pairs might exist in the underdoped regime.

Comparison with BKT theory

Shortly after the discovery of cuprate high–T_c superconductors, many experiments were interpreted in term of the BKT theory for bulk samples [23, 24, 25, 26, 27, 28]. Recently, an important experiment has been performed by Xu *et al.* who have found signs of vortices at temperatures much higher than T_c in underdoped $La_{1-x}Sr_xCuO_4$ in measurements of the Nernst effect [29]. The most recent reanalysis of their data gives an onset temperature for vortex effects of 40 K for an extremely underdoped sample with a doping $x = 0.05$, and even 90 K for $x = 0.07$ [30].

As an example, we show in Fig. 3.3 the superconducting bulk transition temperature T_c for an underdoped cuprate (dashed line). $n_s(x,T)/m$ has been taken from the solutions of the generalized Eliashberg equations. Thus, in the underdoped regime one indeed finds a difference between T_c and T_c^*. As already mentioned above, a finite value of $n_s(T_c < T < T_c^*)$ can be interpreted in terms of local Cooper pairs with a strongly fluctuating phase. In the case of $YBa_2Cu_3O_{6+x}$ (YBCO), this has been recently confirmed by experiment [33].

In Fig. 3.4a results are given for $n_s(T,x)/m$, where m is the effective mass. We again find that Cooper pair phase fluctuations are unimportant in the overdoped regime. Note that $n_s(T,x) \to 0$ for $T \to T_c^*$, since Cooper pairs disappear at T_c^*. However, the phase coherence temperature T_c has to be determined by spatially averaging over the Cooper pair phase fluctuations. In a Ginzburg–Landau (GL) treatment, the phase information is given by the GL wave function $\psi(\mathbf{r})$, where $n_s = |\psi(\mathbf{r})|^2$. In the presence of spatial phase fluctuations of $\psi(\mathbf{r})$, the average superfluid density $\bar{n}_s = |\bar{\psi}(\mathbf{r})|^2$ will vanish at T_c so that no Meissner effect occurs above T_c. The transition temperature T_c has to be determined by taking Cooper pair phase fluctuations into account. The BKT theory, as well as the 2D [32] and 3D XY models [31], predicts that T_c is proportional to $n_s(T_c)/m$. As discussed above, in BKT theory the phase stiffness, which is proportional to n_s/m as shown in (2.134), assumes the value $a = 2/\pi$ at $T = T_c$. Above T_c the renormalized phase stiffness drops to zero owing to the appearance of free vortices. The free vortices also destroy

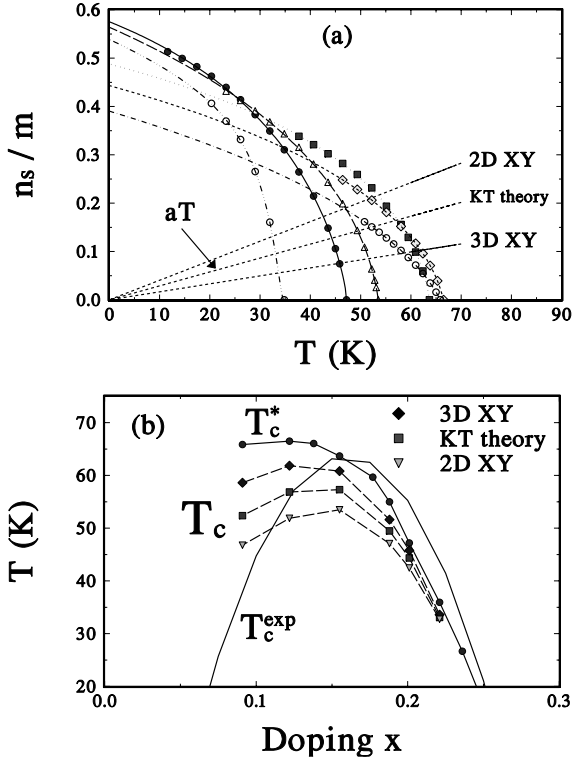

Fig. 3.4. (**a**) Results for the superfluid density divided by m in units of $10^{-2} m_e^{-1}$ Å^{-2} as a function of temperature T for various doping concentrations: $x = 0.221$ (*open circles*), $x = 0.201$ (*filled circles*), $x = 0.188$ (*triangles*), $x = 0.155$ (*squares*), $x = 0.122$ (*diamonds*), $x = 0.091$ (*open circles*). n_s vanishes at $T = T_c^*$. T_c is obtained from the intersection of $n_s(x, T)$ with aT as indicated, where $1/a = 2.202$ (3D XY) [31], $1/a = \pi/2$ (BKT theory), and $1/a = 0.9$ (2D XY) [32]. The results obtained for T_c are shown in (**b**). For comparison, the mean–field result T_c^* is also displayed.

the Meissner effect, since the energy needed to create an additional vortex at the edge of the system vanishes. Nevertheless, the *local* superfluid density n_s remains nonzero up to T_c^*. For the 2D XY model, the corresponding value is $a \approx 1/0.9$ [32] and in the 3D XY model it is $a \approx 1/2.202$ [31]. These three T_c criteria correspond to the intersections of the three straight lines in Fig. 3.4a with the curves of $n_s(T)/m$. The resulting values for $T_c(x)$ are shown in Fig. 3.4b. Note that T_c as obtained within the 3D XY model is larger than the 2D values, since fluctuations are less important in three dimensions.

Analysis of the Timescales

Concerning the dynamics of excited superconductors in general, the phase diagram shown in Fig. 3.2 with characteristic temperatures T^* and T_c should imply various relaxation channels for electronic excitations in high–T_c superconductors due to photon absorption [34, 35]. This is illustrated in Fig. 3.5. We estimate on general grounds that

$$\tau_1 \propto \Delta^{-1} \propto T_c^{-1} \quad , \tag{3.1}$$

since the energy change involved in the excitation is of the order of $\langle \Delta e^{i\phi} \rangle$. Note that above T_c one has $\langle e^{i\phi} \rangle = 0$ owing to phase–incoherent Cooper pairs. Hence, τ_1 describes the dynamics only below T_c. Using data for $T_c(x)$ we estimate τ_1 to be of the order of picoseconds, which is in agreement with experiment [34]. Furthermore, the energy involved because of the gapstructure in the spectral function $A(\mathbf{k}, \omega)$, which occurs at T^* and thus in the corresponding optically induced excitation, is approximately $E_{af} \sim T^*$. One may estimate a corresponding relaxation time from

$$\tau_3 \sim E_{af}^{-1} \sim (T^*)^{-1} \sim \left(\frac{T_c}{T^*} \right) \tau_1 \quad . \tag{3.2}$$

Thus, $\tau_3(x)$ can be estimated to be of the order of a few hundred femtoseconds. Recently, such relaxations with timescales of the order of a few picoseconds and 700 fs have been observed by Kaindl *et al.* [34] by pump–probe spectroscopy.

It would be interesting to check the above analysis by further experiments, using different light frequencies and polarizations, and in particular to study

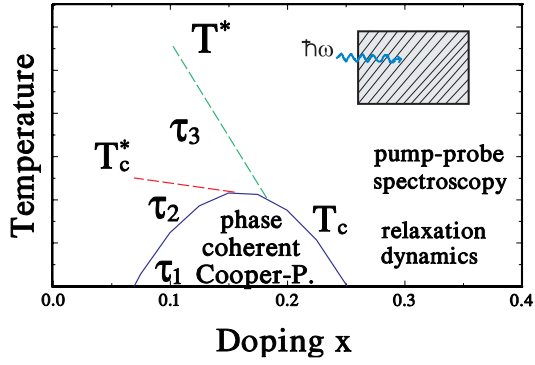

Fig. 3.5. Illustration of the relaxation dynamics expected for excited electrons in cuprate superconductors. The time τ_1 refers to relaxation of excited electrons and the time τ_3 to relaxation involving antiferromagnetic correlations, characterized by T^*. If τ_1 refers to relaxation towards phase–coherent Cooper pairs it is observed only below T_c, since $\langle \Delta e^{i\phi} \rangle \to 0$ for $T > T_c$. The relaxation time τ_2 may refer to dynamics of phase incoherent Cooper pairs.

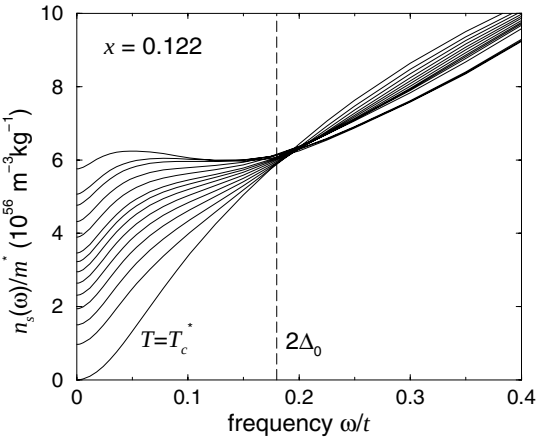

Fig. 3.6. Calculated dynamical phase stiffness $n_s(\omega)/m$ for a doping concentration $x = 0.12$ at temperatures $T/t = 0.012$, 0.015, 0.016, 0.017, 0.018, 0.019, 0.0195, 0.02, 0.0205, 0.021, 0.0215, 0.022, and 0.023 (from *top* to *bottom* at $\omega = 0$). Below $T_c^* \approx 0.023t \approx 67$ K, Cooper pairs start to form.

the relaxation $\tau_3 \sim (T^*)^{-1}$. Note that different dynamics are expected when $x \simeq 0.15$, where $T^*(x) \to T_c$ and also for the overdoped cuprates, where again $T^* > T_c$, and $T^* > T_c$. Circularly polarized light might also couple to magnetic excitations in the cuprates, but then spin–orbit coupling is involved and one obtains much longer relaxation times.

Let us now turn to the important relaxation time τ_2. Recently, Corson *et al.* have measured the complex conductivity of underdoped $Bi_2Sr_2CaCu_2O_{8+\delta}$ and extracted the frequency–dependent phase stiffness $n_s(\omega)/m$ from their data [36]. They have found that $n_s(\omega)/m$ becomes nearly independent of the frequency at a temperature given by the BKT theory. In a simple approximation this frequency should be proportional to $1/\tau_2$ which corresponds to the typical timescale of Cooper pair phase fluctuations. Corson *et al.* interpret their data in terms of dynamical vortex pair fluctuations [37, 38] and conclude that vortices, and thus local Cooper pairs, should be present up to $T = 100$ K.

In order to investigate the timescale τ_2 in more detail, we show in Fig. 3.6 our results for the *dynamical* phase stiffness $n_s(\omega)/m$ for a doping $x = 0.12$ (underdoped) at various temperatures [39]. As derived in the previous chapter, the dynamical phase stiffness is related to the dynamical conductivity $\sigma(\omega)$ via [20]

$$\frac{n_s(\omega)}{m} = \frac{1}{e^2}\,\omega\,\mathrm{Im}\;\sigma(\omega) \quad ,$$

where e is the elementary charge, $\mathrm{Im}\,\sigma(\omega)$ has been obtained from the current–current correlation function and the Kubo formula using the FLEX

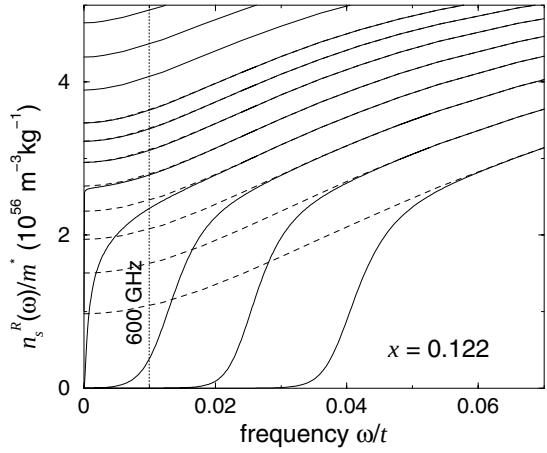

Fig. 3.7. Dynamical phase stiffness $n_s(\omega)/m$ for the same parameters as used in Fig. 3.6, but renormalized by vortex fluctuations using (2.131) and (2.132). The *dashed lines* correspond to the unrenormalized stiffness. The *vertical dotted line* indicates the highest frequency used by Corson *et al.* [36].

approximation (see (2.128)) to the Green's functions as an input. Even slightly below T_c^*, $n_s(\omega)/m$ has a finite value, leading to the Meissner effect, followed by a redistribution of spectral weight from above twice the low-temperature maximum gap, $2\Delta_0$, to frequencies below $2\Delta_0$. This redistribution increases with decreasing T. Furthermore, we find a finite phase stiffness for $\omega > 0$ even in the absence of Cooper pairs, i.e. for $T > T_c^*$.[2]

In Fig. 3.7, we show our results for the renormalized dynamical phase stiffness obtained using (2.131) and (2.132) and $D_\nu/r_0^2 = 10^{17}s^{-1}$ [39]. We can clearly see that a strong renormalization of the stiffness due to Cooper pair phase fluctuations sets in at a certain frequency. The Meissner effect is thus destroyed for all temperatures $T_c < T < T_c^*$ by (slow) vortex diffusion. With increasing temperature the onset of the renormalization shifts to higher frequencies. At frequencies above this onset, the vortices cannot follow the field and thus do not affect the response. However, the onset frequencies are always smaller than $2\Delta_0$. The structure around $2\Delta_0$ is due to Cooper pair formation and is unaffected by the renormalization of the stiffness. Thus, as seen in various experiments, the strong pseudogap around $\omega \sim 2\Delta_0$ evolves continuously into the superconducting gap for temperatures $T < T_c$.

To summarize this subsection, we have solved the generalized Eliashberg equations self–consistently and extended them by including Cooper

[2] As has been discussed in Sect. 2.2, for $T > T_c^*$ the effective action of the phase vanishes. Moreover, the order parameter itself vanishes, so that its phase has no physical meaning. Thus, for $T > T_c^*$, $n_s(\omega)$ is related to the normal-state skin effect.

pair phase fluctuations to calculate some basic properties of the hole–doped cuprate superconductors. In particular, we have shown results for the weak–pseudogap temperature T^*, where a small reduction in the spectral density at the Fermi level appears, for the strong–pseudogap temperature T_c^*, where local incoherent Cooper pairs start to form, and for the superconducting transition temperature T_c, where the phases become coherent. We combined our results with standard many-body theory and used this as an input to the Ginzburg–Landau energy functional $\Delta F\{n_s, \Delta\}$, and found a phase diagram for hole-doped cuprates with two different regions: on the overdoped side we obtain a mean–field–like transition and $T_c \propto \Delta(T = 0)$, whereas in the underdoped regime we find $T_c \propto n_s(T = 0)$.

Finally, we have compared our results with the BKT theory using FLEX data as an input and obtained similar results. We have calculated the dynamical stiffness against fluctuations, $n_s(\omega)/m$, as a function of doping and temperature, taking into account renormalization by Cooper pair phase fluctuations. We have compared our results with dynamical (time–resolved) measurements and found fair agreement. We have also reproduced the observed linear temperature dependence of $1/\lambda^3$ close to T_c, where $\lambda \propto n_s^{-1/2}$ is the in-plane penetration depth.

3.1.2 Electron–Doped Cuprates

It is of general interest to see whether the behavior of hole-doped cuprates described above and that of electron–doped cuprates can be explained within a unified physical picture, using again the exchange of antiferromagnetic spin fluctuations as the relevant pairing mechanism. While hole-doped superconductors have been studied intensively [40], the analysis of electron-doped cuprates has remained largely unclear. As discussed in the Introduction, one expects on general physical grounds, if Cooper pairing is controlled by antiferromagnetic spin fluctuations, that pairing with d–wave symmetry should also occur for electron–doped cuprates [41].[3] Previous experiments in the last decade did not clearly support this expectation and reported mainly s–wave pairing [42, 43, 44]. Maybe as a result of this, electron–doped cuprates have received much less attention than hole–doped cuprates so far. However, phase–sensitive experiments [45] and measurements of the magnetic penetration depth [46, 47] performed recently indeed indicate d–wave symmetry Cooper pairing.

In order to obtain a unified theory for both hole–doped and electron–doped cuprates, it is tempting to use the same Hubbard Hamiltonian, taking

[3] If the dominant *repulsive* pairing contribution in high-T_c superconductors can be described mainly by their spin susceptibility, then the underlying order parameter must change its sign. From group theory we know [25] that for a nested Fermi surface described by $\mathbf{Q} = (\pi, \pi)$, i.e. $\epsilon_{\mathbf{k}+\mathbf{Q}} = -\epsilon_{\mathbf{k}}$, a $d_{x^2-y^2}$-symmetry order parameter is the simplest possibility.

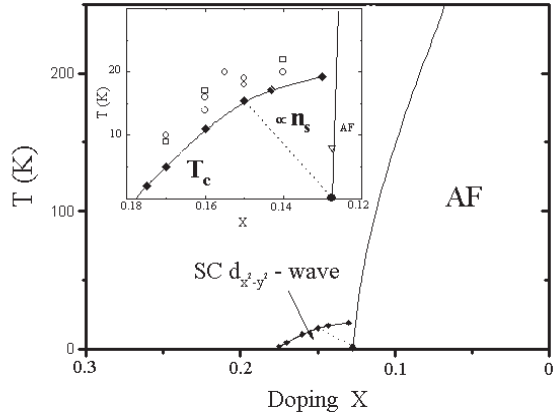

Fig. 3.8. Phase diagram $T(x)$ for electron–doped cuprates. The AF transition curve is taken from [48]. The *solid curve* corresponds to our calculated T_c values obtained from $\phi(\mathbf{k}, \omega) = 0$. The *inset* shows $T_c(x)$ for the doping region $0.18 < x < 0.12$ and experimental data (*squares* from [49], *circles* from [50], and *triangle* from [51]). The *dotted curve* refers to $T_s \propto n_s$.

the different dispersions of the carriers into account of course [52]. This has aleady been discussed in relation to Fig. 2.1. For optimally doped NCCO, the Fermi surface indicated by ARPES measurements [52] and the dispersion (see (2.4))

$$\epsilon_k = -2t \left[\cos k_x + \cos k_y - 2t' \cos k_x \cos k_y + \mu/2\right]$$

have been assumed. The chemical potential μ describes the band filling. We have chosen the parameters $t = 138$ meV and $t' = 0.3$. As discussed in Chap. 2, in the case of NCCO the flat band around $(\pi, 0)$ is approximately 300 meV *below* the Fermi level, whereas for hole-doped superconductors the flat band lies very close to the Fermi level. Thus, using the resulting ϵ_k in a theory of spin–fluctuation–induced pairing in the framework of the generalized Eliashberg equations using the FLEX approximation, we expect a smaller T_c for electron–doped cuprates than for hole–doped ones. Note that in the case of electron doping the electrons occupy copper d–like states of the upper Hubbard band, while the holes are related to oxygen–like p–states, yielding different energy dispersions as used in our calculations. Assuming similar itinerancy of the electrons and holes, the mapping onto the effective one-band Hubbard model (see (2.1)) seems to be justified.

In Fig. 3.8, we present our results for the phase diagram $T_c(x)$. We find, in comparison with hole–doped superconductors, smaller T_c values and superconductivity occurring in a narrower doping range, as also observed in experiments [53]. The poorer nesting properties of the Fermi surface and the flat band around $(\pi, 0)$, which lies well below the Fermi level, are respon-

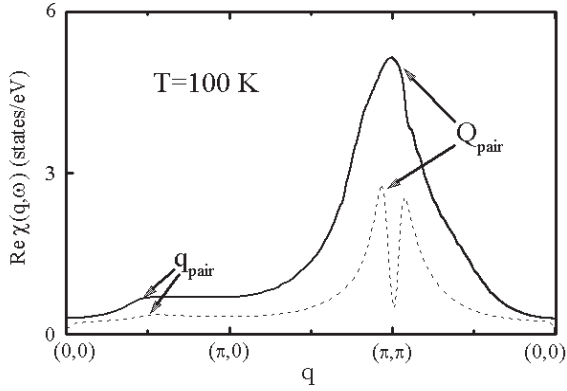

Fig. 3.9. Momentum dependence of the real part of the spin susceptibility along the path through the Brillouin zone $(0,0) \rightarrow (\pi,0) \rightarrow (\pi,\pi) \rightarrow (0,0)$ at $T = 100$ K for $\omega = 0$ (*solid curve*) and $\omega = \omega_{sf} \approx 0.47t$ (*dashed curve*). The main contributions to the corresponding pairing interaction come from $\mathbf{q}_{pair}$ (along the antinodes) and $\mathbf{Q}_{pair}$ (along the "hot spots") as illustrated in Fig. 3.10b.

sible for this. It turns out that the corresponding van Hove singularity lies approximately 300 meV below the Fermi level, yielding smaller T_c values than for hole–doped cuprates. Below T_c we find a $d_{x^2-y^2}$–wave order parameter, which will be discussed later. The narrow doping range for T_c is due to antiferromagnetism up to $x = 0.13$ and rapidly decreasing nesting properties for increasing x. In the inset we show a blowup of the doping region $0.19 < x < 0.12$ and some several experimental data are also displayed. One can clearly see that the overall agreement between our calculated $T_c(x)$ curve and experiment is quite remarkable. However, in the strongly underdoped regime the experiments contradict each other. Thus it is not clear whether $T_c(x)$ should decrease. If this were be the case, one would expect Uemura scaling, i.e. $T_c \propto n_s$, as for hole-doped cuprates (see dotted curve).

In order to understand the behavior of $T_c(x)$ in underdoped electron–doped cuprates, we have calculated the Cooper pair coherence length ξ_0, i.e. the size of a Cooper pair, and find similar and also larger values for electron-doped than for hole-doped superconductors (from 6 Å to 9 Å). If owing to strong–coupling lifetime effects, the superfluid density n_s becomes small, the distance d between Cooper pairs increases. If for $0.15 > x > 0.13$ the Cooper pairs do not overlap significantly, i.e. $d/\xi_0 > 1$, then Cooper pair phase fluctuations become important [3, 4, 35]. Thus we expect, as for hole–doped superconductors, that $T_c \propto n_s$. Assuming that n_s increases approximately linearly from $x \simeq 0.13$ to $x \simeq 0.15$, we estimate a T_c which is smaller than thr value calculated from $\phi(\mathbf{k}, \omega) = 0$, see the dashed curve in Fig. 3.8. Thus more experiments determining T_c for $x \leq 0.15$ should be performed to check the Uemura scaling $T_c \propto n_s$.

d–Wave Order Parameter

In order to investigate first the underlying pairing interaction, we show in Fig. 3.9 results for the real part of the spin susceptibility at 100 K with $U = 4t$ in the weak-coupling limit for $\omega = 0$ (solid curve) and for $\omega = \omega_{sf} \approx 0.47t$ (dashed curve). As discussed earlier, ω_{sf} denotes the spin fluctuation (paramagnon) energy, where a peak in $\mathrm{Im}\,\chi(\mathbf{Q}, \omega)$ occurs. The commensurate peak of $\mathrm{Re}\,\chi(\mathbf{q}, \omega = 0)$ at $\mathbf{Q}$=(π, π) is in accordance with recent calculations in [54], where it was pointed out that the exchange of spin fluctuations yields a good description of the normal–state Hall coefficient R_H for both hole– and electron–doped cuprates. Furthermore, we also find a linear temperature dependence of the in–plane resistivity $\rho_{ab}(T)$, if we do not take into account any additional electron–phonon coupling. This will be discussed later. Concerning the superconducting properties, note that the lower tiny peak would favor d_{xy} pairing symmetry, but the dominant larger peak leads to $d_{x^2-y^2}$ symmetry and is also pair–breaking for d_{xy} symmetry. Evidently, the electron–doped cuprates are not close to d_{xy} pairing symmetry as stated previously [55]. This explains why the resultant superconducting order parameter $\phi(\mathbf{k}, \omega)$ exhibits almost pure $d_{x^2-y^2}$ symmetry.

In Fig. 3.10, we present our results for the superconducting order parameter $\phi(\mathbf{k}, \omega)$ calculated from the generalized Eliashberg equations for electron-doped cuprates using the FLEX approximation. We show $\phi(\mathbf{k}, \omega = 0)$ for an electron doping $x = 0.15$ at $T/T_c = 0.8$, where the gap has just opened. The gap function clearly has $d_{x^2-y^2}$–wave symmetry. This is in agreement with the reported linear and quadratic temperature dependences of the in–plane magnetic penetration depth at low temperatures in the clean and dirty limits, respectively [46, 47], and with phase–sensitive measurements [45]. From our result of a pure $d_{x^2-y^2}$-wave superconducting order parameter, we expect a zero–bias conductance peak (ZBCP) [56] as recently observed in optimally doped NCCO [57] and also in hole–doped superconductors [43]. Note that its absence in some other experiments may be attributed to small changes in the surface quality and roughness [58] or to disorder [59]. The incommensurate structure in the order parameter close to $(\pi, 0)$ results from the double–peak structure in $\mathrm{Re}\,\chi$ at $\omega \approx \omega_{sf} = 0.47t$ shown in Fig. 3.9. This means physically that the Cooper pairing interaction occurs mostly not for a spin–fluctuation wave vector $\mathbf{Q} = (\pi, \pi)$, but mostly for $\omega = \omega_{sf}$ and $\mathbf{Q}^* = (\pi - \delta, \pi + \delta)$. Furthermore, from Figs. 3.9 and 3.10b we conclude that *no* d_{xy}-symmetry component is present in the superconducting order parameter, since the dominant $d_{x^2-y^2}$–type pairing suppresses d_{xy} pairing. ARPES studies might test this.

On general grounds we expect a weakening of the $d_{x^2-y^2}$ pairing symmetry if we include the electron–phonon interaction and if this interaction plays a significant role. The absence of an isotope effect ($\alpha_0 = d \ln T_c / d \ln M \approx 0.05$) for a doping $x = 0.15$ (see [60]) suggests the presence of a pure $d_{x^2-y^2}$ symmetry. As discussed in Sect. 1.4.3, we know from Fig. 3.9 that phonons con-

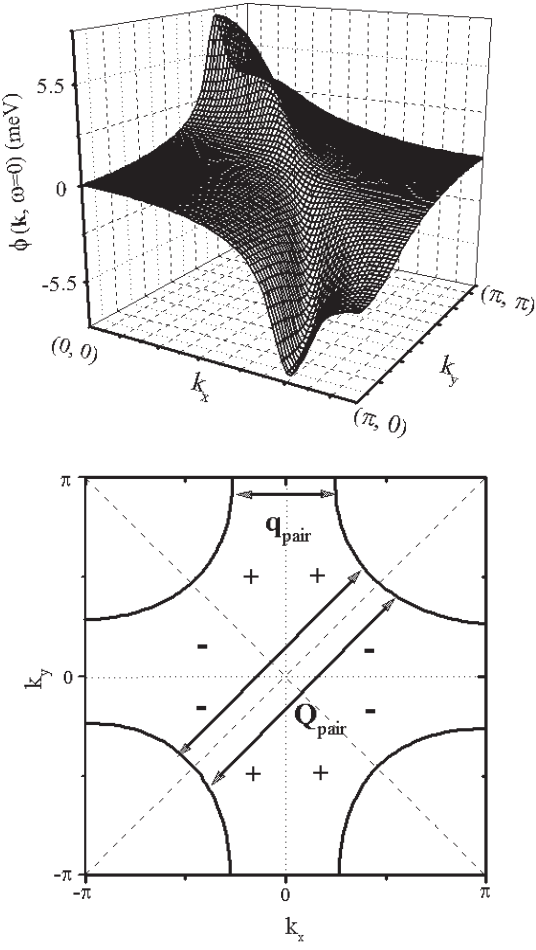

Fig. 3.10. (**a**) Calculated $d_{x^2-y^2}$–wave symmetry of the superconducting order parameter at $T/T_c = 0.8$ for x = 0.15 in the first square of the BZ. (**b**) Calculated Fermi surface for (optimally doped) NCCO. The plus and minus signs and the *dashed lines* refer to the sign of the calculated momentum dependence of the $d_{x^2-y^2}$ gap function $\phi(k, \omega = 0)$ and its nodes, respectively.

necting parts of the the Fermi surface with wave vector $\mathbf{Q}_{pair} = (\pi, \pi)$ will add destructively to the spin fluctuation pairing [61]. If, owing to exchange of spin fluctuations, a $d_{x^2-y^2}$-symmetry instability is the dominant contribution to the pairing interaction, an additional electron–phonon coupling with wave vector $\mathbf{q}_{pair} = (0.5\pi, 0)$ will be pair–building. We generally expect that, owing to the poorer nesting, the pairing instabilities due to electron–phonon and spin fluctuation interactions will become more comparable. In this case

the electron–phonon coupling would definitely favor s–wave symmetry of the underlying superconducting order parameter. This can be analyzed in detail by adding a term $\alpha^2 F(\mathbf{q},\omega)$ to the pairing interaction [61].

To continue the discussion of why the symmetry of the order parameter depends more sensitively on the electron-phonon interaction for electron–doped cuprates, we show in Fig. 3.10b the calculated Fermi surface for optimally doped NCCO. Note that the topology of the Fermi surface for the electron-doped cuprates is very similar to that of optimally hole-doped $Bi_2Sr_2CaCu_2O_{8+\delta}$ (BI2212), as was also pointed out recently in [62]. We estimate that practically no phonons are present along the edges $(-0.25\pi,\pi) \rightarrow (0.25\pi,\pi)$ bridging BZ areas where the superconducting order parameter $\phi(\mathbf{k},\omega)$ is always positive (this condition is denoted by $+/+$). Attractive electron–phonon coupling bridging $+/-$ areas, *i.e.* $(-0.5\pi,-0.5\pi) \rightarrow (0.5\pi,0.5\pi)$, is *destructive* for $d_{x^2-y^2}$–symmetry Cooper pairing. However, owing to poorer nesting conditions, pairing transitions of the type $+/+$ contribute somewhat and then a mixed symmetry $\{d_{x^2-y^2}+\alpha s\}$ may occur [4].

Further experimental study of the doping dependence of the oxygen isotope effect is necessary for a better understanding of the role played by the electron–phonon interaction. For example, if, owing to structural distortion and oxygen deficiency in the CuO_2 plane, the phonon spectrum $F(\mathbf{q},\omega)$ changes significantly, then this affects the isotope coefficient α_0 and reduces T_c. Possibly the reported large isotope effect of $\alpha_0 = 0.15$ for a slightly changed oxygen content, i.e. $Nd_{1.85}Ce_{0.15}CuO_{3.8}$, could be related to this effect [63, 64]. As an example, one might think of the oxygen out-of-plane B_{2u} mode, which becomes active if O_4 is replaced by $O_{3.8}$ [65]. A further signal of a significant electron–phonon coupling might be the quadratic temperature dependence of the resistivity [66].

To summarize this subsection, our unified model for cuprate superconductivity yields for electron–doped cuprates, as for hole-doped ones, pure $d_{x^2-y^2}$ symmetry pairing, in good agreement with recent experiments [45, 46, 47]. Our results seem physically clear in view of the discussion presented in connection with Figs. 3.9 and 3.10b in particular. Moreover, the important input to the calculation, namely the dispersion $\epsilon_{\mathbf{k}}$, was taken in agreement with ARPES measurements. The canonical value used for the strength of the effective Coulomb interaction U is in accordance with this dispersion. In contrast to hole–doped superconductors, we find for electron–doped cuprates smaller T_c values owing to a flat dispersion $\epsilon_{\mathbf{k}}$ around $(\pi,0)$ well below the Fermi level. Furthermore, superconductivity occurs only for a narrow doping range $0.18 > x > 0.13$, because of the onset of antiferromagnetism and, on the other side, poorer nesting conditions. We obtain $2\Delta/k_BT_c = 5.3$ for $x = 0.15$ in reasonable agreement with experiment [42]. We argue that if the electron–

[4] Owing to our tetragonal ansatz, one component of the resulting order parameter must be imaginary, e.g. $\{d_{x^2-y^2}+i\alpha s\}$. However, a slight orthorhombic distortion would allow our proposed $\{d_{x^2-y^2}+\alpha s\}$ symmetry.

phonon coupling becomes important, for example owing to oxygen deficiency, then the s–wave pairing instability competes with $d_{x^2-y^2}$-wave symmetry. This might explain the possible s–wave symmetry order parameter reported in earlier measurements.

3.2 Elementary Excitations in the Normal and Superconducting States: Magnetic Coherence, Resonance Peak, and the Kink Feature

In this section we assume the exchange of antiferromagnetic spin fluctuations to be the relevant Cooper pairing mechanism and calculate the elementary excitations of the spin and charge degrees of freedom in high–T_c superconductors. In most cases it is also possible to describe the temperature dependence and doping dependence. Moreover, we shall study the consequences of the important feedback of superconductivity on the elementary excitations mentioned in Chap. 2 and the relationship between different experimental techniques. Thus, in short, we shall present many fingerprints of spin–fluctuation–mediated pairing that can be seen in the experiments.

3.2.1 Interplay Between Spins and Charges: a Consistent Picture of Inelastic Neutron Scattering Together with Tunneling and Optical–Conductivity Data

If antiferromagnetic spin fluctuations are the main pairing mechanism in high–T_c superconductors, it is important to understand the spin–excitation spectrum as observed by inelastic neutron scattering [67, 68]. This means, in particular that the doping and temperature dependences of the spin susceptibility $\mathrm{Im}\,\chi(\mathbf{q},\omega)$ and their relationship to the superconducting transition temperature T_c are important. INS experiments show the appearance of a resonance peak at ω_{res} only below T_c [67] and find a constant ratio of $\omega_{res}/T_c \simeq 5.4$ for underdoped $YBa_2Cu_3O_{7-\delta}$ (YBCO) and overdoped $Bi_2Sr_2CaCu_2O_{8+\delta}$ (BSCCO) [68, 69, 70][5]. Furthermore, recent INS data on $La_{2-x}Sr_xCuO_4$ (LSCO) reveal strong momentum– and frequency–dependent changes of $\mathrm{Im}\,\chi(\mathbf{q},\omega)$ in the superconducting state [71, 72], which the authors called magnetic coherence effect. In particular, $\mathrm{Im}\,\chi(\mathbf{Q_i})$ for $\mathbf{Q}_i = (1 \pm \delta, 1 \pm \delta)\pi$ is strongly suppressed compared with its normal–state value below $\omega < 8$ meV, while it increases above this frequency. Moreover, the incommensurate peaks become sharper in the superconducting state [71, 72].

Our aim in this section is to use an electronic theory for the spin susceptibility and for Cooper pairing via exchange of antiferromagnetic spin

[5] A closer inspection for the normal-state data of underdoped $YBa_2Cu_3O_{6+x}$ [69] shows that this peak is qualitatively different from the resonance peak [70].

fluctuations to analyze the consequences of the feedback of superconductivity for magnetic coherence and the resonance peak, and on the relationship between INS, tunneling, and optical conductivity. Using the RPA and self–consistent FLEX [73] calculations of the generalized Eliashberg equations for $\mathrm{Im}\,\chi(\mathbf{q},\omega)$, we present results for the kinematic gap (or spin gap) ω_0, and for ω_{res}, ω_{res}/T_c, and the gap function $\Delta(\omega)$ in reasonable agreement with experiments. Thus, most importantly, we find that our electronic theory in the framework of the generalized Eliashberg equations can explain consistently the INS, optical–conductivity, and SIN tunneling data. Moreover, the same physical picture gives results for both underdoped and overdoped cuprates [74, 75, 76]. We find that the resonance peak in the magnetic susceptibility $\mathrm{Im}\,\chi(\mathbf{q},\omega)$ appears *only* in the superconducting state, that it scales with T_c, and that magnetic coherence is a result of a d–wave order parameter.

BCS–Like Analysis of the Spin Susceptibility: Resonance Peak and Magnetic Coherence

In order to analyze the kinematic gap and the position of the resonance peak, it is instructive to start with the bare BCS susceptibility [77]

$$\begin{aligned}\chi_0(\mathbf{q},\omega) = \sum_{\mathbf{k}} \Bigg\{ & \frac{1}{2}\left[1+\frac{\epsilon_{\mathbf{k}}\epsilon_{\mathbf{k+q}}+\Delta_{\mathbf{k}}\Delta_{\mathbf{k+q}}}{E_{\mathbf{k}}E_{\mathbf{k+q}}}\right]\frac{f(E_{\mathbf{k+q}})-f(E_{\mathbf{k}})}{\omega-(E_{\mathbf{k+q}}-E_{\mathbf{k}})+i\delta} \\ & + \frac{1}{4}\left[1-\frac{\epsilon_{\mathbf{k}}\epsilon_{\mathbf{k+q}}+\Delta_{\mathbf{k}}\Delta_{\mathbf{k+q}}}{E_{\mathbf{k}}E_{\mathbf{k+q}}}\right]\frac{1-f(E_{\mathbf{k+q}})-f(E_{\mathbf{k}})}{\omega+(E_{\mathbf{k+q}}-E_{\mathbf{k}})+i\delta} \\ & + \frac{1}{4}\left[1-\frac{\epsilon_{\mathbf{k}}\epsilon_{\mathbf{k+q}}+\Delta_{\mathbf{k}}\Delta_{\mathbf{k+q}}}{E_{\mathbf{k}}E_{\mathbf{k+q}}}\right]\frac{f(E_{\mathbf{k+q}})+f(E_{\mathbf{k}}-1)}{\omega-(E_{\mathbf{k+q}}-E_{\mathbf{k}})+i\delta}\Bigg\} \quad , (3.3)\end{aligned}$$

where its imaginary part reads at $\mathbf{q}=\mathbf{Q}=(\pi,\pi)$

$$\begin{aligned}&\mathrm{Im}\,\chi_0(\mathbf{Q},\omega) \\ &= \frac{1}{2}\sum_k \left\{[1-2f(E_k)]\;\delta(\omega+2E_k)+[2f(E_k)-1]\;\delta(\omega-2E_k)\right\}. \quad (3.4)\end{aligned}$$

Here again, $f(E_k)$ denotes the Fermi function, and $E_{\mathbf{k}}=\sqrt{\epsilon_{\mathbf{k}}^2+\Delta_{\mathbf{k}}^2}$ is the dispersion of the Cooper pairs in the superconducting state. In the following we use a gap function with d–wave symmetry, $\Delta_{\mathbf{k}}=\Delta_0(\cos k_x-\cos k_y)/2$, which can be calculated self-consistently within our FLEX-approach. For the normal–state dispersion, we employ the tight–binding band introduced in (2.4),

$$\epsilon_{\mathbf{k}} = -2t\left[\cos k_x+\cos k_y-2t'\cos k_x\cos k_y-\mu/2\right].$$

Here, t is the nearest–neighbor hopping energy, t' denotes the ratio of the next–nearest–neighbor to the nearest– neighbor hopping energy, and μ is the chemical potential. We use t' as a fitting parameter in order to describe the

Fermi surface topology of the two materials YBCO and LSCO. In evaluating (3.4) we have taken $t' = 0$ and, for simplicity, have not considered a bilayer coupling via a hopping integral $t_\perp$ [78][6].

As can already be seen within a BCS-like approach, the susceptibility $\mathrm{Im}\,\chi_0(\mathbf{Q},\omega)$ involves two characteristic frequencies. The first, ω_{DOS}, arises from the density of states of the Bogoliubov quasiparticles (i.e. the Cooper pairs), which have a gap in their spectrum due to superconductivity, $\omega_{DOS} \simeq 2\Delta(x,T)$. Here and in the following, x is the doping concentration. The second frequency, ω_0, at which $\mathrm{Im}\,\chi_0(\mathbf{Q},\omega)$ starts to increase represents the existence of a d–wave superconducting order parameter and is the so-called kinematic gap [77, 78]. Note that using the full FLEX approach, we find that the kinematic gap is washed out for $t' > 0.3$.

In order to discuss both the resonance peak and magnetic coherence, we show in Fig. 3.11a results for the spin susceptibility $\mathrm{Im}\,\chi(\mathbf{Q},\omega)$ defined in (2.125). We again obtain the two characteristic frequencies ω_0 and $\omega_{res} \simeq \omega_{DOS}$ at which $\mathrm{Im}\,\chi$ is peaked. Furthermore, one can clearly see that with increasing U the peak in $\mathrm{Im}\,\chi$ shifts to lower energies and, most importantly, becomes resonant when $U = U_{cr}$ which satisfies the condition

$$\frac{1}{U_{cr}} = \mathrm{Re}\,\chi_0(\mathbf{q} = \mathbf{Q}, \omega = \omega_{res}) \quad ; \tag{3.5}$$

this signals the occurrence of a spin–density–wave collective mode. The real part is given (at $T = 0$) by

$$\mathrm{Re}\,\chi_0(\mathbf{Q},\omega_{res}) = \sum_{\mathbf{k}} \frac{E_{\mathbf{k}}E_{\mathbf{k+Q}} - \epsilon_{\mathbf{k}}\epsilon_{\mathbf{k+Q}} - \Delta_{\mathbf{k}}\Delta_{\mathbf{k+Q}}}{\left(E_k + E_{k+Q}\right)^2 - \omega^2} \frac{E_{\mathbf{k}} + E_{\mathbf{k+Q}}}{2E_{\mathbf{k}}E_{\mathbf{k+Q}}} \,. \tag{3.6}$$

$\mathrm{Re}\,\chi_0(\mathbf{Q},\omega_{res})$ has been investigated in detail in [79], where it was found that the spin–density–wave collective mode, which satisfies (3.5), can explain the dip and hump feature observed in the photoemission spectra of BSCCO [80]. In particular, it was shown that the broad humps are at the same position for both the normal and the superconducting state.

We find from (2.125) that, in the normal state where no resonance appears, the spin wave spectrum is mainly determined by the spin fluctuation frequency ω_{sf} (roughly the peak position) and, for $\mathbf{q} = \mathbf{Q}$ by the Ornstein–Zernicke form

$$\mathrm{Im}\,\chi(\mathbf{Q},\omega) \propto \frac{\omega\,\omega_{sf}}{\omega^2 + \omega_{sf}^2} \quad . \tag{3.7}$$

On the other hand, in the superconducting state one finds that $\mathrm{Im}\,\chi$ peaks resonantly at ω_{res}, where $\omega_{res} \simeq 2\Delta$, as can already be seen from (3.4). More precisely we find for *optimal doping*, where (3.5) determines the structure of $\mathrm{Im}\,\chi$ the important relation $\omega_{res}(T) \approx 2\Delta_0(T) - \omega_{sf}(T)$. Physically speaking, the resonance peak peak that appears in INS only below T_c is mainly

[6] Bilayer coupling leads to better nesting of the bonding and antibonding bands [89]. Thus a resonance peak might appear for a complicated band structure also.

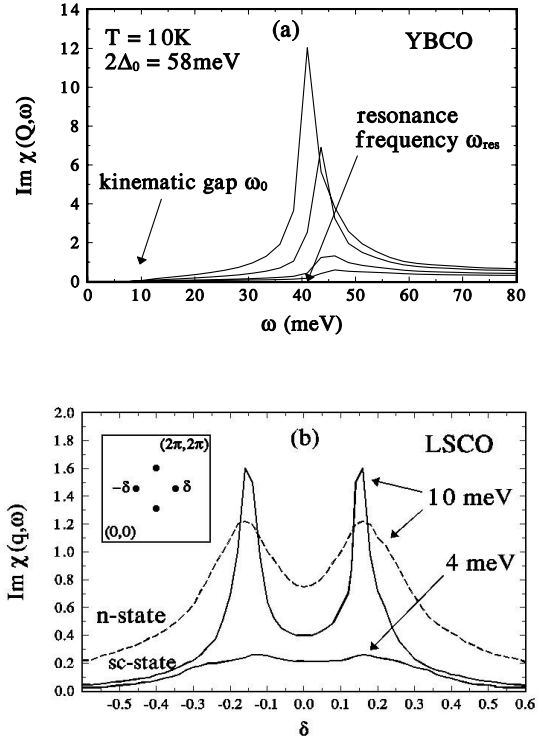

Fig. 3.11. Numerical results for the resonance peak and magnetic coherence in the weak-coupling limit. (**a**) Imaginary part of the RPA spin susceptibility (in units of states/eV) versus ω in the superconducting state at wave vector $\mathbf{q} = \mathbf{Q} = (\pi, \pi)$ for $U/t = 1$, 2, 3, and 4 (from *bottom* to *top*). As in [67], we find $\omega_{res} = 41$ meV. Below the kinematic gap ω_0, $\mathrm{Im}\,\chi(\mathbf{Q}, \omega)$ is zero. (**b**) Calculated magnetic coherence: the *solid curves* correspond to the superconducting state and the *dotted curve* to the normal state. The four peaks observed occur at $\mathbf{Q}_i = (1 \pm \delta, 1 \pm \delta)\pi$, and in the figure we show only the peaks at $\mathbf{Q}_i = (1, 1 \pm \delta)\pi$. In our calculations we find $\delta \approx 0.18$. These results are in fair agreement with experiments, see [71, 72].

determined by the maximum of the superconducting gap, but is renormalized by normal–state spin excitations. This provides a simple explanation for the observed 41 meV resonance peak in optimally doped YBCO [67], because Raman data suggest $2\Delta = 58$ meV [81], and $\omega_{sf} \simeq 17$ meV (at 100 K) as extracted from NMR experiments [82].

We show in Fig. 3.11b results for the $\mathbf{q}$ dependence of $\mathrm{Im}\,\chi(\mathbf{q}, \omega)$ obtained using the same BCS–like analysis. We performed our calculations for $U = 2t$ and a superconducting gap of $2\Delta = 10$ meV, as measured by Raman scattering in optimally doped $La_{1.85}Sr_{0.15}CuO_4$ [83]. For $\omega = 10$ meV, we obtain two peaks at $\mathbf{q} = \mathbf{Q}_i$. In the superconducting state, we find a sharpening of

the peaks due to the occurrence of a gap. This simply means that the lifetime of the quasiparticles is enhanced owing to a reduced scattering rate. At 4 meV these peaks are strongly suppressed, as seen in experiments [71, 72]. Moreover, we find no signal for $\omega < 4$ meV. This is due to the kinematic gap seen in Fig. 3.11a which is independent of $\mathbf{q}$. Note that the situation were to be totally different if LSCO were to have an isotropic gap where all states for $0 < \omega < 2\Delta_0 \simeq 20$ meV were forbidden. In this case no kinematic gap (or spin gap) would be observed.

We conclude from the above analysis and from Fig. 3.11 that, even in the weak–coupling limit where no lifetime of the Cooper pairs (i.e. Δ is independent of ω) is considered, we are able to explain the resonance peak and the magnetic coherence effect within a unified picture using a $d_{x^2-y^2}$–wave order parameter. However, on this level no microscopic justification for a d–wave order parameter can be given. In particular, its ω dependence will also be important.

Feedback Effect of Superconductivity on the Spin Susceptibility: Resonance Peak

In order to consider the important feedback effect of Δ on the spin excitation spectrum, we now discuss our results obtained in the strong-coupling limit (i.e. Δ is ω–dependent) by solving self–consistently the generalized Eliashberg equations within the FLEX approximation [73, 84]. Note that only U/t and the tight–binding dispersion relation $\epsilon(\mathbf{k})$ (with its band filling μ) enter the theory as free parameters. We further assume a rigid–band approximation.

In Fig. 3.12a we present results for $\mathrm{Im}\,\chi(\mathbf{Q},\omega)$ calculated for $U = 4t$ and an optimum doping concentration $x = 0.15$ which corresponds to $\mu = 1.65$ in (2.4). In the normal state (short–dashed curve) we find roughly the spin fluctuation energy $\omega_{sf} = 0.1t$, whereas for $T < T_c$ the resonance peak (solid curve) appears at $\omega_{res} = 0.15t$. The long–dashed curve corresponds to $T = 0.9T_c$, where the superconducting gap starts to open. Thus, the peak position reveals information about the temperature dependence of the superconducting gap. For temperatures $T < 0.75T_c$ the resonance peak remains at $\omega_{res} = 0.15t$ and only the peak height increases further. We find that the height of the peak is of the order of the quasiparticle lifetime $1/\Gamma(\omega_{res})$, where $\Gamma(\mathbf{k},\omega) = \omega\,\mathrm{Im}\,Z(\mathbf{k},\omega)/\mathrm{Re}\,Z(\mathbf{k},\omega)$; Z denotes the mass renormalization within the Eliashberg theory. Thus we can conclude that the resonance peak becomes observable because the scattering rate decreases drastically below T_c [79].

In order to relate ω_{res} to Δ, we show in Fig. 3.12b the corresponding calculated density of states $N(\omega)$. Below $T < 0.75T_c$ we find that the value of 2Δ determined from the peak–to–peak distance stays approximately constant and is very close to the value ω_{res} seen in INS, i.e. 41 meV, as shown in Fig. 3.12a. This is in good agreement with measured STM SIN tunneling data in [85]. However, in SIN tunneling a *renormalized* value of 2Δ is observed.

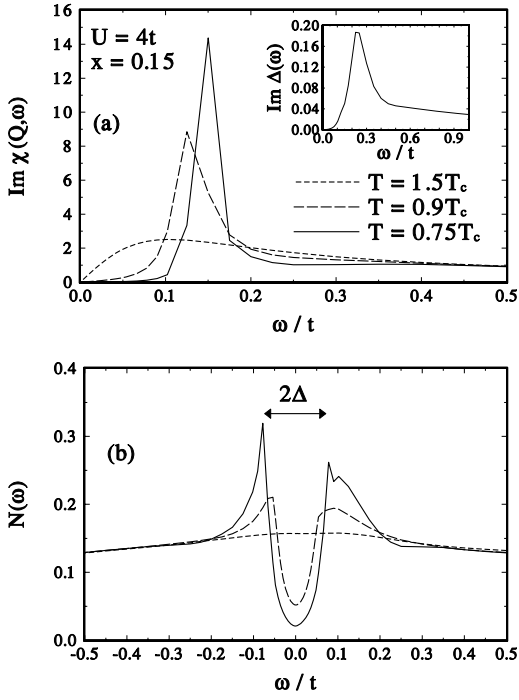

Fig. 3.12. Consistent picture of INS and tunneling data. (**a**) Imaginary part of the RPA spin susceptibility at $\mathbf{q} = \mathbf{Q} = (\pi, \pi)$ calculated within the FLEX approximation for optimum doping $x = 0.15$. For the normal state (*short–dotted line*) we obtain $\omega_{sf} = 0.1t$ and for the superconducting state we obtain $\omega_{res} = 0.15t$. Assuming $t = 250$ meV we find that $0.16t = 40$ meV. *Inset*: imaginary part of the gap function at $T = 0.7T_c$ for wave vector $\mathbf{q} \simeq (\pi, 0)$. (**b**) Calculated density of states for the same parameters and temperatures as in (**a**).

Note that a direct measurement of $\Delta(\omega)$ (e.g. by SIS tunneling) would lead to higher values. For example, we show in the inset of Fig. 3.12a the imaginary part of the gap function at the wave vector $\mathbf{q} \simeq (\pi, 0)$, where the gap has its maximum. It is peaked at $\omega = 0.25t$.

On the other hand, we show in Fig. 3.13 our results for the feedback of superconductivity for the (optimally doped) electron–doped superconductor $Nd_{2-x}Ce_xCuO_4$ (NCCO), obtained using the tight–binding energy dispersion shown in Fig. 2.1 as an input. Clearly, a rearrangement of the spectral weight occurs for small frequencies, but no resonance peak is present. The rearrangement is again due to the structure in $\Delta(\omega)$, which, however, occurs at smaller frequencies because the gap is smaller than in hole-doped superconductors. We obtain no resonance peak for NCCO because the resonance condition (3.5) cannot be fulfilled. Thus we conclude that the occurrence

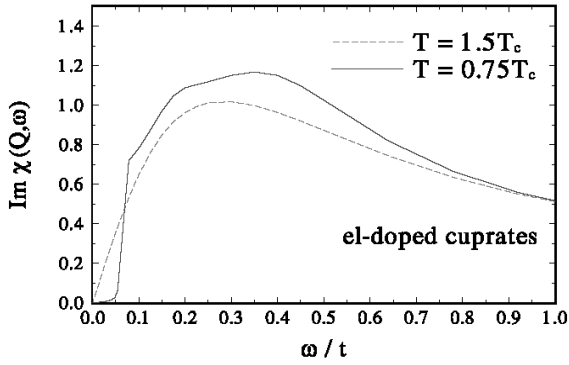

Fig. 3.13. Calculated imaginary part of the spin susceptibility for the electron–doped superconductor NCCO above and below T_c at $\mathbf{q} = \mathbf{Q} = (\pi, \pi)$ obtained using the FLEX approach. The calculations were performed for $U = 4t$ and an optimum doping concentration $x = 0.15$. The band structure was taken from experiment (see Fig. 2.1).

of a resonance peak is *not proof* of spin–fluctuation–induced pairing in the cuprates; the absence of a resonance peak can also be explained within our theory! Instead, the resonance peak should be viewed as an important fingerprint of spin fluctuations. On the other hand we find that a rearrangement of the spectral weight is always present, reflecting the structure in $\Delta(\omega)$ and thus the character of the spin excitations themselves itself (for example, their energy ω_{sf}). Note that in our electronic theory, there is no need for a second CuO_2 plane in order to describe the resonance peak. In our view, a second plane provides another possible way to satisfy (3.5), but is not needed in general. Thus we also expect a resonance peak in the single–layer thallium compound. This indeed has been observed recently [86].

Let us come back to the hole–doped cuprates, where a resonance peak is clearly present. In order to discuss the consequences of our analysis for the optical conductivity and, in particular, the consequences of the feedback of superconductivity on $\mathrm{Im}\,\chi$ for various superconducting properties we have derived the following result (see Appendix B)[7]

$$\mathrm{Im}\;\Sigma(\omega) = -\frac{U^2}{4}\int_{-\infty}^{\infty} d\omega' \left[\coth\left(\frac{\omega'}{2T}\right) - \tanh\left(\frac{\omega'-\omega}{2T}\right)\right] \times \mathrm{Im}\;\chi(\mathbf{Q},\omega') \sum_{\mathbf{k}} \delta(|\omega-\omega'| - E_{\mathbf{k}}) \quad , \tag{3.8}$$

[7] We have calculated the self-energy of an electron due to spin fluctuations in the lowest order. We have assumed further that the main contribution to the momentum sum comes from the nesting vector $\mathbf{Q}$.

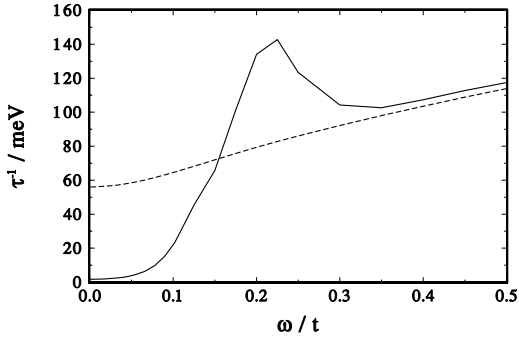

Fig. 3.14. Calculated scattering rate in the normal state for $T = 1.5T_c$ (*dashed curve*) obtained using (3.8) and in the superconducting state at $0.75T_c$ (*solid curve*) obtained using the Kubo formula [20, 87], yielding a threshold $(2\Delta + \omega_{res})$. The results are in fair agreement with [88].

where $N(\omega) = \sum_{\mathbf{k}} \delta(|\omega| - E_{\mathbf{k}})$ is the density of states. Equation (3.8) is valid in *both* the normal *and* the superconducting state. It permits discussion of how much $\Sigma(\omega)$ reflects ω_{sf} and ω_{res}, for example. We see that the feedback of superconductivity on $\operatorname{Im}\chi$ causes, approximately, a shift of the elementary excitations $\omega \to \omega + \Delta_0$ for the superconducting state in the spectral density $U^2 \operatorname{Im}\chi(\mathbf{Q}, \omega)/4$. Using (3.7) in (3.8) would not take into account the important feedback of superconductivity on $\operatorname{Im}\chi$. Equation (3.8) can be used to demonstrate the relationship between INS and optical conductivity measurements for the normal state, but note that for the superconducting state we calculate σ from $(GG + FF)$ [20]. Using Drude theory, we find that the scattering rate $\tau^{-1}(\omega)$ (which is a two–particle quantity) agrees qualitatively with $-2 \operatorname{Im}\Sigma(\omega)$ for the normal state. However, in order to obtain quantitative agreement with experimental data one has to use $\tau^{-1}(\omega) = \Gamma(\mathbf{Q}, \omega)$ or the Drude formula. This is shown in Fig. 3.14, and the results are in good agreement with [88]. From this analysis we can conclude that the optical–conductivity data, the lifetime of the quasiparticles, the resonance peak, and the SIN tunneling data can be understood within our electronic theory.

Doping Dependence of the Resonance Peak

As mentioned above, the doping dependence of the resonance peak is of significant interest for understanding the spin excitations in high–T_c cuprates. In Fig. 3.15, we show results for ω_{res} as a function of the doping concentration. We find that, for a fixed U, (3.5) cannot be fulfilled in the overdoped case[8]. Thus we find that in this regime, the resonance peak is determined

[8] Note that away from optimal doping, by determining formally the minimum of $1 - U \operatorname{Re}\chi_0$ one obtains $\omega_{min} = 2\Delta_0 - \omega_{sf}$. However, the physically relevant condition $1 = U \operatorname{Re}\chi_0$ yields ω_{res}.

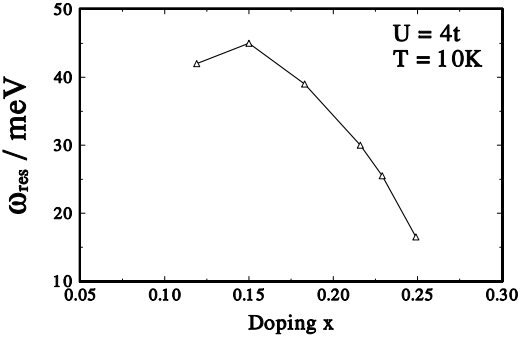

Fig. 3.15. Calculated results for the resonance frequency ω_{res} versus doping, obtained using the FLEX approximation. In the overdoped regime, where $T_c \propto \Delta_0$ [76], we find a constant ratio $\omega_{res}/T_c \simeq 8$.

mainly by $\mathrm{Im}\,\chi_0(\mathbf{Q},\omega)$ and thus by $2\Delta_0$. On general grounds one expects $T_c \propto \Delta_0$ in the overdoped regime, where the system behaves in accordance with mean–field (BCS) theory. This has been discussed in the previous section and in [76]. Thus we conclude that ω_{res}/T_c should be a constant ratio. We find $\omega_{res}/T_c \simeq 8$, which is larger than the observed value in BSCCO [68]. This is due to an underestimation of T_c within the FLEX approximation and to phonons, which are neglected in our work.

In contrast to the overdoped case, we find in the underdoped regime, where $T_c \propto n_s$ (n_s denotes the superfluid density) [76], that the resonance condition (3.5) yields $\omega_{res} \propto \omega_{sf}$, which decreases. Note that the superconducting gap guarantees that (3.5) is fulfilled. Thus we find a decreasing resonance frequency for decreasing doping, in agreement with earlier calculations [89, 90]. To summarize our discussion, we have the following result:

$$\omega_{res} \approx \begin{cases} \omega_{sf}\ , & \text{underdoped} \\ 2\Delta_0 - \omega_{sf}\ , & \text{optimal doping} \\ 2\Delta_0\ , & \text{overdoped} \end{cases} \tag{3.9}$$

where the optimally doped case corresponds to $x_{opt} = 0.15$ holes per copper site. This predicted doping dependence of the resonance peak position should be tested further experimentally.

In short, we are able to explain consistently all characteristic facts about the spin excitation spectrum of high–T_c cuprates seen in INS and its doping dependence within an electronic theory using the generalized Eliashberg equations. In particular, we find that the resonance peak is a rearrangement of the spectral weight of the normal state which happens only below T_c. Thus it is rather difficult to reconcile the resonance peak with the stripe picture, for example. Furthermore, we have shown that magnetic coherence is connected with the resonance peak and can be explained by a kinematic gap

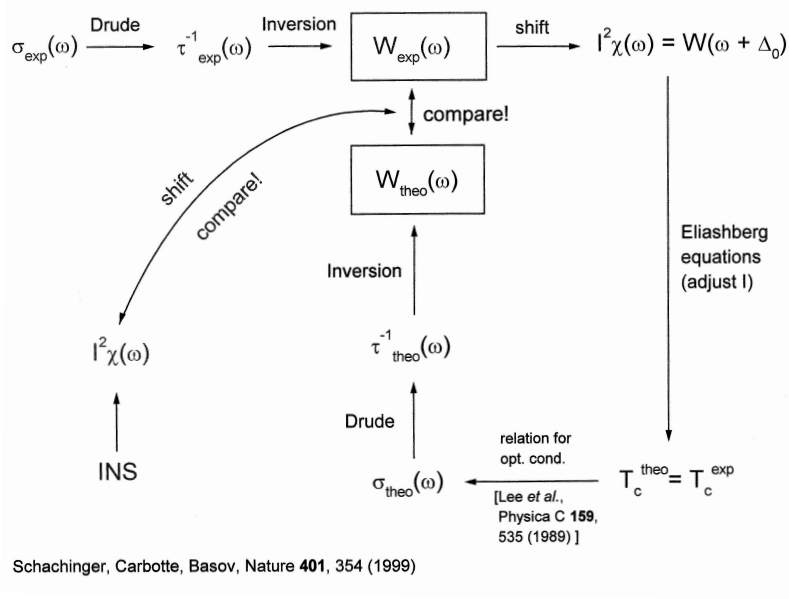

Fig. 3.16. Self–consistent scheme used by Carbotte *et al.* in order to describe the coupling of quasiparticles to spin fluctuations using conductivity scattering rates and Eliashberg equations within the semiclassical approximation. This procedure has been successfully applied for many hole–doped cuprates [75].

and d–wave symmetry of the superconducting order parameter. By taking into account the feedback of superconductivity on $\mathrm{Im}\,\chi(\mathbf{q},\omega)$ we argue that the ARPES results, the tunneling data, and the measurements of the optical conductivity are consistent.

Comparison with Other Approaches

Carbotte and Schachinger made also look an important step towards a unified description of the optical conductivity of hole–doped cuprates and their spin spectrum seen in INS [75, 91]. They extended some work by Marsiglio *et al.* [92], in which the pairing potential $W(\omega)$ is related to the optical scattering rate $\tau^{-1}(\omega)$ by

$$W(\omega) = \frac{1}{2\pi}\frac{\mathrm{d}^2}{\mathrm{d}\omega^2}\left[\frac{\omega}{\tau(\omega)}\right] \quad . \tag{3.10}$$

The procedure used is shown in Fig. 3.16. Using the extracted pairing potential (shifted by Δ_0) as an input to the Eliashberg equations within the semi–classical approximation (i.e. restricted to the Fermi surface) Carbotte *et al.* calculate T_c and a new scattering rate $\tau^{-1}(\omega)$. This leads to a new pairing potential, which has to be compared with the original potential extracted from experimental data. After changing parameters in the Eliashberg

equations, this procedure is repeated until one reaches convergence. However, despite the fact that material–dependent predictions can be made (knowing only one quantity, $\sigma(\omega)$ or $\mathrm{Im}\,\chi(\omega)$), this procedure cannot provide a *microscopic* explanation of both types of experimental data. This is the main advantage of our theory where the spin excitations follow from an electronic theory. The parameters used are only those of the original Hubbard Hamiltonian.

Another possible explanation for the resonance peak has been provided by Demler and coworkers [93], who claim, within the t–J model, that the resonance peak follows from a π–resonance in the particle–particle channel that couples to the dynamical spin correlation function within the framework of the SO(5) theory [94] only below T_c. However, Chubukov and coworkers [95] have argued against that explanation. They have demonstrated that the π–resonance always exceeds 2Δ, twice the maximum of the d–wave gap, and might be observed only around 100 meV. Instead, a bound state of a particle and a hole, a spin exciton, seems to yield good agreement with experimental data. In our approach, we also consider a particle–hole excitation, via the spin susceptibility $\chi(\mathbf{q},\omega)$, where in addition the superconducting gap is calculated self–consistently and doping–dependently. In other words, $\Delta(\mathbf{q},\omega)$ does not enter as a parameter into our theory. We obtain also the correct spin spectrum for electron–doped cuprates, whereas this is not considered in the theories mentioned above (and also not in some earlier approaches [96, 97, 98]).

Finally, we would like to mention that Brinckmann and Lee [89, 99] and Li and coworkers [90, 100] studied the doping dependence of the resonance peak in hole–doped cuprates within a slave–boson approach with the t–J model, and Norman and coworkers [101] have connected their result to available ARPES data and find a consistent picture. But again, neither a connection to optical–conductivity data nor an electronic theory for electron–doped cuprates has been presented. In the future, we believe that a good test for those theories might be the sensitivity of the resonance peak to impurities of nonmagnetic or magnetic kind [102, 103, 104, 105]. Note that in the clean limit our theory is able to account for the most important properties, such as the peak position and the doping dependence of ω_{res}/T_c.

3.2.2 The Spectral Density Observed by ARPES: Explanation of the Kink Feature

For understanding the high-T_c cuprates, their elementary excitations are of central significance. In particular, angular–resolved photoemission spectroscopy is a powerful tool for studying the observed elementary excitations $A(\mathbf{k},\omega)$ in high–T_c superconductors because the spectral density contains all information about self-energy effects.

In general, in a photoemission experiment, incident photons excite electrons (or holes) above the vacuum level, where they can be collected and analyzed. A simplified spectrum of a single-band material would consist of

only a single peak in the intensity and some background. If the momentum of the corresponding quasiparticle is assumed to be

$$|\mathbf{k}| = \left(\frac{2m_e E_{kin}}{\hbar^2} \right)^{1/2} \quad , \tag{3.11}$$

where m_e denotes the (band mass) of the quasiparticle and E_{kin} its kinetic energy, one can obtain a relation between the binding energy of an electron E_{bin} and the energy of an incident photon E_{photon} via $E_{bin} = E_{photon} - E_{kin}$. Furthermore, if the angle Θ of the emitted electron or hole with respect to the Fermi surface is varied (ARPES), it is possible to analyze the dependence of E_{bin} on the momentum $k_{\|}$, where

$$k_{\|} = |\mathbf{k}| \cos(\Theta) \quad . \tag{3.12}$$

It has turned out that for the layered cuprates, E_{bin} versus $k_{\|}$ is sufficient to determine the band structure and the elementary excitations in the whole Brillouin zone.

In a simple approximation, the peak obtained in the intensity for energies below the Fermi level is proportional to the local density of states, i.e. $\propto A(\mathbf{k}, \omega)$ [106]. Recently, owing to an improved angular resolution (which allows one to obtain the momentum distribution curve and energy distribution curve), data have become available which provide new insight into the momentum and frequency dependence of the self-energy $\Sigma(\mathbf{k}, \omega)$. These data reveal a "kink" feature at $\hbar\omega \sim 50 \pm 15$ meV, which has been observed in hole–doped cuprates such as $Bi_2Sr_2CaCu_2O_8$, Pb–doped $Bi_2Sr_2CuO_6$, $YBa_2Cu_3O_7$, and $La_{2-x}Sr_xCuO_4$ [107, 108, 109, 110, 111]. Furthermore, it is interesting that the experiments also observe a change in the dispersion of the elementary excitations on going from the normal to the superconducting state [107, 108, 109]. In contrast, the electron–doped counterparts (*e.g.* $Nd_{2-x}Ce_xCuO_4$) do not show a "kink" [112]. In hole–doped superconductors, experiments by Shen and coworkers [110, 111] have observed the kink feature in the nodal and $(0,0) \rightarrow (\pi, 0)$ directions of the first Brillouin zone and the "kink" exists in both the normal and the superconducting state. On the other hand, Kaminski *et al.* [109] discussed only the break along the $(0,0) \rightarrow (\pi, \pi)$ direction that occurs when one goes from the normal to the superconducting state. Therefore, they did not analyze the feature observed by the group mentioned previously [110, 111]. However, it is quite interesting that a closer inspection of the data of Kaminski *et al.* [109] for the normal state reveals the same changes of the Fermi velocity v_F as noted by Shen and coworkers [110, 111]. Thus, there seems to exist a "new" energy scale in hole–doped cuprates. Shortly after its discovery, interpretations where given in terms of the presence of a strong electron–phonon interaction [111, 112], stripe formation [113], or coupling to a resonating mode [80, 109].

In this subsection we show that the kink in the spectral density can be naturally explained as arising from the interaction of the quasiparticles (holes)

with spin fluctuations. We present results for the spectral density $A(\mathbf{k},\omega)$ corresponding to the crossover from $\mathrm{Im}\,\Sigma(\mathbf{k},\omega) \propto \omega$ to $\mathrm{Im}\,\Sigma(\mathbf{k},\omega) \propto \omega^2$, for the feedback of superconductivity on the excitations, and for the superconducting order parameter $\Delta(\mathbf{k},\omega)$. In agreement with recent experiments, we demonstrate that the kink feature in the nodal direction is present in both the normal and the superconducting state [108, 110, 111, 112]. Thus, we are able to explain recent ARPES experiments which study in detail the spectral density and, in particular, the energy dispersion $\omega(\mathbf{k}) = \epsilon(\mathbf{k}) + \Sigma(\mathbf{k},\omega)$. It is significant that the self–energy $\Sigma(\mathbf{k},\omega)$ resulting from the scattering of the quasiparticles by spin fluctuations can explain the main features observed. These results relate also to the inelastic neutron scattering and tunneling experiments discussed in the previous section, and shed important light on the essential ingredients that a theory of the elementary excitations in the cuprates must contain. We also analyze the feedback effects due to superconductivity on the elementary excitations and find fair agreement with [109].

Results for the Spectral Density

In Fig. 3.17, we present results for the frequency and momentum dependence of the spectral density given by (2.122) in the normal state along the $(0,0) \rightarrow (\pi,0)$ direction, calculated using the canonical parameters $U = 4t$, and $t = 250$ meV.[9] The changes in the $\mathbf{k}$ dependence of the peak in $A(\mathbf{k},\omega)$ reflect the characteristic features in the self–energy $\Sigma(\mathbf{k},\omega)$ or in the velocity $v_{\mathbf{k}}$ of the quasiparticles. The kink occurs at energies of about $\hbar\omega \approx 65 \pm 15$ meV for optimal doping ($x = 0.15$), and $T_c \approx 65$ K. We also find that the kink feature is present in nearly all directions in the BZ ($\omega \approx \omega_{sf} + \mathbf{v}_F(\phi)\cdot\mathbf{k}$, $\mathbf{k} = \mathbf{k}(k,\phi)$) and, in particular, along the diagonal $(0,0) \rightarrow (\pi,\pi)$ direction as shown in the inset of Fig. 3.17. We find that the kink is more pronounced in the $(0,0) \rightarrow (\pi,0)$ direction. This is in agreement with ARPES experiments, see for example Fig. 1.6. Moreover, we see from our calculations that this feature has only a weak temperature dependence over a wide temperature range. It changes only at very small temperatures, as we shall describe later.

Next, we come to the discussion of the effective dispersion relation (see (2.123)) of the quasiparticles due to strong correlation effects. In Fig. 3.18, we show the positions of the peaks along $(0,0) \rightarrow (\pi,0)$ shown in Fig. 3.17 as a function of $(\mathbf{k} - \mathbf{k}_F)$ for different temperatures. We obtain only small changes due to superconductivity which almost coincide with the position of the kink. Remarkably, the deviation at $\mathbf{k} - \mathbf{k}_F \approx 0.05$ Å^{-1} is due to the frequency dependence of the self–energy and reflects the transition from Fermi liquid to non–Fermi liquid behavior along the path $(0,0) \rightarrow (\pi,0)$ in

[9] Our calculations were performed in the "clean-limit" and thus do not consider the additional scattering of the carriers by impurities. Also, the intrinsic width of the spectral function due to scattering by the antiferromagnetic spin fluctuations provides a small uncertainty.

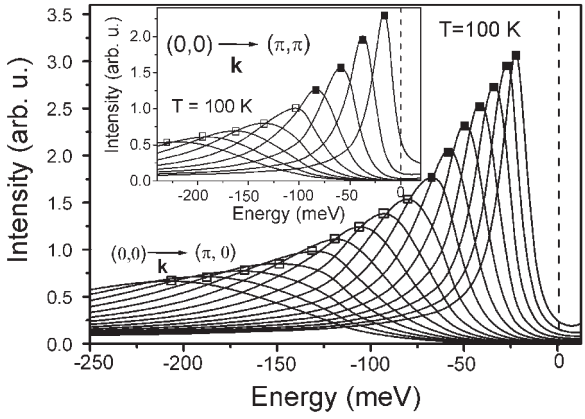

Fig. 3.17. Calculated self–energy effects in the spectral density (see (2.122)) of the quasiparticles in hole-doped superconductors in the normal state at $T = 100$ K along the $(0,0) \rightarrow (\pi,0)$ direction. The *dashed line* at $\omega = 0$ denotes the unrenormalized chemical potential. In the *inset*, the spectral density along the $(0,0) \rightarrow (\pi,\pi)$ direction is shown. In both cases a kink occurs at energies of about $\hbar\omega \approx 65 \pm 15$ meV, since the velocity of the quasiparticles changes.The results are in good agreement with experiments (see, for example Fig. 3 in [110] or Fig. 4b in [111]). Note that the width of the spectral density peak for $(0,0) \rightarrow (\pi,0)$ is twice the width for $(0,0) \rightarrow (\pi,\pi)$.

the BZ for both the normal and the superconducting state. In the inset, we show results for the difference between the peak positions for the normal and the superconducting state along the $(0,0) \rightarrow (\pi,0)$ direction in order to see the feedback of superconductivity. Note that this difference disappears at $\mathbf{k}-\mathbf{k}_F \approx 0.05$, corresponding to approximately 65 meV. We obtain changes of about 10 meV, while Kaminski *et al.,* [109] observe along the $(0,0) \rightarrow (\pi,\pi)$ direction a larger difference of about 20 meV. This might be due to the antibonding bands of Bi2212. This can be expected from an inspection of (3.8) since the feedback effect of superconductivity on χ is larger for $\mathbf{Q} \approx (\pi,\pi)$. In order to understand the feedback of superconductivity and the crossover from non–Fermi liquid to Fermi liquid behavior, we shall analyze the frequency and temperature dependence of the self–energy more in detail.

How can one understand the kink feature in a simple way? At first glance the occurrence of a kink in the nodal direction seems to be surprising, since the main interaction of the carriers with spin fluctuations occurs at the hot spots. Note that the kink feature is present along the diagonal of the BZ close to the cold spots. However, slightly away from the Fermi level but still close to it (along $(0,0) \rightarrow (\pi,\pi)$), the quasiparticles couple strongly to spin fluctuations. Most importantly, as can be seen from Fig. 3.19, the largest scattering will occur at values of $\mathbf{k} - \mathbf{k}_F = \mathbf{Q}$ and $\omega = \omega_{sf}$. In Appendix B we show that

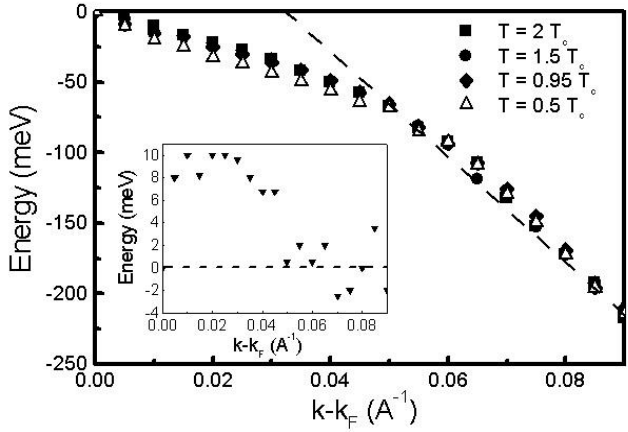

Fig. 3.18. Positions of the peaks in the spectral density $A(\mathbf{k},\omega)$ versus $\mathbf{k}$ - $\mathbf{k}_F$ (energy dispersion, see (2.123)) along the $(0,0) \rightarrow (\pi,0)$ direction of the BZ calculated within the FLEX approximation. These results should be compared with the positions of the peaks derived from the momentum distribution curve for a hole–doped superconductor measured experimentally. The curves show a kink at energies of about $\hbar\omega \approx 65 \pm 15$ meV. The *dashed line* is a guide to the eye. We find small changes due to superconductivity which almost coincide with the kink position. *Inset*: change in the peak position in $\mathrm{A}(\mathbf{k},\omega)$ in the superconducting state ($T = 0.5T_c$). The results are in fair agreement with ARPES data [109].

$$\Sigma(\mathbf{k}, i\omega_n) = -T^2 \sum_{\omega_m,\nu_m} \sum_{\mathbf{k}',\mathbf{q}} \tilde{\tau}_0 G(\mathbf{k}-\mathbf{k}', i\omega_n - i\nu_m)\tilde{\tau}_0 U^2$$
$$\times \frac{1}{2}\mathrm{Tr}\left[\tilde{\tau}_0 G(\mathbf{k}+\mathbf{q}, i\omega_m + i\nu_m)\tilde{\tau}_0 G(\mathbf{q}, i\omega_m)\right] \quad . \tag{3.13}$$

Approximating the Green's function,

$$G(\mathbf{k}, i\omega_n) \approx G_0(\mathbf{k}, i\omega_m) = \frac{i\omega_n\tilde{\tau}_0 + \epsilon_{\mathbf{k}}\tilde{\tau}_3 - \phi_{\mathbf{k}}\tilde{\tau}_1}{(i\omega_n)^2 - E_{\mathbf{k}}^2} \quad , \tag{3.14}$$

one obtains the following, after some algebra using the fact that $E_{\mathbf{k}}^2 = \epsilon_{\mathbf{k}}^2 + \phi_{\mathbf{k}}^2$, on the real axis:

$$\Sigma(\mathbf{k},\omega) \approx -\frac{U^2}{4}\sum_{\mathbf{k}'}\int_0^\infty d\omega' \frac{\mathrm{Im}\chi_{RPA}(\mathbf{k}-\mathbf{k}',\omega')}{\omega - \omega' - E_{\mathbf{k}'}}$$
$$\times \left[\coth\left(\frac{\omega'}{2T}\right) - \tanh\left(\frac{\omega'-\omega}{2T}\right)\right] \quad . \tag{3.15}$$

The imaginary part of the spin susceptibility is approximately given by the Ornstein–Zernicke expression, which has a peak structure at the wave vector $\mathbf{q}$ and the frequency $\omega = \omega_{sf}$. Furthermore, the self–energy is mainly

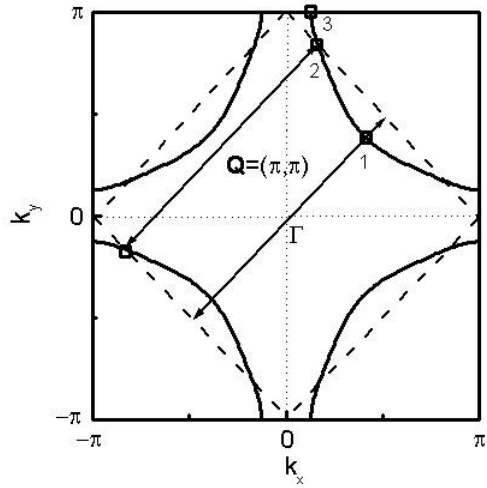

Fig. 3.19. Illustration of the anisotropy of the elementary excitations using the calculated Fermi surface for hole–doped cuprates in the first Brillouin zone for a single CuO_2 layer. The anisotropy can be characterized by three different points on the Fermi surface. Point number 1 (called the nodal point or cold spot) is related to the diagonal part of the BZ and point number 3 (called the antinodal point) is close to $(0, \pi)$. The *dashed line* denotes the magnetic BZ, which crosses the electronic Fermi surface exactly at the "hot spots" (labeled 2). The antiferromagnetic wave vector $\mathbf{Q}$ connects the two pieces of the Fermi surface via scattering by spin fluctuations mainly at the hot spots. At the $(0, \pi)$ points and along the diagonals the wave vector $\mathbf{Q}$ connects quasiparticle states below the Fermi level only. Note that the characteristic anisotropic behavior of the elementary excitations may help one to distinguish the resultant kink structure from any structure that might be caused by electron–phonon coupling (see Appendix C).

frequency-dependent, while the bare dispersion of the carriers is not. Even in the normal state, the self–energy $\Sigma(\mathbf{k}, \omega)$ has a maximum, reflecting a corresponding maximum of $\mathrm{Im}\,\chi$ at $\mathbf{q} \approx \mathbf{Q}$ and $\omega' \approx \omega_{sf}$. The position of the kink follows from the pole of the denominator of (3.15). This leads to the "kink condition"

$$\omega_{kink} \approx E_{\mathbf{k}-\mathbf{Q}} + \omega_{sf}(x) \quad . \tag{3.16}$$

Note that this gives an estimate of the position of the kink and explains the behavior of the spectral density $A(\mathbf{k}, \omega)$ in the nodal direction.

Next, we focus on an important antinodal direction that has been measured by Dessau and coworkers [114]. Interestingly, these researchers find a kink only below T_c. In Fig. 3.20a, we show our results for the spectral density $A(\mathbf{k}, \omega)$ along the path $(\pi, 0) \rightarrow (\pi, \pi)$, i.e. the antinodal direction of the first BZ, in the normal state. Note that the spectral density at the $(0, \pi)$ point is broader than at the antinodal point owing to stronger coupling to spin excitations peaked at $\mathbf{q} = \mathbf{Q} = (\pi, \pi)$, as discussed in the caption of Fig. 3.19.

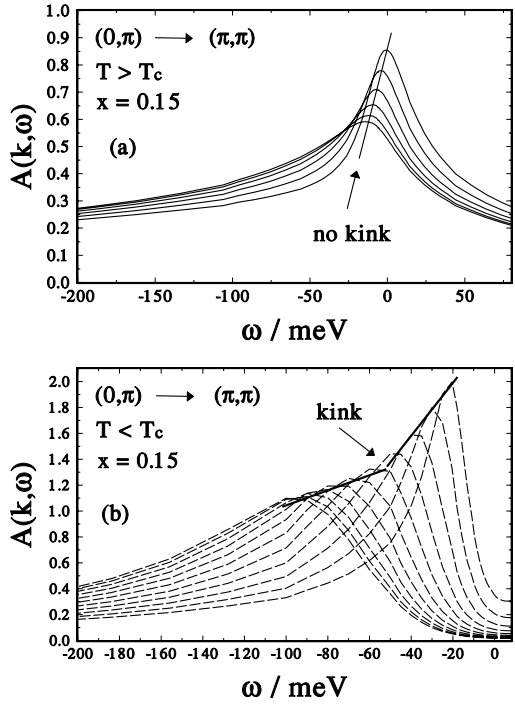

Fig. 3.20. Calculated spectral density $A(\mathbf{k},\omega)$ along the antinodal $(\pi,0) \rightarrow (\pi,\pi)$ direction in the first BZ as a function of frequency in the normal (**a**) and the superconducting (**b**) state. Owing to the flat band close to the Fermi level, the spectral density shows no kink structure in the normal state. Below T_c, the superconducting gap $\phi(\omega)$ opens, yielding a kink structure in the spectral density that occurs at energies $\omega_{kink} \approx 50 \pm 10$ meV for optimal doping.

Clearly, no kink is present. The absence of a kink structure can be explained by the flat structure of the CuO_2 plane around the M point (see Fig. 2.1). Simply speaking, for a flat band the frequency dependence of Σ in (2.123) does not play a significant role, and therefore no change in the velocity and no kink structure are present.

What happens in the superconducting state? Below T_c, the superconducting gap $\phi(\mathbf{k},\omega)$ opens rapidly with decreasing temperature T and becomes maximal in momentum space around the M point, reflecting the momentum dependence of the effective pairing interaction (see (2.28)). In addition, owing to the frequency dependence of the gap, the flat band around M disappears. In Fig. 3.20b we show results for $A(\mathbf{k},\omega)$ at a temperature $T = 0.5T_c$ where the superconducting gap has opened. A kink structure around $\omega_{kink} \approx 50 \pm 10$ meV is present, reflecting the magnitude of ϕ. Hence, in the $(\pi,0) \rightarrow (\pi,\pi)$ direction, this kink feature is present only below T_c and is connected to the feedback effect of ϕ on the elementary excitations. This is similar to the

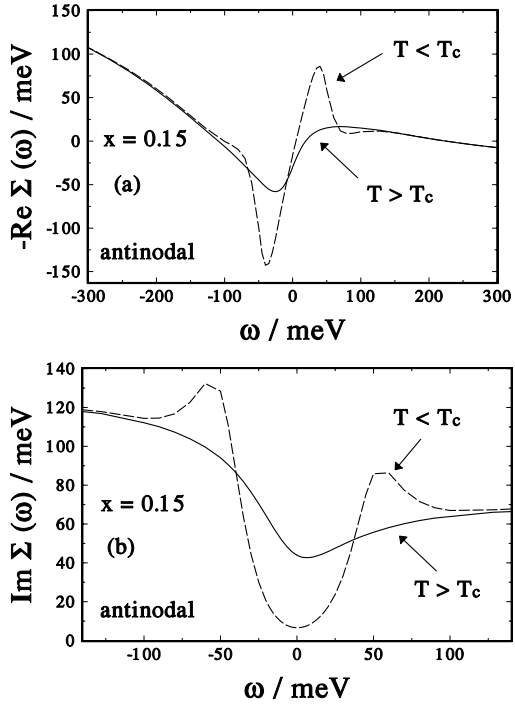

Fig. 3.21. (**a**) Calculated frequency dependence of the self-energy $\mathrm{Re}\,\Sigma(\mathbf{k}_a, \omega)$ at the antinodal point $\mathbf{k}_a$ of the first BZ in the normal state (*solid curve*) and superconducting state (*dashed curve*). Owing to the feedback effect of the superconducting gap $\phi(\omega)$, a peak and a dip occur for $\omega > 0$ ($\omega < 0$), respectively, which roughly define the position of the kink structure. (**b**) The corresponding imaginary part at the antinodal point $\mathrm{Im}\,\Sigma(\mathbf{k} = \mathbf{k}_a, \omega)$. Again, owing to the feedback effect of $\phi(\omega)$, a maximum occurs below T_c. Note that $\mathrm{Re}\,\Sigma$ is not fully antisymmetric and $\mathrm{Im}\,\Sigma$ is not fully symmetric with respect to ω at the optimum doping $x = 0.15$.

feedback effect that yields the resonance peak seen in INS. Note that the superconducting gap $\phi(\mathbf{k}, \omega)$ is calculated self–consistently in our theory and reflects the underlying spin fluctuations which dominate the pairing potential V_{eff}. Therefore, the occurrence of a kink structure *only* below T_c in the antinodal direction is a direct fingerprint of the spin excitation spectrum. Furthermore, as we have discussed above, $\mathrm{Im}\,\chi(\mathbf{Q}, \omega)$ in (3.15) is peaked at the resonance frequency ω_{res} (roughly $\omega_{sf} + \Delta$). Therefore, the kink condition is given by

$$\omega_{kink} \approx E_{\mathbf{k}-\mathbf{Q}} + \omega_{res}(x) \quad . \tag{3.17}$$

In Fig. 3.21a, the frequency dependence of $\mathrm{Re}\,\Sigma(\mathbf{k}_a, \omega)$ in the normal and superconducting states at the antinodal point $\mathbf{k} = \mathbf{k}_a$ is shown. Owing to the occurrence of the resonance feature in $\mathrm{Im}\,\chi(\mathbf{Q}, \omega)$ and the related feedback of the superconducting gap $\phi(\omega)$, $\mathrm{Re}\,\Sigma$ shows a pronounced structure below

T_c at energies of about $\omega_{res} + \Delta_0$. Also the corresponding imaginary part $\mathrm{Im}\,\Sigma(\mathbf{k} = \mathbf{k}_a, \omega)$ shows a peak below T_c (see Fig. 3.21b). This pronounced behavior is responsible for the formation of a kink along the $(\pi, 0) \rightarrow (\pi, \pi)$ direction in the BZ.

Therefore, while kink features are present along the $(0, 0) \rightarrow (\pi, \pi)$ and $(\pi, 0) \rightarrow (\pi, \pi)$ directions in the superconducting state of hole-doped cuprates, their nature is qualitatively different. Along the nodal direction the superconducting gap is zero (for $\omega = 0$) and thus the feedback effect of superconductivity on the elementary and spin excitations is small. Therefore, ω_{sf} is the main factor that determines the kink feature. On the other hand, along the antinodal direction, the gap is maximal and leads to a strong feedback of superconductivity on χ. Thus, in the superconducting state, ω_{res} and Δ_0 yield a kink structure along the $(\pi, 0) \rightarrow (\pi, \pi)$ direction that is not present in the normal state.

The different reasons for the kink structures in hole-doped cuprates along different directions in the first BZ will also be reflected in their doping dependence. The results that we have shown so far were for the optimal doping concentration $x = 0.15$. This corresponds to a band filling of $n = 0.85$. Note that the superconducting transition temperature T_c behaves differently in the overdoped (OD) and underdoped (UD) regimes:

$$\begin{aligned} T_c &\propto \Delta(T \rightarrow 0)\,, \quad \text{OD-regime} \quad , \\ T_c &\propto n_s(T \rightarrow 0)\,, \quad \text{UD-regime} \quad , \end{aligned}$$

where n_s is the superfluid density calculated self-consistently from the generalized Eliashberg equations.

In the antinodal $(0, \pi) \rightarrow (\pi, \pi)$ direction, the kink is present only below T_c owing to the feedback of $\phi(\omega)$. In the OD case the gap $\phi(\omega)$ decreases, reflecting a mean–field–like behavior. Thus, the energy where the kink occurs must decrease with overdoping:

$$\omega_{kink}(x) \propto \Delta_0(x) \quad . \tag{3.18}$$

This behavior is indeed observed by Dessau and coworkers [114]. Note that the above argument remains true in the strongly OD case, where no resonance peak in $\mathrm{Im}\,\chi(\mathbf{Q}, \omega)$ occurs, because the feedback effect of $\phi(\omega)$ should always be present.

Regarding the kink along the nodal $(0, 0) \rightarrow (\pi, \pi)$ direction, we note the following: ω_{sf} increases with increasing doping from underdoped to overdoped cuprates. Since ω_{sf} determines the kink position along the $(0, 0) \rightarrow (\pi, \pi)$ direction, we expect that

$$\omega_{kink}(x) \propto \omega_{sf}(x) \quad . \tag{3.19}$$

This is in qualitative agreement with experimental data [129] (for the underdoped regime and for optimally doped superconductors). On the other

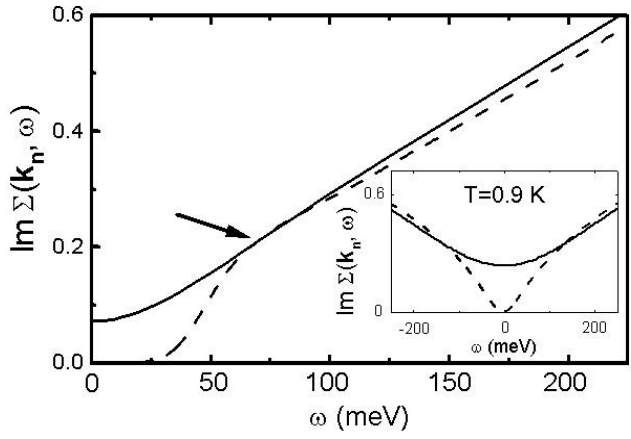

Fig. 3.22. Calculated frequency dependence of the quasiparticle self–energy at the node $\Sigma(\mathbf{k}_n, \omega)$, $\mathbf{k}_n = (0.4, 0.4)\pi$. The *solid curves* correspond to the normal state at $T = 2T_c$, whereas the *dashed curves* refer to the superconducting state at $T = 0.5T_c$. At $\mathbf{k} = \mathbf{k}_n$, where the superconducting gap vanishes, one clearly sees approximately at $\hbar\omega = 65$ meV a crossover from Fermi liquid behavior ($\Sigma \propto \omega^2$) to a non–Fermi liquid behavior ($\Sigma \propto \omega$) for low–energy frequencies as a function of temperature. We show in the *inset* the behavior of $\Sigma(\mathbf{k}_n, \omega)$ calculated at very low temperature $T = 0.003t \simeq 0.9$K (*dashed line*).

hand, the spectral weight of $\mathrm{Im}\,\chi(\mathbf{Q}, \omega)$ decreases drastically with overdoping. Therefore, the coupling of the quasiparticles to spin fluctuations becomes much weaker in the OD case. These two competing effects seem to be responsible for the nonmonotonic weak doping dependence of the kink position in the nodal direction [114].

It is remarkable that for electron–doped superconductors with a different dispersion ϵ_k [115], in particular with a flat band lying 300 meV below ϵ_F at $(\pi, 0)$, we obtain no kink feature up to frequencies of about 100 meV. This is also in agreement with experiment [112]. The reason behind this is that $\mathrm{Im}\,\chi(\mathbf{q}, \omega)$ has a peak at larger frequencies which is much less pronounced than for hole–doped cuprates [116].

Results for the One–Particle Self–Energy: Fermi Liquid Versus Non–Fermi liquid behavior

There is a broad discussion about whether or not layered cuprate superconductors behave like conventional Fermi liquids. Early experiments (for a review, see [88]) revealed non–Fermi liquid properties, in particular a linear resistivity $\rho(T)$ for optimal doping, poorly defined quasiparticle peaks above the superconducting transition temperature T_c seen in ARPES [117], and a strong temperature dependence of the uniform spin susceptibility observed by NMR [118]. The phenomenological concepts of a marginal–Fermi

liquid (MFL) and a nested–Fermi liquid (NFL) have been introduced in order to explain the deviations in the normal state from Fermi liquid theory [119, 120]. Our results shed more light on this question. In agreement with the picture of Ruvalds and coworkers, we obtain the ω and T dependence of the self–energy, which is mainly due to scattering of the quasiparticles by spin fluctuations, this is strongest for a nested Fermi topology. This also provides a microscopic justification for the MFL approach[10]. Thus, for optimal doping ($x = 0.15$), the microscopic FLEX approximation includes the phenomenological concepts of both the NFL and the MFL [35].

In order to investigate the effect of the self–energy $\Sigma(\mathbf{k}, \omega)$ on the dispersion $\omega(\mathbf{k}, T)$, we show in Fig. 3.22 the results of our calculations of $\mathrm{Im}\,\Sigma(\mathbf{k}_n, \omega)$ for a wave vector along the node line of the superconducting order parameter in the first BZ. The transition from $\Sigma(\mathbf{k}, \omega) \propto \omega^2$ to $\Sigma(\mathbf{k}, \omega) \propto \omega$ for low–lying frequencies is shown for various temperatures. Note that the deviation from Landau's theory (see solid curve in Fig. 3.22), $\mathrm{Im}\,\Sigma \sim \omega$, results from the strong scattering of the quasiparticles by the spin fluctuations in our picture and is expected to disappear at temperatures $\mathrm{T} \rightarrow 0$, see inset of Fig. 3.22. In particular, the changes in the velocity of the quasiparticles with frequency are determined in energy distribution curves (EDC) by $v_F^* = v_F/(1 + d\Sigma_k'(\omega)/d\omega)$. At frequencies around 65 meV, $\mathrm{Re}\,\Sigma_k(\omega)$ shows a flattening, as can be seen via a Kramers–Kronig analysis of $\mathrm{Im}\,\Sigma$. Therefore, at this frequency, the effect of the scattering by spin fluctuations almost disappears. Thus, we find Fermi liquid behavior. In our microscopic theory we also recover Fermi liquid behavior for $T \sim \omega \ll \omega_{sf}$. Here, ω_{sf} is the characteristic spin fluctuation energy measured in INS (roughly the peak position of $\mathrm{Im}\,\chi(\mathbf{Q}, \omega)$ [116]) and is typically around 25 meV for hole–doped superconductors [121]. We have shown previously that our ω_{sf} gives a good description of INS data [76]. On the other hand, for $T < T_c$, the scattering is also strongly reduced, owing not only to $\omega < \omega_{sf}$ but also to a feedback effect of superconductivity.

In Fig. 3.23, we demonstrate the feedback of superconductivity on $\Sigma(\mathbf{k}, \omega)$. We expect that it is strongest for $\mathbf{k} \approx (\pi, 0.1\pi)$, where the gap $\Delta(\omega)$ is maximal. One can see that the superconducting properties demonstrated, $\Delta(\mathbf{k}, \omega)$ and in particular in $\mathrm{Im}\,\Delta(\mathbf{k}, \omega)$, are the main factor that induces changes in the self–energy. For a comparison with experiment, we also present our results for the superconducting gap. Note that this behavior of $\Sigma(\mathbf{k}, \omega)$ and $\Delta(\mathbf{k}, \omega)$ is also related to INS and optical–conductivity experiments. In particular, the peak position of $\mathrm{Im}\,\Sigma(\mathbf{k}_a, \omega)$ is approximately at $3\Delta_0 - \omega_{sf} \approx \omega_{res} + \Delta_0$ (ω_{res} denotes the resonant frequency observed in INS), according to our previous analysis [76]. This is in a good agreement with results obtained within

[10] Note that although the results of our microscopic calculations agree with MFL theory, we have not proved the existence of a quantum critical point suggested there.

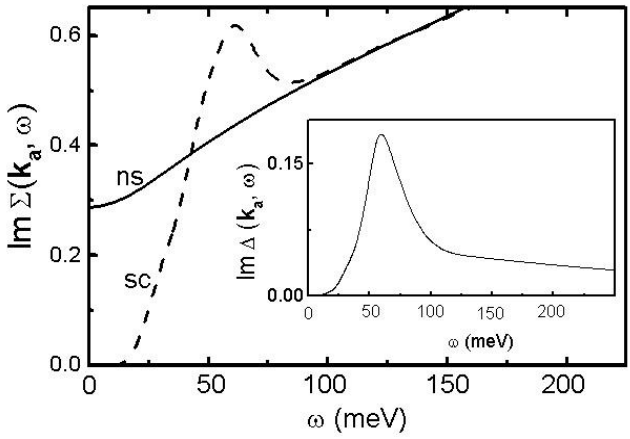

Fig. 3.23. Calculated frequency dependence of the quasiparticle self–energy $\Sigma(\mathbf{k}_a, \omega)$ at the wave vector $\mathbf{k} = \mathbf{k_a} \approx (1, 0.1)\pi$ (antinode). The *solid curves* correspond to the normal state at $T = 2T_c$, whereas the *dashed curves* refers to the superconducting state at $T = 0.5T_c$. This shows $\mathbf{k_a}$ the feedback effect of superconductivity on the self–energy at the wave vector $\mathbf{k}_a$. *Inset*: superconducting gap function $\Delta(\omega)$ at wave vector $\mathbf{k} = \mathbf{k_a}$ versus frequency. Since the behavior of Δ and Σ is controlled by $\mathrm{Im}\,\chi(\mathbf{q}, \omega)$, we are able to connect these results also to the resonance peak observed by INS in cuprates [76].

the framework of the spin–fermion model [122]. It is an important result that $\Delta(\omega)$ also agrees well with tunneling experiments [76].

To summarize this subsection, we have calculated the pronounced momentum and frequency dependence of the quasiparticle self–energy Σ in hole-doped high-T_c cuprates and find that this results in a kink structure in the dispersion $\omega(\mathbf{k})$, which agrees well with recent ARPES experiments. An important result for describing the physics in the cuprates is that the origin of this is the coupling of the quasiparticles to the spin fluctuations. The reason for the kink structure is the strong coupling and inelastic scattering of holes to and by spin fluctuations. At the Fermi level, this is reflected in a change of the ω dependence of the self–energy Σ from non–Fermi liquid to Fermi liquid behavior. Owing to a different spectrum $\mathrm{Im}\,\chi(\mathbf{q}, \omega)$ of the spin fluctuations in electron–doped cuprates, we do not find a kink in the corresponding spectral density. Furthermore, the feedback effects due to superconductivity on the elementary excitations clearly reflect the symmetry of the superconducting order parameter, and the calculated density of states $N(\omega) \equiv A(\omega) = \sum_{\mathbf{k}} A(\mathbf{k}\omega)$ compares well with SIN tunneling data. However, owing to spatial averaging such experiments do not exhibit a kink structure.

3.3 Electronic Raman Scattering in Hole–Doped Cuprates

The use of optical techniques to investigate low–energy excitations in high–T_c superconductors has traditionally been of great importance, not only allowing the study of the superconducting gap directly, but also providing detailed information on the unusual normal and superconducting states in these compounds. One optical probe is polarization–dependent inelastic light (Raman) scattering. Using Raman spectroscopy, not only electronic or magnetic, but also phononic excitations can be investigated. In this regard, the renormalization of phonons due to interaction with the pair–breaking peak is of particular interest. A well–known example is the B_{1g} Raman–active phonon at ≈ 340 cm^{-1} in $R\mathrm{Ba_2Cu_3O_{7-\delta}}$, where R denotes a rare-earth atom such as yttrium [123, 124]. This phonon corresponds to an out–of–plane vibration of the planar oxygen (e.g. [125]). Owing to the coupling of this mode to the low–energy electronic excitations, it has a Fano–type lineshape. The change of the lineshape at low temperatures was identified from the superconducting redistribution of the electronic spectrum and was investigated in detail in [126]. However, in this section, we shall focus on the electronic part of the Raman intensity after all phonons have been subtracted. The remaining signal due purely to electronic Raman scattering (and its polarization dependence) provides important information about the quasiparticle scattering rate $\tau^{-1}(\omega)$ in the normal state and the anisotropy of the gap function $\Delta(\mathbf{k}, \omega)$ in the superconducting state.

Polarization–dependent Raman scattering data below T_c from optimally doped $\mathrm{Bi_2Sr_2CaCu_2O_{8+\delta}}$ (Bi2212) for the polarization channels of A_{1g}, B_{1g}, and B_{2g} symmetry have been analyzed by weak–coupling BCS theory and found to be in agreement with a $d_{x^2-y^2}$ pairing symmetry [127]. In the weak–coupling limit, it has been shown that good agreement with the $A^{x'x'}$ and B_{1g} Raman data from $\mathrm{YBa_2Cu_3O_7}$ (YBCO) can be obtained if vertex corrections due to the pairing interaction and short–range Hubbard–type interactions between the electrons are taken into account [128]. The relationship between the normal-state anomalous Raman spectrum and the optical conductivity of high-T_c superconductors has been discussed in the context of marginal Fermi liquid theory, where it has been noted that a linear variation of the quasiparticle damping with frequency is responsible for these phenomena [119]. This is consistent with the results of the nested–Fermi liquid model, which describes the qualitative features of the optical conductivity and Raman response in the normal state correctly and can be generalized in a simple way to the superconducting state [129]. Strong–coupling calculations with anisotropic Eliashberg equations have been carried out by using a phenomenological anisotropic spin fluctuation interaction in a nearly–antiferromagnetic Fermi liquid theory [130]. These theories are capable of explaining many features of the observed Raman spectra in $\mathrm{La_{2-x}Sr_xCuO_4}$ [131], Bi2212 [132], and YBCO [133]. In the last of these works, it is shown that the Raman response is extremely

sensitive to the details of the band structure and the anisotropy of the spin fluctuation interaction. Comparison of the low–frequency B_{1g} and B_{2g} responses in the normal state could provide an indication of the strength and anisotropy of the interaction. The pair–breaking peak in the B_{1g} response carries information about quasiparticle scattering. However, no microscopic theory exists which is able to describe simultaneously

- the different peak positions in the relevant scattering geometries,
- the particular lineshape of the pair-breaking spectrum,
- the power laws for small Raman shifts, and
- the relative scattering intensities.

In this section, we present results for electronic Raman scattering from hole–doped cuprates and the quasiparticle scattering rate for optimally doped and overdoped cuprates, based on the FLEX approximation for the spin and quasiparticle excitations which solve the generalized Eliashberg equations for the two–dimensional one–band Hubbard model. We find for $T > T_c$ and intermediate coupling strengths a flat background in the Raman intensity; this can be understood in terms of the quasiparticle scattering rate, which turns out to be strongly anisotropic in momentum space but less temperature dependent for large ω. For $\omega > 4T$, a linear behavior of the quasiparticle damping (as suggested within a nested–Fermi liquid picture) is obtained. Below T_c, the feedback effect of the one-particle properties on the spin fluctuation spectrum is taken into account self–consistently and has important consequences in the superconducting state. For example, the quasiparticle damping which varies linearly with frequency in the normal state in accordance with the MFL [119] and NFL [129] theories, is strongly suppressed at lower frequencies in the superconducting state. These properties of the quasiparticle damping determine to a large extent the Raman spectra and also the results of INS, ARPES, tunneling, and optical–conductivity experiments in the normal and superconducting states, as discussed earlier. Thus, below T_c, we find a large pair–breaking peak in the Raman intensity and a gap developing in the B_{1g} spectrum, while the effect of superconductivity on the B_{2g} spectrum is found to be much smaller.

3.3.1 Raman Response and its Relation to the Anisotropy and Temperature Dependence of the Scattering Rate

First we present our results for the Raman response function given in (2.141) in the absence of vertex corrections to the bare Raman vertices in (2.142) ($J = 0$ in (2.154)). For this purpose, we have solved the generalized Eliashberg equations within the FLEX approximation for the 2D tight–binding band mentioned above with $B = 0.45$ and $\mu = -1.1$. This describes approximately the Fermi surfaces of the Bi2212 and YBCO compounds. Furthermore, we have taken an effective Coulomb repulsion $U(\mathbf{q})$ which has a maximum value $U = 3.6$ at $\mathbf{q} = \mathbf{Q}$ and decreases monotonically with decreasing $\mathbf{q}$ to a

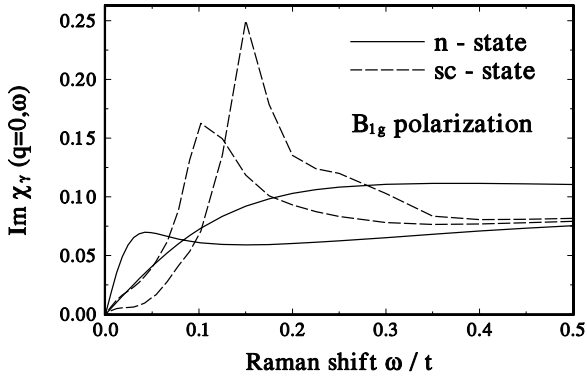

Fig. 3.24. Raman spectra $\mathrm{Im}\,\chi_\gamma(\mathbf{q}=0,\omega)$ for B_{1g} polarization in the normal state at $T = 0.1t$ and $0.023t$ (*solid lines* with increasing slopes), and in the superconducting state ($T_c = 0.022t$) at $T = 0.021t$ and $0.017t$, or $T/T_c = 0.77$ (*dashed lines* with increasing peaks).

value $U(0) = 0.62$ at $\mathbf{q} = 0$. This functional form provides good agreement with INS data and also approximates the calculated vertex corrections to the spin susceptibility χ_{s0}. With these parameters, we obtain a superconducting transition at $T_c = 0.022t$. We remark that the vertex corrections for the irreducible spin susceptibility $\chi_{s0}(\mathbf{q},\omega)$ are similar to those in (2.155) apart from an opposite sign and the dependence on $\mathbf{q}$. It turns out that the frequency and temperature dependences are rather weak and that the dispersion with respect to $\mathbf{q}$ around $\mathbf{Q}$ can be well approximated by the phenomenological spin–spin coupling which has been used to describe the NMR data for YBCO compounds [130].

One can see from Figs. 3.24 and 3.25, for B_{1g} and B_{2g} symmetry, respectively, that in the normal state (solid curves) both spectra start linearly in the frequency ω and become flat at high frequencies. The slope at $\omega = 0$ increases with decreasing temperature T, while the spectrum at high frequencies decreases with decreasing T. In the B_{2g} spectrum, a low–frequency peak develops with decreasing T. These results are similar to normal–state results obtained from the theory of nearly antiferromagnetic Fermi liquids in the $z = 1$ pseudo-scaling and $z = 2$ mean–field–scaling regimes [132]. The experimental data available at present do not show a peak in the normal–state B_{2g} response. It has been pointed out that observation of this structure in the B_{2g} response and its absence in the B_{1g} response would lend support to the current models of the Fermi topology and of the strength and anisotropy of the interaction [133].

In Fig. 3.24, for the B_{1g} response, we recognize that a gap at lower ω and a pair-breaking peak at a threshold energy of $\omega = 0.15t \simeq (3/2)\Delta_0$ develop as T decreases below T_c (dashed curves). Here, Δ_0 is the amplitude of the

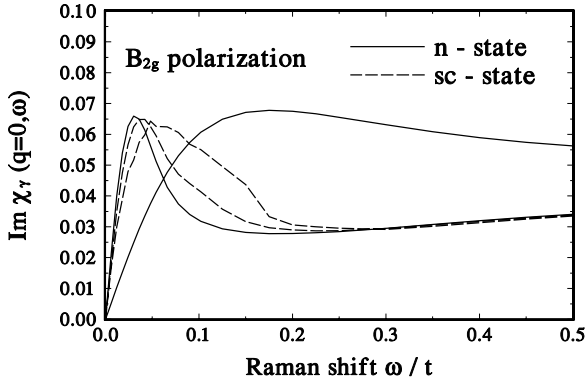

Fig. 3.25. Raman response function for the B_{2g} channel for the same temperatures as in Fig. 3.24. In the superconducting state, the slope at $\omega = 0$ decreases with decreasing T.

$d_{x^2-y^2}$–wave gap, which can be estimated from the binding energy at the midpoint of the leading edge in the calculated photoemission spectrum near the antinode of the gap [134]. This gap amplitude Δ_0 rises much more rapidly below T_c than does the BCS d–wave gap and reaches a value of about $\Delta_0 = 0.1t$ at our lowest temperature $T = 0.017t$ ($T/T_c = 0.77$). Comparison with the weak-coupling theory shows that the singularity at the pair–breaking threshold [127] is removed here by strong quasiparticle damping, while according to the weak–coupling theory of [76] this singularity is removed by a screening term arising from vertex corrections due to the pairing interaction. Electron–electron scattering due to short–range Coulomb interaction can describe the observed broadening above the pair–breaking peak in the B_{1g} Raman spectrum of YBCO [76]. Our results for the B_{1g} response in the superconducting state (see Fig. 3.24) agree qualitatively with the results of non–self–consistent calculations which include the effect of inelastic scattering [133].

The Raman response function for B_{2g} symmetry shown in Fig. 3.25 does not exhibit such dramatic effects below T_c as those for B_{1g} symmetry shown in Fig. 3.24. One notices that the spectrum is linear in ω for small ω, and that the slope at $\omega = 0$ decreases and the normal–state peak broadens and shifts to somewhat higher frequency as T decreases below T_c (dashed curves in Fig. 3.25). The spectrum above this peak is somewhat enhanced up to frequencies near the pair-breaking threshold. In contrast to our results shown in Fig. 3.25, the non–self–consistent calculation yields a distinct pair–breaking peak below T_c in the B_{2g} response which occurs much closer to the B_{1g} pair–breaking peak [133]. We do not show the calculated Raman spectrum for A_{1g} symmetry because it is quite similar to that for the B_{1g} symmetry. In order to obtain the measured $A^{x'x'}$ spectrum, we have to add the B_{2g} spectrum to the A_{1g} spectrum. The resulting $A^{x'x'}$ response starts linearly in ω because,

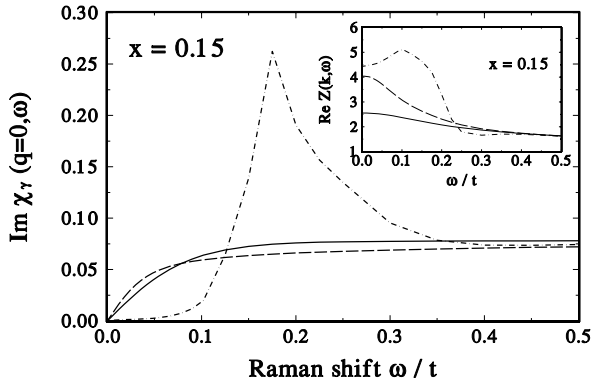

Fig. 3.26. Results for optimum doping concentration ($x = 0.15$): Raman scattering intensity $I \propto \mathrm{Im}\,\chi_\gamma(\mathbf{q} = 0, \omega)$ for $\gamma = t[\cos k_x - \cos k_y]$ (B_{1g} polarization) as a function of the transferred energy ω/t. The *solid curve* corresponds to $T \approx 2T_c$ and the *dashed curve* corresponds to $T \approx 1.05T_c$. For comparison, the result for the superconducting state ($T \approx 0.75T_c$, *dash–dotted curve*) is also displayed. *Inset*: effective–mass ratio $\mathrm{Re}\,Z(\mathbf{k}, \omega)$ for $\mathbf{k} = \mathbf{k}_a = (0.15, 1)\pi$ as a function of ω/t.

at low frequencies, it is dominated by the B_{2g} spectrum up to a shoulder corresponding to the small peak in the B_{2g} spectrum. At higher frequencies, the $A^{x'x'}$ spectrum is dominated by the A_{1g} component, which exhibits a the large pair–breaking peak.

We come now to the discussion of the effect of vertex corrections on the Raman response functions derived in Sect. 2.3.3. From (2.154), one sees that the general trend of the vertex correction J is to suppress the response in the B_{1g} channel and to enhance the response in the B_{2g} channel, while we have a mixed effect on the A_{1g} channel because the component of $\gamma_{A_{1g}}$ proportional to t is suppressed and the component proportional to $t' = -Bt$ is enhanced.

In Figs. 3.26 and 3.27a, we use the canonical parameters $U = 4t$ and $t' = 0$ and focus on optimum doping ($x = 0.15$). Below T_c, a pair–breaking peak in the Raman scattering intensity develops. For $T \leq 0.75T_c$, the threshold position $2\Delta_0$ is approximately the peak–to–peak value calculated for the superconducting density of states, which has been discussed in Sect. 3.2.1. For temperatures $T > T_c$, we find a structureless (incoherent) background for large Raman shifts and only a small temperature dependence, which is in good agreement with experiment. Such a behavior is also expected in nested–Fermi liquid theory [120], where $\mathrm{Im}\,\chi \propto \tanh(\omega/4T)$. We indeed find the linear behavior of Γ for $\omega > 4T$ predicted in NFL theory. However, to calculate the scattering rate τ^{-1}, one has to take into account $\mathrm{Re}\,Z$ also (see inset). For example, we can clearly see that $m^*/m = \mathrm{Re}\,Z(\omega = 0)$ depends strongly on temperature.

In Fig. 3.27b, we show our results for Γ and $\mathrm{Re}\,Z$ for the overdoped case $x = 0.22$. Again, the quasiparticle damping Γ is anisotropic. Furthermore,

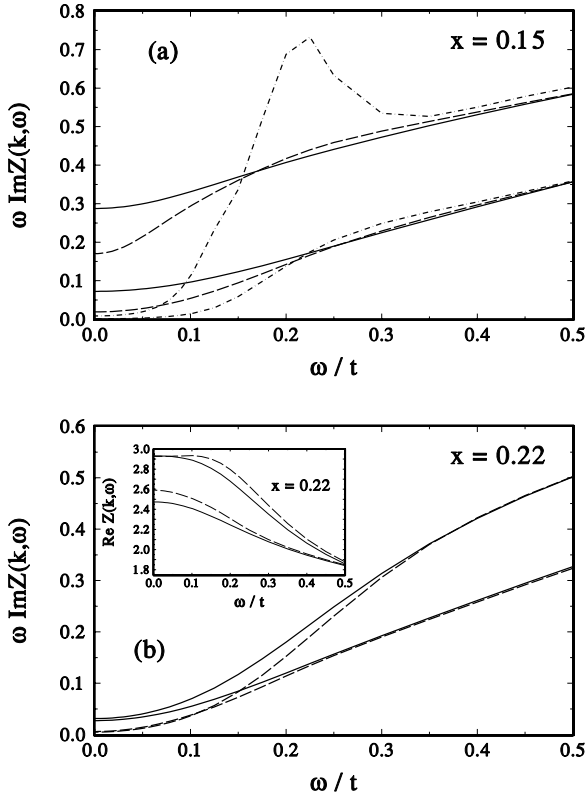

Fig. 3.27. Comparison of the quasiparticle damping $\Gamma = \omega \,\mathrm{Im}\, Z(\mathbf{k}, \omega)$ for (**a**) optimum doping ($x = 0.15$) and (**b**) the overdoped case ($x = 0.22$): we use the same notation as in Fig. 3.26. The *upper curves* correspond again to $\mathbf{k} = \mathbf{k}_a = (0.15, 1)\pi$, whereas the lower curves correspond to $\mathbf{k} = \mathbf{k}_b = 0.41\pi(1, 1)$ on the Fermi line. *Inset*: effective–mass ratio $\mathrm{Re}\, Z(\mathbf{k}, \omega)$ for $x = 0.22$.

we find that the effective–mass ratio and Γ have decreased. Such a behavior is expected far away from the antiferromagnetic phase; this behavior is responsible for the pairing and for the lifetime effects via spin fluctuations. Note that for small ω we do not even find an anisotropy for different $\mathbf{k}$ vectors at the same temperature. From these pictures we can conclude that the scattering rate in optimally and overdoped cuprates is strongly anisotropic. Furthermore, for large frequencies we find a linear behavior in ω, in agreement with NFL theory. This provides a possible explanation for the structureless background in the Raman scattering intensity of high–T_c superconductors in the normal state. Below T_c, a gap opens in the quasiparticle scattering at approximately $\omega = 3\Delta - \omega_{sf}$, where ω_{sf} denotes the spin fluctuation energy (the position of the peak in the Ornstein–Zernicke–type spin susceptibility),

as discussed in Sect. 3.2.1. This leads to the observed pair–breaking Raman peak and thus reflects mainly the density of states in the superconducting state.

Finally, in order to discuss the influence of vertex corrections in the A_{1g} channel (which are more complicated), it is intructive to go back to the weak-coupling limit and (2.156). In Fig. 3.28, we present our results for an expansion of the bare Raman vertex in Fermi surface harmonics (FSH), i.e.

$$\gamma(\mathbf{k}) = \sum_{L,\mu} \gamma_L^{\mu} \Phi_L^{\mu}(\mathbf{k}) \quad , \tag{3.20}$$

and for the integration over the Fermi circle. The unscreened response (i.e. the first term on the right-hand side) in the A_{1g} and B_{1g} scattering geometries diverges logarithmically at the threshold $\omega = 2\Delta_0$, whereas the B_{2g} scattering intensity is small. The screening term in the B_{1g} channel cancels the divergence without changing its position. A similar situation is realized for the A_{1g} polarization, where a cusp remains at the threshold energy $\omega = 2\Delta_0$. However, existence of the same threshold energy for the A_{1g} and B_{1g} scattering geometries is in clear contradiction to experiment. Therefore, one might introduce higher harmonics in the expansion,

$$\gamma_k^{A_{1g}} = \gamma_0 + \gamma_{A_{1g}} \left[\cos(4\phi) + \alpha \cos(8\phi)\right] \quad . \tag{3.21}$$

This leads to the results presented in the inset of Fig. 3.28, where only the A_{1g} response is shown ($\gamma_0 = 0$). Although the low–frequency Raman response remains less affected, one can clearly see that the peak position is extremely sensitive to the admixture of higher harmonics. Because neither the expansion coefficients nor the convergence behavior of such an expansion is known, we may safely conclude that this approach is an unsatisfactory way to obtain a detailed description of the Raman response in the A_{1g} polarization. The problem concerning the position of the A_{1g} pair–breaking peak also remains in the effective–mass approximation, which has the advantage that no additional parameters are introduced. It has been shown in [35] that the effective mass approximation depends strongly on the details of the tight–binding band structure used in the calculation. Recently, several groups have shown that if magnon states at higher energies are taken into account, the peak position in the A_{1g} polarization becomes more stable and resonable agreement with experiment can be achieved.

To briefly summarize this section, we have calculated the electronic Raman response function within the framework of the generalized Eliashberg equations using the 2D Hubbard model. The FLEX approximation is capable of describing the most important properties of the high–T_c cuprates, namely, their unusual normal–state behavior arising from strong electronic correlations, and the unconventional superconducting state, which is widely believed to have $d_{x^2-y^2}$ wave pairing. These properties are reflected in the

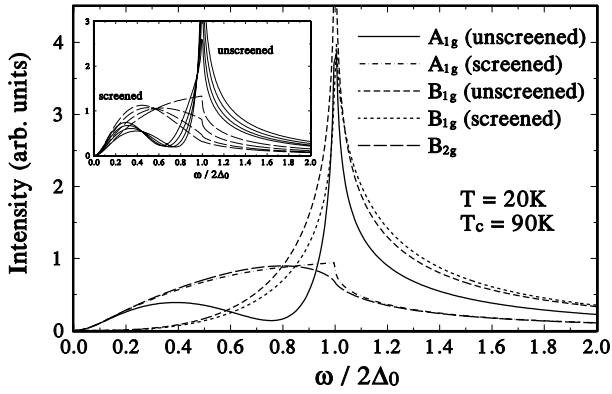

Fig. 3.28. Raman scattering intensity versus Raman shift for a clean superconductor with a d–wave gap $\Delta(\phi) = \Delta_0 \cos(2\phi)$ calculated using an expansion in FSHs. The unscreened A_{1g} (*solid line*) and B_{1g} (*medium–dashed line*) responses diverge logarithmically at the threshold energy $\omega = 2\Delta_0$. The screened B_{1g} intensity (*short–dashed line*) and the B_{2g} channel (*long–dashed line*) have approximately the same (small) scattering intensity; for A_{1g} a cusp at the threshold energy remains. *Inset*: unscreened (*solid lines*) and screened (*dashed lines*) A_{1g} Raman response due to the admixture of higher harmonics $\alpha = 0$, -0.15, -0.30, and -0.45 (peak positions of the screened response from *right* to *left* in this sequence). For $\alpha \geq 0$, no screening occurs.

calculated Raman response functions for the A_{1g} or $A^{x'x'}$, B_{1g}, and B_{2g} polarizations. In the normal state these spectra start linearly in the frequency ω with a slope that increases with decreasing temperature T, and at high frequencies these spectra become almost constant. The latter property is a consequence of the linear frequency variation of the quasiparticle damping. In the superconducting state one obtains a gap and a pair–breaking peak in the B_{1g} channel because this polarization probes the region in momentum space around the antinode of the gap. The effect of superconductivity on the B_{2g} spectrum is much smaller, which is not surprising, because the B_{2g} channel probes the region around the node of the gap. Thus our results for the Raman spectra agree qualitatively with experiments on optimally doped cuprates.

3.4 Collective Modes in Hole–Doped Cuprates

In general, the internal structure of a Cooper pair can be investigated through its dynamics, i.e. the ω (and $\mathbf{k}$) dependence of the condensate. In particular, in unconventional superconductors, where at least one an additional symmetry is broken, many low–frequency collective modes are present. For example, a wide variety of collective modes has been observed in the three phases of

superfluid ^{3}He [135]. These fluctuations of the spin–triplet p–wave gap have been calculated from coupled Bethe–Salpeter equations for the T–matrices in the particle–particle and particle-hole channels [136, 137]. This method has also been used to investigate the collective modes in hypothetical p–wave pairing superconductors such as heavy fermion superconductors [138]. A detailed study of the collective modes in 3D d–wave superconductors, including different order parameter symmetries, has been made in [139]. Recently, pair fluctuations and the associated Raman scattering intensity have been calculated for a two–dimensional d–wave weak–coupling superconductor [140].

In this section, the role of collective modes in various experiments on hole–doped cuprates is investigated. We again show results for neutron scattering, photoemission (ARPES), and Raman scattering intensities below T_c obtained from the generalized Eliashberg equations using the two–dimensional Hubbard model and describe them in a unified picture. Previous work on collective modes in high–T_c superconductors [140, 141, 142, 143, 144] has been restricted to weak–coupling and mean–field calculations. As described in Chap. 2, the FLEX approach what we have used here is a self–consistent and conserving approximation scheme, which goes well beyond the mean–field approximation. As discussed in connection with the resonance peak (Sect. 3.2.1), the feedback effect of the one-particle properties on the collective modes in the superconducting state is included self–consistently and thus the importance of the quasiparticle damping becomes clear. To be more precise, we shall show that the large peak in the dynamical spin susceptibility (i.e. the resonance peak) can also be interpreted as being due to the occurrence of a weakly damped spin–density–wave collective mode. This gives rise to a dip between the sharp low–energy peak and the higher–binding–energy hump in the ARPES spectrum. Furthermore, we demonstrate that the collective mode of the amplitude fluctuations of the d–wave gap yields a broad peak above the pair–breaking threshold in the B_{1g} Raman spectrum.

3.4.1 A Reinvestigation of Inelastic Neutron Scattering

In order to discuss the occurrence of a spin–density–wave collective mode in inelastic neutron scattering experiments, we have investigated first the imaginary part of the dynamical spin susceptibility. Below T_c, large peaks evolve in the spectral density $\mathrm{Im}\,\chi_s(\mathbf{q},\omega)$, i.e. four distinct peaks at wave vectors $\mathbf{q}$ near $\mathbf{Q}=(\pi,\pi)$ for next-nearest neighbor hopping $t'=0$ [145], and a broad peak centered at $\mathbf{Q}$ for $t'=-0.45t$ (t is the nearest–neighbor hopping energy) [146]. As discussed earlier, these results are in qualitative agreement with neutron scattering experiments on $La_{2-x}Sr_xCuO_4$ and $YBa_2Cu_3O_{7-\delta}$ [147]. Similar results have been obtained within the t–J model [148].

In Fig. 3.29, we again show the resonating behavior of $\mathrm{Im}\,\chi_s(\mathbf{Q},\omega)$ for $U=3.6t$ and $t'=-0.45t$ this time in the underdoped regime ($x=0.10$). One can see that a large peak evolves at about $\omega_0=0.08t$ as T decreases below $T_c=0.022t$. The amplitude Δ_0 of the $d_{x^2-y^2}$-wave gap rises

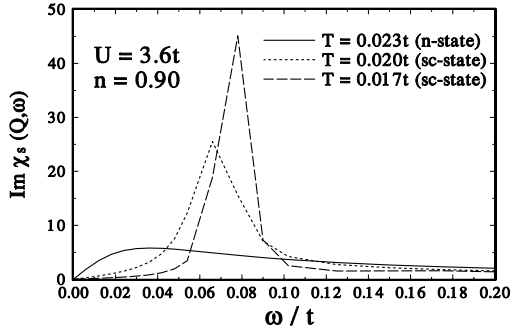

Fig. 3.29. Spectral density of the spin susceptibility in the underdoped regime at wave vector $\mathbf{Q} = (\pi, \pi)$, $\mathrm{Im}\,\chi_s(\mathbf{Q}, \omega)$, for temperatures $T = 0.023t$, $0.020t$, and $0.017t$ ($T_c = 0.022t$). Here, $U = 3.6t$ is the on-site Coulomb repulsion, t the near–neighbor hopping energy, $t' = -0.45t$ the next-nearest neighbor hopping, and $n = 0.90$ the renormalized band filling. The resonance peak for optimum doping is shown in Fig. 3.12.

much more rapidly below T_c than does the BCS d–wave gap and reaches, at our lowest temperature $T = 0.017t$ ($T/T_c = 0.77$), a value of about $\Delta_0 = 0.1t$. We find that the resonance peak seen in INS which is calculated in Fig. 3.29 might be interpreted as being due to a slightly damped collective mode because the susceptibilty has a pole at ω_0, more exactly, it fulfills the resonance condition $\mathrm{Re}\,\chi_{s0}(\mathbf{Q}, \omega_0) - U^{-1} = 0$ (see (3.5)), and the height of the peak is of the order of the quasiparticle lifetime $1/\Gamma(\omega_0)$. Here, $\Gamma(\mathbf{k}, \omega) = \omega\,\mathrm{Im}\,Z(\mathbf{k}, \omega)/\mathrm{Re}\,Z(\mathbf{k}, \omega)$ is the quasiparticle scattering rate. Since this is decisive for the observability of the collective modes in the cuprates, we show in Fig. 3.30 the quasiparticle scattering $\omega\,\mathrm{Im}\,Z(\mathbf{k}, \omega)$ and the mass renormalization $\mathrm{Re}\,Z(\mathbf{k}, \omega)$ at the antinode $\mathbf{k}_a$ and at the node $\mathbf{k}_b$ of the gap on the Fermi line for the same parameters as in Fig. 3.29. One can see from Fig. 3.30 that for T below T_c, the scattering rate decreases strongly for frequencies ω below the pair–breaking threshold $3\Delta_0 - \omega_{sf} \simeq 0.2t$. This has also been discussed in Sect. 3.2.1.

In order to understand somewhat better the origin of this spin–density–wave collective mode, we have calculated $\chi_{s0}(\mathbf{Q}, \omega)$ in the weak–coupling limit. The sums over Matsubara frequencies were carried out with the help of methods developed for superfluid ^{3}He [137]. The results have already been given in (3.6) and (2.161)–(2.168). In this weak–coupling approach, the peak of $\mathrm{Re}\,\chi_{s0}$ as a function of ω occurs approximately at $\omega \simeq 2\Delta_0$. This result has been checked by carrying out numerically the sum over $\mathbf{k}$ in (2.160) for $t' = -0.45t$ and for different amplitudes Δ_0 and chemical potentials μ. In fact, we find that the function $\mathrm{Re}\,\chi_{s0}(\mathbf{Q}, \omega)$ exhibits a peak at about $\omega \simeq 2\Delta_0$ whose height decreases as μ increases, for example from -1.3 (unrenomalized band filling $n_0 = 0.84$) to -0.8 ($n_0 = 1.03$). A solution $\omega_0 < 2\Delta_0$ of the

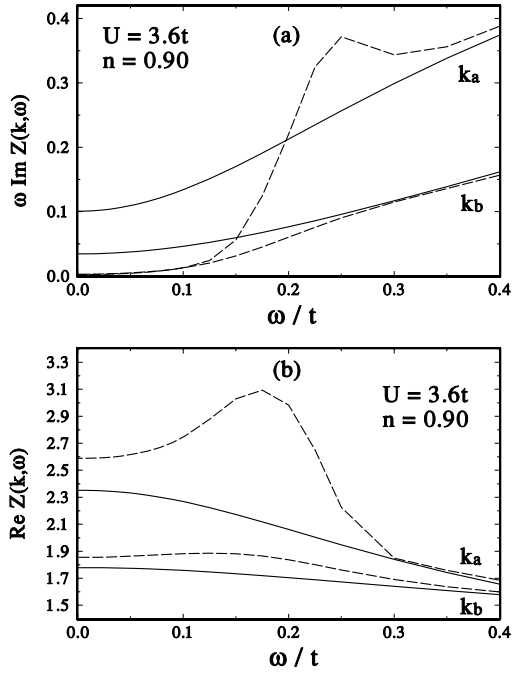

Fig. 3.30. Quasiparticle scattering rate $\Gamma(\mathbf{k},\omega) = \omega\,\mathrm{Im}\,Z(\mathbf{k},\omega)/\mathrm{Re}\,Z(\mathbf{k},\omega)$ at the antinode $\mathbf{k}_a$ and node $\mathbf{k}_b$ of the d–wave gap, in the normal state at $T = 0.023t$ (*solid lines*), and in the superconducting state at $T = 0.017t$ ($T/T_c = 0.77$) (*dashed lines*). (**a**) $\omega\,\mathrm{Im}\,Z(\mathbf{k},\omega)$; (**b**) mass enhancement $\mathrm{Re}\,Z(\mathbf{k},\omega)$.

equation $\mathrm{Re}\,\chi_{s0}(\mathbf{Q},\omega_0) = 1/U$ exists only for a small range of U values near $U \simeq 3t$–$4t$. The strong–coupling FLEX calculation yields a smaller resonance energy. Another difference in comparison with the weak–coupling result is the fact that the self-consistent strong-coupling calculations yield a collective mode for much higher values of U, for example $U = 6.8t$ in [146]. This shows how important it is to take into account the feedback effect of the self–energy on the dynamical spin susceptibility χ_s. These strong renormalization effects might also be responsible for the observed broadening and decrease of the resonance frequency ω_{res} of the neutron scattering peak in underdoped $YBa_2Cu_3O_{6+x}$, which has been observed to be proportional to the decrease of T_c or to the doping level [67]. In fact, in our calculation for decreasing doping $x = n - 1$ or increasing chemical potential μ, the position and height of the function $\mathrm{Re}\,\chi_{s0}(\mathbf{Q},\omega)$ decrease, which means that the position of the peak of $\mathrm{Im}\,\chi_s$ is decreased and its width is increased.

3.4.2 Explanation of the "Dip–Hump" Feature in ARPES

We show now that the spin–density–wave collective mode has a large effect on the angle–resolved photoemission intensity below T_c. In Fig. 3.31a, we have plotted our results for $N(\mathbf{k},\omega)f(\omega)$ (where $N(\mathbf{k},\omega)$ is the quasiparticle spectral function and $f(\omega)$ is the Fermi function) for several $\mathbf{k}$–vectors ranging from $\mathbf{k} = (\pi,0)$, $(7\pi/8,0)$, $(13\pi/16,0)$, ... , down to $(0,0)$. The parameter values are the same as in Figs. 3.29 and 3.30. For $\mathbf{k}$–vectors near $(\pi,0)$, we have a sharp low–energy peak followed by a dip and then a hump at higher energy. As $\mathbf{k}$ moves from $(\pi,0)$ to $(0,0)$, the sharp peak at first remains at about the same position, while the broad hump moves to higher binding energy. In Fig. 3.31b, we show the corresponding normal state spectra at $T = 0.023t$. One notices that the broad hump at higher binding energy remains at the same position when the normal state is entered, while the sharp peak and the dip feature disappear. In the superconducting state, we do not find the dip feature along the nodal direction of the d–wave order parameter. These results are in qualitative agreement with the photoemission spectra from $Bi_2Sr_2CaCu_3O_{8+\delta}$ (Bi 2212) of [149]. In that paper it was argued that the dip in the spectrum stems from a step–like edge in the quasiparticle scattering rate, which arises from interaction with a collective mode. This scenario is confirmed by our results for the collective mode shown in Fig. 3.29 and by the scattering rate shown in Fig. 3.30. We estimate, from the edge of the peak in Fig. 3.31, a gap amplitude $\Delta_0 \simeq 0.1t$ at $T/T_c = 0.77$ and a spectral dip at a binding energy of about $2.3\Delta_0$ corresponding to a mode frequency $\omega_0 \simeq 1.3\Delta_0$ according to the estimates of [149]. However, here we have a discrepancy with regard to the latter estimates because our mode frequency shown in Fig. 3.29 is much lower, i.e. $\omega_0 \simeq 0.8\Delta_0$. We note that we obtain also a dip in the density of states $N(\omega)$ below the gap peak at negative ω values, which agrees qualitatively with STM measurements on Bi 2212 [10].

It should be mentioned that higher–order peaks in the photoemission spectra due to the collective mode, as have been observed for example in solid hydrogen [150], are not visible here. This is due to the fact that in our case the spin–density–wave collective mode is a damped mode and the high quasi-particle damping rate washes out higher– order peaks. In addition, the self-energy contains an average over momentum, further reducing this effect. This is documented by the fact that the normal–state spectrum in Fig. 3.31b, where there is no collective mode present, is not much different from the spectrum in the superconducting state in Fig. 3.31a at higher binding energies.

In short, we can say that the idea of the occurrence of a spin–density–wave collective mode below T_c gives rise to large effects in the magnetic–neutron–scattering and photoemission intensities and the tunneling density of states which are in agreement with experiment. In order to explain the physical basis of our strong–coupling results, we have presented analytical expressions derived from weak–coupling theory in Sect. 2.3.3 (2.161)–(2.168). This also

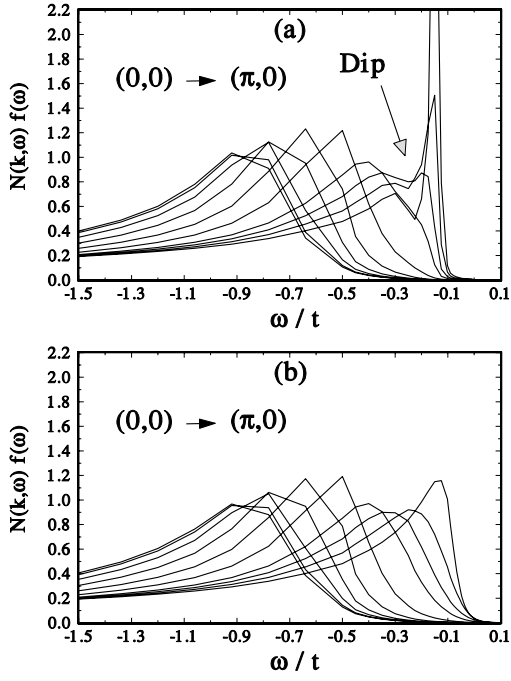

Fig. 3.31. Photoemission intensity $N(\mathbf{k},\omega)f(\omega)$ (here N is the quasiparticle spectral function and f the Fermi function) for $\mathbf{k} = (k\pi, 0)$, where $k = 1$, 7/8, 13/16, 3/4, 5/8, 1/2, 3/8, 1/4, 1/8, and 0. (**a**) in the superconducting state at $T/T_c = 0.77$. The narrow peaks at low binding energy decrease and vanish, and the binding energies of the broad humps increase in the sequence of k values. (**b**) In the normal state at $T = 0.023t$. Note that the broad humps are at the same positions as in the superconducting state.

shows that the gap in the scattering rate and the strong mass enhancement of the quasiparticles below T_c are decisive for the observability of this mode.

3.4.3 Collective Modes in Electronic Raman Scattering?

One can see from Fig. 3.30 that the resonance condition is approximately satisfied for $\omega_0 = 2\Delta_0 \simeq 0.2t$ because then one enters the pair–breaking continuum, where $\Gamma \sim \omega/2$ near the antinode $\mathbf{k}_a$. Thus the mode frequency is about $\omega_0 = 2\Delta_0$ for a damping $\Gamma = \Delta_0$, in agreement with the numerical results. In the weak–coupling limit, it has been shown that vertex corrections due to the d–wave pairing interaction together with electron–electron scattering lead to good agreement with the B_{1g} Raman data on YBCO [151]. In Fig. 3.32, we show our strong-coupling results for the Raman response functions $\mathrm{Im}\,\chi_\gamma(\mathbf{q} = 0, \omega)$, where γ is the vertex $\gamma = t[\cos(k_x) - \cos(k_y)]$ and the vertex $\gamma = -4t' \sin(k_x)\sin(k_y)$ for B_{1g} and B_{2g} symmetry, respectively. One

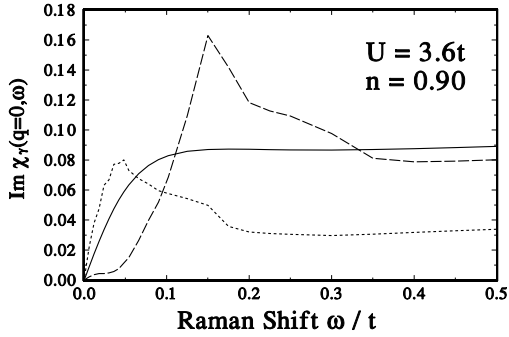

Fig. 3.32. Raman spectra $\mathrm{Im}\,\chi_\gamma(\mathbf{q}=0,\omega)$ for B_{1g} symmetry at $T=0.023t$ (*solid line*) and $T/T_c=0.77$ (*dashed line*), and Raman spectrum for B_{2g} symmetry at $T/T_c=0.77$ (*dotted line*). $T_c=0.022t$.

can see that for B_{1g} symmetry a gap and a pair–breaking threshold develop below T_c, with a threshold at about $0.15t \simeq (3/2)\Delta_0$ at $T/T_c=0.77$ (see Fig. 3.31). Unfortunately, this means that the peak of the order parameter collective mode at $\omega_0 \simeq 2\Delta_0$ with a width Δ_0 lies in the pair-breaking continuum. The question arises of whether or not the contribution of $\mathrm{Im}\,\chi_{fl}$ to the B_{1g} Raman spectrum is sizable, because the coupling strength proportional to N_F'/N_F in (2.164) arising from particle–hole asymmetry is rather small. However, in the strong–coupling calculation, the coupling strength of this mode to the charge density, given by $T\sum_k \sum_n G(\mathbf{k}, i\omega_{n+m})F(\mathbf{k}, i\omega_n)$, is much larger. The reason is that besides the term proportional to $\epsilon(\mathbf{k})$ yielding N_F'/N_F, one obtains additional terms proportional to the self-energy components $\mathrm{Re}\,\xi(\mathbf{k},\omega)$ and $\mathrm{Im}\,\xi(\mathbf{k},\omega)$ which give relatively large contributions. In addition, one obtains a contribution from the imaginary part of the gap function, i.e. $\mathrm{Im}\,\phi(\mathbf{k},\omega)$.

Thus, the amplitude fluctuation mode of the d–wave gap derived in Sect. 2.3.3 couples only weakly to the charge fluctuations and yields a broad peak above the pair–breaking threshold in the B_{1g} Raman spectrum. This peak may be, at least partially, responsible for the observed broadening above the pair–breaking peak because the coupling strength due to particle–hole asymmetry is enhanced by strong–coupling self-energy effects. As already mentioned above previous work on collective modes in high–T_c superconductors has been restricted to weak-coupling and mean–field calculations. The FLEX approach that we have used here, is a self-consistent and conserving approximation scheme, which goes well beyond the mean–field approximation. The feedback effect of the one-particle properties on the collective modes in the superconducting state is included self–consistently and the importance of the quasiparticle damping becomes clear. It is therefore a highly nontrivial and satisfactory result that the resonance in the spin susceptibility, the step–like edge in the quasiparticle scattering rate, and the dip features in the

ARPES and tunneling spectra can all be understood within one theory in a self-consistent fashion. The self-consistent calculation also yields a larger coupling strength of the d–wave amplitude mode to the charge density and a lower resonance frequency of the s–wave exciton–like mode of the order parameter, which makes it more likely that these modes might be observable in the B_{1g} Raman scattering channel.

3.5 Consequences of a $d_{x^2-y^2}$–Wave Pseudogap in Hole–Doped Cuprates

A few years ago, a normal–state pseudogap was inferred from inelastic neutron scattering (see [152] for a review), nuclear magnetic resonance [118], heat capacity [153], and resistivity [27] data on underdoped $YBa_2Cu_3O_{7-\delta}$ and $YBa_2Cu_4O_8$. Furthermore, angular–resolved photoemission spectroscopy measurements also indicated the presence of a $d_{x^2-y^2}$–wave gap well above T_c in the underdoped regime for many hole–doped cuprates [154]. Now, numerous experiments have established the fact that the underdoped cuprate superconductors exhibit a "pseudogap" behavior in both the spin and the charge degrees of freedom below a characteristic temperature T^*, which can be well above the superconducting transition temperature T_c. This has been discussed also in the Introduction. Furthermore, we have already demonstrated in Fig. 2.4 that the FLEX approach with the generalized Eliashberg equations yields the correct doping dependence $T^*(x)$. However, the magnitude of the pseudogap shown in the inset of Fig. 2.4 is too small compared with experiment. Thus, we have extended our theory as described in detail in Sect. 2.2.

Many interpretations of the pseudogap have been advanced (see, for example the discussion in [155]); however, no consensus has been reached so far as to which of the various microscopic theories is the correct one. It has been shown by Williams et al. [155] that the specific–heat, susceptibility, and NMR data of many underdoped cuprates can be successfully modeled using a phenomenological normal–state pseudogap that has d–wave symmetry and an amplitude which is temperature–independent but increases upon lowering the doping level into the underdoped regime. The strong anisotropy of the pseudogap is also in accordance with ARPES experiments on underdoped $Bi_2Sr_2CaCu_2O_{8-\delta}$ (Bi2212) [154, 156]. This model yields a smooth evolution of the normal–state pseudogap into the superconducting gap, as has been found in STM experiments [10]. Also, measurements of the resistivity, Hall coefficient, and thermoelectric power can be reconciled with this model [27],[157]. In this section we follow this idea using the magnitude of the pseudogap E_g (see (2.67)) as an input into the generalized Eliashberg equations. The corresponding theory is described in Sect. 2.2. In the following we shall demonstrate the consequences of such a $d_{x^2-y^2}$-wave pseudogap for various

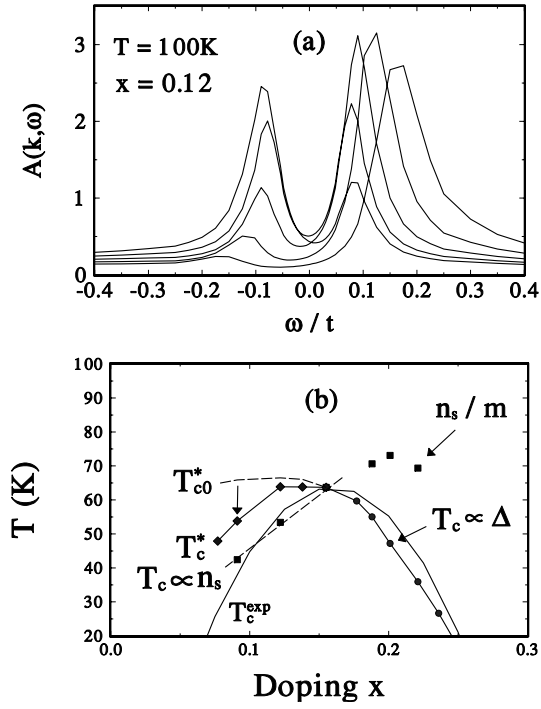

Fig. 3.33. (**a**) Results for the quasiparticle spectral function $A(\mathbf{k}, \omega)$ versus ω for different $\mathbf{k}$-vectors near the gap antinode: $\mathbf{k} = (0.14, 1)$, $(0.16, 1)$, $(0.17, 1)$, $(0.19, 1)$, and $(0.20, 1)$ (in units of π). The Fermi wave vector is $\mathbf{k}_a = (0.18, 1)\pi$. (**b**) Doping dependence of T_c^* and T_c obtained using a dispersion relation $\tilde{\epsilon}(\mathbf{k})$ in accordance with ARPES data. T_c^* is reduced from T_{c0}^* (without pseudogap) to smaller values. For clarity, $T_c^{exp}(x)$ and $n_s(0)/m$ are also displayed. T_{c0}^* refers to a mean–field transition not taking the pseudogap in the tight–binding energy dispersion into account.

physical quantities, calculated self–consistently, of course. However, the origin of the pseudogap is still unknown.

3.5.1 Elementary Excitations and the Phase Diagram

As mentioned in Chap. 2, we obtain the right doping dependence of the (weak–) pseudogap temperature T^*; however, the calculated magnitude of the pseudogap is too small in comparison with experiment. In general, the magnitude of this pseudogap should also influence the mean–field transition temperature T_c^* and thus the temperature range where preformed Cooper pairs are formed, because fewer holes (or electrons) can pair if fewer states at the Fermi level are present. In order to investigate this question in detail, we have performed calculations with an appropriate energy dispersion $\tilde{\epsilon}(\mathbf{k})$ which

exhibits, in accordance with recent photoemission data, d–wave symmetry. Furthermore, we have chosen $\tilde{\epsilon}(\mathbf{k})$ to be doping–dependent in accordance with [16, 17, 155, 158, 159].

In Fig. 3.33a, we present results for the spectral density $A(\mathbf{k},\omega)$ calculated within our FLEX theory in the underdoped regime from the Green's function $G(\mathbf{k},\omega)$ [35]. We have used the Fermi surface observed by Marshall *et al.* [159] and a dispersion $\tilde{\epsilon}(\mathbf{k}) = \sqrt{\epsilon^2(\mathbf{k}) + \Delta^2(\mathbf{k})}$, including for $\mathbf{k} \simeq (\pi, 0)$ the pseudogap structure [35], as an input. The results show the interplay of the pseudogap and superconducting gap and the different features for underdoped and overdoped superconductors, and should be compared with SIN tunneling experiments and with ARPES data [159]. Of course, ARPES can measure only occupied states, i.e. the spectral density for $\omega < 0$. As an example, we show in Fig. 3.33a our calculated spectral function for a doping concentration of $x = 0.12$ at $T = 100$ K, where the magnitude of the pseudogap is $0.1t = 25$ meV. One can see that the spectral function does not cross the Fermi level ($\omega = 0$). This has consequences for the Cooper pairing.

In Fig. 3.33b, we present the corresponding results for the phase diagram and for $T_c^*(x)$ and $T_c(x)$, obtained by using as an input dispersions $\tilde{\epsilon}(\mathbf{k})$ which are, for underdoped cuprates, in accordance with recent angular–dependent photoemission results. As expected, if for $\mathbf{k} \simeq (\pi, 0)$, where pairing is most favorable, we take proper account of the observed pseudogaps [159], we obtain smaller values for T_c^* and T_c and for $(T_c^* - T_c)$ as well (T_{c0}^* is equivalent to T_c^* without a pseudogap in Fig. 2.4). The latter result signals that the pseudogap decreases the reduction of $T_c^* \rightarrow T_c$ due to Cooper pair phase fluctuations [160]. Thus we conclude that even if the reason for the pseudogap forming below T^* is unrelated to superconductivity, it will indeed influence T_c^* and T_c. Both temperatures are renormalized to smaller values owing to a reduced density of states at the Fermi level available for Cooperpairing. Also, the region where preformed pairs occur, $T_c < T < T_c^*$, is reduced.

Now we present results for the dynamical spin susceptibility, the NMR spin–lattice relaxation rate $1/T_1T$, and the Knight shift, obtained by solving the generalized Eliashberg equations with inclusion of the pseudogap using the extended FLEX approximation. We have again assumed that the pseudogap $\phi_c(\mathbf{k})$ has the simple form of a BCS–like d–wave gap, i.e. $\phi_c(\mathbf{k}) \equiv \Delta_c(\mathbf{k}) = E_g\,(\cos k_x - \cos k_y)$, derived in Sect. 2.2.1. Furthermore, we have employed a tight–binding band $\epsilon(\mathbf{k})$ with first– and second–nearest–neighbor hopping ($t' = -0.45t$), an effective on–site repulsion $U(\mathbf{q})$ having a maximum $U = 3.6t$ at $\mathbf{q} = \mathbf{Q}$ (t denotes the nearest–neighbor hopping energy), and a doping concentration $x = 0.09$.

Instead of solving the full set of equations (2.51)–(2.67), we have approximated these equations here by the simpler form which they acquire at the hot spots where the nesting condition $\epsilon_2 = -\epsilon_1$ is satisfied. This seems to be a reasonable approximation because these distinct points on the Fermi line yield the dominant contribution to the right–hand side of (2.51): first, the

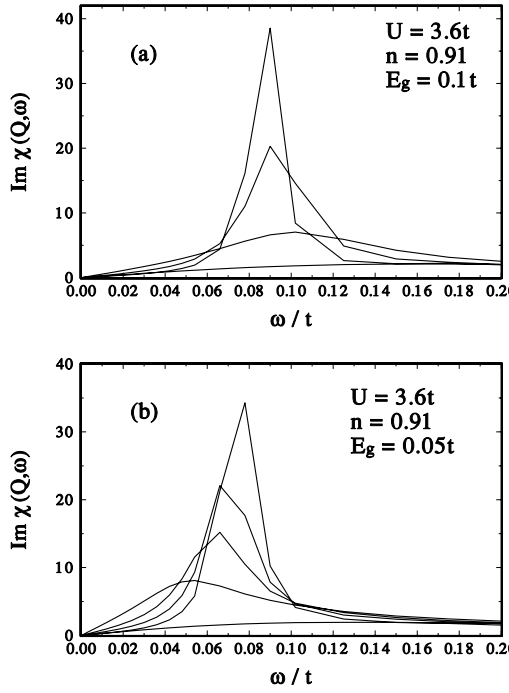

Fig. 3.34. Spectral density of spin susceptibility, $\mathrm{Im}\,\chi_s(\mathbf{Q},\omega)$ (where $\mathbf{Q}=(\pi,\pi)$), versus ω in the underdoped regime. (**a**) The amplitude of the pseudogap taken as $E_g = 0.1t$ and calculated for temperatures $T = 0.1$, 0.04, 0.025, and $0.02t$ (rising peaks in this sequence). (**b**) Comparison with results for $E_g = 0.05t$ and $T = 0.1, 0.025t, 0.021, 0.020$, and $0.019t$, the latter three temperatures corseponding to the superconducting state (rising peaks in this sequence).

denominator of $G_{ij}(k')$ becomes small, and second, the interaction $P_s(k-k')$ for scattering of quasiparticles from one hot spot to the other becomes large because $\mathbf{k}-\mathbf{k}'$ is of the order of $\mathbf{Q}' = (-\pi,\pi)$ (see Fig. 2.8). This treatment of the d–wave pseudogap is somewhat similar to that of the CDW state in the work of Rice and Scott [161], although in our case the hot spots do not exactly coincide with the saddle points at $(0,\pi)$ and $(\pi,0)$ (see Fig. 2.8). Hlubina and Rice [162] have shown that in the case of the resistivity, it is important not to restrict consideration to the hot spots, since a proper average over the whole Fermi surface can lead to different results. However, we would like to point out that we have performed our integrations over the whole Brillouin zone. For the pseudogap channel, we have approximated the Green's functions using the form that they obey at the hot spots. This approximation is different in spirit from considering only the hot spots. All scattering processes due to spin fluctuations at all momentum points are taken into account. In addition, we have made this approximation only in the calculation of the self–energies

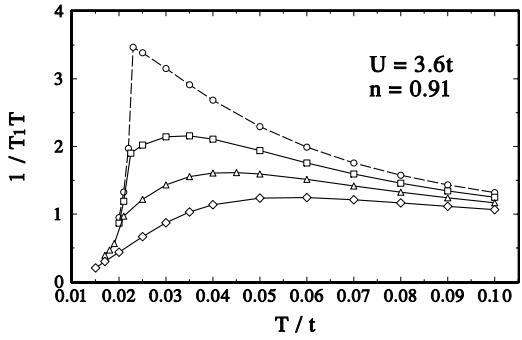

Fig. 3.35. The spin–lattice relaxation rate divided by T, $1/T_1T$, versus T, for amplitudes of the pseudogap $E_g = 0$ (*dashed line*) and $E_g = 0.05$, 0.075 and $0.1t$ (*solid lines* from *top* to *bottom*). The parameters are $J(\mathbf{Q}) = U = 3.6t$ (t is the next–nearest–neighbor hopping energy), and band filling $n = 0.91$ for an YBCO–like band, i.e. a doping concentration of $x = 0.09$. The superconducting transition temperatures are $T_c = 0.023$, 0.022, 0.021, and $0.0155t$ (from *top* to *bottom*).

and used these results for the calculation of the resistivity, which includes a full momentum average.

First, we consider the NMR and neutron scattering intensity in the underdoped regime, which we calculated from the spectral density of the dynamical spin susceptibility, $\mathrm{Im}\,\chi_s(\mathbf{q},\omega)$. This function has a broad peak as a function of $\mathbf{q}$ which is centered at $\mathbf{Q} = (\pi,\pi)$, and it exhibits a peak as a function of ω at the antiparamagnon energy ω_{sf}. The slope of this function at $\omega = 0$ first increases with decreasing T down to a crossover temperature, i.e. the pseudogap temperature T^*, and then it decreases with further decrease of T (see Fig. 3.34). At the same time, the peak at $\omega_s \sim E_g$ narrows and increases with decreasing T. The suppression of spectral weight is accompanied by a peak at higher energies, which resembles the resonance peak below T_c. Indeed, Dai *et al.* have observed a resonance-like peak in the underdoped regime of YBCO in the normal state [69]. However, this peak in $\mathrm{Im}\,\chi(\mathbf{Q},\omega)$ is *not* the resonance peak, since it has properties different from those seen in experiment (see footnote 5 in Sect. 3.2.1). This peak also does not follow from an ω–dependent gap and fulfills no resonance condition. The true resonance peak is a result of the feedback effect of superconductivity, while the peak in the normal state is due to the pseudogap.

In Fig. 3.35, we have plotted the corresponding nuclear spin–lattice relaxation rate divided by T, $1/T_1T$, versus T. One can recognize that this quantity first increases with decreasing T, acquires a maximum at about the crossover temperature T^*, and then decreases rapidly as T tends to T_c. This behavior is plausible in view of the behavior of $\mathrm{Im}\,\chi_s(\mathbf{Q},\omega)$, because $1/T_1T$ is essentially given by the slope of this function at $\omega = 0$. The occurrence of a maximum of $1/T_1T$ is in agreement with the NMR data in the underdoped

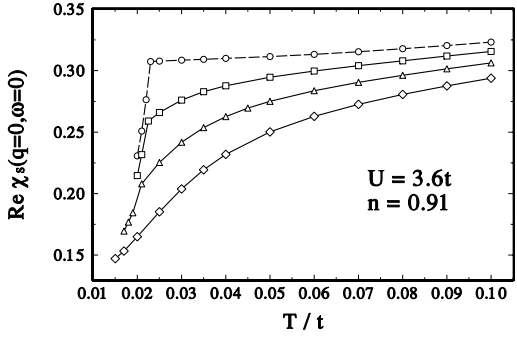

Fig. 3.36. The static, uniform spin susceptibility $\chi_s(\mathbf{q} = 0, \omega = 0)$, which is proportional to the Knight shift, versus T for pseudogap amplitudes $E_g = 0$, 0.05, 0.075, and $0.1t$ (curves in this sequence from *top* to *bottom*). The parameters are the same as in Fig. 3.35.

regime (see [163] for a review, and also [164]). In the overdoped regime of the cuprates, $1/T_1T$ increases monotonically with decreasing T (again, see [163] for a review, and also [164]).

The temperature behavior of $\mathrm{Im}\,\chi_s(\mathbf{Q}, \omega)$ is also in agreement with the temperature dependence of the neutron scattering intensity at a fixed small energy ω. This neutron scattering intensity first increases with decreasing T up to a maximum at about T^* and then decreases [152]. This behavior has been interpreted as a signature of the opening of a spin pseudogap in the spin excitation spectrum [152].

In Fig. 3.35, we also show $1/T_1T$ for three different values of the amplitude E_g of the pseudogap in (2.67): $E_g = 0.1t$, $0.075t$, and $0.05t$. One can recognize that for this sequence of E_g values the position of the maximum at T^* decreases from about $T^* = 0.06t$ to $0.045t$ and then to $0.035t$, and that T_c (where the curve drops downwards) increases from about $T_c = 0.0155$ to 0.0206 and then to 0.0223. For $E_g = 0$, $1/T_1T$ increases monotonically with decreasing T down to $T_{c0} \simeq 0.023t$. The decrease of T_c and the increase of T^* with increasing gap amplitude E_g are in qualitative agreement with the phase diagram of the Knight shift, magnetic susceptibility, and resistivity data in the underdoped regime [12, 165]. Here we assume implicitly that E_g increases as the doping away from half-filling, $x = 1 - n$, decreases.

The static, uniform spin susceptibility is proportional to $\chi_s(\mathbf{q} = 0, \omega = 0) = [1 - J(\mathbf{q} = 0)\chi_0]^{-1}\chi_0(\mathbf{q} = 0, \omega = 0)$. In Fig. 3.36, we have plotted our results for $\chi_s(0, 0)$ versus T for $E_g = 0.1$, 0.075 and $0.05t$, and $E_g = 0$. One can see that χ_s decreases with decreasing T, and that the overall reduction down to T_c increases with increasing gap amplitude E_g in qualitative agreement with the fits of the NMR Knight shift data [165]. Here it should be pointed out that in our strong–coupling calculation, the pseudogap in (2.67) is reduced by $\mathrm{Re}\,Z$ and is smeared out by the quasiparticle damping $\omega \mathrm{Im}\,Z$.

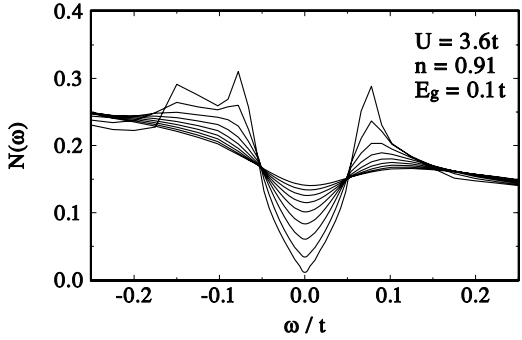

Fig. 3.37. Density of states $N(\omega)$ in the underdoped regime versus ω for $U(\mathbf{Q}) = U = 3.6t$, band filling $n = 0.91$, size of the pseudogap $E_g = 0.1t$, and temperatures $T = 0.1,\ 0.09,\ \ldots\ ,\ 0.02t$ (curves in this sequence from *top* to *bottom*). Only below T_c does the coherence peak develop.

The decrease of $\chi_s(0,0)$, or $\chi_0(0,0)$, for decreasing T is plausible because $\chi_0(0,0)$ is approximately given by the BCS expression

$$\chi_0 = \int_{-\infty}^{\infty} d\omega\, N(\omega)\,[-\partial f(\omega)/\partial\omega] \quad , \tag{3.22}$$

where the density of states $N(\omega)$ is shown in Fig. 3.37 for $E_g = 0.1t$. One can see that $N(\omega)$ exhibits a typical d–wave gap, where $N(\omega)$ is linear in ω for $\omega < E_g$. For decreasing T, $N(0)$ decreases rapidly and therefore χ_0 decreases with T.

Let us now come back to the spin–lattice relaxation rate. We have continued our calculation into the superconducting state somewhat below T_c. One can see from Fig. 3.35 that with decreasing T, the curve for $1/T_1T$ exhibits a sharp downturn at T_c for $E_g = 0$, while the decrease of $1/T_1T$ at T_c becomes slower and more continuous for increasing E_g. Similar results are obtained for χ_s, as shown in Fig. 3.36: the drop below T_c is abrupt for $E_g = 0$, while the decrease with T at T_c becomes slower and more continuous for increasing E_g. These results agree qualitatively with the spin–lattice relaxation rate and Knight shift data in the overdoped (corresponding to $E_g = 0$) and underdoped (corresponding to $E_g > 0$) regimes [164, 165]. For example, the experimental curves for $1/T_1T$ in $YBa_2Cu_3O_7$ and $YBa_2Cu_3O_{6.52}$ [164] have a shape qualitatively similar to our curves for $E_g = 0$ and $E_g > 0$, respectively, in Figs. 3.35 and 3.36. The data in $YBa_2Cu_4O_8$ etc. [165] are qualitatively similar to our results for $E_g > 0$ in Fig. 3.36.

To briefly summarize, the extension of the generalized Eliashberg equations by the inclusion of a $d_{x^2-y^2}$–wave pseudogap yields fair agreement with the spectral density, spin susceptibility, NMR spin–lattice relaxation rates, and Knight shift data. In particular, a peak in $\mathrm{Im}\,\chi(\mathbf{Q},\omega)$ develops (which resembles the resonance peak below T_c) as has been observed experimentally.

Furthermore, when the phase diagram for hole–doped cuprates calculated one finds even better agreement with experiment in the underdoped regime. Interestingly, both of the temperatures T_c^* and T_c are renormalized to smaller values, and the region where preformed pairs are expected is also reduced.

3.5.2 Optical Conductivity and Electronic Raman Response

We come now to the discussion of the consequences of a $d_{x^2-y^2}$–wave pseudogap for the optical conductivity. While the c-axis conductivity in $YBa_2Cu_3O_{7-\delta}$ shows a pseudogap with a size of approximately 300–400 cm^{-1} [166, 167], the size of the pseudogap extracted from the ab–plane conductivity is of the order of 600–700 cm^{-1} [168, 169]. This difference *cannot* be attributed to the charge reservoir layers between the CuO_2 planes, since recently it has been convincingly shown that the pseudogap seen in the c–axis conductivity indeed has its origin in the CuO_2 planes [170]. In the following we shall demonstrate that the self–consistency of our calculation of the spin fluctuation interaction with the single–particle properties, especially the pseudogap itself, provided by the FLEX approximation leads to a natural understanding of the difference in the size of the pseudogap seen in the ab–plane and c–axis conductivities. Also, the semiconducting behavior of the c–axis resistivity can be understood qualitatively [166, 167, 171].

We have calculated the c–axis and ab–plane conductivities in the presence of a temperature–independent but doping–dependent pseudogap as suggested by the work of Williams *et al.* [155], using ARPES data as an input. To do so, it is necessary also to take into account some scattering mechanism within the CuO_2 planes. In particular, the self–consistently calculated interaction due to exchange of spin and charge fluctuations yields a quasiparticle scattering rate which varies linearly with frequency in the normal–state, and exhibits a gap-like suppression at lower frequencies in the superconducting state. At the same time, the effective–mass ratio is increased at lower frequencies in the superconducting state. Thus, we can safely conclude that the FLEX approximation accounts for the damping and mass enhancement needed to extend the theory for thermodynamic quantities of Williams *et al.* [155] to dynamical quantities.

First, we discuss our normal–state results for the optical in–plane conductivity $\sigma_{ab} \equiv \sigma_1(\omega)$ in the presence of a d–wave pseudogap $E_g(\mathbf{k})$. We have assumed for the pseudogap the simple but doping dependent form (introduced in (2.67))

$$E_g(\mathbf{k}) = E_g \left[\cos k_x - \cos k_y\right] \quad ,$$

where E_g is temperature–independent and increases with decreasing doping level below the optimal doping level. The extended version of the generalized equations derived in Sect. 2.2.1 was solved self–consistently in the presence of this pseudogap, and yields the quasiparticle self–energy components $Z(\mathbf{k},\omega)$ and $\xi(\mathbf{k},\omega)$, as well as the superconducting gap $\phi(\mathbf{k},\omega)$.

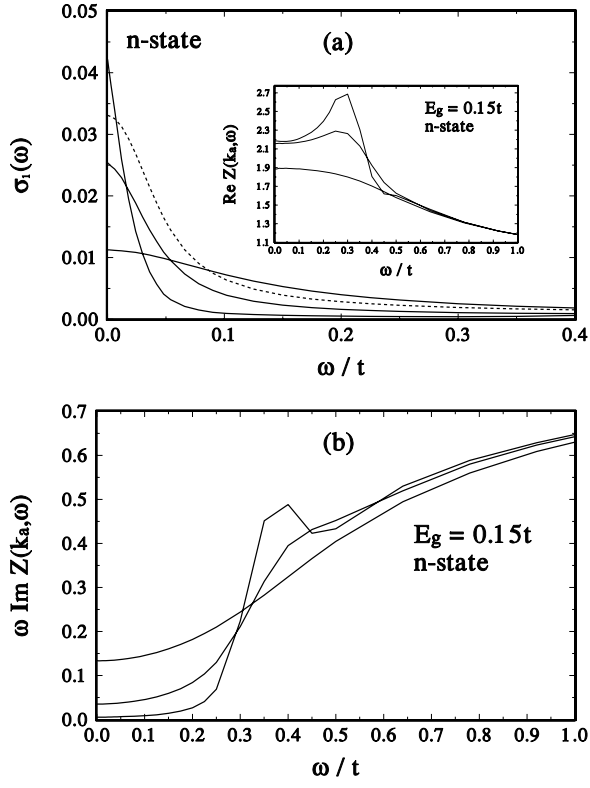

Fig. 3.38. (**a**) Optical conductivity $\sigma_1 \equiv \sigma_{ab}(\omega)$ for an amplitude $E_g = 0.15t$ of the pseudogap, at temperatures $T = 0.1$, 0.050, and $0.030t$. *Inset*: $\mathrm{Re}\, Z(\mathbf{k}_a, \omega)$ for the same temperatures (increasing peaks at $\omega = 0$ in this sequence). *Dashed line*, for $E_g = 0$ and $T = 0.030t$. (**b**) Quasiparticle damping, $\omega\, \mathrm{Im}\, Z(\mathbf{k}_a, \omega)$, at antinode $\mathbf{k}_a$, for an amplitude $E_g = 0.15t$ of the pseudogap, at temperatures $T = 0.1$, 0.050, and $0.030t$ (decreasing values at $\omega = 0$ in this sequence of temperatures).

Our results for $\sigma_{ab}(\omega)$ are displayed in Fig. 3.38a, where one can see that the in–plane conductivity is coherent in character and shows a Drude peak at low frequencies even in the underdoped compounds [168, 172]. However, the size of the pseudogap structure seen in the *ab*–plane conductivity for underdoped YBCO has been measured to be 600–700 cm^{-1} [168, 169], while the gap extracted from the *c*–axis conductivity in the same compounds is of the order of 300–400 cm^{-1} [166, 167]. The corresponding quasiparticle damping, $\Gamma(\mathbf{k}, \omega) = \omega\, \mathrm{Im}\, Z(\mathbf{k}, \omega)$, is highly anisotropic and exhibits, for $\mathbf{k}$ along the direction of the antinode of the gap and decreasing T, a gap of the order of E_g (see Fig. 3.38b, for $E_g = 0.15t$). At the same time, the effective–mass ratio $m^*/m = \mathrm{Re}\, Z(\mathbf{k}, \omega)$ is enhanced at about $\omega \simeq 2E_g$ above its value at $\omega = 0$, where $\mathrm{Re}\, Z \approx 2$ (see inset in Fig. 3.38a). In the absence of the pseudo-

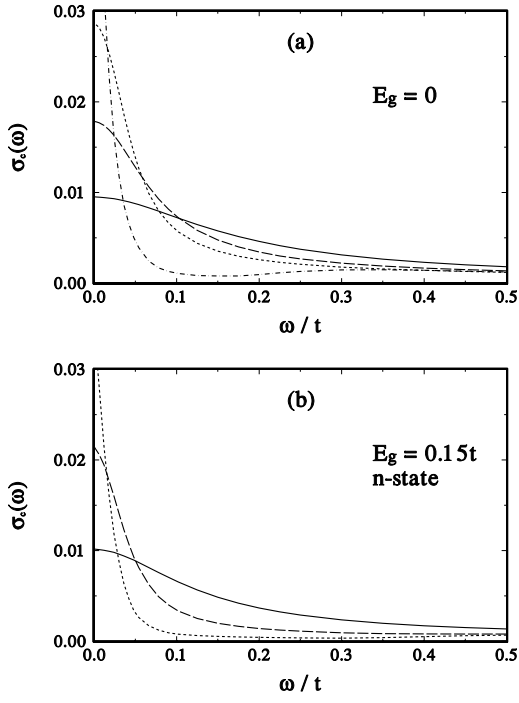

Fig. 3.39. The coherent dynamical c–axis conductivity (2.170) for three temperatures $T = 0.1t$ (*solid lines*), $0.05t$ (*dashed lines*), and $0.03t$ (*dotted lines*), (**a**) for a pseudogap amplitude $E_g = 0$, and (**b**) for $E_g = 0.15t$. The *dashed–dotted line* in (**a**) applies to the superconducting state for $E_g = 0$ ($T_c = 0.023t$) at $T = 0.017t$.

gap the scattering rate Γ varies linearly with frequency ω, as can be seen in Fig. 3.38b for higher temperatures. These results are in qualitative agreement with optical–conductivity data and the frequency–dependent scattering rate and effective–mass spectra obtained from the complex optical conductivity for underdoped Bi 2212, YBCO, and LSCO compounds [173]. For example, for underdoped Bi 2212 with $T_c = 67$ K, the scattering rate $1/\tau(\omega)$ is linear in ω at $T > T^* \simeq 200$ K, and for $T < T^*$ the low-frequency scattering rate is suppressed for $\omega < 500$–$700\,\mathrm{cm}^{-1}$ (62–87meV) [173]. This is in qualitative agreement with our results shown in Fig. 3.38b from which we estimate a crossover temperature $T^* \simeq 0.1t \simeq 250$ K and a threshold energy for the steep rise of about $0.3t \simeq 75$ meV. It should be stressed that we have *calculated* the frequency-dependent scattering rate and mass enhancement with the help of the extended Eliashberg equations, while these quantities were obtained in [173] from theoretical expressions involving the complex conductivity.

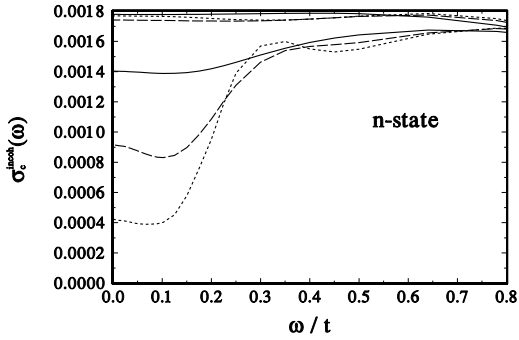

Fig. 3.40. The incoherent dynamical c–axis conductivity (2.172) for three temperatures $T = 0.1t$ (*solid line*), $0.05t$ (*dashed line*), and $0.03t$ (*dotted line*) and two values of $E_g = 0$ (*upper three curves*) and $0.15t$ (*lower three curves*).

Let us now turn to the c-axis conductivity. We shall see that, in our model, incoherent conductance gives a good description of the underdoped regime, while coherent conductance is more appropriate for the overdoped regime, confirming previous interpretations of the c–axis conductivity. In Fig. 3.39a, we show our results for the coherent c–axis conductivity $\sigma_c(\omega)$ calculated from (2.170) for different temperatures. Here we have taken $E_g = 0$. For decreasing temperature T, a coherent Drude peak develops at low frequencies. Such a development of a coherent Drude peak has been observed in overdoped cuprates [166, 170], where the pseudogap is absent or small. Thus, our coherent–conductance results account well for this observation in the overdoped compounds. In the superconducting state, a suppression of $\sigma_c(\omega)$ at intermediate frequencies sets in, as shown by the dashed–dotted line in Fig. 3.39a for $T = 0.017t$. Here, $T_c = 0.023t$. At the same time, the Drude peak continues to sharpen.

Figure 3.39b shows the normal–state coherent conductivity $\sigma_c(\omega)$ in the presence of a pseudogap with amplitude $E_g = 0.15t$. While the pseudogap leads to a suppression of $\sigma_c(\omega)$ at intermediate frequencies, the coherent Drude peak at low frequencies still remains and even sharpens, similarly to the superconducting state in Fig. 3.39a. These results are *completely different* from the experimental results for the normal state of underdoped cuprates, which show, instead of a coherent Drude peak, a gap–like *suppression* at low frequencies. Thus, it is not sufficient to simply introduce a pseudogap in order to account for the c–axis conductivity in underdoped compounds! As has been noted earlier [167, 174], the c–axis conductance becomes incoherent in the underdoped regime the same time, and therefore it is necessary to calculate the incoherent conductivity in the presence of a pseudogap.

Figure 3.40 shows the *incoherent* conductivity $\sigma_c^{\rm incoh}(\omega)$ for $E_g = 0$ and $E_g = 0.15t$ at three different temperatures $T = 0.1$, 0.05, and $0.03t$. For $E_g = 0.15t$, a gap develops below a threshold frequency of about $\omega \sim 2\tilde{E}_g$

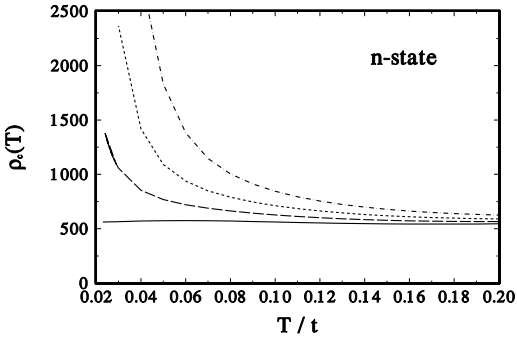

Fig. 3.41. The incoherent c–axis resistivity ρ_c as a function of temperature for $E_g = 0$ (*solid line*), $0.1t$ (*dashed line*), $0.15t$ (*dotted line*), and $0.2t$ (*dashed–dotted line*).

upon lowering the temperature, while the conductivity stays almost constant for frequencies above this threshold energy. Here, $\tilde{E}_g = 2E_g/\mathrm{Re}\, Z(E_g)$ is the renormalized amplitude of the d–wave pseudogap, and $\mathrm{Re}\, Z(\omega)$ is the average mass renormalization at the Fermi surface, which is of the order of 2 for the parameters considered here. For $E_g = 0$, $\sigma_c^{\mathrm{incoh}}$ is almost independent of frequency and temperature. These results are indeed in qualitative agreement with the measured interplane conductivity in underdoped YBCO compounds [166]. The gap in the c-axis conductivity $\sigma_c^{\mathrm{incoh}}(\omega)$ for frequencies ω below $2\tilde{E}_g$ develops below a characteristic temperature $T^* \sim \tilde{E}_g/2$. We want to stress that the temperature evolution of all physical quantities arises exclusively from the Fermi and Bose functions occurring in the FLEX equations in our real–frequency formulation [145] and in the expressions for the susceptibilities, since we have assumed that the pseudogap $E_g(\mathbf{k})$ defined in (2.67) is temperature–independent. Physically, this means that above T^* the effect of the pseudogap is smeared out such that the normal–state behavior (corresponding to the FLEX equations for $E_g = 0$) is recovered, while the effect of the pseudogap on the quasiparticle and spin excitation spectra increases as T decreases below T^* towards T_c.

From our incoherent conductivity, we can extract the c-axis resistivity $\rho_c = [\sigma_c^{\mathrm{incoh}}(\omega = 0)]^{-1}$ in the presence of the pseudogap. The temperature dependence of ρ_c is shown in Fig. 3.41 for different values of the pseudogap amplitude $E_g = 0, 0.1, 0.15$, and $0.2t$, corresponding to different doping levels. For $E_g = 0$, ρ_c is almost constant. For finite E_g, it starts to increase above the curve for $E_g = 0$ at lower temperatures. This "semiconducting" behavior of ρ_c is directly related to the depth of the pseudogap at zero frequency in $\sigma_c^{\mathrm{incoh}}(\omega = 0)$, which increases with increasing E_g and decreasing temperature (see Fig. 3.40). The results in Fig. 3.41 are consistent with the estimate of the characteristic temperature given above, i.e. $T^* \sim \tilde{E}_g/2 = E_g/\mathrm{Re}\, Z$, because the steep rise of ρ_c for a given E_g appears approximately below

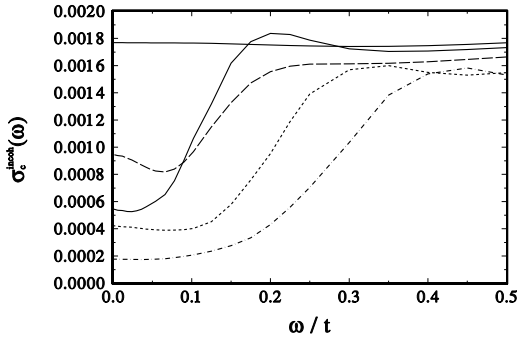

Fig. 3.42. The incoherent dynamical c-axis conductivity (2.172) for $T = 0.03t$ and $E_g = 0$ (*solid line*), $0.1t$ (*dashed line*), $0.15t$ (*dotted line*), and $0.2t$ (*dashed–dotted line*). For comparison we also show the result in the superconducting state for $E_g = 0$ ($T_c = 0.023t$) at $T = 0.017t$ (*lower solid line*).

T^*. Our results are in qualitative agreement with c–axis resistivity data for underdoped YBCO [166, 167]. Note that the definition of the characteristic temperature $T^* \sim \tilde{E}_g/2$ corresponds to the scaling procedure in [155], where it was shown that the NMR Knight shift for a wide range of doping values follows closely a universal scaling curve if the data are plotted against a scaling parameter $z = 2T/\tilde{E}_g$. The downturn of ${}^{89}K_n(T)$ for decreasing z occurs at about $z = 1$, which corresponds to $T^* \sim \tilde{E}_g/2$.

In Fig. 3.42, we show $\sigma_c^{\rm incoh}(\omega)$ at a fixed temperature $T = 0.03t$ and different values of E_g. From Fig. 3.42, we can see that the renormalized size $2\tilde{E}_g$ of the gap in $\sigma_c^{\rm incoh}$ follows E_g. If one assumes that E_g changes strongly with doping level, as has been proposed in [155], the results shown in Fig. 3.42 cannot provide an explanation for the doping independence of the pseudogap seen in the c–axis conductivity of underdoped cuprates. This is an apparent inconsistency of the model of Williams *et al.*, which can describe thermodynamic quantities well, but does not give a satisfactory account of the doping dependence of the *ab*–plane and c–axis conductivities, which are dynamical quantities. On the other hand, our results rather indicate that there are two independent energy scales involved in the pseudogap problem: first, the width of the pseudogap (here $2\tilde{E}_g$) as seen in the ω dependence of the c–axis and *ab*–plane conductivities, which are largely doping–independent, and second, the depth of the pseudogap as seen in the $\omega = 0$ value of the incoherent c–axis conductivity, corresponding to the characteristic temperature T^* for the c–axis resistivity and the thermodynamic quantities, which increases upon lowering the doping level. Two such energy scales could be introduced into the problem by considering more complicated forms for the pseudogap than (2.67). For example, the pseudogap could have a frequency dependence or a momentum dependence which changes with temperature, as suggested by a

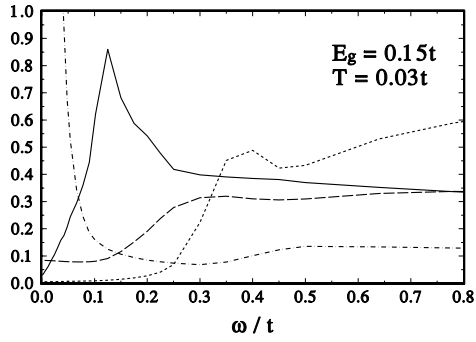

Fig. 3.43. Density of states $N(\omega)$ (*solid line*), incoherent c–axis conductivity $\sigma_c^{\rm incoh}(\omega)$ (*dashed line*), quasiparticle damping rate $\omega\,{\rm Im}\,Z(\mathbf{k_a},\omega)$ (*dotted line*), and ab–plane conductivity $\sigma_{ab}(\omega)$ (*dashed–dotted*) as a function of frequency for $E_g = 0.15t$ and $T = 0.03t$ (arbitrary units). All four quantities show gap-like suppressions at low frequencies. The sizes of these gaps have a ratio of roughly 1:2:3:4. The ab–plane conductivity $\sigma_{ab}(\omega)$ shows a strong Drude peak at low frequencies within the gap.

recent analysis of ARPES data [155, 156]. However, this is beyond the scope of this book.

In addition, the lower solid line in Fig. 3.42 shows the result for the incoherent c–axis conductivity in the superconducting state for $T = 0.017t$ and $E_g = 0$ ($T_c = 0.023t$). This compares well with the experimental results for optimally doped YBCO [166], which show a suppression at low frequencies, similar to the suppression due to the normal-state pseudogap. In addition, a weak enhancement at the gap edge develops. Again, this behavior is completely different from the corresponding behavior of the coherent c–axis conductivity (see the dashed–dotted line in Fig. 3.39a). It is instructive to compare all of the results obtained for the optical conductivity described above with the corresponding density of states. In Fig. 3.43, we show our results for $\sigma_{ab}(\omega)$ and $\sigma_c^{\rm incoh}(\omega)$ for $E_g = 0.15t$ and $T = 0.03t$, along with the density of states $N(\omega)$ (2.171) and the quasiparticle damping rate $\omega\,{\rm Im}\,Z(\mathbf{k_a},\omega)$ at the antinodal momentum $\mathbf{k}_a$ at the Fermi surface (in arbitrary units). Here we see that the sizes of the pseudogap appearing in these four quantities are quite different. In fact, the gaps have an approximate ratio of 1:2:3:4 for the density of states, incoherent c–axis conductivity, quasiparticle damping rate, and ab–plane conductivity, respectively. In particular, we find that the gap structure for $\sigma_{ab}(\omega)$ is about twice as big as that for $\sigma_c^{\rm incoh}(\omega)$, being about $4\tilde{E}_g$ for $\sigma_{ab}(\omega)$ while only $2\tilde{E}_g$ for $\sigma_c^{\rm incoh}(\omega)$, with $\tilde{E}_g \approx 0.12t$, in rough agreement with experiment. We believe that this relation among the gaps is a direct consequence of the electronic origin of the spin fluctuation scattering process and the self–consistency of the FLEX equations: the opening of the pseudogap leads to a suppression of the spin fluctuation interaction

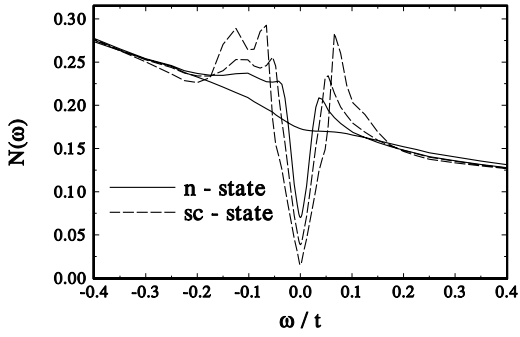

Fig. 3.44. Density of states $N(\omega)$ for a d–wave pseudogap with amplitude $E_g = 0.05t$, in the normal state at $T = 0.1t$ and $0.023t$ (*solid lines*), and in the superconducting state at $T = 0.021t$ and $0.018t$ ($T/T_c = 0.78$ (*dashed lines*). The values $N(0)$ decrease for this sequence of temperatures.

via (2.62) and (2.61) at frequencies below $\sim 2\tilde{E}_g$. This in turn results in a reduction of the self–energy below $\sim 3\tilde{E}_g$ and a corresponding structure at $\sim 4\tilde{E}_g$ in $\sigma_{ab}(\omega)$. However, in the incoherent c–axis conductivity, a gap of only $\sim 2\tilde{E}_g$ in size appears because of the momentum average of the spectral functions, resulting in a frequency convolution of the density of states with itself. The appearance of a gap of $4\Delta_0$ in the ab–plane conductivity in the superconducting state for an electronic pairing mechanism has been noted earlier in connection with marginal–Fermi liquid theory [175, 176, 177]. Here we suggest that a corresponding effect may take place in the pseudogap state of underdoped high–T_c compounds.

The pseudogap structures in the curves in Fig. 3.43 appear to be washed out somewhat and show more complex behavior than a simple suppression at the effective pseudogap. This is due to the fact that the pseudogap (2.67) is renormalized owing to self–energy effects. The structures seen in the conductivity, density of states, and quasiparticle damping rate do not display a pure d–wave gap, but a renormalized one, similar to that in the superconducting state.

To summarize the results for the optical conductivity, we have investigated the influence of a normal–state d–wave pseudogap on the c–axis and ab–plane conductivities for spin fluctuation exchange scattering using an extension of the generalized Eliashberg equations and the self–consistent FLEX approximation as described in Sect. 2.2.1. We find that coherent conduction can describe the c–axis conductivity in the overdoped compounds, while it is necessary to consider incoherent c–axis conduction in the underdoped regime. Only *incoherent* conduction can account well for the dynamical c–axis conductivity and the c–axis resistivity in the underdoped compounds, which show "semiconducting" behavior. However, it is difficult to reconcile the doping

dependence of the amplitude of the pseudogap obtained from a microscopic theory with the doping–independent size of the pseudogap seen in the dynamical c–axis and ab–plane conductivities. This suggests that the pseudogap has a nontrivial momentum or frequency dependence, which changes with temperature. We find that the difference between the sizes of the pseudogaps for ab–plane conductivity and c–axis conductivity finds a natural explanation in the electronic origin of spin fluctuation scattering and its self–consistency with the single-particle properties. This leads to a gap structure of size $\sim 4\tilde{E}_g$ in the ab–plane conductivity, while the gap seen in the incoherent c–axis conductivity has a size of only $\sim 2\tilde{E}_g$.

In order to investigate the influence of a d–wave pseudogap on the Raman response, it is instructive to start with the density of states, which is the main factor that determines the pair–breaking peak in all scattering geometries. In Fig. 3.44, we show our results for the density of states

$$N(\omega) = \frac{1}{N}\sum_k N(\mathbf{k},\omega) = -\frac{1}{\pi}\mathrm{Im}\frac{\omega Z + \epsilon_k + \xi}{(\omega Z)^2 - (\epsilon_k + \xi)^2 - E_g^2 - \phi^2} \quad , \qquad (3.23)$$

for a pseudogap amplitude $E_g = 0.05t$ which is assumed to be temperature–independent. One can see that with decreasing T, a typical d–wave gap develops in the normal state and that this spectrum merges continuously into the superconducting spectrum as T decreases through $T_c = 0.022t$. One can see that below T_c, a dip develops at negative ω below the quasiparticle peak and that the spectrum is quite asymmetric with respect to the Fermi energy at $\omega = 0$. These results are quite similar to the measured tunneling spectra for underdoped Bi2212.

The results discussed in the previous sections encourage us to calculate the Raman response functions above and below T_c in the presence of this d–wave pseudogap $E_g(\mathbf{k})$. The Raman response function, including vertex corrections, then reads

$$\begin{aligned}&\mathrm{Im}\,\chi_\gamma(\mathbf{q}=0,\omega)\\ &= \pi\int_{-\infty}^{\infty} \mathrm{d}\omega'\,[f(\omega') - f(\omega'+\omega)]\sum_{\mathbf{k}} \Gamma(\mathbf{k},\omega',\omega)\,[N(\mathbf{k},\omega'+\omega)N(\mathbf{k},\omega')\\ &-A_1(\mathbf{k},\omega'+\omega)A_1(\mathbf{k},\omega') - A_g(\mathbf{k},\omega'+\omega)A_g(\mathbf{k},\omega')]\,\gamma(\mathbf{k}) \quad . \qquad (3.24)\end{aligned}$$

In Fig. 3.45a, we show our results for the B_{1g} symmetry, again for a gap amplitude $E_g = 0.05t$ as in Fig. 3.44. Comparison with the results for $E_g = 0$ in Fig. 3.24 shows that the most prominent effect of the pseudogap is to produce a broad peak at about a frequency $\omega \simeq 0.075t \simeq (3/2)E_g$ as T approaches T_c from above. This frequency is nearly the same as the frequency difference between the quasiparticle peaks in the density of states in Fig. 3.44. We have also carried out calculations for larger values of the gap amplitude E_g corresponding to lower doping levels [10, 165], i.e. $E_g = 0.075t$ and $0.1t$ [146]. There we find analogous results, namely, that with decreasing T in the

normal state a peak evolves in the B_{1g} Raman spectrum at a frequency of about $(3/2)E_g$, which corresponds to the frequency difference between the peaks in the density of states. The continuous evolution of the B_{1g} Raman peak with decreasing T as shown in Fig. 3.44b for $E_g = 0.15t$ is similar to the observed evolution of the peak in slightly underdoped Bi2212 [178]. We note that the position of the peak at about $\omega \simeq 0.25t \simeq 62$ meV for $t = 250$ meV is of the order of magnitude of the observed resonance at 75 meV [178]. The increase of the normal–state peak with decreasing T is accompanied by a suppression of the low–frequency spectral weight, as is seen in the experiments (see Fig. 3.45b) [178].

Next we discuss the interesting question of whether the pseudogap can also explain the normal–state data for B_{2g} Raman spectra of YBCO and Bi2212 in the underdoped regime, where a reduction of spectral weight with decreasing temperature is observed [179]. We find indeed that spectral weight is lost at higher Raman shifts, while the slope at $\omega = 0$ is increased with decreasing temperature T (see Fig. 3.45c for $E_g = 0.15t$). The broad peak arising below the pair-breaking threshold $2E_g$ is much less pronounced than the sharp peak occurring in the B_{1g} Raman spectrum (see Fig. 3.45b). In the superconducting state, the slope at $\omega = 0$ decreases with decreasing T in agreement with the experimental data for the B_{2g} channel; however, our pair–breaking maximum (see Fig. 3.25) is much less pronounced than the experimental one [179]. This deserves further investigation. In particular, a frequency–dependent pseudogap would be required.

3.5.3 Brief Summary of the Consequences of the Pseudogap

In this section, we have investigated the influence of a d–wave pseudogap on many physical quantities in the underdoped regime of hole–doped superconductors. The general equations were derived in Sect. 2.2.1. The resulting neutron scattering intensity, spin–lattice relaxation rate $1/T_1$, Knight shift, resistivity, and photoemission intensity are in qualitative agreement with the data on underdoped high-T_c cuprates. The value of T_c for superconductivity and also that of T_c^* decrease and the crossover temperature T^* for $1/T_1T$ increases with increasing pseudogap amplitude of ϕ_c, which is in qualitative agreement with the phase diagram for underdoped cuprates. We consider this as an important step towards an understanding of the whole phase diagram within one microscopic theory. Furthermore, we find that the pseudogap leads, with decreasing temperature, to the development of a d–wave gap structure in the density of states, which merges continuously into the superconducting spectrum. A corresponding pair-breaking peak evolves continuously in the B_{1g} Raman spectrum as T decreases in the normal state and below T_c. We have also calculated the c-axis infrared conductivity $\sigma_c(\omega)$ in underdoped cuprate superconductors and find, below a temperature $T^* \sim E_g/2$, that a gap develops in $\sigma_c(\omega)$ for $\omega < 2E_g$ in the *incoherent* (diffuse) transmission limit. The corresponding resistivity shows "semiconducting" behavior, i.e. it increases

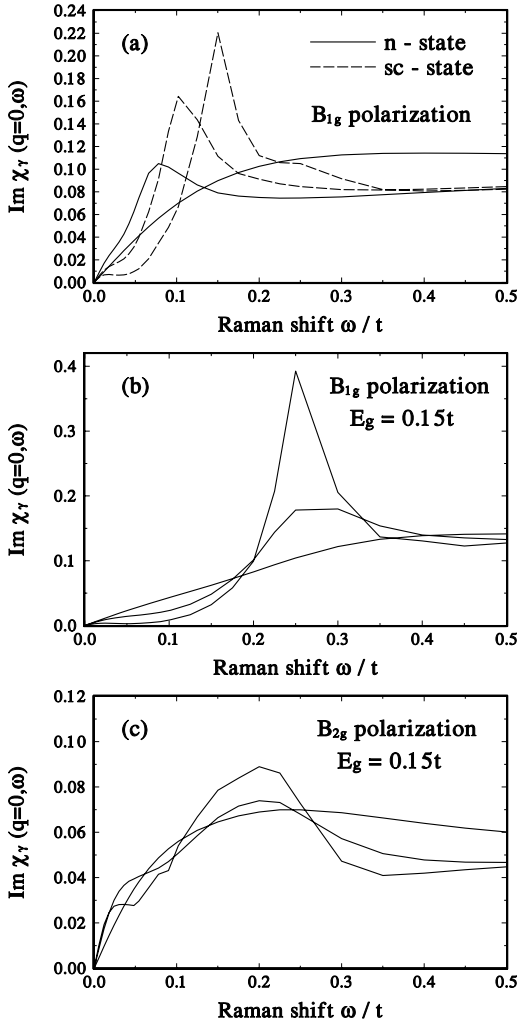

Fig. 3.45. (**a**) Raman intensity for B_{1g} polarization with d–wave pseudogap amplitude $E_g = 0.05t$ in the normal state at $T = 0.1t$ and $0.023t$ (*solid lines* with increasing slopes), and in the superconducting state at $T = 0.021t$ and $0.018t$ ($T/T_c = 0.78$ (*dashed lines* with increasing peaks). (**b**) The same for $E_g = 0.15t$ and $T = 0.1$, 0.050, and $0.030t$ in the normal state (increasing peaks in this sequence). (**c**) B_{2g} Raman response for $E_g = 0.15t$ and the same values of T as in (**b**) (increasing peaks in this sequence).

at low temperatures above the constant behavior for $E_g = 0$. We find that the pseudogap structure in the in–plane optical conductivity is about twice as big as that in the interplane conductivity $\sigma_c(\omega)$, in qualitative agreement with

experiment. This is a consequence of the fact that the exchange of antiferromagnetic spin fluctuations is suppressed at low frequencies as a result of the opening of the pseudogap. While the c-axis conductivity in the underdoped regime is described best by incoherent transmission, in the overdoped regime coherent conductance gives a better description. Thus, we can safely conclude that the extension of the generalized Eliashberg equations to include a $d_{x^2-y^2}$–wave pseudogap (as derived in Sect. 2.2.1) yields fair agreement with experimental data for the underdoped regime of hole–doped cuprates. However, the microscopic origin of the pseudogap is still unknown. A possible candidate is a charge density wave, which is discussed in Sect. 2.2.1, rather than the fluctuation effects analyzed in Sect. 2.2.2. Those latter effects will be more relevant close to T_c.

References

1. Y. J. Uemura *et al.*, Phys. Rev. Lett. **62**, 2317 (1989). 99, 102
2. S. Doniach and M. Inui, Phys. Rev. B **41**, 6668 (1990). 99, 100
3. B. K. Chakraverty, A. Taraphder, and M. Avignon, Physica C **235–240**, 2323 (1994); B. K. Chakraverty and T. V. Ramakrishnan, Physica C **282–287**, 290 (1997). 99, 100, 101, 111
4. V. J. Emery and S. A. Kivelson, Nature **374**, 434 (1995). 99, 100, 101, 111
5. J. R Schrieffer, *Theory of Superconductivity*, Addison-Wesley, Redwood City (1964). 100
6. J. Schmalian, S. Grabowski, and K. H. Bennemann, Phys. Rev. B **56**, R509 (1997). 100
7. F. Schäfer, C. Timm, D. Manske, and K. H. Bennemann, J. Low Temp. Phys. **117**, 223 (1999). 100
8. W. W. Warren, R. E. Walstedt, G. F. Brennert, R. J. Cava, R. Tycko, R. F. Bell, and G. Dabbagh, Phys. Rev. Lett. **62**, 1193 (1989). 100
9. H. J. Tao, F. Lu, and E. J. Wolf, Physica C **282–287**, 1507 (1997). 100
10. C. Renner, B. Revaz, J.-Y. Genoud, K. Kadowaki, and Ø. Fischer, Phys. Rev. Lett. **80**, 149 (1998). 100, 148, 151, 166
11. H. Takagi, B. Batlogg, H. L. Kao, J. Kwo, R. J. Cava, J. J. Krajewski, and W. F. Peck, Phys. Rev. Lett. **69**, 2975 (1992). 100
12. B. Batlogg, H. Y. Hwang, H. Takagi, R. J. Cava, H. L. Kao, and J. Kwo, Physica C **235–240**, 130 (1994). 100, 156
13. T. Timusk and B. Statt, Rep. Prog. Phys. **62**, 61 (1999). 100
14. D. Matthey, S. Gariglio, B. Giovannini, and J. M. Triscone, Phys. Rev. B **64**, 024513 (2001). 100
15. C. Bernhard, J. L. Tallon, T. Blasius, A. Golnik, and C. Niedermeyer, Phys. Rev. Lett. **86**, 1614 (2001). 102
16. C. Renner, private communication. 102, 153
17. N. Miyakawa, J. F. Zasadzinski, L. Ozyuzer, P. Guptasarma, D. G. Hinks, C. Kendziora, and K. E. Gray, Phys. Rev. Lett. **83**, 1018 (1999). 102, 153
18. M. R. Presland, J. L. Tallon, R. G. Buckley, R. S. Liu, and N. E. Flower, Physica C **176**, 95 (1991); J. R. Cooper and J. W. Loram, J. Phys. I **6**, 1 (1996); J. L. Tallon and J. W. Loram, Physica C **349**, 53 (2001). 102

19. J. L. Tallon, C. Bernhard, H. Shaked, R. L. Hittermann, and J. D. Jorgensen, Phys. Rev. B **51**, 12911 (1995). 102
20. G. D. Mahan, *Many-Particle Physics*, Plenum Press, New York (1981). 102, 107, 122
21. F. London and H. London, Proc. Roy. Soc. (London) A **149**, 71 (1935). 102
22. S. Kamal, Ruixing Liang, A. Hosseini, D. A. Bonn, and W. N. Hardy, Phys. Rev. B **58**, R8933 (1998); S. Kamal, D. A. Bonn, N. Goldenfeld, P. J. Hirschfeld, Ruixing Liang, and W. N. Hardy, Phys. Rev. Lett. **73**, 1845 (1994). 102, 103, 104
23. P. C. E. Stamp, L. Forro, and C. Ayache, Phys. Rev. B **38**, 2847 (1988). 104
24. S. N. Artemenko, I. G. Gorlova, and Y. I. Latyshev, Phys. Lett. A **138**, 428 (1989). 104
25. S. Martin, A. T. Fiory, R. M. Fleming, G. P. Espinosa, and A. S. Cooper, Phys. Rev. Lett. **62**, 677 (1989). 104
26. N. C. Yeh and C. C. Tsuei, Phys. Rev. B **39**, 9708 (1989). 104
27. T. Freltoft, H. J. Hensen, and P. Minnhagen, Solid State Commun. **78**, 635 (1991). 104
28. A. K. Pradhan, S. J. Hazell, J. W. Hodby, C. Chen, Y. Hu, and B. M. Wanklyn, Phys. Rev. B **47**, 11374 (1993). 104
29. Z. A. Xu, N. P. Ong, Y. Wang, T. Kakeshita, and S. Uchida, Nature **406**, 486 (2000). 104
30. Y. Wang, Z. A. Xu, T. Kekeshita, S. Uchida, S. Ono, Y. Ando, and N. P. Ong, Phys. Rev. B **64**, 224519 (2001). 104
31. J. Adler, C. Holm, and W. Janke, Physica A **201**, 581 (1993). 104, 105
32. P. Olsson and P. Minnhagen, Phys. Sc. **43**, 203 (1991). 104, 105
33. C. Meingast, V. Pasler, P. Nagel, A. Gykov, S. Tajima, and P. Olsson, Phys. Rev. Lett. **86**, 1606 (2001). 104
34. R. Kaindl, M. Woerner, T. Elsaesser, D. C. Smith, J. F. Ryan, G. A. Farnan, M. P. McCurry, and D. G. Walsmley, Science **287**, 470 (2000). 106
35. D. Manske and K. H. Bennemann, Physica C **341–348**, 83 (2000); D. Manske, T. Dahm, and K.H. Bennemann, Phys. Rev. B **64**, 144520 (2001). 106, 111, 135, 143, 153
36. J. Corson, R. Malozzi, J. Orenstein, J. N. Eckstein, and I. Bosovic, Nature **398**, 221 (1999). 107, 108
37. V. Ambegeokar, B. I. Halperin, D. R. Nelson, and E. D. Siggia, Phys. Rev. Lett. **40**, 783 (1978); V. Ambegeokar and D. Seitel, Phys. Rev. B **19**, 1667 (1979); V. Ambegeokar, B. I. Halperin, D. R. Nelson, and E. D. Siggia, Phys. Rev. Lett. **21**, 1806 (1980). 107
38. P. Minnhagen, Rev. Mod. Phys. **59**, 1001 (1987). 107
39. C. Timm, D. Manske, and K. H. Bennemann, Phys. Rev. B **66**, 094515 (2002). 107, 108
40. D. J. Scalapino, Phys. Rep. **250**, 329 (1995). 109
41. M. Sigrist and T. M. Rice, Z. Phys. B: Condens. Matter **68**, 9 (1987). 109
42. B. Stadlober, G. Krug. R. Nemetschek, R. Hackl, J. L. Cobb, and J. T. Markert, Phys. Rev. Lett. **74**, 4911 (1995). 109, 114
43. L. Alff, A. Beck, R. Gross, A. Marx, S. Kleefisch, T. Bauch, H. Sato, M. Naito, and G. Koren, Phys. Rev. B. **58**, 11197 (1998). 109, 112
44. S. M. Anlage, D.-H. Wu, S. N. Mao, X. X. Xi, T. Venkatesan, J. L. Peng, and R. L. Greene, Phys. Rev. B. **50**, 523 (1994). 109

45. C. C. Tsuei and J. R. Kirtly, Phys. Rev. Lett. **85**, 182 (2000). 109, 112, 114
46. J. D. Kokales, P. Fournier, L. V. Mercaldo, V. V. Talanov, R. L. Greene, and S. M. Anlage, Phys. Rev. Lett. **85**, 3696 (2000). 109, 112, 114
47. R. Prozorov, R. W. Gianetta, P. Furnier, and R. L. Greene, Phys. Rev. Lett. **85**, 3700 (2001). 109, 112, 114
48. G. Baumgärtel, J. Schmalian, and K. H. Bennemann, Phys. Rev. B **48**, 3983 (1993). 110
49. E. F. Paulus, I. Yehia, H. Fuess, J. Rodriguez, T. Vogt, J. Ströbel, M. Klauda, and G. Saemann-Ischenko, Solid State Commun. **73**, 791 (1990). 110
50. H. Takagi, S. Uchida, and Y. Tokura, Phys. Rev. Lett. **62**, 1197 (1989). 110
51. G. Liang, J. Chen, M. Croft, K. V. Ramanujachary, M. Greenblatt, and M. Hegde, Phys. Rev. B **40**, 2646 (1989). 110
52. D. M. King, Z.-X. Shen, D. S. Dessau, B. O. Wells, W. E. Spicer, A. J. Arko, D. S. Marshall, J. DiCarlo, A. G. Loeser, C. H. Park, E. R. Ratner, J. L. Peng, Z. Y. Li, and R. L. Greene, Phys. Rev. Lett. **70**, 3159 (1993). 110
53. C. Almasan, and M. B. Maple, in *Chemistry of High-Temperature Superconductors*, edited by by C. N. R. Rao, World Scientific, Singapore (1991). 110
54. H. Kontoni, K. Kanki, and K. Ueda, Phys. Rev. B **59**, 14723 (1999). 112
55. K. Kuroki and H. Aoki, J. Phys. Soc. Jpn. **67**, 1533 (1998). 112
56. M. Fogelström, D. Rainer, and J. A. Sauls, Phys. Rev. Lett. **79**, 281 (1997). 112
57. F. Hayashi, E. Ueda, M. Sato, K. Kurahashi, and K. Yamada, J. Phys. Soc. Jpn. **67**, 3234 (1998). 112
58. J. A. Appelbaum, Phys. Rev. **154**, 633 (1967). 112
59. M. Aprili, M. Covington, E. Paraoani, B. Niedermeier, and L. H. Greene, Phys. Rev. B **57**, 8139 (1998). 112
60. B. Batlogg, S.-W. Cheong, G. A. Thomas, S. L. Cooper, L. W. Rupp, D. H. Rapkine, and A. S. Cooper, Physica C **185-189**, 1385 (1991). 112
61. T. Dahm, D. Manske, D. Fay, and L. Tewordt, Phys. Rev. B **54**, 12006 (1996). 113, 114
62. T. Tohoyama and S. Maekawa, Supercond. Sci. Technol. **13**, R17 (2000). 114
63. J. P. Franck, in *Physical properties of High Temperature Superconductors*, edited by D. Ginsberg, World Scientific, Singapore (1994). 114
64. M. Onada, S. Kondoh, and M. Sato, Solid State Comm. **70**, 1141 (1989). 114
65. E. T. Heyen, G. Kliche, W. Kress, W. König, M. Cardona, E. Rampf, J. Prade, F. W. de Wette, S. Pinol, D. McK. Paul, E. Moran, and M. A. Alario-Franco, Solid State Commun. **74**, 1299 (1990). 114
66. J. L. Peng, E. Maiser, T. Venkatesan, R. L. Greene, and G. Czyzek, Phys. Rev. B **55**, 6145 (1997). 114
67. H. F. Fong, B. Keimer, D. Reznik, D. L. Milius and I. A. Aksay, Phys. Rev. B **54**, 6708 (1996). 115, 118, 147
68. H. He, Y. Sidis, P. Bourges, G. D. Gu, A. Ivanov, N. Koshizuka, B. Liang, C. T. Lin, L. P. Regnault, E. Schoenherr, and B. Keimer, Phys. Rev. Lett. **86**, 1610 (2001). 115, 123
69. P. Dai, H. A. Mook, S. M. Hayden, G. Aeppli, T. G. Perring, R. D. Hunt, and F. Dogan, Science **284**, 1344 (1999). 115, 155
70. P. Bourges, B. Keimer, L. P. Regnault, and Y. Sidis, Science **288**, 1234 (2000). 115
71. T. E. Mason, A. Schröder, G. Aeppli, H. A. Mook, and S. M. Hayden, Phys. Rev. Lett. **77**, 1604 (1996). 115, 118, 119

72. B. Lake, G. Aeppli, T. E. Mason, A. Schröder, D. F. McMorrow, K. Lefmann, M. Isshiki, M. Nohara, H. Takagi, and S. M. Hayden, Nature **400**, 43 (1999). 115, 118, 119
73. N. E. Bickers, D. J. Scalapino, and S. R. White, Phys. Rev. Lett. **62**, 961 (1989); N. E. Bickers and D. J. Scalapino, Ann. Phys. (N.Y.) **193**, 206 (1989). 116, 119
74. J. P. Carbotte, E. Schachinger, and D. N. Basov, Nature **401**, 354 (1999). 116
75. E. Schachinger and J. P. Carbotte, Phys. Rev. B **62**, 9054 (2000). 116, 124
76. D. Manske, T. Dahm and K. H. Bennemann, preprint cond-mat/9912062. 116, 123, 135, 136, 140
77. N. Bulut and D. J. Scalapino, Phys. Rev. B **53**, 5149 (1996). 116, 117
78. T. Dahm, D. Manske, and L. Tewordt, Phys. Rev. B **54**, 6640 (1996). 117
79. T. Dahm, D. Manske, and L. Tewordt, Phys. Rev. B **58**, 12454 (1998). 117, 119
80. M. R. Norman, H. Ding, J. C. Campuzano, T. Takeuchi, M. Randeria, T. Yokoya, T. Takahashi, T. Mochiku, and K. Kadowaki, Phys. Rev. Lett. **79**, 3506 (1997). 117, 126
81. X. K. Chen, E. Altendorf, J. C. Irwin, R. Liang, and W. N. Hardy, Phys. Rev. B **48**, 10530 (1993). 118
82. Y. Zha, V. Barzykin, and D. Pines, Phys. Rev. B **54**, 7561 (1996). 118
83. X. K. Chen, J. C. Irwin, H. J. Trodahl, T. Kimura, and K. Kishio, Phys. Rev. Lett. **73**, 3290 (1994). 118
84. M. Langer, J. Schmalian, S. Grabowski, and K. H. Bennemann, Phys. Rev. Lett. **75**, 4508 (1995). 119
85. I. Maggio-Aprile, C. Renner, A. Erb, E. Walker, and Ø. Fischer, Phys. Rev. Lett. **75**, 2754 (1995). 119
86. H. He, P. Bourges, Y. Sidis, C. Ulrich, L. P. Regnault, S. Pailhes, N. S. Berzigiarova, N. N. Kolesnikov, and B. Keimer, Science **295**, 1045 (2002). 121
87. S. Wermbter and L. Tewordt, Physica C **211**, 132 (1993). 122
88. A. Puchkov, D. N. Basov, and T. Timusk, J. Phys.: Condens. Matter **8**, 10049 (1996). 122, 134
89. J. Brinckmann and P. A. Lee, Phys. Rev. Lett. **82**, 2915 (1999). 123, 125
90. J.-X. Li, C.-Y. Mou, and T. K. Lee, Phys. Rev. **B 62**, 640 (2000). 123, 125
91. F. Marsiglio, J. P. Carbotte, and E. Schachinger, Phys. Rev. B **65**, 014515 (2001); E. Schachinger and J. P. Carbotte, Phys. Rev. B **64**, 094501 (2001); E. Schachinger, J. P. Carbotte, and F. Marsiglio, Phys. Rev. B **56**, 2738 (1997). 124
92. F. Marsiglio, T. Startseva, and J. P. Carbotte, Phys. Lett. A **345**, 172 (1998); F. Marsiglio, Mol. Phys. Rep. **24**, 73 (1999). 124
93. E. Demler, H. Kohno, and S.-C. Zhang, Phys. Rev. B **58**, 5719 (1998). 125
94. S.-C. Zhang, Science **275**, 1089 (1997); M. G. Zacher, W. Hanke, E. Arrigoni, and S.-C. Zhang, Phys. Rev. Lett. **85**, 824 (2000); A. Dorneich, W. Hanke, E. Arrigoni, M. Troyer, and S.-C. Zhang, Phys. Rev. Lett. **88**, 057003 (2002). 125
95. O. Tchernyshyov, M. R. Norman, and A. V. Chubukov, Phys. Rev. B **63**, 144507 (2001); A. V. Chubukov, B. Janko, and O. Tchernyshyov, Phys. Rev. B **63**, 180507(R) (2001). 125

96. F. Onufrieva and J. Rossat-Mignod, Phys. Rev. B **52**, 7572 (1999). 125
97. D. Munzar, C. Bernhard, and M. Cardona, Physica C **312**, 121 (1999). 125
98. L. Yin, S. Chakravarty, and P. W. Anderson, Phys. Rev. Lett. **78**, 3559 (1997). 125
99. J. Brinckmann and P. A. Lee, Phys. Rev. B **65**, 014502 (2001). 125
100. J.-X. Li and C.-D. Gong, Phys. Rev. **B 66**, 014506 (2002). 125
101. M. Eschrig and M. R. Norman, Phys. Rev. Lett. **85**, 3261 (2000); M. R. Norman, Phys. Rev. B **63**, 092509 (2001). 125
102. Y. Sidis, P. Bourges, H. F. Fong, L. P. Regnault, J. Bossy, A. Ivanov, B. Hennion, P. Gautier-Picard, G. Collin, D. L. Millius, and I. A. Aksay, Phys. Rev. Lett. **84**, 5900 (2000). 125
103. H. F. Fong, P. Bourges, Y. Sidis, L. P. Regnault, J. Bossy, A. Ivanov, D. L. Millius, I. A. Aksay, and B. Keimer, Phys. Rev. Lett. **82**, 1939 (1999). 125
104. N. Bulut, Phys. Rev. B **61**, 9051 (2000). 125
105. M. Vojta, C. Buragohain, and S. Sachdev, Phys. Rev. B **61**, 15152 (2000). 125
106. Z.-X. Shen and D. S Dessau, Phys. Rep. **253**, 1 (1995). 126
107. T. Valla, A. V. Fedorov, P. D. Johnson, B. O. Wells, S. L. Hulbert, Q. Li, G. D. Gu, and N. Koshizuka, Science **285**, 2110 (1999). 126
108. P. D. Johnson, T. Valla, A. V. Fedorov, Z. Yusof, B. O. Wells, Q. Li, A. R. Moodenbaugh, G. D. Gu, N. Koshizuka,, C. Kendziora, S. Jian, and D. G. Hinks, Phys. Rev. Lett. **87**, 177007 (2001). 126, 127
109. A. Kaminski, M. Randeria, J. C. Campuzano, M. R. Norman, H. Fretwell, J. Mesot, T. Sato, T. Takahashi, and K. Kadowaki, Phys. Rev. Lett. **86**, 1070 (2001). 126, 127, 128, 129
110. P. V. Bogdanov, A. Lanzara, S. A. Kellar, X. J. Zhou, E. D. Lu, W. J. Zheng, G. Gu, J.-I. Shimoyama, K. Kishio, H. Ikeda, R. Yoshizaki, Z. Hussain, and Z.-X. Shen, Phys. Rev. Lett. **85**, 2581 (2000). 126, 127, 128
111. A. Lanzara, P. V. Bogdanov, X. J. Zhou, S. A. Kellar, W. J. Zheng, E. D. Lu, Y. Yoshida, H. Elsaki, A. Fijimori, K. Kishio, J.-I. Shimoyama,, T. Noda, S. Uchida, Z. Hussain, and Z.-X. Shen, Nature **412**, 510 (2001). 126, 127, 128
112. Z. X. Shen, A. Lanzara, and N. Nagaosa, preprint cond-mat/0102244 (unpublished). 126, 127, 134
113. M. Zacher, R. Eder, E. Arrigoni, and W. Hanke, preprint cond-mat/0103030 (unpublished). 126
114. A. D. Gromko, S. V. Fedorov, Y.-D. Chuang, J. D. Koralek, Y. Aiura, Y. Yamaguchi, K. Oka, Y. Ando, and D. S. Dessau, Phys. Rev. B **68**, 174520 (2003). 130, 133, 134
115. D. Manske, I. Eremin, and K. H. Bennemann, Phys. Rev. B **62**, 13922 (2000). 134
116. D. Manske, I. Eremin, and K. H. Bennemann, Europhys. Lett. **53**, 371 (2001). 134, 135
117. M. R. Norman, H. Ding, H. Fretwell, M. Randeria, and J. C. Campuzano, Phys. Rev. B **60**, 7585 (1999). 134
118. N. J. Curro, T. Imai, C. P. Slichter, and B. Dabrowski, Phys. Rev B **56**, 877 (1997). 134, 151
119. C. M. Varma, P. B. Littlewood, S. Schmitt-Rink, E. Abrahams, and A. E. Ruckenstein, Phys. Rev. Lett. **63**, 1996 (1989). 135, 137, 138
120. J. Ruvalds, C. T. Rieck, S. Tewari, J. Thoma, and A. Virosztek, Phys. Rev. B **51**, 3797 (1995). 135, 141

121. A. J. Millis, H. Monien, and D. Pines, Phys. Rev. B **42**, 167 (1990). 135
122. R. Haslinger, A. V. Chubukov, and A. Abanov, Phys. Rev. B **63**, 020503 (2000). 136
123. R. M. Macfarlane, H. Rosen, and H. Seki, Solid State Commun. **63**, 831 (1987). 137
124. S. L. Cooper, F. Slakey, M. V. Klein, J. P. Rice, E. D. Bukowski, and D. M. Ginsberg, Phys. Rev. B **38**, 11934 (1988). 137
125. C. Thomsen in *Light Scattering in Solids VI*, edited by M. Cardona and G. Güntherodt, Springer, Berlin, Heidelberg (1991). 137
126. A. Bock, Ann. Phys. (Leipzig) **8**, 441 (1999). 137
127. D. Einzel and R. Hackl, J. Raman Spectrosc. **27**, 307 (1996). 137, 140
128. D. Manske, C. T. Rieck, R. Das Sharma, A. Bock, and D. Fay, Phys. Rev. B **56**, R2940 (1997). 137
129. J. Ruvalds, Supercond. Sci. Technol. **9**, 905 (1997). 133, 137, 138
130. P. Monthoux and D. Pines, Phys. Rev. B **50**, 16015 (1994). 137, 139
131. D. Branch and J. P. Carbotte, Phys. Rev. B **54**, 13288 (1996). 137
132. T. P. Devereaux and A. Kampf, preprint cond-mat/9711039 137, 139
133. A. Bille, C. T. Rieck, and K. Scharnberg, in *Proceedings of the NATO Advanced Research Workshop on Symmetry and Pairing in Superconductors*, Yalta, Ukraine, edited by M. Ausloos and S. Kruchinin, Kluwer, Dordrecht (1998). 137, 139, 140
134. T. Dahm, D. Manske, and L. Tewordt, Phys. Rev. B **58**, 12454 (1998). 140
135. D. M. Lee, in *Proceedings of the Conference on Spectroscopies in Novel Superconductors*, Sept. 14–18, 1997, Cape Cod, Massachusetts. 145
136. L. Tewordt, D. Fay, P. Dörre, and D. Einzel, J. Low Temp. Phys. **21**, 645 (1975). 145
137. N. Schopohl and L. Tewordt, J. Low Temp. Phys. **45**, 67 (1981). 145, 146
138. H. Monien, K. Scharnberg, N. Schopohl, and L. Tewordt, J. Low Temp. Phys. **65**, 13 (1986). 145
139. D. S. Hirashima and H. Namaizawa, J. Low Temp. Phys. **73**, 137 (1988). 145
140. Wen-Chin Wu and A. Griffin, Phys. Rev. B **51**, 1190 (1995). 145
141. M. I. Salkola and J. R. Schrieffer, Phys. Rev. B **58**, R5944 (1998). 145
142. Z.-X. Shen and J. R. Schrieffer, Phys. Rev. Lett. **78**, 1771 (1997). 145
143. T. Dahm, Phys. Rev. B **53**, 14051 (1996). 145
144. D. Coffey, Europhys. Lett. **40**, 563 (1997). 145
145. T. Dahm and L. Tewordt, Phys. Rev. Lett. **74**, 793 (1995). 145, 162
146. T. Dahm and L. Tewordt, Physica C **246**, 61 (1995); T. Dahm, Solid State Commun. **101**, 487 (1997). 145, 147, 166
147. T. E. Mason, G. Aeppli, S. M. Hayden, A. P. Ramirez, and H. A. Mook, Phys. Rev. Lett. **71**, 919 (1993); J. Rossat-Mignod, L. P. Regnault, C. Vettier, P. Bourges, P. Burlet, J. Bossy, J. Y. Henry, and G. Lapertot, Physica C **185–189**, 86 (1991); J. Rossat-Mignod, L. P. Regnault, P. Bourges, C. Vettier, P. Burlet, and J. Y. Henry, Physica B **186–188**, 1 (1993). 145
148. K. Maki and H. Won, Phys. Rev. Lett. **72**, 1758 (1994); T. Tanamoto, H. Kohno, and H. Fukuyama, J. Phys. Soc. Jpn. **63**, 2739 (1994). 145
149. M. R. Norman *et al.*, Phys. Rev. Lett. **79**, 3506 (1997). 148
150. G. A. Sawatzky, Nature **342**, 480 (1989). 148
151. D. Manske, C. T. Rieck, R. Das Sharma, A. Bock, and D. Fay, Phys. Rev. B **56**, R2940 (1997). 149

152. L. P. Regnault, P. Bourges, P. Burlet, J. Y. Henry, J. Rossat-Mignod, Y. Sidis, and C. Vettier, Physica B **213–214**, 48 (1995). 151, 156
153. J. Loram, K. A. Mirza, J. R. Cooper, and W. Y. Liang, Phys. Rev. Lett. **71**, 1740 (1993); J. W. Loram, J. Supercond. **7**, 234 (1994). 151
154. J. M. Harris, P. J. White, Z.-X. Shen, H. Ikeda, R. Yoshizaki, H. Eisaki, S. Uchida, W. D. Si, J. W. Xiong, Z.-X. Zhao, and D. S. Dessau, Phys. Rev. Lett. **79**, 143 (1997). 151
155. G. V. M. Williams, J. L. Tallon, and J. W. Loram, Phys. Rev. B **58**, 15053 (1998). 151, 153, 158, 163, 164
156. M. R. Norman, M. Randeria, H. Ding, and J. C. Campuzano, Phys. Rev. B **57**, R11093 (1998). 151, 164
157. J. R. Cooper and J. W. Loram, J. Phys. I **6**, 2237 (1996). 151
158. H. Ding, M. R. Norman, T. Yokoya, T. Takeuchi, M. Randeria, J. C. Campuzano, T. Takahashi, T. Mochiku, and K. Kadowaki, Phys. Rev. Lett. **78**, 2628 (1997). 153
159. D. S. Marshall, D. S. Dessau, A. G. Loeser, C.-H. Park, A. Y. Matsuura, J. N. Eckstein, I. Bozovic, P. Fournier, A. Kapitulnik, W. E. Spicer, and Z.-X. Shen, Phys. Rev. Lett. **76**, 4841 (1996). 153
160. D. G. Xenikos, J.-T. Kim, and T. R. Lemberger, Phys. Rev. B **48**, 7742 (1993). 153
161. T. M. Rice and G. K. Scott, Phys. Rev. Lett. **35**, 120 (1975). 154
162. H. Hlubina and T.M. Rice, Phys. Rev. B **51**, 9253 (1995). 154
163. C. P. Slichter, in *Strongly Correlated Electronic Systems*, edited by K. S. Bedell, Addison Wesley, Reading, MA (1994). 156
164. M. Horvatić *et al.*, Phys. Rev. B **47**, 3461 (1993). 156, 157
165. G. V. M. Williams, J. L. Tallon, E. M. Haines, R. Michalak, and R. Dupree, Phys. Rev. Lett. **78**, 721 (1997); G. V. M. Williams, J. L. Tallon, and J. W. Loram, Phys. Rev. B **58**, 15053 (1998). 156, 157, 166
166. C. C. Homes, T. Timusk, R. Liang, D. A. Bonn, and W. N. Hardy, Physica C **254**, 265 (1995). 158, 159, 161, 162, 163, 164
167. S. Uchida, Physica C **282–287**, 12 (1997). 158, 159, 161, 163
168. A. V. Puchkov, D. N. Basov, and T. Timusk, J. Phys. B: Condens. Matter **8**, 10049 (1996). 158, 159
169. D. N. Basov, R. Liang, B. Dabrowski, D. A. Bonn, and W. N. Hardy, Phys. Rev. Lett. **77**, 4090 (1996). 158, 159
170. C. Bernhard, R. Henn, A. Wittlin, M. Kläser, T. Wolf, G. Müller-Vogt, C. T. Lin, and M. Cardona, Phys. Rev. Lett. **80**, 1762 (1998). 158, 161
171. P. Prelovšek, A. Ramšak, and I. Sega, Phys. Rev. Lett. **81**, 3745 (1998). 158
172. T. Startseva, T. Timusk, A. V. Puchkov, D. N. Basov, H. A. Mook, M. Okuya, T. Kimura, and K. Kishio, Phys. Rev. B **59**, 7184 (1999). 159
173. A. V. Puchkov, D. N. Basov, and T. Timusk, J. Phys. Condens. Matter **8**, 10049 (1996); T. Startseva, T. Timusk, A. V. Puchkov, D. N. Basov, H. A. Mook, M. Okuya, T. Kimura, and K. Kishio, preprint cond-mat/9812134. 160
174. P. J. Hirschfeld, S. M. Quinlan, and D. J. Scalapino, Phys. Rev. B **55**, 12742 (1997). 161
175. P. B. Littlewood and C. M. Varma, Phys. Rev. B **46**, 405 (1992); J. Appl. Phys. **69**, 4979 (1991). 165
176. E. J. Nicol, J. P. Carbotte, and T. Timusk, Phys. Rev. B **43**, 473 (1991). 165

177. T. Dahm, S. Wermbter, and L. Tewordt, Physica C **190**, 537 (1992); J. Low Temp. Phys. **88**, 41 (1992). 165
178. G. Blumberg, M. Kang, M. V. Klein, K. Kadowaki, and C. Kendziora, Science **278**, 1427 (1997). 167
179. R. Nemetschek, M. Opel, C. Hoffmann, P. F. Müller, R. Hackl, H. Berger, L. Forro, A. Erb, and E. Walker, Phys. Rev. Lett. **78**, 4837 (1997). 167
180. C. Timm and K. H. Bennemann, Phys. Rev. Lett. **84**, 4994. 99

4 Results for Sr_2RuO_4

In this chapter, we focus on our results for the elementary excitations and Cooper pairing in strontium ruthenate (Sr_2RuO_4). The novel spin-triplet superconductivity with $T_c = 1.5$ K observed recently in layered Sr_2RuO_4 is a new example of unconventional superconductivity [1]. Clearly, it is important and of general interest to analyze in more detail the origin of the superconductivity, and to calculate the transition temperature T_c and also the symmetry of the order parameter on the basis of an electronic theory. This is difficult, since there are three Ru^{4+} t_{2g} bands that cross the Fermi level, with approximately two–thirds filling of every band in Sr_2RuO_4. The coupling between all three bands seems to cause a single T_c. Furthermore, the presence of incommensurate antiferromagnetic (IAF) and ferromagnetic spin fluctuations, confirmed recently by inelastic neutron scattering [2] and the NMR ^{17}O Knight shift [3], respectively, suggests a pairing mechanism for Cooper pairs due to spin fluctuations. Also, a non–s–wave symmetry of the order parameter has been observed. This makes the theoretical investigation of ruthenates very interesting.

To be more precise, recent studies by means of INS [2] and NMR [4] of the spin dynamics in Sr_2RuO_4 reveal the presence of strong incommensurate fluctuations in the RuO_2 planes at the antiferromagnetic wave vector $\mathbf{Q}_i = (2\pi/3, 2\pi/3)$. As was found in band structure calculations [5], these fluctuations result from the nesting properties of the quasi–one–dimensional d_{xz} and d_{yz} bands. The two–dimensional d_{xy} band contains only weak ferromagnetic fluctuations. The very recent observation of the possibility of line nodes between the RuO_2 planes [6, 7] suggests strong spin fluctuations between the RuO_2 planes in the z direction also [8, 9]. However, INS [10] shows that the magnetic fluctuations are purely two–dimensional and originate from the RuO_2 planes. Both behaviors could be a consequence of the magnetic anisotropy within the RuO_2 planes, as indeed was observed in recent NMR experiments by Ishida *et al.* [11]. In particular, by analyzing the temperature dependence of the nuclear spin–lattice relaxation rate for ^{17}O in the RuO_2 planes at low temperatures (but still in the normal state), Ishida *et al.* have demonstrated that the out-of-plane component of the spin susceptibility can become almost up to three times larger than the in–plane component. This

D. Manske: Theory of Unconventional Superconductors, STMP 202, 177–199 (2004)

strong and unexpected anisotropy disappears with increasing temperature [11].

Below T_c, NMR [12, 13] and polarized neutron scattering [14] measurements indicate spin-triplet state Cooper pairing. From the analogy to ^{3}He, this led Rice, Sigrist, and coworkers [15, 16], as well as Tewordt [17, 18] and others [19, 20, 21], to conclude that p–wave superconductivity is present. However, by fitting the specific heat and the ultrasound attenuation, Maki and coworkers [22], as well as others [23, 24, 25], found reason to doubt the presence of p–wave superconductivity and have proposed an f–wave symmetry of the superconducting order parameter. A similar conclusion was drawn in [26]. Recently it has been reported that thermal–conductivity measurements are also most consistent with f–wave symmetry [7]. In view of these facts, we shall reexamine the previous theoretical analysis of the gap symmetries and the competition between p– and d–wave superconductivity [5, 25, 27]. We shall also investigate superconductivity within an electronic theory and derive the symmetry of the order parameter from general arguments.

This chapter is organized as follows: In the next section, we shall analyze the normal–state spin dynamics of Sr_2RuO_4 using the two–dimensional three-band Hubbard Hamiltonian for the three bands crossing the Fermi level. In the first subsection, we calculate the dynamical spin susceptibility $\chi(\mathbf{q},\omega)$ within the random–phase approximation and show that the observed magnetic anisotropy in the RuO_2 planes arises mainly from the spin–orbit coupling. Its further enhancement with decreasing temperature is due to the vicinity of a magnetic instability. Thus we demonstrate that, as in the superconducting state [28], the spin–orbit coupling also plays an important role in the normal–state spin dynamics of Sr_2RuO_4. Then, in Sect. 4.1.2, we present an electronic theory which takes into account only hybridization between the three bands. This is enough to demonstrate how triplet pairing due mainly to AF spin excitations is possible. For this purpose, we calculate the Fermi surface (FS), the energy dispersion, and the spin susceptibility χ including *all* cross-susceptibilities. In the last subsection we compare our results with experiment. By analyzing experimental results for the ^{17}O Knight shift and INS data as well as the FS observed by ARPES [29], we can obtain values for the hopping integrals and the effective Coulomb repulsion U. Taking this as an input to the pairing interaction, we analyze the p–, d– and f–wave superconducting gap symmetries in Sect. 4.2 and demonstrate how triplet pairing is possible. This will be compared with the result obtained from the inclusion of spin–orbit coupling alone (i.e. without hybridization). In this case the parameters of the Hamiltonian are taken from band structure calculations. The delicate competition between weak ferromagnetic spin fluctuations and relatively strong incommensurate antiferromagnetic spin fluctuations due to nesting of the FS causes triplet Cooper pairing if spin–orbit coupling is taken into account. We shall also demonstrate that singlet $d_{x^2-y^2}$–wave symmetry (which is present in cuprates) is energetically less favorable. We summarize

our results, compare them with cuprate high–temperature superconductors, and give an opinion of the outlook in Sect. 4.3.

4.1 Elementary Spin Excitations in the Normal State of Sr_2RuO_4

4.1.1 Importance of Spin–Orbit Coupling

First, we show in Fig. 4.1 the results for the Lindhard response functions for the different bands, calculated using their tight–binding dispersions *without* taking into account the spin–orbit coupling using (2.34) and (2.35). As expected, owing to the pronounced nesting of the xz and yz bands, the susceptibilities of those bands display peaks at $\mathbf{Q}_i = (2\pi/3, 2\pi/3)$, while the xy band does not show any significant feature. On the other hand, the response of the xy band is enhanced owing to the presence of the van Hove singularity close to the Fermi level. It becomes clear that the features observed by INS relate mainly to the magnetic response of the xz and yz bands. However, the present results cannot account for the observed magnetic anisotropy, since both the longitudinal and the transverse components of the total spin susceptibility are the same if the term which transfers the anisotropy from the orbital subspace into the spin subspace is not taken into account. In order to do this, we include a spin–orbit coupling as we discussed in Chap. 2. Using in addition the random–phase approximation for each band (see Chap. 2 for

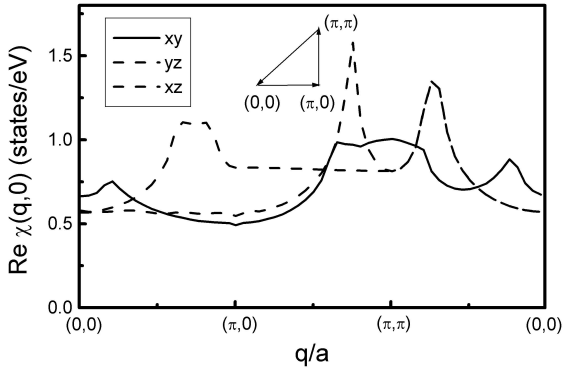

Fig. 4.1. Calculated real part of the Lindhard spin susceptibility $\chi_0^l(\omega = 0)$ in the normal state of Sr_2RuO_4 along the path $(0,0) \rightarrow (\pi,0) \rightarrow (\pi,\pi) \rightarrow (0,0)$ in the first two–dimensional square BZ for the $k_z = 0$ dispersion of the three different orbitals (xz, yz, and xy) crossing the Fermi level. Owing to the nesting of the xz and yz bands, their susceptibilities show an enhancement at the incommensurate antiferromagnetic wave vector $\mathbf{Q}_i = (2\pi/3, 2\pi/3)$. Note that the response of the xy band is more isotropic but significantly larger than that in the normal metal owing to the nearness of the van Hove singularity.

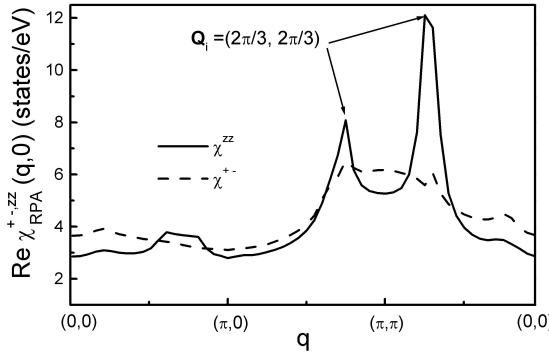

Fig. 4.2. Results for the real part of the out–of–plane (i.e. longitudinal, *solid curve*) and in–plane (i.e. transverse, *dashed curve*) magnetic response of an RuO_2 plane to H_z and H_{xy}, respectively. $\mathrm{Re}\chi(\mathbf{q}, \omega = 0)$ was calculated within the RPA including spin–orbit coupling, using $U = 0.505$ eV and $t_{hyb} = 0$, along the path $(0,0) \rightarrow (\pi,0) \rightarrow (\pi,\pi) \rightarrow (0,0)$ within the first Brillouin zone at a temperature T = 100 K using (2.45) and (2.46). (Note that χ^{zz} and χ^{+-} refer to the response of the projection of the orbitals d_{xy}, d_{xz}, and d_{yz} on the xy plane).

details) we have calculated the longitudinal and transverse components of the total susceptibility in the RuO_2 planes.

In Fig. 4.2, we show the results for the static limit of the real part of the transverse and longitudinal total susceptibilities $\chi^{+-,zz}_{RPA} = \sum_i \chi^{+-,zz}_{RPA,i}$ along the path $(0,0) \rightarrow (\pi,0) \rightarrow (\pi,\pi) \rightarrow (0,0)$ in the first Brillouin zone for $U = 0.505$ eV obtained using (2.45) and (2.46). Note the important difference between the two components. Most importantly, the IAF fluctuations at $\mathbf{Q}_i = (2\pi/3, 2\pi/3)$ are present in the case of xz and yz bands *only* in the longitudinal components of the spin susceptibility, and not in the transverse components. This is connected to the fact that matrix elements of type $u_{\mathbf{k}}$ and $v_{\mathbf{k}}$ are important because they suppress transition between "+" and "−" bands for the transverse susceptibilities. The transverse susceptibility is larger than the longitudinal one at small values of $\mathbf{q}$, indicating ferromagnetic fluctuations. These point mainly in the RuO_2 plane. On the other hand, the longitudinal component shows a structure at the IAF wave vector indicating a direction of the IAF fluctuations perpendicular to the RuO_2 plane.

We also want to emphasize that our results are in accordance with earlier estimates made by Ng and Sigrist [30], with one important difference. In addition to what was done in that work, we have included, in accordance with the mixing of the spin and orbital degrees of freedom, the orbital contribution to the magnetic susceptibility χ (i.e. we have used the g-factor for the vertex function). For example, owing to l_z and l_+ and (l_-) vertices at $\mathbf{Q}_i = (2\pi/3, 2\pi/3)$, χ^{zz} is affected by a factor of 2 from spin–orbit coupling. Moreover, in [30], it was found that the IAF fluctuations are slightly enhanced in the longitudinal components of the xz and yz bands in comparison with

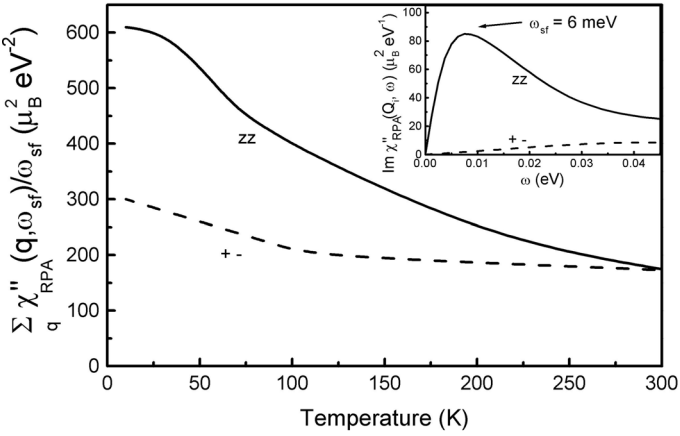

Fig. 4.3. Temperature dependence of the imaginary part of the spin susceptibility including spin–orbit coupling (but no hybridization), divided by the spin fluctuation energy ω_{sf} and summed over $\mathbf{q}$. Note, as in Fig. 4.2, that the notation zz and $+-$ refers to the out–of–plane (*solid curve*) and in–plane (*dashed curve*) components of the RPA spin susceptibility calculated for a single RuO_2 plane. In the *inset* we show the corresponding frequency dependence of $\mathrm{Im}\,\chi_{RPA}(\mathbf{Q_i}, \omega)$ at the IAF wave vector $\mathbf{Q}_i = (2\pi/3, 2\pi/3)$. The results for the out-plane component (*solid curve*) are in quantitative agreement with INS experiments [2].

the transverse component. In our case there are roughly *no* IAF fluctuations in the transverse component of the spin susceptibility. Furthermore, by taking into account the correlation effects within the RPA, we have shown that the IAF fluctuations will be further enhanced in the z direction.

This is illustrated further in the inset of Fig. 4.3, where we present the results for the frequency dependence of the imaginary parts of the total susceptibilities at $\mathbf{Q}_i = (2\pi/3, 2\pi/3)$ and a temperature $T = 20$ K. The longitudinal component has a peak at approximately $\omega_{sf} = 6$ meV, in quantitative agreement with experimental data from INS [2]. On the other hand, the transverse component is featureless, showing the absence of IAF spin fluctuations. This also indicates that the IAF fluctuations are aligned perpendicular to the RuO_2 plane.

In order to see the temperature dependence of the magnetic anisotropy induced by the spin–orbit coupling we display in Fig. 4.3 the temperature dependence of the quantity $\sum_{\mathbf{q}}(Im\,\chi_{RPA}(\mathbf{q}, \omega_{sf})/\omega_{sf})$ for both components. At room temperature, the longitudinal and transverse susceptibilities are almost identical, since thermal effects wash out the influence of the spin–orbit interaction. With decreasing temperature, the magnetic anisotropy arises and, at low temperatures, we find the important result that the out-of-plane component χ^{zz} is about two times larger than the in-plane one ($\chi^{zz} > \chi^{+-}/2$).

4.1.2 The Role of Hybridization

In order to contrast the influence of spin–orbit coupling with the effect of hybridization between all bands, we show in this subsection results for $t_{hyb} \neq 0$, but *without* spin-orbit coupling. We shall see that we obtain similar results (except for the spin anisotropy) in both cases, but with one important difference: hybridization transfers much more nested spectral weight from the d_{xz} and d_{yz} orbitals into the d_{xy} orbital. Thus the γ band will have much stronger nesting properties than in the case of spin–orbit coupling. For the moment, the neglect of spin–orbit coupling should be justified because the generalized Eliashberg equations are much easier to solve for the case of hybridization if one wishes to demonstrate how triplet pairing arises.

As an example, we show in Fig. 4.4 the momentum dependence of the real part of $\chi_0^{\gamma\gamma}$. While hybridization between bands has little effect on the energy dispersion, it changes significantly the susceptibility of the γ band. In particular, the nesting properties of the xz and yz orbitals, reflected by the peak again at $\mathbf{Q}_i = (2\pi/3, 2\pi/3)$ in $\chi_0^{\gamma\gamma}$, are caused by the hybridization between the xz, yz and xy bands. Note that without taking the hybridization into account one would not obtain the peak at $\mathbf{Q}_i$ in the γ band, but only a broad hump, as discussed earlier in [21] and which can be seen roughly from the χ^{+-} component in Fig. 4.2. The small peak at $\mathbf{q}_i \approx (0.2\pi, 0)$ is due to the original tendency towards ferromagnetism of the xy band and is not affected by the hybridization. Our results for $\chi(\mathbf{q}, \omega)$ will have important consequences for the pairing theory.

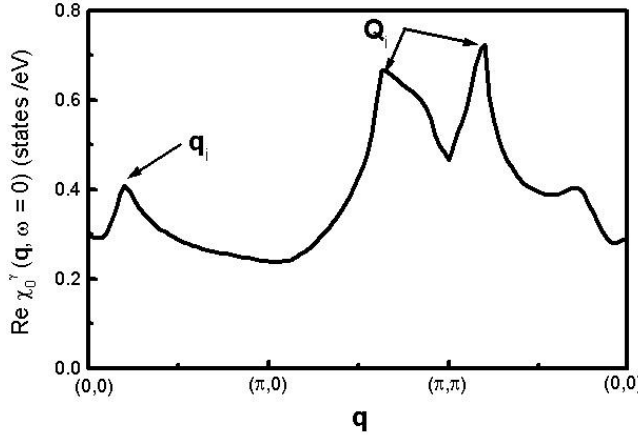

Fig. 4.4. Calculated susceptibility $\mathrm{Re}\chi_0^{\gamma\gamma}(\mathbf{q}, \omega = 0)$ obtained from electronic calculations without spin–orbit coupling using the hybridized bands. The wave vectors $\mathbf{Q}_i = (2\pi/3, 2\pi/3)$ and $\mathbf{q}_i \approx (0.2\pi, 0)$ reflect nesting transferred from the α and β bands and the original tendency of the γ band towards ferromagnetism, respectively.

In the next step, the susceptibility matrix $[\chi^{ij}]$ was calculated, where i, j refer to the hybridized bands. Our results for $\chi^{\alpha\alpha}$ and $\chi^{\beta\beta}$ are shown in Fig. 4.5a. For comparison, $\chi^{\gamma\gamma}$ is also displayed again. In Fig. 4.5b, our results for the cross–susceptibilities (i.e. the non diagonal elements of $[\chi_0^{ij}]$) are shown. As already mentioned, we find the important result that all elements

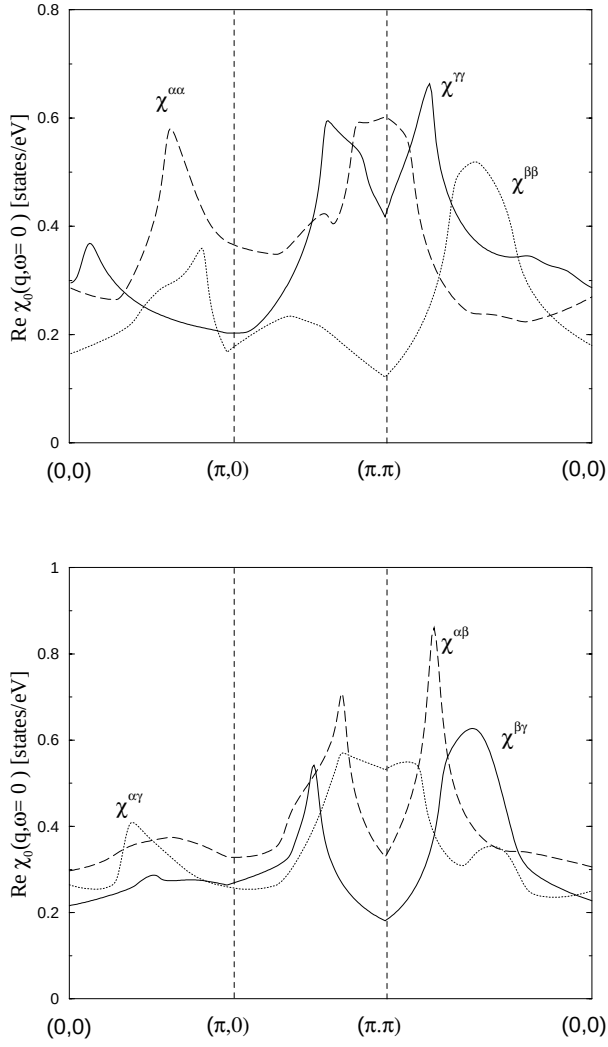

Fig. 4.5. (a) Calculated momentum dependence of $\mathrm{Re}\,\chi_0^{\alpha\alpha}$ (*dashed curve*) and $\mathrm{Re}\,\chi_0^{\beta\beta}$ (*dotted curve*) obtained using (2.35) and hybridized bands. For comparison, $\mathrm{Re}\,\chi^{\gamma\gamma}$ (*solid curve*) is also displayed. (b) Calculated momentum dependence of the corresponding cross–susceptibilities.

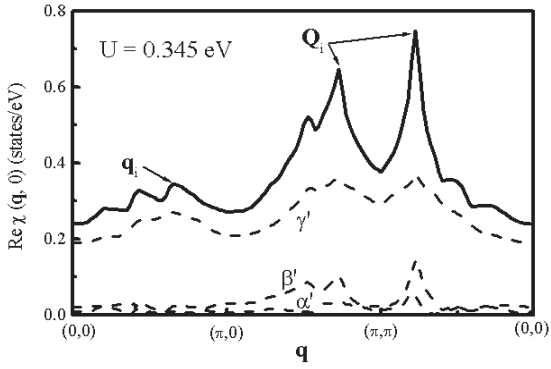

Fig. 4.6. Results for the static susceptibility at T = 50 K without spin–orbit coupling using hybridized bands obtained using (2.36) and (2.37). The *solid curve* refers to the total susceptibility within the RPA resulting from the partial susceptibilities $\mathrm{Re}\chi_0^{i'}$ ($i = \alpha', \beta', \gamma'$), shown by the *dashed curves*. The $\chi_0^{i'}$ refer to the diagonal elements of the diagonalized matrix $[\chi_0^{ij}]$. Note that the pairing wave vectors ($\mathbf{Q}_i$, $\mathbf{q}_i$) are nearly the same as in Fig. 4.4. Note also the smallness of $\chi_0^{\alpha'}$ and $\chi_0^{\beta'}$ compared with $\chi_0^{\gamma'}$.

of $[\chi_0^{ij}]$ are of the same order. In particular, the nondiagonalized susceptibilities are not small and thus cannot be neglected.

In Fig. 4.6, we present the results for the susceptibilities $\chi_0^{i'}(\mathbf{q},\omega)$ obtained after diagonalization of $[\chi_0^{ij}(\mathbf{q},\omega)]$ and the results for $\chi(\mathbf{q},\omega)$, obtained from (2.36) and (2.37). Here, we have approximated $U(\mathbf{q})$ by $U = 0.345$ eV which gives agreement with INS[1]. This will be discussed later. Remarkably, the peak in $\mathrm{Re}\chi$ at $\mathbf{Q}_i$ remains nearly the same as for $\chi_0^{\gamma\gamma}$. The peak at $\mathbf{q}_i$ is also present, but shifted slightly to a larger value. Clearly, $\chi_0^{\gamma'}$ is much larger than $\chi_0^{\alpha'}$ and $\chi_0^{\beta'}$. This clearly demonstrates again that the cross–susceptibilities χ_0^{ij} ($i \neq j$) cannot be neglected.

To conclude this subsection, we mention that the effective spin response of Sr_2RuO_4 after hybridization but without spin–orbit coupling consists mainly of *antiferromagnetic* spin fluctuations (see the peaks at wave vectors $\mathbf{Q}_i$) whereas the ferromagnetic fluctuations (i.e. $\mathbf{q} \to 0$) are much smaller. However, the antiferromagnetic fluctuations are incommensurate, yielding to a relatively long wavelength λ_{af}. Therefore, if the coherence length of a Cooper pair is smaller than λ_{af}, the effective pairing potential has locally a ferromagnetic character which favors triplet pairing. This will be discussed later.

[1] While the exact $\mathbf{q}$ dependence of U is unknown, it is reasonable to assume that $U(\mathbf{q})$ increases with $\mathbf{q}$. Thus, to fit the peak at $\mathbf{q} = \mathbf{Q}_i$ to the INS data one may need $U(\mathbf{Q}_i) > U(0)$, where $U(0)$ refers to $\chi(0,0)$.

4.1.3 Comparison with Experiment

In order to compare our results with experimental data, we have calculated the nuclear spin–lattice relaxation rate for an ^{17}O ion in an RuO_2 plane for different external magnetic field orientations (i $= a, b,$ and c),

$$\left[\frac{1}{T_1T}\right]_i = \frac{2k_B\gamma_n^2}{(\gamma_e\hbar)^2}\sum_{\mathbf{q}}|A_{\mathbf{q}}^p|^2\frac{\chi_p''(\mathbf{q},\omega_{sf})}{\omega_{sf}} \quad , \tag{4.1}$$

where $A_{\mathbf{q}}^p$ is the q–dependent hyperfine coupling constant and χ_p'' is the imaginary part of the corresponding spin susceptibility, *perpendicular* to the direction i. Similary to the experiment [11], we have used an isotropic hyperfine coupling constant ($^{17}A_{\mathbf{q}} \sim 22$ kOe/μ_B).

First, we discuss the spin anisotropy due to inclusion of spin–orbit coupling. In Fig. 4.7 we show the calculated temperature dependence of the spin–lattice relaxation for an external magnetic field parallel and perpendicular to the RuO_2 plane, together with experimental data. At $T = 250$ K, the spin–lattice relaxation rate is almost isotropic. Owing to the anisotropy in the spin susceptibilities arising from spin–orbit coupling, the relaxation rates become different with decreasing temperature. The largest anisotropy occurs close to the superconducting transition temperature, in good agreement with experimental data [11]. Thus, our results clearly demonstrate the essential significance of spin–orbit coupling for the spin–dynamics even in the normal state of the triplet superconductor Sr_2RuO_4. We find that the magnetic response becomes strongly anisotropic even within an RuO_2 plane: while the in–plane response is mainly ferromagnetic, the out–of–plane response is mainly antiferromagnetic–like.

In order to discuss both the long–wavelength and the short–wavelength limit of $\chi(\mathbf{q},\omega)$ we compare in Fig. 4.8a our calculation of the temperature dependence of the uniform spin susceptibility $\chi(0,0)$ with experiment, where this quantity is measured by the ^{17}O Knight shift [3]. For the calculation of $\chi(0,0)$, we have approximated $U(\mathbf{q})$ by $U(0) = 0.177$ eV [31] which gives agreement with Knight shift measurements and was also used in previous calculations. In agreement with experiment, we obtain a tendency towards ferromagnetism[2]. Note that we also take into account the fact that there are four electrons for three t_{2g} bands, which gives every $\chi_0^{i'}$ an additional weight of 4/3. The maximum in $\chi_{RPA}(0,0)$ at about 25 K results from thermally activated changes in the populations of the bands near E_F. Because the agreement with experiment is remarkably good (although the results were obtained without consideration of spin–orbit coupling), these comparisons shed light on the validity of our results for $\chi(\mathbf{q},\omega)$.

In Fig. 4.8b, we compare our results for $\mathrm{Im}\chi(\mathbf{Q}_i,\omega)$, again without spin–orbit coupling, with INS data [2]. In this case we must take $U_{\mathbf{Q}_i} = 0.345$ eV

[2] In the original paper [3], the effect of cross-susceptibilities was not considered. Therefore, we compare our results with the total susceptibility $\chi_{xy} + \chi_{yz} + \chi_{xz}$.

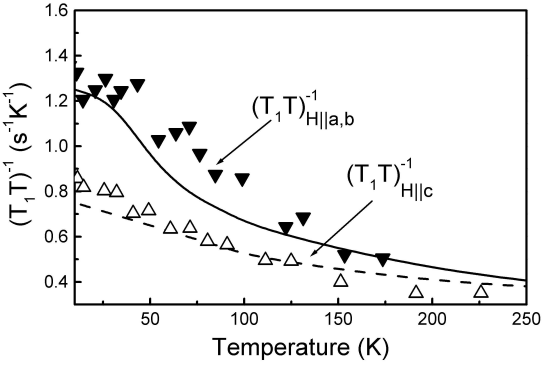

Fig. 4.7. Calculated normal–state temperature dependence of the nuclear spin–lattice relaxation rate T_1^{-1} of ^{17}O in an RuO_2 plane for an external magnetic field applied parallel to the c axis (*dashed curve*) and to the ab plane (*solid curve*). The corresponding susceptibilities include spin–orbit coupling. The *triangles* pointing up and down are experimental points taken from [11] for the corresponding magnetic–field directions.

in order to fit $\chi(\mathbf{q},\omega)$ to the position and height of the peak at $\omega = 6$ meV observed in INS. While an uncertainty in the INS data (shown in Fig. 4.8b) is present, our results for $\chi(\mathbf{q},\omega)$ should be a useful basis for further calculations. In general, the normal-state properties of $\chi(\mathbf{q},\omega)$ control also the symmetry of the superconducting order parameter. Physically speaking, the antiferromagnetic spin excitations result in incommensurate antiferromagnetic alignment Ru spin at distances larger than the nearest–neighbor spacing. Hence, if Cooper pairing involves nearest neighbor Ru spins, incommensurate antiferromagnetic fluctuations will also cause triplet pairing because neighboring Ru spins see a partly *ferromagnetic* environment.

In order to briefly summarize the comparison with experimental data, we can say the following: using hybridized bands and taking into account all cross–susceptibilities, we are able to explain successfully the ^{17}O Knight shift and INS data from our calculated dynamical spin susceptibility $\chi(\mathbf{q},\omega)$ based on the Fermi surface topology. However, in order to explain the anisotropy of the spin–lattice relaxation rate of ^{17}O in the RuO_2 planes with respect to the crystallographic direction of the external applied field, one needs to include spin–orbit coupling. As a result of this, the anisotropy of the orbital subspace is reflected in the spin response of the system. Note that the γ band is approximately a circle, whereas the α and β bands are quasi–one–dimensional and have strong nesting properties. Using $\lambda = 100$ meV as a parameter for the strength of the spin–orbit coupling and taking into account the large Stoner enhancement factor of the spin susceptibility (within the RPA), we are able to explain the unexpected by large anisotropy of the spin response of Sr_2RuO_4, namely that the in-plane response is mainly ferromagnetic–like

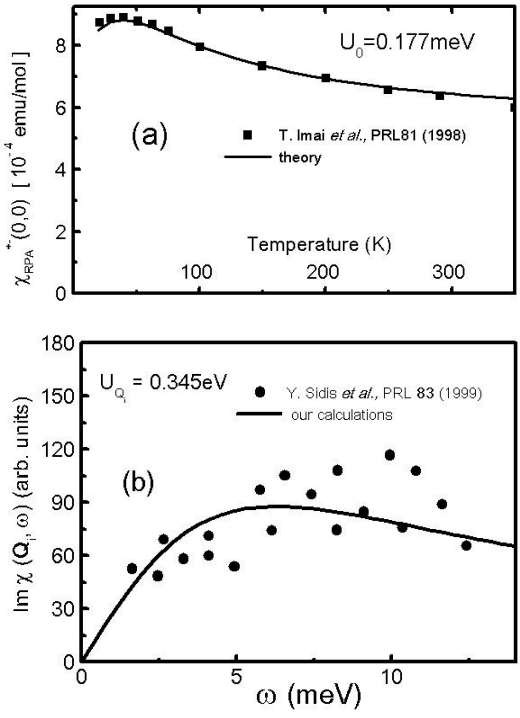

Fig. 4.8. (a) Calculated temperature dependence of the uniform spin susceptibility with $U_0 = 0.177$ eV, compared with ^{17}O Knight shift measurements. The peak is due to thermal activation involving the γ, α and β bands. **(b)** Calculated frequency dependence of $\mathrm{Im}\chi(\mathbf{Q}_i, \omega)$ using $U_{\mathbf{Q}_i} = 0.345$ eV, compared with INS data. Note that in order to obtain good agreement with both quantities (Knight shift and INS data), only hybridized bands, and no spin–orbit coupling, are needed.

and that the out–of–plane response is mainly antiferromagnetic-like. The implications of these findings for triplet Cooper pairing, following the equations derived in Chap. 2, will be discussed in the following section.

4.2 Symmetry Analysis of the Superconducting Order Parameter

For the analysis of superconductivity in Sr_2RuO_4, we take into account the fact that experiment indicates non–s–wave symmetry of the order parameter, which strongly suggests spin–fluctuation–mediated Cooper pairing. Then, assuming spin–fluctuation–induced pairing as derived in Chap. 2, it is possible to analyze in general the symmetry of the superconducting state on the basis of the gap equation and our calculated results for the spin excitation spectrum $\chi(\mathbf{q}, \omega)$, which consists of pronounced peaks at wave vectors $\mathbf{Q}_i$ and

$\mathbf{q}_i$. Thus we demonstrate how triplet pairing arising from ferromagnetic and strong antiferromagnetic excitations is possible.

4.2.1 Triplet Pairing Arising from Spin Excitations

Let us first discuss our results *without* spin–orbit coupling. Using appropriate symmetry representations [26], we discuss the solutions of the self–consistency equation for the superconducting order parameter (i.e. the gap equation, (2.49)) for the p–, d–, and f–wave symmetries of the order parameter:

$$\Delta_p(\mathbf{k}) = \Delta_0 \hat{\mathbf{z}}(\sin k_x + i \sin k_y) \ , \tag{4.2}$$

$$\Delta_d(\mathbf{k}) = \Delta_0(\cos k_x - \cos k_y) \ , \tag{4.3}$$

$$\Delta_f(\mathbf{k}) = \Delta_0 \hat{\mathbf{z}}(\cos k_x - \cos k_y)(\sin k_x + i \sin k_y) \quad . \tag{4.4}$$

The largest eigenvalue λ_l of (2.49) will yield the superconducting symmetry of Δ_l in Sr_2RuO_4. When we solve (2.49) for the γ band numerically in the first Brillouin zone down to 5 K, we find f–wave symmetry to be slightly favored. As expected, p– and f–wave symmetry Cooper pairing are close in energy ($\lambda_f = 0.76 > \lambda_p = 0.51$). However, these calculations were restricted to a single RuO_2 plane. A more complete analysis taking into account the coupling between RuO_2 planes and an interband U might yield a more definite answer. For example, if the energy difference between p– and f–wave symmetry in the RuO_2 planes is larger than the energy gain for superconductivity resulting from interplane coupling, one may determine the pairing symmetry from the in–plane electronic structure. Note that to obtain a combined energy gain from the antiferromagnetism and Cooper pairing, one would require an order parameter with nodes in the RuO_2 plane and possibly also with respect to the c direction. However, this question cannot be answered if 2.49 is solved for the two–dimensional case.

Let us now come back to the question of why triplet pairing is possible as a result of antiferromagnetic spin excitations. To be more precise, the solutions of (2.49) can be characterized by Fig. 4.9, where we present our results for the Fermi surface, the wave vectors $\mathbf{Q}_i$ and $\mathbf{q}_i$ defined in Fig. 4.6, and symmetry of the order parameter in Sr_2RuO_4. The areas with $\Delta_f > 0$ and $\Delta_f < 0$ are denoted by $+$ and $-$, respectively. The summation over $\mathbf{k}'$ in the first BZ is dominated by the contributions due to $\mathbf{Q}_i$ and a contribution due to the background and $\mathbf{q}_i$. Thus, we obtain approximately the following for the γ–band contribution ($l = f$ or p)

$$\Delta_l(\mathbf{k}) \approx \sum_i \frac{V_1^{eff}(\mathbf{Q}_i)}{2\epsilon^{\gamma}_{\mathbf{k}+\mathbf{Q}_i}} \Delta_l(\mathbf{k}+\mathbf{Q}_i) + \sum_i \frac{V_1^{eff}(\mathbf{q}_i)}{2\epsilon^{\gamma}_{\mathbf{k}+\mathbf{q}_i}} \Delta_l(\mathbf{k}+\mathbf{q}_i) \quad , \tag{4.5}$$

where the sum is over all contributions due to $\mathbf{Q}_i$ and $\mathbf{q}_i$. As can be seen from Fig. 4.9, in the case of f–wave symmetry the wave vector $\mathbf{q}_i$ in (1.14) bridges the same number of portions of the FS with opposite and equal signs.

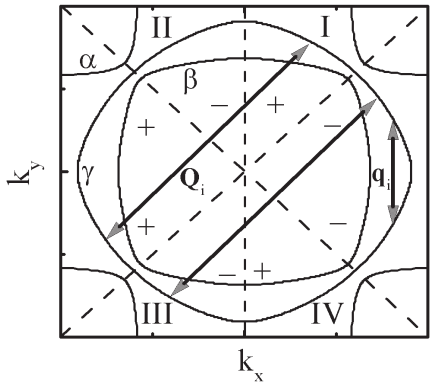

Fig. 4.9. Illustration of possible triplet pairing due to antiferromagnetic spin excitations in the first BZ. α, β, and γ denote the Fermi surfaces of the corresponding hybridized bands. For simplicity, no spin–orbit coupling has been taken into account. The wave vectors $\mathbf{Q}_i$ and $\mathbf{q}_i$ are the wave vectors of the pronounced features in the susceptibility shown in Fig. 4.6. In a weak–coupling approach, these wave vectors of the γ band dominate the pairing potential entering the gap equation (2.49) yielding to (4.5). Thus these wave vectors would then determine the symmetry of the order parameter in a simple way. Also, for f–wave symmetry, the nodes of the real part of the order parameter are shown (*dashed lines*), together with the regions where the f–wave superconducting gap is positive and negative (+ and −, respectively). Note that for the real part of the p–wave order parameter the node occurs along $k_x = 0$. It is clear from Fig. 4.6 that increasing nesting favors triplet f-wave symmetry. Our illustration shows also that singlet d–wave Cooper pairing is not possible.

Therefore, the second term in (1.14) is approximately zero for triplet pairing. We see from Fig. 4.9 that $\mathbf{Q}_i$ bridges portions of the FS with *equal* signs of the superconducting order parameter. Thus, a solution of (1.14) for Δ_f is indeed possible.

In the case of p–wave pairing, the real part of the order parameter has a node only along $k_x = 0$ in the k_x, k_y plane. Then, the wave vectors $\mathbf{Q}_i$ bridge portions of the FS where $\mathrm{Re}\Delta_p$ has either the same or the opposite sign. Regarding the $\mathbf{q}_i$ contributions, the situation is similar to that in the case of f–wave symmetry. Hence, we expect $\lambda_p \leq \lambda_f$ for the eigenvalues, as in the result of the algebraic solution of (2.49). Note that for increasing nesting, Fig. 4.9 also suggests that f–wave symmetry is favored more than p–wave. An eigenvalue analysis of the possible solutions Δ_f and $\Delta_p + i\Delta_f$ should increasingly rule out the latter for stronger nesting.

Also, using similar arguments, we can rule out singlet pairing on the basis of (2.47). In particular, assuming $d_{x^2-y^2}$ symmetry for Sr_2RuO_4, we obtain a change of sign of the order parameter upon crossing the diagonals of the BZ. According to (2.49), wave vectors around $\mathbf{Q}_i$ connecting areas marked + and

– contribute constructively to the pairing. Contributions due to $\mathbf{q}_i$ and the background connecting areas with the same sign subtract from the pairing (see Fig. 4.9, with nodes at the diagonals, for an illustration). Therefore, we find that the four contributions due to $\mathbf{q}_i$ and the background cancel the pair-building contribution due to $\mathbf{Q}_i$. As a consequence, we obtain no $d_{x^2-y^2}$-wave symmetry.

Thus, without spin–orbit coupling, as a result only of the topology of the FS and the spin susceptibility, we obtain the strongest pairing for p and f waves and can definitely exclude d–wave pairing. This is in agreement with the numerical solution of (2.49). We have used general arguments which become exact for a given frequency (e.g. $\omega = 0$) if the main pairing occurs at the Fermi level. However, strong feedback effects of the self–energy on the one–particle spectrum, and mode–mode coupling effects have been neglected. Nevertheless, our general arguments seem still to be valid in our approximation. Within this approximation, we also find that f–wave symmetry pairing is slightly favored over p–wave symmetry in Sr_2RuO_4 owing to strong nesting of the bands.

Consideration of Spin–Orbit Coupling

What, now, is the role of spin–orbit coupling in determining the symmetry of the superconducting order parameter? First, the spin–orbit coupling affects the spin dynamics and, as we have shown, induces an anisotropy in the spin subspace. In particular, the two–dimensional IAF fluctuations at $\mathbf{Q}_i = (2\pi/3, 2\pi/3)$ are polarized along the z direction. This simply means that the antiferromagnetic moments associated with these fluctuations are aligned parallel to the z direction, and roughly no nested spectral weight is transferred to the γ band. At the same time, the ferromagnetic fluctuations are in the ab plane. This is in striking contrast to the case discussed above, where when we neglect spin–orbit coupling but include the hybridization between the xy, xz and yz bands, *both* the ferromagnetic *and* the IAF fluctuations are located within the ab plane. This would lead to nodes within an RuO_2 plane. However, owing to the magnetic anisotropy induced by spin–orbit coupling, a nodeless p–wave pairing is possible in an RuO_2 plane, as experimentally observed, and a node would lie *between* the RuO_2 planes. The corresponding situation is illustrated in Figs. 4.10 and 4.11. The important IAF wave vector $\mathbf{Q}_i$ now connects the nested portions of the β band, while the small $\mathbf{q}_i$ bridges the γ band. Therefore, since the interaction in the RuO_2 planes ($k_z = 0$) is mainly ferromagnetic, nodeless p–wave pairing is indeed possible, and the superconducting order parameters in all three bands will not have nodes. On the other hand, the situation between the RuO_2 planes will be determined mainly by the IAF excitations, which are mainly located in the β band and polarized along the z direction. This implies that the magnetic interaction between the planes has to be antiferromagnetic rather than

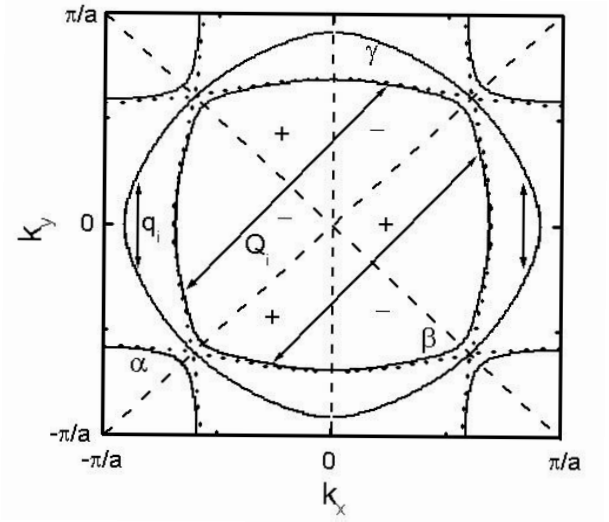

Fig. 4.10. Symmetry analysis of the superconducting order parameter for triplet pairing due mainly to $\mathbf{q}_i$ in the first BZ for $k_z = 0$ (*solid curves*) and $k_z = \pi/2c$ (*dotted curves*), after inclusion of spin-orbit coupling. α, β, and γ denote the corresponding Fermi surfaces and the wave vectors $\mathbf{Q}_i$ and $\mathbf{q}_i$ are the corresponding spin excitations shown in Fig. 4.2. For clarity, again the nodes of the real part of an order parameter with $f_{x^2-y^2}$–wave symmetry are shown, and also the regions + and − where the gap has positive and negative sign, respectively. Note that although a p–wave order parameter has no nodes, for the symmetry analysis we consider the real part of it, which has a node for $k_x = 0$. The γ band plays the dominant role in Cooper pairing ($N_\gamma(0) > N_{\alpha,\beta}(0)$).

ferromagnetic. In the superconducting state, this antiferromagnetic interaction would disturb triplet Cooper pairing and induce a line of nodes between neighboring RuO_2 planes. This was shown by two groups in a phenomenological approach [8, 9].

The second result of the spin–orbit coupling is the orientation of the orbital moment of the Cooper pair. As is known from experimental data, the superconducting state is characterized by violation of time–reversal symmetry [32] and equal spin pairing within the basal plane of the tetragonal crystal lattice [33]. The single symmetry representation consistent with these experiments is $\mathbf{d}(\mathbf{k}) = \tilde{\mathbf{z}}(\sin k_x \pm i \sin k_y)$ in an RuO_2 plane in the standard vector notation. The important consequence of this order parameter is the orbital angular momentum of the Cooper pair (the "chiral" state). Taking into account the fact that there are other symmetry representations that possess p–wave symmetry, the important question is why the "chiral" state has a lower energy than the other representations. A theoretical study of this question, assuming magnetically mediated Cooper pairing, was done by Ng and Sigrist [30] and partly by Kuwabara and Ogata [27]. As we indicated previ-

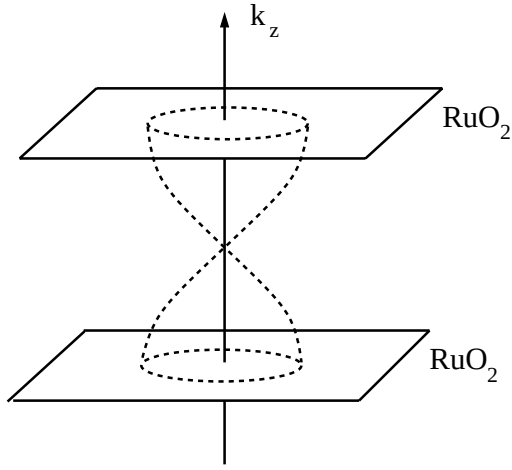

Fig. 4.11. Schematic representation of the k_z dependence of the superconducting order parameter. Here, the amplitude of the order parameter along k_z has been drawn in cylindrical coordinates between RuO_2 planes. Owing to inclusion of spin–orbit coupling, one expects nodes between these planes.

ously, spin–orbit coupling results in mixing of the spin and orbital degrees of freedom. The new quasiparticles are labeled with pseudo–spin and pseudo–orbital quantum numbers. Furthermore, the spin–orbit coupling introduces a magnetic anisotropy along the z direction and, as a result, a superconducting state with a preferred direction of the orbital moment is realized. As has been shown in [30], the "chiral" state is indeed lower in energy in an RuO_2 plane for a realistic set of parameters, suggesting that the d_{xy} orbital is the orbital mostly involved in superconductivity.

4.3 Summary, Comparison with Cuprates, and Outlook

In summary, using a two-dimensional Hubbard Hamiltonian for the three electronic bands crossing the Fermi level in Sr_2RuO_4, we have employed a tight–binding description of the band structure and calculated the spin susceptibility $\chi(\mathbf{q}, \omega)$ and have found the results to be in quantitative agreement with nuclear magnetic resonance and inelastic neutron scattering experiments. The susceptibility has two peaks at $\mathbf{Q}_i = (2\pi/3, 2\pi/3)$ due to the nesting properties of the Fermi surface and a peak at $\mathbf{q}_i = (0.6\pi, 0)$ due to the tendency towards ferromagnetism.

First, we have considered hybridization between all three bands and shown that this is important because it transfers the nesting properties of the xz and yz orbitals to the γ band in Sr_2RuO_4. Taking into account all cross-susceptibilities, we can successfully explain the ^{17}O Knight shift and INS data. Most importantly, by applying spin–fluctuation exchange theory, have

shown, on the basis of only the Fermi surface topology and the calculated spin susceptibility $\chi(\mathbf{q},\omega)$, that triplet pairing is present in Sr_2RuO_4. We can exclude s and d wave symmetry for the superconducting order parameter. These calculations we done *without* spin–orbit coupling and we found that f–wave symmetry pairing is slightly favored over p–wave symmetry. To decide whether p– or f–wave symmetry pairing or nodes between the RuO_2 planes are present in Sr_2RuO_4, one needs to perform more complete calculations, including coupling between RuO_2 planes for example. If the interplane coupling also involves nesting, then corresponding nodes reflecting the incommensurability of the excitations are expected. In view of Fig. 4.9, we also remark that while $\mathrm{Re}\Delta_f$ exhibits three line nodes that can be seen by phase–sensitive experiments, $|\Delta_f|^2$ shows nodes only along the diagonals, as recently found in measurements of ultrasound attenuation below T_c [34]. However, in view of the low eigenvalues for the p– and f–wave symmetries and the different approximations used, we cannot definitely conclude that f–wave symmetry is favored over p–wave.

Secondly, we have considered the inclusion of spin–orbit coupling and have found that this is important because it couples the orbital and spin degrees of freedom. Thus the orbital anisotropy (the nested α and β bands are quasi–one–dimensional and the γ band is almost a circle) is then reflected in the spin response of the system, which can be measured by the NMR spin–lattice relaxation rate $1/T_1T$ vs. T, for example. In the normal state we find the important result that $\chi^{zz} > \chi^{+-}$ for small temperatures T, in good agreement with experiment. Simply speaking, the in–plane response is mainly ferromagnetic-like and the out–of–plane response is mainly antiferromagnetic–like and dominated by the wave vectors $\mathbf{Q}_i$. We also have investigated the symmetry of the order parameter when spin–orbit coupling is included. We find that triplet p–wave pairing within the RuO_2 planes is favored owing to the importance of the small wave vectors $\mathbf{q}_i$ and the fact that the γ band is not nested. The nesting properties are now present mainly in the quasi–one–dimensional β band and the corresponding antiferromagnetic spin excitations point along the z direction. Thus, in an electronic theory, if coupling between the RuO_2 planes is taken into account, we expect nodes *between* the RuO_2 planes and nodeless p–wave pairing within the RuO_2 planes.

In comparison with high–T_c cuprate superconductors, we can say the following. In both hole–doped and electron-doped cuprates, a one–band tight–binding description is appropriate for explaining the electronic properties, whereas in Sr_2RuO_4 a three–band picture with hybridization between the bands and the inclusion of spin–orbit coupling is necessary. For Sr_2RuO_4 as well as for the cuprates, one finds that spin fluctuations are present and are mainly of antiferromagnetic character. However, owing to the tendency towards ferromagnetism and the presence of *incommensurate* spin fluctuations in Sr_2RuO_4, this material is close to a spin-triplet superconducting phase transition. Physically speaking, if the spins of the quasiparticles are already

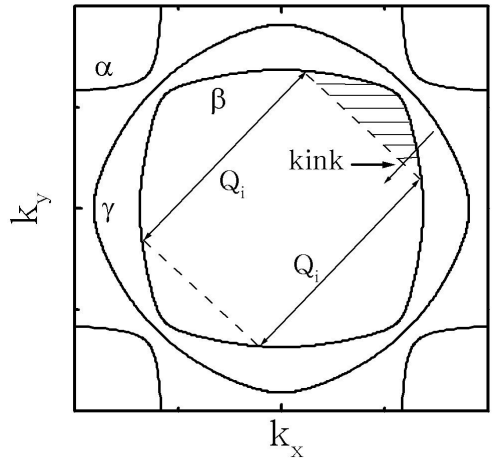

Fig. 4.12. Illustration of a possible kink structure in Sr_2RuO_4. The nesting properties of the β band lead to the formation of two–dimensional incommensurate spin fluctuations at $\mathbf{Q}_i = (2\pi/3, 2\pi/3)$ and $\omega_{sf} \approx 6$ meV. Therefore, the quasiparticles in the β band should be strongly renormalized owing to coupling to spin fluctuations.

(almost) aligned in the normal state (at least within the RuO_2 planes), the superconducting state will be of triplet type because the energy gain in a simple Ginzburg–Landau description, $\Delta F = F_S - F_N$ (as discussed in Chap. 3), is large. In addition the antiferromagnetic spin excitations in the cuprates act within a CuO_2 plane, yielding singlet d–wave pairing, whereas in Sr_2RuO_4 the antiferromagnetic spin excitations point along the z direction. The remaining ferromagnetic spin excitations within the RuO_2 planes yield (also because of a high density of states) triplet p–wave pairing.

In order to compare the pairing mechanisms in more detail, we would like to point out that the main difference between Fig. 3.10b for the electron–doped cuprate superconductor $Nd_{2-x}Ce_xCuO_4$ (NCCO) and Fig. 4.9 is the sign change of the order parameter along the diagonal directions in the first Brillouin zone. This is consistent with the fact that the pairing potentials for singlet and triplet pairing (see (2.47) and (2.48)) also yield different signs owing to Pauli's principle. Simply speaking, singlet pairing in cuprates consists of a *repulsive* interaction in $\mathbf{k}$–space[3], whereas the exchange of spin fluctuations yielding triplet pairing is *attractive* in momentum space and thus similar to phonons. Therefore, singlet Cooper pairing in cuprates naturally leads to d-wave symmetry of the superconducting order parameter Δ, because nodes and sign changes in Δ are required to solve the corresponding

[3] Of course, in real space on a lattice, after Fourier transformation, quasiparticles on nearest-neighbor sites interact with an attractive pairing potential. The terms "repulsive" and "attractive" that we use here refer to momentum space in the spirit of the BCS theory.

gap equation. On the other hand, an attractive pairing in **k**–space, which is present in Sr_2RuO_4, does not favor the existence of nodes in general. Thus, to a first approximation, one would expect a p–wave symmetry of Δ. However, if spin fluctuations are mainly antiferromagnetic and the nesting of the corresponding bands is strong, it is also possible to find f–wave pairing and thus nodes in Sr_2RuO_4. Finally, we have included spin–orbit coupling and find that these nodes should occur *between* the RuO_2 planes. Phase-sensitive measurements (as in cuprates) should be performed in order to clarify this issue.

Finally, we want to emphasize that the important formation of the kink feature due to spin fluctuations is not expected to be restricted to cuprates. As discussed above, Sr_2RuO_4 reveals pronounced incommensurate antiferromagnetic spin fluctuations at a wave vector $\mathbf{Q}_i = (2\pi/3, 2\pi/3)$ and frequency $\omega_{sf} \approx 6$ meV that originate from the nesting properties of the quasi–one–dimensional α and β bands. Thus, on general grounds, one would expect a kink structure in the renormalized energy dispersion of the quasiparticles (see Fig. 4.12 for an illustration). Although the correlation effects are weaker in Sr_2RuO_4 (U is smaller and it is a Fermi liquid), and $\mathbf{Q}_i$ is an incommensurate wave vector, similar conditions to those in cuprates are present. Note that the kink feature should occur at smaller energies than in cuprates owing to the lower value of ω_{sf} in the ruthenates. Recent ARPES data support this picture [35].

What are the next steps for a theory of strontium ruthenate? Interestingly, in $Ca_{2-x}Sr_xRuO_4$ various phase transitions occur, and a transition from triplet superconductivity in Sr_2RuO_4 to an antiferromagnetic Mott–Hubbard insulator in Ca_2RuO_4 has been found [36]. For example, for $x < 0.2$, $Ca_{2-x}Sr_xRuO_4$ is an insulator, and for the doping range $0.2 < x < 0.5$ this material is a metal with short-range antiferromagnetic order. At $x \simeq 0.5$ there is a crossover which is accompanied by a sharp enhancement of the ferromagnetic fluctuations in the uniform spin susceptibility. Only for $x \to 2$ the system does become superconducting with triplet Cooper pairing.

Recently, an attempt to explain the magnetic phase diagram of the material $Sr_{2-x}Ca_xRuO_4$ has been made on the basis of *ab initio* band structure calculations [37]. It has been shown that the rotations of the RuO_6 octahedra around the c axis stabilize the ferromagnetic state, since they are sufficient to reduce the pd–π hybridization between the xy orbitals and the oxygen $2p$ states. Consequently the xy band becomes narrower and the van Hove singularity shifts towards the Fermi level. At the same time, the xz and yz bands are only slightly affected. On the other hand, the rotation around axes within the ab plane changes all three bands completely and increases the nesting of the xz and yz bands, and may stabilize the antiferromagnetic phase [37].

In such a picture, it is easy to understand why the ferromagnetic fluctuation are strongly enhanced around the so–called critical doping $x \simeq 0.5$. Using the LDA parameters for the tight–binding energy dispersion, we have calcu-

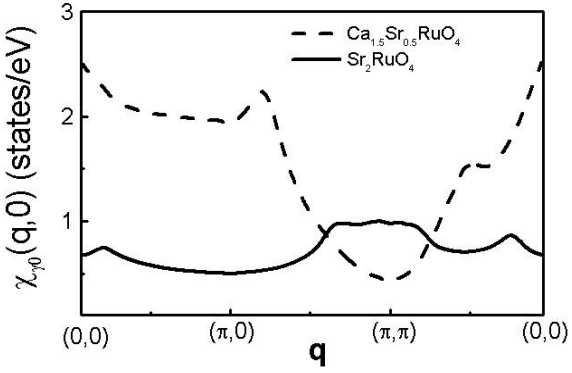

Fig. 4.13. The calculated real part of the Lindhard response function $\chi_{\gamma 0}(\mathbf{q}, 0)$ along the symmetry points in the BZ, for the γ band in $Ca_{0.5}Sr_{1.5}RuO_4$ and Sr_2RuO_4. Owing to the closeness of the van Hove singularity, the response of the γ band is strongly enhanced and ferromagnetic (around $\mathbf{q} = 0$). This is in fair agreement with experiment [38].

lated the Lindhard response function of the xy band for $Ca_{0.5}Sr_{1.5}RuO_4$ and Sr_2RuO_4, as shown in Fig. 4.13. One can clearly see that the ferromagnetic response of the $xy(\gamma)$ band is strongly enhanced at $\mathbf{q} = 0$ owing the closeness of the van Hove singularity. Furthermore, since the α and β bands are almost unchanged, the ferromagnetic response becomes much stronger than the antiferromagnetic response, indicating the dominance of the ferromagnetic fluctuations around this critical point $x \simeq 0.5$. This is in good agreement with experiment [38]. However, this model cannot explain the Mott–Hubbard transition in Ca_2RuO_4 at finite temperatures, of course, since Ca_2RuO_4 remains an insulator even above T_N. Therefore, strong electronic correlations have to be taken into account, as proposed recently by Ovchinnikov [39]. He suggested that while the xz and yz bands are split into lower and upper Hubbard bands, the xy band does not split although it is close to the Mott–Hubbard transition.

Finally, although our calculations we performed in the clean limit, one might ask what happens if impurities are added to Sr_2RuO_4. It is well known that unconventional superconductors show peculiar behavior if one adds magnetic or nonmagnetic impurities. In contrast to conventional (s–wave) superconductors, both nonmagnetic and magnetic impurities act as strong pair breakers and suppress the transition temperature T_c. This reflects the sensitivity to translational symmetry breaking and is characteristic of anisotropic Cooper pairing. The effects induced by magnetic and nonmagnetic impurities in cuprates are not well understood. For example, when these materials are doped with nonmagnetic Zn, local magnetic moments within the CuO_2 planes are induced around these impurities, which show a Kondo–like behavior [40].

Recently, the first study of the effects induced by the substitution of the magnetic impurity (Ir^{4+}) and the nonmagnetic impurity (Ti^{4+}) in the RuO_2 planes has been performed [41]. Here, the observed effects are also quite peculiar. Similarly to cuprates, the substitution of the nonmagnetic impurity Ti^{4+} ($3d^0$) in Sr_2RuO_4 induces a local magnetic moment with an effective moment $\sim 0.5\mu_B$/Ti [42]. The induced moment has Ising anisotropy with an easy axis along the c direction. Furthermore, magnetic ordering with glassy behavior appears for $x(\mathrm{Ti}) > 0.025$ in $Sr_2Ru_{1-x}Ti_xO_4$, while the metallic conduction in the in–plane direction is retained. When x is increased further to 0.09, elastic neutron scattering measurements detect an incommensurate Bragg peak whose wave vector $\mathbf{Q}_{ic} \sim (2\pi/3, 2\pi/3)$ is close to the position of the inelastic neutron scattering peak in pure Sr_2RuO_4 [43]. Most interestingly, in the vicinity of a magnetic ordering, a deviation from the pure Fermi liquid behavior seen in Sr_2RuO_4 is observed by means of resistivity and transport measurements, which show linear and logarithmic temperature dependence, respectively [44]. These results indicate that the two–dimensional incommensurate antiferromagnetic spin fluctuations arising from the nesting of xz and yz bands become a static spin density wave state when Ti is substituted. On the other hand, the system $Sr_2Ru_{1-x}Ir_xO_4$ in which the substitutional impurity is the magnetic Ir^{4+} ($5d^5$ in the low spin configuration), shows a weak ferromagnetism for $x(\mathrm{Ir}) > 0.3$ [45]. Thus, substitution of magnetic and nonmagnetic impurities in Sr_2RuO_4 leads to different ground states. In short, despite these differences, both magnetic and nonmagnetic impurities act similarly because both reduce T_c. Thus, one might conclude that magnetic and nonmagnetic impurities act mainly as potential scatterers and that magnetic scattering does not play a particular role. To some extent, this observation is consistent with the existence of a spin triplet state because magnetic impurities break up singlet Cooper pairs, mainly as a result of exchange splitting, while an equally paired spin state would not be affected.

References

1. Y. Maeno, H. Hashimoto, K. Yoshida, S. Nishizaki, T. Fujita, J. G. Bednorz, and F. Lichtenberg, Nature **372**, 532 (1994); Y. Maeno, T.M. Rice, and M. Sigrist, Phys. Today **54**, 42 (2001). 177
2. Y. Sidis, M. Braden, P. Bourges, B. Hennion, S. Nishizaki, Y. Maeno, and Y. Mori, Phys. Rev. Lett. **83**, 3320 (1999). 177, 181, 185
3. T. Imai, A. W. Hunt, K. R. Thurber, and F. C. Chou, Phys. Rev. Lett. **81**, 3006 (1998). 177, 185
4. H. Mukuda, K. Ishida, Y. Kitaoka, K. Asayama, Z. Mao, Y. Mori, and Y. Maeno, J. Phys. Soc. Jpn. **67**, 3945 (1998); H. Mukuda, K. Ishida, Y. Kitaoka, K. Asayama, R. Kanno, and M. Takano, Phys. Rev. B. **60**, 12279 (1999). 177
5. I. I. Mazin and D. J. Singh, Phys. Rev. Lett. **82**, 4324 (1999); D. J. Singh, Phys. Rev. B. **52**, 1358 (1995). 177, 178

6. M. A. Tanatar, M. Suzuki, S. Nagai, Z. Q. Mao, Y. Maeno, and T. Ishiguro, Phys. Rev. Lett. **86**, 2649 (2001). 177
7. K. Izawa, H. Takahashi, H. Yamaguchi, Y. Matsuda, M. Suzuki, T. Sasaki, T. Fukase, and Y. Yoshida, Phys. Rev. Lett. **86**, 2653 (2001). 177, 178
8. M. E. Zhitomirsky, and T. M. Rice, Phys. Rev. Lett. **87**, 057001 (2001). 177, 191
9. J. F. Annett, G. Litak, B. L. Gyorffy, and K. I. Wysokinsi, preprint cond-mat/0109023 (unpublished). 177, 191
10. F. Servant, S. Raymond, B. Fak, P. Lejay, and J. Flouquet, Solid State Commun. **116**, 489 (2000). 177
11. K. Ishida, H. Mukuda, Y. Minami, Y. Kitaoka, Z. Q. Mao, H. Fukazawa, and Y. Maeno, Phys. Rev. B **64**, 100501(R) (2001). 177, 178, 185, 186
12. K. Ishida, Y. Kitaoka, K. Asayama, S. Ikeda, S. Nishizaki, Y. Maeno, Y. Yoshida, and T. Fujita, Phys. Rev. B **56**, R505 (1997). 178
13. K. Ishida, H. Mukuda, Y. Kitaoka, Z. Q. Mao, H. Fukazawa, and Y. Maeno, Phys. Rev. B **63**, 060507(R) (2001). 178
14. J. A. Duffy, S. M. Hayden, Y. Maeno, Z. Mao, J. Kulda, and G. J. McIntyre, Phys. Rev. Lett. **85**, 5412 (2000). 178
15. T. M. Rice and M. Sigrist, J. Phys.: Condens. Matter **7**, L643 (1995). 178
16. M. Sigrist, D. Agterberg, A. Furusaki, C. Honerkamp, K. K. Ng, T. M. Rice, and M. E. Zhitomirsky, Physica C **317–318**, 134 (1999); D. F. Agterberg, T. M. Rice, and M. Sigrist, Phys. Rev. Lett. **78**, 3374 (1997). 178
17. L. Tewordt, Phys. Rev. Lett. **83**, 1007 (1999). 178
18. L. Tewordt and T. Dahm, Phys. Rev. B **63**, 092505 (2001); L. Tewordt and D. Fay, Phys. Rev. B **64**, 024528 (2001); L. Tewordt and D. Fay, Phys. Rev. B **65**, 104510 (2002). 178
19. M. Sato and M. Kohmoto, J. Phys. Soc. Jpn. **69**, 3505 (2000). 178
20. T. Nomura and K. Yamada, J. Phys. Soc. Jpn. **69**, 3678 (2000). 178
21. T. Takimoto, Phys. Rev. B **62**, R14641 (2000). 178, 182
22. H. Won and K. Maki, Europhys. Lett. **52**, 427 (2000); T. Dahm, H. Won, and K. Maki, preprint cond-mat/0006301 (unpublished). 178
23. M. J. Graf and A. V. Balatsky, Phys. Rev. B **62**, 9697 (2000). 178
24. D. K. Morr, P. F. Trautmann, and M. J. Graf, Phys. Rev. Lett. **86**, 5978 (2001). 178
25. K. Kuroki, M. Ogata, R. Arita, and H. Aoki, Phys. Rev. B **63**, 060506(R) (2001). 178
26. Y. Hasegawa, K. Machida, and M. Ozaki, J. Phys. Soc. Jpn. **69**, 336 (2000). 178, 188
27. T. Kuwabara and M. Ogata, Phys. Rev. Lett. **85**, 4586 (2000). 178, 191
28. A. K. Gupta and K.-W. Ng, Phys. Rev. B **58**, R8901 (1998). 178
29. A. Damascelli, D. H. Lu, K. M. Shen, N. P. Armitage, F. Ronning, D. L. Feng, C. Kim, Z. X. Shen, T. Kimura, Y. Tokura, Z. Q. Mao, and Y. Maeno, Phys. Rev. Lett. **85**, 5194 (2000); A. Liebsch, Phys. Rev. Lett. **87**, 239701 (2001); A. Damascelli, K. M. Shen, D. H. Lu, and Z.-X. Shen, Phys. Rev. Lett. **87**, 239702 (2001). 178
30. K. K. Ng and M. Sigrist, Europhys. Lett. **49**, 473 (2000). 180, 191, 192
31. A. Liebsch and A. Lichtenstein, Phys. Rev. Lett. **84**, 1591 (2000). 185
32. G. M. Luke, Y. Fudamoto, K. M. Kojima, M. I. Larkin, J. Merrin, B. Nachumi, Y. J. Uemura, Y. Maeno, Z. Q. Mao, Y. Mori, H. Nakamura, and M. Sigrist, Nature **394**, 558 (1998). 191

33. K. Ishida, H. Mukuda, Y. Kitaoka, K. Asayama, Z. Q. Mao, Y. Mori, and Y. Maeno, Nature **396**, 658 (1998). 191
34. C. Lupien, W. A. MacFarlane, C. Proust, L. Taillefer, Z. Q. Mao, and Y. Maeno, Phys. Rev. Lett. **86**, 5986 (2001). 193
35. P. D. Johnson, private communication. 195
36. S. Nakatsuji and Y. Maeno, Phys. Rev. Lett. **84**, 2666 (2000); Phys. Rev. B **62**, 6458 (2000). 195
37. Z. Fang and K. Terakura, Phys. Rev. B **64**, 020509 (2001). 195
38. O. Friedt, M. Braden, G. Andre, P. Adelmann, S. Nakatsuji and Y. Maeno, Phys. Rev. B **63**, 174432 (2001). 196
39. S. G. Ovchinnikov, in *Ruthenate and Rutheno-Cuprate Materials*, Lecture Notes in Physics, Vol. 603, Springer, Berlin, Heidelberg (2002), Eds.: C. Noce, A. Veccione, M. Cuoko, and A. Romano. 196
40. A. V. Mahajan, H. Alloul, G. Collin, J. F. Marucco, Phys. Rev. Lett. **72**, 3100 (1994). 196
41. N. Kikigawa, A. P. Mackenzie, and Y. Maeno, J. Phys. Soc. Jpn. **72**, 237 (2003). 197
42. M. Minakata and Y. Maeno, Phys. Rev. B **63**, 180504(R) (2001). 197
43. M. Braden, O. Friedt, Y. Sidis, P. Bourges, M. Minakata and Y. Maeno, Phys. Rev. Lett. **88**, 197002 (2002). 197
44. N. Kikigawa and Y. Maeno, Phys. Rev. Lett. **89**, 117001 (2002). 197
45. R. J. Cava, B. Batlogg, K. Kiyono, and H. Takagi, Phys. Rev. B **49** 11890 (1994). 197

5 Summary, Conclusions, and Critical remarks

In the work presented in this book, we have developed an electronic theory for singlet Cooper pairing in the high-T_c cuprates and for triplet Cooper pairing in Sr_2RuO_4 due to spin excitations. In particular, we have studied the corresponding phase diagrams, the symmetry of the superconducting order parameter, and the elementary excitations of these materials in both the normal and the superconducting state. In this chapter, we summarize and discuss our main results and arguments and illustrate them in a few figures. We also discuss what would be the additional role of phonons in our theory. Finally, we point out a few weak points of our theory.

Using as a model the Hubbard Hamiltonian and solving the generalized Eliashberg equations, we have determined the phase diagram for both hole-doped and electron-doped cuprate superconductors for a spin-fluctuation-induced pairing mechanism (Fig. 5.1). In both cases we find a $d_{x^2-y^2}$-wave order parameter below the superconducting transition temperature T_c. While hole-doped superconductors have been studied intensively, the analysis of electron-doped cuprates has remained largely unclear. Older experiments reported mainly s-wave pairing [1, 2, 3]. However, recent phase-sensitive experiments [4], magnetic-penetration-depth measurements [5, 6], and ARPES data [7, 8] have shown d-wave symmetry Cooper pairing.

To investigate the phase diagram of hole-doped cuprates in more detail, we have used the generalized self-consistent Eliashberg theory, extended by including Cooper pair phase fluctuations and solved using the FLEX approximation, and have calculated some basic properties of hole-doped cuprate superconductors. Results have been presented for the characteristic temperature T^* at which a gap appears in the spectral density; for T_c^*, at which Cooper pairs are formed; for T_c, at which Cooper pairs become phase-coherent; and for the superfluid density n_s. Furthermore, we have combined our FLEX calculations with standard many-body theory and used this as in input for the Ginzburg–Landau energy functional $\Delta F\{n_s, \Delta\}$. In particular, we have calculated the superfluid density n_s/n, n_s/m (where m is the effective mass of the quasiparticles), and the critical temperature T_c as a function of the doping concentration.

We find a phase diagram for hole-doped cuprates with two different regions: on the overdoped side we obtain a mean-field-like transition and

D. Manske: Theory of Unconventional Superconductors, STMP 202, 201–209 (2004)

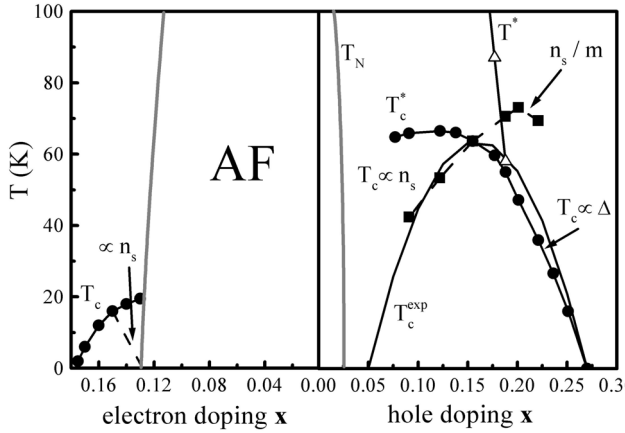

Fig. 5.1. Phase diagram $T(x)$ for hole- and electron-doped high-T_c superconductors resulting from spin-fluctuation-induced Cooper pairing. Note that the phase diagram does not show electron–hole symmetry owing to the doping of different bands and the different normal-state dispersions $\epsilon_{\mathbf{k}}$ used as an input. The antiferromagnetic (AF) phase and the curve for T_c^{exp} (in the hole-doped case) are also displayed for clarity. Below T^*, we find a pseudogap in the density of states, and T_c^* denotes the temperature below which Cooper pairs are formed. The *dashed curves* correspond to $T_c \propto n_s(0)$. In agreement with experiment, we find that superconductivity occurs in a narrower doping range for electron-doped cuprates and obtain smaller values for T_c owing to poorer nesting conditions.

$$T_c \propto \Delta(T=0) \quad ,$$

whereas in the underdoped regime we find

$$T_c \propto n_s(T=0) \quad .$$

This results from the fact that, with increasing doping, for $x > 0.15$, the phase coherence energy become larger than the Cooper pair condensation energy. For temperatures $T_c < T < T_c^*$, we find a finite *dynamical* superfluid density but no Meissner effect. This region may be attributed to preformed Cooper pairs without long-range phase coherence. The overall agreement with experiments is remarkably good and suggests spin-fluctuation exchange as the dominant pairing mechanism for superconductivity. In this connection, we have also investigated the timescale of Cooper pair phase fluctuations and find fair agreement with experiment.

We have also compared our results with the BKT theory, taking $n_s(\omega, T)/m$ from our electronic theory and find similar results. In both cases we find an optimum doping concentration at around $x_{opt} = 0.15$. For $x < x_{opt}$, $T_c^* \propto \Delta(T \to 0)$ saturates as $x \to 0$, whereas T_c decreases, and for x larger than x_{opt}, the mean-field temperature T_c^* and the critical temperature T_c

differ only slightly. The inclusion of coupling between phase and amplitude fluctuations, which was neglected here, may lead to a single transition for $x > x_{opt}$, where local pairs are created and immediately become phase-coherent, as in the BCS theory.

For electron-doped cuprates, we find a narrow range of superconductivity, and the superconducting transition temperatures $T_c(x)$ are calculated to be much smaller than for hole-doped cuprates owing to the different energy dispersion and a flat band well below the Fermi level. Furthermore, lattice disorder may also sensitively distort the symmetry $d_{x^2-y^2}$ via electron–phonon interaction. We have also calculated the Cooper-pair coherence length ξ_0 and find similar and also larger values for electron-doped than for hole-doped superconductors (from 6 Å to 9 Å). If, due to strong-coupling lifetime effects, the superfluid density n_s becomes small, the distance d between Cooper pairs increases. We obtain the result that, for $0.15 > x > 0.13$, the Cooper-pairs do not overlap significantly, i.e. $d/\xi_0 > 1$, and thus Cooper pair phase fluctuations become important. Thus we expect, as for hole-doped superconductors that $T_c \propto n_s$ in the underdoped region and $T_c \propto \Delta$ for the overdoped case. This is a subject of further investigation.

What do our studies teach us about the pairing mechanism? Because the pairing interaction itself cannot be measured directly, one needs to analyze key experiments which reveal fingerprints of it. We believe that the two key experiments are (1) ARPES experiments that measure the one-particle spectral density (and thus the elementary excitations) directly, and (2) inelastic neutron scattering experiments, in which the interdependence of the elementary excitations with spin excitations can be studied. In both cases our theory is in good agreement with the available experimental data.

In particular, we show again in Fig. 5.2 the calculated spectral density $N(\mathbf{k}, \omega)$, i.e. the local density of states, as a function of frequency and the momentum $\mathbf{k}-\mathbf{k}_F$. The peak positions correspond to the renormalized energy dispersion. Due to coupling of holes to antiferromagnetic spin fluctuations, the quasiparticle dispersion changes its slope and shows a pronounced kink feature at an energy $\omega_{kink} \approx 75 \pm 15$ meV. From a simple calculation, we have obtained a kink condition

$$\omega_{kink} \approx E_{\mathbf{k}-\mathbf{Q}} + \omega_{sf}(x)$$

in the nodal direction and

$$\omega_{kink} \approx E_{\mathbf{k}-\mathbf{Q}} + \omega_{res}(x)$$

in the antinodal direction (see Fig. 3.20), where the spin excitations become resonant below T_c. Thus, the two kink features are strongly related as shown in Fig. 5.3. While in the normal state of hole-doped cuprates ω_{sf} is of the order of 25 meV, in the electron-doped cuprates its value is much larger ($\omega_{sf} \approx 70$ meV) and $\mathrm{Im}\,\chi$ is much less pronounced. Therefore, antiferromagnetic spin fluctuations are much weaker in the electron-doped

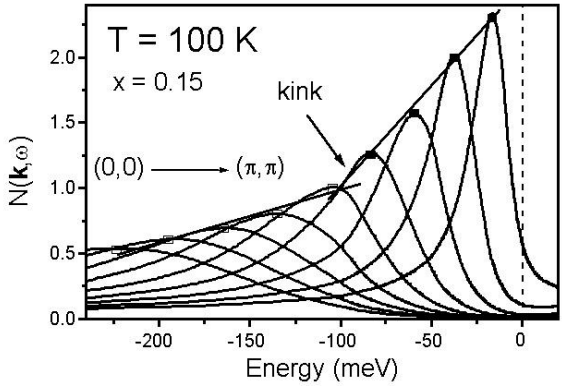

Fig. 5.2. Calculated spectral density $N(\mathbf{k},\omega)$ in the normal state along the nodal $(0,0) \rightarrow (\pi,\pi)$ direction (from *left* to *right*) as a function of frequency in the first Brillouin zone. The peak positions (connected by the *solid line* to guide the eye) refer to the renormalized energy dispersion $\omega_{\mathbf{k}}$, which was calculated self-consistently. One can clearly see the kink structure at an energy of approximately $\omega_{kink} = 75 \pm 15$ meV; this results from coupling of the quasiparticles to spin fluctuations.

cuprates due to weaker nesting of the Fermi surface and smaller density of states due to the flat band well below the Fermi level. In the superconducting state we find $\Delta_0 \sim \omega_{sf}$, leading to a resonance peak at $\omega = \omega_{res}$ (see Fig. 5.3b), because a resonance condition

$$\frac{1}{U_{cr}} = \mathrm{Re}\,\chi_0(\mathbf{q} = \mathbf{Q}, \omega = \omega_{res}) \quad ,$$

which signals the occurrence of a spin-density-wave collective mode, is fulfilled. In electron-doped cuprates, the spin excitations do not obey the resonance condition and thus only a rearrangement of spectral weight occurs below T_c, but no resonance peak. Therefore, the kink feature is intimately connected with the resonance peak. As we see from Fig. 5.3a there is only a small feedback of superconductivity below T_c on $\mathrm{Im}\,\chi$ in the electron-doped cuprates because $\omega_{sf} \gg \Delta_0$. Thus, we also find no kink feature in the superconducting state of electron-doped cuprates in the antinodal direction.

What is the role of phonons in the pairing mechanism? One of the interpretations of the kink structure in hole-doped cuprates has been an electron–phonon interaction suggested by Lanzara *et al.* [9]. Indeed, it is clear that phonons would also cause a kink structure in the energy dispersion if one assumes the Eliashberg function $\alpha^2 F(\mathbf{q},\omega)$ has the same features as $\chi(\mathbf{q},\omega)$, namely that it is peaked at the wave vector $\mathbf{Q}$ and at the Debye frequency ω_D, i.e. $\omega = \omega_D \approx \omega_{sf}$. If we analyze Fig. 3.19 it is clear that both spin fluctuations and electron–phonon coupling can cause a kink structure. However, in general, one would expect that the position and doping dependence

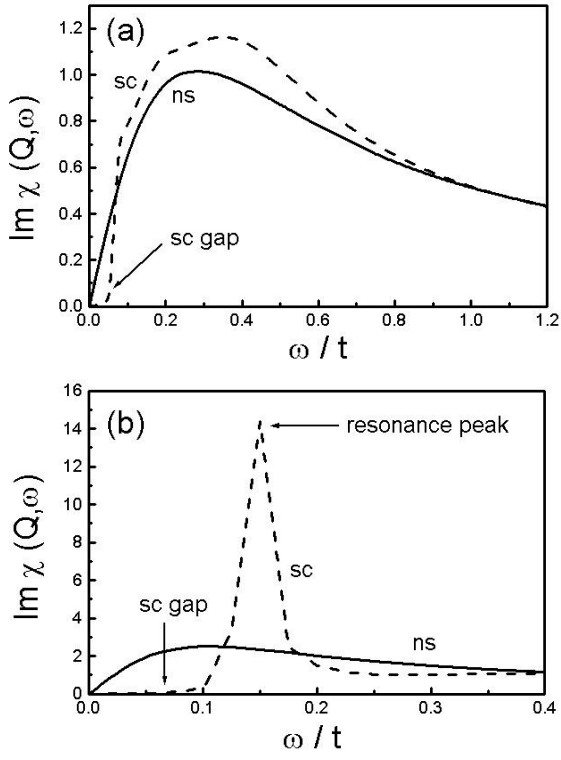

Fig. 5.3. Calculated feedback of superconductivity on the spin susceptibility $\mathrm{Im}\,\chi(\mathbf{q},\omega)$ for electron-doped **(a)** and hole-doped **(b)** cuprates at optimal doping (x = 0.15). The *solid curves* refer to the normal state (T = $1.5\mathrm{T}_c$), while the *dashed curves* denote the renormalized spin susceptibility in the superconducting state at T = $0.7\mathrm{T}_c$. Due to large $\omega_{sf} = 0.3t$ and the small superconducting gap, the feedback of superconductivity is small in electron-doped cuprates. On the other hand, due to a small $\omega_{sf} = 0.09t$ and the large gap $\Delta(\omega)$ in hole-doped cuprates, the feedback of superconductivity fulfills a resonance condition for $\mathrm{Im}\,\chi$ yielding a strong renormalization of the spin excitation spectrum and the formation of a resonance peak. Note that the hopping integral t is different for hole- and electron-doped cuprates, as discussed in the Introduction.

of the kink structure would be different in the two cases. For example, only in the case of dominant spin fluctuation coupling the kink structure can be related to the results of INS experiments, i.e. $\mathrm{Im}\,\chi(\mathbf{Q},\omega)$, and, furthermore, the kink position is given by $\omega_{kink} \approx E_{\mathbf{k}-\mathbf{Q}} + \omega_{sf}(x)$. As discussed earlier, the kink feature along the antinodal $(0,\pi) \rightarrow (\pi,\pi)$ direction results from the structure in $\Delta(\omega)$. Thus, additional structure in $\Delta(\omega)$ due to the electron–phonon interaction may also contribute. Therefore, the question remains: How do we distinguish between spin fluctuations and phonons as the

reason for the formation of the kink? To answer this question one has to understand how consistent the two scenarios are with available experimental data. For example, as was shown Zeyher and Greco [10], the value of the electron–phonon coupling extracted from an analysis of the kink yields values of the electron–phonon coupling λ and of T_c that are too low to account for high-T_c superconductivity in the cuprates. Furthermore, assuming that the kink structure arises only from the electron–phonon interaction, it is difficult to understand the $d_{x^2-y^2}$ symmetry of the superconducting order parameter and the related observed anisotropy of the kink structure (see Appendix C). Only the spin fluctuation scenario yields $T_c \approx 70$ K, a $d_{x^2-y^2}$-wave order parameter, and a kink feature in qualitative agreement with experiment. Also, the doping dependence of the kink is difficult to explain within the phonon scenario. In contrast to (3.16) one would expect $\omega_{kink} \approx E_{\mathbf{k}-\mathbf{Q}} + \omega_D(x)$ in the case of electron–phonon coupling.

Thus, in short, in the case of hole-doped cuprates we have shown that:

- A $d_{x^2-y^2}$-wave order parameter results from the exchange of antiferromagnetic spin fluctuations.
- Their phase diagram, in particular the occurrence of three characteristic temperature scales, i.e. the pseudogap temperature $T^*(x)$, the mean-field crossover $T_c^*(x)$, and the superconducting temperature $T_c(x)$, can be naturally explained by Cooper pairing due to antiferromagnetic spin fluctuations.
- The pseudogap could be due to a charge density wave (or d-density wave) or to inelastic scattering of holes by spin excitations and $T_c(x)$ has a maximum at nearly optimum doping due to the interplay of the Cooper pair condensation energy $\propto \Delta(x)$ and the energy costs resulting from Cooper pair phase fluctuations $\propto n_s(x)$.
- The kink feature in the spectral density of holes observed in ARPES experiments can be explained as being due to their coupling to spin fluctuations. In particular, in the nodal direction $(0,0) \rightarrow (\pi,\pi)$ the kink is present both above and below T_c, but it occurs in the antinodal direction $(0,\pi) \rightarrow (\pi,\pi)$ *only* below T_c. The latter observation signals the opening of the superconducting gap $\Delta(\mathbf{k},\omega)$ and is a direct fingerprint of the pairing interaction.
- The occurrence of a resonance peak at $\omega_{res} \approx 41$ meV in INS experiments on optimally doped YBCO only below T_c reflects $\Delta(\mathbf{k},\omega)$ and the $d_{x^2-y^2}$-wave symmetry of the superconducting order parameter and the closeness to a spin-density-wave collective mode. The theory predicts a doping dependence $\omega_{res}(x)$ and the presence of a similar effect in single-layer cuprates, both of which have been observed now.
- Various other physical quantities, such as the electronic Raman response, the magnetic coherence observed in INS experiments, the role of collective modes in ARPES experiments, and the optical conductivity in the *ab* and

in c directions have been calculated in this work and good agreement with experiment is found.

In the case of electron-doped cuprates, we have pointed out the similarities to the hole-doped cuprates in their phase diagram, in particular that:

- Superconductivity occurs only in a narrow doping region because of the strong antiferromagnetism at small doping concentrations and the weaker nesting properties of the Fermi surface in the overdoped case.
- $T_c(x)$ is smaller than for hole-doped cuprates due to fewer density of states around $(\pi, 0)$ where the van Hove singularity lies about 300 meV below the Fermi level.
- A $d_{x^2-y^2}$-wave order parameter is expected if the pairing potential is generated mainly by the exchange of antiferromagnetic spin fluctuations. The magnitude of Δ is calculated to be about 5 meV.
- No kink feature and no resonance peak is found in electron-doped cuprates, which is also in agreement with experiment. This is the case because Δ is too small to fulfill the resonance condition. Thus, only a rearrangement of spectral weight occurs.
- Also, the main difference in the interplay between magnetism and superconductivity with respect to hole-doped cuprates is the fact that in the hole-doped case Zhang–Rice-like quasiparticles are doped into the oxygen states, whereas for electron-doped cuprates the Cu d states are the most important. Thus, in the latter case, one has a dilute antiferromagnet with no frustrated spins or spin glass state.

In the case of the analysis of triplet pairing in Sr_2RuO_4 we find that a three-band Hubbard Hamiltonian including spin–orbit coupling (or hybridization) can explain the main interesting normal and superconducting properties:

- Spin–orbit coupling plays an important role in both the superconducting and the normal state. In particular, it explains the unexpected and important normal-state spin anisotropy and the occurrence of an orbital moment below T_c (i.e. the chiral p-wave state).
- The strong anisotropy of the t_{2g} orbitals is reflected in the anisotropic spin response, $\chi^{zz} > \chi^{+-}$, if spin–orbit coupling is taken into account.
- The nesting of the α and β bands plays a major role in Sr_2RuO_4 (the γ band alone would lead to pure p-wave pairing, as expected earlier).
- The calculated magnetic response is in good agreement with INS and NMR experiments. In the superconducting state, we find that in two dimensions the strong antiferromagnetic spin excitations would lead to a suppression of the p-wave state and would then lead to f-wave pairing if no (or weak) spin–orbit coupling were present or if pressure were applied in order to increase the nesting of the γ band, for example.
- In three dimensions, if interplanar pairing is assumed, one finds a superconducting order parameter with p-wave symmetry, but with nodes

between the RuO_2 planes. The exact position of the nodes reflects the incommensurability of the pairing interaction. This has to be confirmed by an electronic, self-consistent calculation.

What are the weak points of our theory? As we have discussed in Sect. 2.5, the main problem of our approach is the fact that when the doping x tends to zero no Mott transition is obtained. Therefore, as soon as the nearness of a Mott transition becomes important, i.e. in the (strongly) underdoped regime, our theory has problems. For optimal doping and the overdoped case, however, we believe that our results demonstrate that the physics related to a Mott–Hubbard insulator plays no dominant role, and hence can safely be neglected. In particular, our approximation is better for Sr_2RuO_4, which is a material with weaker correlations than in cuprates and is also a good Fermi liquid.

Further weak points are the following: for cuprates we have used only an effective one-band Hubbard model that neglects the difference between oxygen p states and Cu d states. In addition, we have employed a simple perturbation theory (effectively second order) and the RPA, and thus consider only a special selection of Feynman diagrams. The corresponding vertex corrections can often be treated only within certain approximations. In defence of our work, however, we believe we have followed an intuitive method and formulated a theory similar to the well-known Eliashberg equations for phonons given by Scalapino, Schrieffer, and Wilkins [11], yielding fair agreement with experiment.

To conclude, we have studied the interplay between magnetism and superconductivity, in particular the connection between antiferromagnetism and singlet d-wave superconductivity in high-T_c cuprates, and between ferromagnetism and triplet pairing in Sr_2RuO_4. We have developed an electronic theory of Cooper pairing due to spin fluctuations and understood the main physics in these materials. However, in connection with cuprates many questions still have to be answered. For example, what is the role of spatial [12] or electronic [13] inhomogeneities, do surface properties differ strongly from their bulk counterparts ([14] and references therein), and how should one interpret the recent c-axis tunneling data [15]? We believe that further material-dependent studies are necessary to clarify these questions [16]. Nevertheless, many fingerprints of the corresponding pairing potential due to spin excitations are found in various normal and superconducting properties. Because the doping dependence of the key physical quantities and the elementary excitations are correctly described, we conclude that spin fluctuations play the most important role in Cooper pairing in these materials.

References

1. B. Stadlober, G. Krug. R. Nemetschek, R. Hackl, J. L. Cobb, and J. T. Markert, Phys. Rev. Lett. **74**, 4911 (1995). 201

2. L. Alff, A. Beck, R. Gross, A. Marx, S. Kleefisch, T. Bauch, H. Sato, M. Naito, and G. Koren, Phys. Rev. B. **58**, 11197 (1998). 201
3. S. M. Anlage, D.-H. Wu, S. N. Mao, X. X. Xi, T. Venkatesan, J. L. Peng, and R. L. Greene, Phys. Rev. B. **50**, 523 (1994). 201
4. C. C. Tsuei and J. R. Kirtly, Phys. Rev. Lett. **85**, 182 (2000). 201
5. J. D. Kokales, P. Fournier, L. V. Mercaldo, V. V. Talanov, R. L. Greene, and S. M. Anlage, Phys. Rev. Lett. **85**, 3696 (2000). 201
6. R. Prozorov, R. W. Gianetta, P. Furnier, and R. L. Greene, Phys. Rev. Lett. **85**, 3700 (2001). 201
7. N. P. Armitage, D. H. Lu, D. L. Feng, C. Kim, A. Damascelli, K. M. Shen, F. Ronning, Z. X. Shen, Y. Onose, Y. Taguchi, and Y. Tokura, Phys. Rev. Lett. **86**, 1126 (2001). 201
8. T. Sato, T. Kamiyama, T. Takahashi, K. Kurahashi, K. Yamada, Science **291**, 1517 (2001). 201
9. A. Lanzara, P. V. Bagdanov, X. J. Zhou, S. A. Kellar, D. L. Feng, E. D. Lu, H. Eisaki, A. Fujimori, K. Kishio, J.-I. Shimoyama, T. Noda, S. Uchida, Z. Hussain, and Z. X. Shen, Nature **412**, 510 (2001). 204
10. R. Zeyher and A. Greco, Phys. Rev. Lett. **89**, 177004 (2002). 206
11. D. J. Scalapino, J. R. Schrieffer, and J. W. Wilkins, Phys. Rev. **148**, 263 (1966). 208
12. K. M. Lang, V. Madhavan, J. E. Hoffman, E. W. Hudson, H. Eisaki, S. Uchida, and J. C. Davis, Nature **415**, 412 (2002). 208
13. S. H. Pan, J. P. O'Neal, R. L. Badzey, C. Chamon, H. Ding, J. R. Engelbrecht, Z. Wang, H. Eisaki, S. Uchida, A. K. Gupta, K.-W. Ng, E. W. Hudson, K. M. Lang, and J. C. Davis, Nature **413**, 282 (2001). 208
14. K. A. Müller, Phil. Mag. Lett. **82**, 279 (2002). 208
15. R. A. Klemm, Physica B **329–333**, 1325 (2003). 208
16. J. Bobroff, H. Alloul, S. Quazi, P. Mendels, A. Mahajan, N. Blanchard, G. Collin, V. Guillen, and J.-F. Marucco, Phys. Rev. Lett. **89**, 157002 (2002). 208

A Solution Method for the Generalized Eliashberg Equations for Cuprates

While earlier attempts were restricted to solving the set of equations (2.28)–(2.32) on the imaginary axis [1, 2, 3, 4] or slightly above the real axis [5, 6, 7], we solve the generalized Eliashberg equations directly on the real ω axis. Thus we avoid continuation methods such as the Padé approximation after solving the set of equations for the self-energy. The generalized Eliashberg equations in the two-dimensional (effective) one-band Hubbard model read

$$\mathrm{Im}\,\chi_G(\mathbf{q},\omega) = \frac{\pi}{N}\sum_{\mathbf{k}}\int_{-\infty}^{\infty} \mathrm{d}\omega\ [f(\omega)-f(\omega+\Omega)]\,N(\mathbf{k},\omega)N(\mathbf{k}+\mathbf{q},\omega+\Omega)\,, \tag{A.1}$$

$$\mathrm{Im}\,\chi_F(\mathbf{q},\omega) = \frac{\pi}{N}\sum_{\mathbf{k}}\int_{-\infty}^{\infty} \mathrm{d}\omega\ [f(\omega)-f(\omega+\Omega)]\,A_1(\mathbf{k},\omega)A_1(\mathbf{k}+\mathbf{q},\omega+\Omega)\,, \tag{A.2}$$

$$\mathrm{Re}\,\chi_{G,F}(\mathbf{q},\omega) = \frac{1}{\pi}P\int_{-\infty}^{\infty} d\omega\,\frac{\mathrm{Im}\,\chi_{G,F}(\mathbf{q},\omega)}{\omega-\Omega} \quad , \tag{A.3}$$

$$\chi_{c0} = \chi_G - \chi_F \quad , \tag{A.4}$$

$$\chi_{s0} = \chi_G + \chi_F \quad , \tag{A.5}$$

$$P_s \equiv \frac{1}{\pi}\,\mathrm{Im}\left[\frac{3}{2}\frac{U^2\chi_{s0}}{1-U\chi_{s0}}\right] \quad , \tag{A.6}$$

$$P_c \equiv \frac{1}{\pi}\,\mathrm{Im}\left[\frac{3}{2}\frac{U^2\chi_{c0}}{1+U\chi_{c0}}\right] \quad , \tag{A.7}$$

$$P_G \equiv P_s + P_c - \frac{1}{\pi}\,\mathrm{Im}\left[\frac{1}{2}U^2\left(\chi_{s0}+\chi_{c0}\right)\right] \quad , \tag{A.8}$$

$$P_F \equiv -P_s + P_c + \frac{1}{\pi}\,\mathrm{Im}\left[\frac{1}{2}U^2\left(\chi_{s0}-\chi_{c0}\right)\right] \quad , \tag{A.9}$$

$$\mathrm{Im}\,\phi(\mathbf{k},\omega) = \frac{\pi}{N}\sum_{\mathbf{q}}\int_{-\infty}^{\infty} \mathrm{d}\Omega\ [b(\Omega)+f(\Omega-\omega)]\ P_F(\mathbf{q},\omega)A_1(\mathbf{k}-\mathbf{q},\omega-\Omega)\,, \tag{A.10}$$

D. Manske: Theory of Unconventional Superconductors, STMP 202, 211–228 (2004)

$$\begin{aligned}&\operatorname{Im}\Sigma(\mathbf{k},\omega)\\&=-\frac{\pi}{N}\sum_{\mathbf{q}}\int_{-\infty}^{\infty}d\Omega\,\left[b(\Omega)+f(\Omega-\omega)\right]\,P_G(\mathbf{q},\omega)N(\mathbf{k}-\mathbf{q},\omega-\Omega)\,,\end{aligned}\tag{A.11}$$

$$\operatorname{Re}\phi(\mathbf{k},\omega)=\frac{1}{\pi}\mathrm{P}\int_{-\infty}^{\infty}\mathrm{d}\omega'\,\frac{\operatorname{Im}\phi(\mathbf{k},\omega')}{\omega'-\omega}\quad,\tag{A.12}$$

$$\operatorname{Re}\Sigma^G(\mathbf{k},\omega)=\frac{1}{\pi}\mathrm{P}\int_{-\infty}^{\infty}\mathrm{d}\omega'\,\frac{\operatorname{Im}\Sigma^G(\mathbf{k},\omega')}{\omega'-\omega}\quad,\tag{A.13}$$

$$\xi\equiv\frac{1}{2}\left[\Sigma^G(\mathbf{k},\omega)+\Sigma^{G*}(\mathbf{k},-\omega)\right]\quad,\tag{A.14}$$

$$\omega Z\equiv\omega-\frac{1}{2}\left[\Sigma^G(\mathbf{k},\omega)-\Sigma^{G*}(\mathbf{k},-\omega)\right]\quad,\tag{A.15}$$

$$N(\mathbf{k},\omega)=-\frac{1}{\pi}\operatorname{Im}\left[\frac{\omega Z+\epsilon_{\mathbf{k}}+\xi}{(\omega Z)^2-(\epsilon_{\mathbf{k}}+\xi)^2-\phi^2}\right]=A_0(\mathbf{k},\omega)+A_3(\mathbf{k},\omega)\quad,\tag{A.16}$$

$$A_1(\mathbf{k},\omega)=-\frac{1}{\pi}\operatorname{Im}\left[\frac{\phi}{(\omega Z)^2-(\epsilon_{\mathbf{k}}+\xi)^2-\phi^2}\right]\quad.\tag{A.17}$$

Our numerical calculations were performed on a square lattice with 256×256 points in the Brillouin zone and with 200 points on the real ω axis up to $16t$ with an almost logarithmic mesh. The full momentum and frequency dependence of the quantities was kept. The convolutions in $\mathbf{k}$-space were carried out with fast Fourier transforms [8]. The real parts of the susceptibilities, gap, and self-energy were calculated with the help of the Kramers–Kronig relations (P denotes the corresponding principal value of the integral). The spectral functions A_1, $P_{G,F}$, $\operatorname{Im}\phi$, $\operatorname{Im}\xi$, and $\operatorname{Im}\chi_{G,F}$ are antisymmetric and the corresponding real parts are symmetric with respect to ω. Thus the spectral function for the interacting electrons (or holes) $N(\mathbf{k},\omega)$ is separated into a symmetric part A_0 and an antisymmetric part A_3 (see (A.16)). The corresponding equations for the normal state can be recovered by setting the off-diagonal terms of the self-energy, ϕ, A_1, and χ_F, identically to zero.

For an illustration, we show in Fig. A.1 how we solve (2.28)–(2.32). We start with a dynamical spin susceptibility $\chi(\mathbf{q},\omega)$ and constructs the effective pairing interaction using (A.8). Then, the strong-coupling gap equation for the superconducting order parameter $\phi(\mathbf{k},\omega)$ and the corresponding Dyson equation $G^{-1}(\mathbf{k},\omega)=G_0^{-1}(\mathbf{k},\omega)-\Sigma(\mathbf{k},\omega)$ have to be solved. Having solved these two equations, we have new appropriate starting input values for an electron propagator G, which is again used to calculate χ. This procedure is repeated until all equations are solved.

In order to determine the superconducting transition temperature T_c we solve the linearized gap equation, i.e. the linearized version of (A.12),

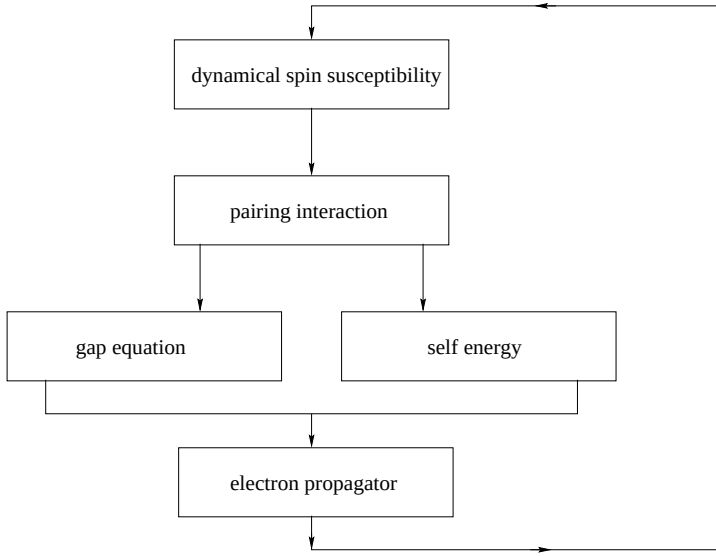

Fig. A.1. Illustration of the procedure used to solve (2.28)–(2.32). The full momentum and frequency dependence of the quantities is kept. Thus, our calculations include pair-breaking effects for the Cooper pairs resulting from lifetime effects of the elementary excitations.

$$\lambda \,\mathrm{Im}\,\phi(\mathbf{k},\omega) = -\frac{1}{N}\sum_{\mathbf{k}}\int_{-\infty}^{\infty} \mathrm{d}\omega' \; [b(\Omega) + f(\Omega-\omega)] \; P_F(\mathbf{q},\omega)$$

$$\times \,\mathrm{Im}\left[\frac{\phi(\mathbf{k}',\omega')}{(\omega Z)^2 - (\epsilon_{\mathbf{k}'}+\xi)^2}\right] \quad , \tag{A.18}$$

where χ_F in P_F is set identically to zero. With decreasing temperature T, the eigenvalue $\lambda(T)$ increases and passes through unity at $T = T_c$. The spectral functions calculated during the solution of (A.18) are then appropriate starting values for the solution of the equations below T_c. After solving the generalized Eliashberg equations for cuprates, we find that below T_c the superconducting gap function has $d_{x^2-y^2}$-wave symmetry for both hole- and electron-doped superconductors. Vertex corrections for the two-particle correlation function are not included.

As mentioned earlier, there exists an important feedback effect of the self-energy on the spectral functions of the corresponding quasiparticles (dressed holes or electrons). This is the case, in particular if these quasiparticles become superconducting. Below T_c a gap appears in the spectral density of the quasiparticles which not only condense into Cooper pairs but also provide the effective pairing interaction $V^{eff}(\mathbf{q},\omega)$. This gap corresponds to the superconducting gap function $\phi(\mathbf{k},\omega) = Z(\mathbf{k},\omega)\Delta(\mathbf{k},\omega)$, which is nonzero below T_c

and can be calculated self-consistently, including all scattering and damping effects of the quasiparticles by the procedure described above. This strong feedback effect has important consequences: for example, the dynamical spin susceptibility $\mathrm{Im}\,\chi_s(\mathbf{Q},\omega)$ (for simplicity we restrict our discussion to the antiferromagnetic nesting vector $\mathbf{q}=\mathbf{Q}=(\pi,\pi)$) shows a rearrangement of its spectral weight for small frequencies $\omega < 2\phi(\mathbf{Q},\omega)$, followed by a peak at approximately $\omega = 2\phi$. As discussed in the Introduction, this behavior provides a possible explanation for the observed "resonance peak" in inelastic neutron scattering for many cuprate superconductors. Therefore, the strong feedback effect of superconductivity on the elementary excitations and thus on $\mathrm{Im}\,\chi_s(\mathbf{Q},\omega)$ can be viewed as a general phenomenon of a strongly interacting system and, in particular, as an important fingerprint of spin-fluctuation-mediated pairing in cuprate high-T_c superconductors. To demonstrate this, the self-consistent procedure shown in Fig. A.1 is required.

References

1. N. E. Bickers, D. J. Scalapino, and S. R. White, Phys. Rev. Lett. **62**, 961 (1989); N. E. Bickers and D. J. Scalapino, Ann. Phys. (N.Y.) **193**, 206 (1989). 211
2. C.-H. Pao and N. E. Bickers, Phys. Rev. Lett. **72**, 1870 (1994); Phys. Rev. B **51**, 16310 (1995). 211
3. D. J. Scalapino, Phys. Rep. **250**, 329 (1995). 211
4. P. Monthoux and D. J. Scalapino, Phys. Rev. Lett. **72**, 1874 (1994). 211
5. M. Langer, J. Schmalian, S. Grabowski, and K. H. Bennemann, Phys. Rev. Lett. **75**, 4508 (1995). 211
6. J. Schmalian, S. Grabowski, and K. H. Bennemann, Phys. Rev. B **56**, R509 (1997). 211
7. J. Schmalian, M. Langer, S. Grabowski, and K. H. Bennemann, Comput. Phys. Comunn. **93**, 141 (1996). 211
8. J. W. Serene and D. W. Hess, Phys. Rev. B **44**, 3391 (1991). 212

B Derivation of the Self-Energy (Weak-Coupling Case)

The self-energy in the one-loop approximation is given by

$$\Sigma(\mathbf{k},\omega) = -T^2 \sum_{\omega_n,\nu_m} \sum_{\mathbf{p},\mathbf{q}} \hat{\tau}_i \, G(\mathbf{k}-\mathbf{p}, i\omega_n - i\nu_m) \, \hat{\tau}_i \, U^2(\mathbf{p}) \times \frac{1}{2} \mathrm{Tr} \left[\hat{\tau}_i \, G(\mathbf{p}+\mathbf{q}, i\omega_n + i\nu_m) \, \hat{\tau}_i \, G(\mathbf{k}, i\omega_n) \right] \quad . \tag{B.1}$$

For spin fluctuations, we have $\hat{\tau}_i = \hat{\tau}_0$. The Coulomb interaction $U(\mathbf{p})$ is taken to be a constant and the full Green's function is approximated by its noninteracting counterpart

$$G(\mathbf{k}, i\omega_n) \simeq G_0(\mathbf{k}, i\omega_n) = \frac{i\omega_n \hat{\tau}_0 + \epsilon_k \hat{\tau}_3 - \Delta_k \hat{\tau}_1}{(i\omega_n)^2 - \epsilon_k^2 - \Delta_k^2} \quad . \tag{B.2}$$

Using (B.2), the trace in (B.1) can be rewritten as

$$\begin{aligned} &\frac{1}{2} \mathrm{Tr} \left[G(\mathbf{p}+\mathbf{q}, i\omega_n + i\nu_m) G(\mathbf{k}, i\omega_n) \right] \\ &\quad = \frac{1}{\left[(i\omega_n + i\nu_m)^2 - \epsilon_{p+q}^2 - \Delta_{p+q}^2 \right] \left[(i\omega_n)^2 - \epsilon_q^2 - \Delta_q^2 \right]} \\ &\times \left[(i\omega_n + i\nu_m) \, i\omega_n + \epsilon_{p+q}\epsilon_q + \Delta_{p+q}\Delta_p \right] \\ &= \frac{1}{4} \left[\frac{c_+(\mathbf{p}+\mathbf{q},\mathbf{q})}{(i\omega_n + i\nu_m - E_{p+q})(i\omega_n - E_q)} + \frac{c_-(\mathbf{p}+\mathbf{q},\mathbf{q})}{(i\omega_n + i\nu_m - E_{p+q})(i\omega_n + E_q)} \right. \\ &\left. + \frac{c_-(\mathbf{p}+\mathbf{q},\mathbf{q})}{(i\omega_n + i\nu_m + E_{p+q})(i\omega_n - E_q)} + \frac{c_+(\mathbf{p}+\mathbf{q},\mathbf{q})}{(i\omega_n + i\nu_m + E_{p+q})(i\omega_n + E_q)} \right] \quad , \end{aligned} \tag{B.3}$$

where we have introduced the quasiparticle energy dispersion

$$E_p^2 = \epsilon_p^2 + \Delta_p^2 \tag{B.4}$$

and the coherence factors

$$c_{\pm}(\mathbf{p}+\mathbf{q},\mathbf{q}) = 1 \pm \frac{\epsilon_{p+q}\epsilon_q + \Delta_{p+q}\Delta_q}{E_{p+q}E_q} \quad . \tag{B.5}$$

Now, summation of (B.3) over ω_n can easily be performed. Noting that

$$T\sum_{\omega_n} \frac{1}{(i\omega_n + i\nu_m - y)(i\omega_n - x)} = \frac{f(x)-f(y)}{i\nu_m + x - y} \quad , \tag{B.6}$$

we obtain

$$\begin{aligned} & T\sum_{\omega_n} \frac{1}{2}\,\mathrm{Tr}\left[G(\mathbf{p}+\mathbf{q}, i\omega_n + i\nu_m)\, G(\mathbf{q}, i\omega_n)\right] \\ & = \frac{1}{4}\left[\left[\frac{f(E_q)-f(E_{p+q})}{i\nu_m + E_q - E_{p+q}} + \frac{f(-E_q)-f(-E_{p+q})}{i\nu_m - E_q + E_{p+q}}\right] c_+(\mathbf{p}+\mathbf{q},\mathbf{q})\right. \\ & \left. + \left[\frac{f(-E_q)-f(E_{p+q})}{i\nu_m - E_q - E_{p+q}} + \frac{f(E_q)-f(-E_{p+q})}{i\nu_m + E_q + E_{p+q}}\right] c_-(\mathbf{p}+\mathbf{q},\mathbf{q})\right] \quad . \end{aligned} \tag{B.7}$$

Equation (B.7) has to be multiplied by

$$\begin{aligned} \frac{i\omega_n - i\nu_m}{(i\omega_n - i\nu_m)^2 - E_{k-p}^2} &= \frac{1}{2}\left[\frac{1}{i\omega_n - i\nu_m - E_{k-p}} + \frac{1}{i\omega_n - i\nu_m + E_{k+p}}\right] \\ &= -\frac{1}{2}\left[\frac{1}{i\nu_m - i\omega_n + E_{k-p}} + \frac{1}{i\nu_m - i\omega_n - E_{k-q}}\right] \end{aligned} \tag{B.8}$$

for the $\hat{\tau}_0$ component and

$$\begin{aligned} \frac{1}{(i\omega_n - i\nu_m)^2 - E_{k-p}^2} &= \frac{1}{2E_{k-p}}\left[\frac{1}{i\omega_n - i\nu_m - E_{k-p}} - \frac{1}{i\omega_n - i\nu_m + E_{k-p}}\right] \\ &= -\frac{1}{2E_{k-p}}\left[\frac{1}{i\nu_m - i\omega_n + E_{k-p}} - \frac{1}{i\nu_m - i\omega_n - E_{k-p}}\right] \end{aligned} \tag{B.9}$$

for the $\hat{\tau}_3$ and $\hat{\tau}_1$ components, and summed over ν_m. Using (where n is the Bose function)

$$n(-x) = -(1+n(x)) \qquad \text{and} \qquad f(-x) = 1 - f(x)$$

and

$$-T\sum_{\nu_m} \frac{1}{(i\nu_m - x)(i\nu_m - y)} = \frac{n(x)-n(y)}{x-y} \tag{B.10}$$

in the form

$$-T\sum_{\nu_m}\frac{1}{(i\nu_m-i\omega_n-x)(i\nu_m-y)}=\frac{n(i\omega_n+x)-n(y)}{i\omega_n+x-y}$$

$$=-\frac{f(x)+n(y)}{i\omega_n+x-y}\quad , \tag{B.11}$$

we obtain

$$-T\sum_{\nu_m}\frac{1}{(i\nu_m-i\omega_n+E_{k-p})}\pm\frac{1}{(i\nu_m-i\omega_n-E_{k-p})}$$

$$\times\left[\left[\frac{f(E_q)-f(E_{p+q})}{i\nu_m+E_q-E_{p+q}}+\frac{f(-E_q)-f(-E_{p+q})}{i\nu_m-E_q+E_{p+q}}\right]c_+(\mathbf{p}+\mathbf{q},\mathbf{q})\right.$$

$$\left.+\left[\frac{f(-E_q)-f(E_{p+q})}{i\nu_m-E_q-E_{p+q}}+\frac{f(E_q)-f(-E_{p+q})}{i\nu_m+E_q+E_{p+q}}\right]c_-(\mathbf{p}+\mathbf{q},\mathbf{q})\right]$$

$$=-\left[c_+(\mathbf{p}+\mathbf{q},\mathbf{q})\left[[f(E_q)-f(E_{p+q})]\right.\right.$$

$$\times\left[-\frac{f(E_{k-p})+n(E_q-E_{p+q})}{i\omega_n-E_{k-p}+E_q-E_{p+q}}\pm\frac{f(E_{p+q})-n(E_q-E_{p+q})-1}{i\omega_n+E_{k-p}+E_q-E_{p+q}}\right]$$

$$+\ [-f(E_q)+f(E_{p+q})]$$

$$\left.\times\left[\frac{1-f(E_{k-p})+n(E_q-E_{p+q})}{i\omega_n-E_{k-p}-E_q+E_{p+q}}\pm\frac{f(E_{k-p})+n(E_q-E_{p+q})}{i\omega_n+E_{k-p}-E_q+E_{p+q}}\right]\right]$$

$$+\ c_-(\mathbf{p}+\mathbf{q},\mathbf{q})\left[\ [1-f(E_{k-q})-f(E_{p+q})]\right.$$

$$\times\left[\frac{1-f(E_{k-p})+n(E_q+E_{p+q})}{i\omega_n-E_{k-p}-E_q-E_{p+q}}\pm\frac{f(E_{k-p})+n(E_q+E_{p+q})}{i\omega_n+E_{k-p}-E_q-E_{p+q}}\right]$$

$$+\ [f(E_q)+f(E_{p+q})-1]$$

$$\left.\left.\times\left[-\frac{f(E_{k-p})+n(E_q+E_{p+q})}{i\omega_n-E_{k-p}+E_q+E_{p+q}}\pm\frac{f(E_{k-p})-n(E_q+E_{p+q})-1}{i\omega_n+E_{k-p}+E_q+E_{p+q}}\right]\right]\right]$$

$$=c_+(\mathbf{p}+\mathbf{q},\mathbf{q})\,[f(E_q)-f(E_{p+q})]\left[[f(E_{k-p})+n(E_q-E_{p+q})]\right.$$

$$\left.\times\left[\frac{1}{i\omega_n-E_{k-p}+E_q-E_{p+q}}\pm\frac{1}{i\omega_n+E_{k-p}-E_q+E_{p+q}}\right]\right.$$

$$
\begin{aligned}
&+ \left[1 - f(E_{k-p}) + n(E_q - E_{p+q})\right] \\
&\times \left[\pm \frac{1}{i\omega_n + E_{k-p} + E_q - E_{p+q}} + \frac{1}{i\omega_n - E_{k-p} - E_q + E_{p+q}}\right]\Bigg] \\
&+ c_-(\mathbf{p}+\mathbf{q},\mathbf{q})\left[f(E_q) + f(E_{p+q}) - 1\right] \\
&\times \Bigg[\left[f(E_{k-p}) + n(E_q + E_{p+q})\right] \\
&\times \left[\pm \frac{1}{i\omega_n + E_{k-p} - E_q - E_{p+q}} + \frac{1}{i\omega_n - E_{k-p} + E_q + E_{p+q}}\right] \\
&+ \left[1 - f(E_{k-p}) + n(E_q + E_{p+q})\right] \\
&\times \left[\frac{1}{i\omega_n - E_{k-p} - E_q - E_{p+q}} \pm \frac{1}{i\omega_n + E_{k-p} + E_q + E_{p+q}}\right]\Bigg] \quad . \qquad \text{(B.12)}
\end{aligned}
$$

Now the analytic continuation $i\omega_n \to \omega + i\eta$ can be performed and the components of the self-energy can be obtained. The imaginary part of the self-energy which corresponds to the $\hat{\tau}_0$ component then reads

$$
\begin{aligned}
\mathrm{Im}\,\Sigma_0(\mathbf{k},\omega) = \frac{\pi U^2}{8} &\Bigg[\sum_{\mathbf{p}} \left[f(E_{k-p}) + n(E_{p+q} + \omega)\right] \\
&\times \sum_{\mathbf{q}} \Bigg[c_+(\mathbf{p}+\mathbf{q},\mathbf{q})\left[f(E_q) - f(E_{p+q})\right] \\
&\times \left[\delta(\omega + E_{k-p} - E_q + E_{p+q}) - \delta(\omega + E_{k-p} + E_q - E_{p+q})\right] \\
&+ c_-(\mathbf{p}+\mathbf{q},\mathbf{q})\left[1 - f(E_q) - f(E_{p+q})\right] \\
&\times \left[\delta(\omega + E_{k-p} + E_q + E_{p+q}) - \delta(\omega + E_{k-p} - E_q - E_{p+q})\right]\Bigg] \\
&+ \sum_{\mathbf{p}} \left[f(E_{k-p}) + n(E_{k-p} - \omega)\right] \sum_{\mathbf{q}} \Bigg[c_+(\mathbf{p}+\mathbf{q},\mathbf{q})\left[f(E_q) - f(E_{p+q})\right] \\
&\times \left[\delta(\omega - E_{k-p} + E_q - E_{p+q}) - \delta(\omega - E_{k-p} - E_q + E_{p+q})\right] \\
&+ c_-(\mathbf{p}+\mathbf{q},\mathbf{q})\left[1 - f(E_q) - f(E_{p+q})\right]
\end{aligned}
$$

$$\times\ [\delta(\omega - E_{k-p} - E_q - E_{p+q}) - \delta(\omega - E_{k-p} + E_q + E_{p+q})]\Bigg]\Bigg]. \quad \text{(B.13)}$$

For the $\hat{\tau}_3$ component, we find

$$\begin{aligned}
\Sigma_3(\mathbf{k},\omega) = \frac{U^2}{8}\sum_{\mathbf{p},\mathbf{q}}\frac{\epsilon_{k-p}}{E_{k-p}}\Bigg[& c_+(\mathbf{p}+\mathbf{q},\mathbf{q})\,[f(E_q) - f(E_{p+q})] \\
& \times \Bigg[[f(E_{k-p}) + n(E_q - E_{p+q})] \\
& \times \left[\frac{1}{\omega + i\eta - E_{k-p} + E_q - E_{p+q}} - \frac{1}{\omega + i\eta + E_{k-p} - E_q + E_{p+q}}\right] \\
& + [1 - f(E_{k-p}) - n(E_q + E_{p+q})] \\
& \times \left[-\frac{1}{\omega + i\eta + E_{k-p} + E_q - E_{p+q}} - \frac{1}{\omega + i\eta - E_{k-p} - E_q + E_{p+q}}\right]\Bigg] \\
& + c_-(\mathbf{p}+\mathbf{q},\mathbf{q})\,[f(E_q) + f(E_{p+q}) - 1] \\
& \times \Bigg[[f(E_{k-p}) + n(E_q - E_{p+q})] \\
& \times \left[-\frac{1}{\omega + i\eta + E_{k-p} - E_q - E_{p+q}} + \frac{1}{\omega + i\eta - E_{k-p} + E_q + E_{p+q}}\right] \\
& + [1 - f(E_{k-p}) + n(E_q - E_{p+q})] \\
& \times \left[\frac{1}{\omega + i\eta - E_{k-p} - E_q - E_{p+q}} - \frac{1}{\omega + i\eta + E_{k-p} + E_q + E_{p+q}}\right]\Bigg]\Bigg]
\end{aligned} \quad \text{(B.14)}$$

and thus, for the corresponding imaginary part,

$$\begin{aligned}
\operatorname{Im}\Sigma_3(\mathbf{k},\omega) = \frac{\pi U^2}{8}\Bigg[& \sum_{\mathbf{p}}\frac{\epsilon_{k-p}}{E_{k-p}}\,[f(E_{k-p}) + n(E_{p-q} + \omega)] \\
& \times \sum_{\mathbf{q}}\Bigg[c_+(\mathbf{p}+\mathbf{q},\mathbf{q})\,[f(E_q) - f(E_{p+q})] \\
& \times [\delta(\omega + E_{k-p} + E_q - E_{p+q}) - \delta(\omega + E_{k-p} - E_q + E_{p+q})]
\end{aligned}$$

$$
\begin{aligned}
&+\ c_-(\mathbf{p}+\mathbf{q},\mathbf{q})\,[1-f(E_q)-f(E_{p+q})] \\
&\times\ [\delta(\omega+E_{k-p}-E_q-E_{p+q})-\delta(\omega+E_{k-p}+E_q+E_{p+q})]\ \Bigg] \\
&+\ \sum_{\mathbf{p}} \frac{\epsilon_{k-p}}{E_{k-p}}\,[f(E_{k-p})+n(E_{k-p}-\omega)] \\
&\times\ \sum_{\mathbf{q}} \Bigg[c_+(\mathbf{p}+\mathbf{q},\mathbf{q})\,[f(E_q)-f(E_{p+q})] \\
&\times\ [\delta(\omega-E_{k-p}+E_q-E_{p+q})-\delta(\omega-E_{k-p}-E_q+E_{p+q})] \\
&+\ c_-(\mathbf{p}+\mathbf{q},\mathbf{q})\,[1-f(E_q)-f(E_{p+q})] \\
&\times\ [\delta(\omega-E_{k-p}-E_q-E_{p+q})-\delta(\omega-E_{k-p}+E_q+E_{p+q})]\ \Bigg]\Bigg] \quad .
\end{aligned}
\tag{B.15}
$$

The self-energy which corresponds to the $\hat{\tau}_1$ component can be evaluated as

$$
\begin{aligned}
&\Sigma_1(\mathbf{k},\omega) \\
&\quad = \frac{\pi U^2}{8} \sum_{\mathbf{p},\mathbf{q}} \frac{\Delta_{k-p}}{E_{k-p}} \Bigg[c_+(\mathbf{p}+\mathbf{q},\mathbf{q})\,[f(E_q)-f(E_{p+q})] \\
&\times\ \Bigg[[f(E_{k-p})+n(E_q-E_{p+q})] \\
&\times\ \left[\frac{1}{\omega+i\eta-E_{k-p}+E_q-E_{p+q}}-\frac{1}{\omega+i\eta+E_{k-p}-E_q+E_{p+q}}\right] \\
&+\ [1-f(E_{k-p})+n(E_q-E_{p+q})] \\
&\times\ \left[-\frac{1}{\omega+i\eta+E_{k-p}+E_q-E_{p+q}}-\frac{1}{\omega+i\eta-E_{k-p}-E_q+E_{p+q}}\right]\Bigg] \\
&+\ c_-(\mathbf{p}+\mathbf{q},\mathbf{q})\,[f(E_q)+f(E_{p+q})-1] \\
&\times\ [f(E_{k-p})+n(E_q+E_{p+q})] \\
&\times\ \left[-\frac{1}{\omega+i\eta+E_{k-p}-E_q-E_{p+q}}+\frac{1}{\omega+i\eta-E_{k-p}+E_q+E_{p+q}}\right]
\end{aligned}
$$

$$
\begin{aligned}
&+\ [1 - f(E_{k-p}) + n(E_q + E_{p+q})] \\
&\times\ \left[\frac{1}{\omega + i\eta - E_{k-p} - E_q - E_{p+q}} - \frac{1}{\omega + i\eta + E_{k-p} + E_q + E_{p+q}}\right]\Bigg] \ .
\end{aligned}
\tag{B.16}
$$

Thus, for the corresponding imaginary part, we find

$$
\begin{aligned}
\operatorname{Im}\Sigma_3(\mathbf{k},\omega) = \frac{\pi U^2}{8}\Bigg[&\sum_{\mathbf{p}} \frac{\Delta_{k-p}}{E_{k-p}} \left[f(E_{k-p}) + n(E_{p+q} + \omega)\right] \\
&\times \sum_{\mathbf{q}} \Bigg[c_+(\mathbf{p}+\mathbf{q},\mathbf{q}) \left[f(E_q) - f(E_{p+q})\right] \\
&\times \left[\delta(\omega + E_{k-p} + E_q - E_{p+q}) - \delta(\omega + E_{k-p} - E_q + E_{p+q})\right] \\
&+\ c_-(\mathbf{p}+\mathbf{q},\mathbf{q}) \left[1 - f(E_q) - f(E_{p+q})\right] \\
&\times \left[\delta(\omega + E_{k-p} - E_q - E_{p+q}) - \delta(\omega + E_{k-p} + E_q + E_{p+q})\right]\Bigg] \\
&+ \sum_{\mathbf{p}} \frac{\Delta_{k-p}}{E_{k-p}} \left[f(E_{k-p}) + n(E_{k-p} - \omega)\right] \\
&\times \sum_{\mathbf{q}} \Bigg[c_+(\mathbf{p}+\mathbf{q},\mathbf{q}) \left[f(E_q) - f(E_{p+q})\right] \\
&\times \left[\delta(\omega - E_{k-p} + E_q - E_{p+q}) - \delta(\omega - E_{k-p} - E_q + E_{p+q})\right] \\
&+\ c_-(\mathbf{p}+\mathbf{q},\mathbf{q}) \left[1 - f(E_q) - f(E_{p+q})\right] \\
&\times \left[\delta(\omega - E_{k-p} - E_q - E_{p+q}) - \delta(\omega - E_{k-p} + E_q + E_{p+q})\right]\Bigg]\Bigg] \ .
\end{aligned}
\tag{B.17}
$$

Now, introducing the susceptibility in the superconducting state,

$$
\chi(\mathbf{p}, i\nu_m) = -T \sum_{\omega_n} \sum_{\mathbf{q}} \frac{1}{2} \operatorname{Tr}\left[G(\mathbf{p}+\mathbf{q}, i\omega_n + i\nu_m) G(\mathbf{q}, i\omega_n)\right]
$$

$$
\begin{aligned}
&= -\frac{1}{4}\sum_{\mathbf{q}}\Bigg[\, c_+(\mathbf{p}+\mathbf{q},\mathbf{q})\,[f(E_q)-f(E_{p+q})] \\
&\times \left[\frac{1}{i\nu_m + E_q - E_{p+q}} - \frac{1}{i\nu_m - E_q + E_{p+q}}\right] \\
&+\; c_-(\mathbf{p}+\mathbf{q},\mathbf{q})\,[1-f(E_q)-f(E_{p+q})] \\
&\times \left[\frac{1}{i\nu_m - E_q - E_{p+q}} - \frac{1}{i\nu_m + E_q + E_{p+q}}\right]\Bigg] \quad ,
\end{aligned}
\tag{B.18}
$$

and its imaginary part

$$
\begin{aligned}
\mathrm{Im}\,\chi(\mathbf{p}, i\nu_m) = \frac{\pi}{4}\sum_{\mathbf{q}}\Bigg[&c_+(\mathbf{p}+\mathbf{q},\mathbf{q})\,[f(E_q)-f(E_{p+q})] \\
&\times\; [\delta(\nu + E_q - E_{p+q}) - \delta(\nu - E_q + E_{p+q})] \\
&+\; c_-(\mathbf{p}+\mathbf{q},\mathbf{q})\,[1-f(E_q)-f(E_{p+q})] \\
&\times\; [\delta(\nu - E_q - E_{p+q}) - \delta(\nu + E_q + E_{p+q})]\Bigg], \qquad \text{(B.19)}
\end{aligned}
$$

we can write

$$
\begin{aligned}
\mathrm{Im}\,\Sigma_0(\mathbf{k},\omega) = \frac{U^2}{2}\sum_{\mathbf{p}}&[-[f(E_{k-p}) + n(E_{k-p}+\omega)]\;\mathrm{Im}\,\chi(\mathbf{p},\omega+E_{k-p}) \\
&\times\; [f(E_{k-p}) + n(E_{k-p}-\omega)]\;\mathrm{Im}\,\chi(\mathbf{p},\omega-E_{k-p})] \quad . \qquad \text{(B.20)}
\end{aligned}
$$

With the help of

$$
\begin{aligned}
f(x)+n(y) &= \frac{1}{2}\left[1-\tanh\left(\frac{x}{2T}\right)\right] + \frac{1}{2}\left[\coth\left(\frac{y}{2T}\right)-1\right] \\
&= \frac{1}{2}\left[\coth\left(\frac{y}{2T}\right) - \tanh\left(\frac{x}{2T}\right)\right] \quad , \qquad \text{(B.21)}
\end{aligned}
$$

we find

$$
\begin{aligned}
\mathrm{Im}\,\Sigma_0(\mathbf{k},\omega) = \frac{U^2}{2}\sum_{\mathbf{p}}&\left[\int_0^\infty \mathrm{d}\epsilon\,\delta(\epsilon - E_p)\,\left[\coth\left(\frac{\epsilon-\omega}{2T}\right) - \tanh\left(\frac{\epsilon}{2T}\right)\right]\right. \\
&\times\; \mathrm{Im}\;\chi(\mathbf{k}-\mathbf{p},\omega-\epsilon)
\end{aligned}
$$

$$
\begin{aligned}
&- \int_{-\infty}^{0} \mathrm{d}\epsilon\, \delta(-\epsilon - E_p) \left[\coth\left(\frac{-\epsilon+\omega}{2T}\right) - \tanh\left(\frac{-\epsilon}{2T}\right) \right] \\
&\times \operatorname{Im}\chi(\mathbf{k}-\mathbf{p}, \omega-\epsilon) \Bigg] \\
&= -\frac{U^2}{4} \sum_{\mathbf{p}} \int_{-\infty}^{\infty} \mathrm{d}\omega' \left[\coth\left(\frac{\omega'}{2T}\right) - \tanh\left(\frac{\omega'-\omega}{2T}\right) \right] \\
&\times \operatorname{Im}\chi(\mathbf{k}-\mathbf{p}, \omega')\, \delta(|\omega-\omega'| - E_p) \quad . \qquad \text{(B.22)}
\end{aligned}
$$

In the other cases of the $\hat{\tau}_1$ and $\hat{\tau}_3$ components we obtain similar results, which can be written in a unified way using the nesting approximation. In this approximation one assumes that the main contribution to the momentum sum comes from $\operatorname{Im}\chi$ at the (transferred) nesting vector $\mathbf{Q} = (\pi, \pi)$. In this case, the self-energy no longer depends on $\mathbf{k}$ and one can write ($\nu = 0, 1, 3$)

$$
\begin{aligned}
\operatorname{Im}\Sigma_\nu(\omega) = -\frac{U^2}{4} &\int_{-\infty}^{\infty} \mathrm{d}\omega' \left[\coth\left(\frac{\omega'}{2T}\right) - \tanh\left(\frac{\omega'-\omega}{2T}\right) \right] \\
&\times \operatorname{Im}\chi(\mathbf{Q}, \omega)\, N_\nu(|\omega-\omega'|) \quad , \qquad \text{(B.23)}
\end{aligned}
$$

where

$$
N_0(x) = \sum_{\mathbf{p}} \delta(|x| - E_p) \quad , \qquad \text{(B.24)}
$$

$$
N_1(x) = -\mathrm{signx} \sum_{\mathbf{p}} \frac{\Delta_p}{E_p}\, \delta(|x| - E_p) \quad , \qquad \text{(B.25)}
$$

and

$$
N_3(x) = \mathrm{signx} \sum_{\mathbf{p}} \frac{\epsilon_p}{E_p}\, \delta(|x| - E_p) \quad . \qquad \text{(B.26)}
$$

This completes the derivation of (3.8).

C $d_{x^2-y^2}$-Wave Superconductivity Due to Phonons?

In this appendix we analyze how the magnetic mode which is usually peaked at $\mathbf{q} = \mathbf{Q} = (\pi, \pi)$ leads to a kink in the ARPES results and to a $d_{x^2-y^2}$-wave order parameter that is maximal around $(\pi, 0)$. In particular, we consider to what extend phonons contribute to this result. This is an extension of the general remarks made in sect. 1.4.3.

In general, the generalized Eliashberg equations read, after the inclusion of *attractive* phonons (branch i) via their spectral function $\alpha^2 F_i(\mathbf{q}, \Omega)$,

$$\begin{aligned} &\Sigma_\nu^{(i)}(\mathbf{k}, \omega) \\ &= N^{-1} \sum_{\mathbf{k}'} \int_0^\infty \mathrm{d}\Omega \, V_{\mathrm{eff}}(\mathbf{k} - \mathbf{k}', \Omega) - \alpha^2 F_i(\mathbf{k} - \mathbf{k}', \Omega) \\ &\times \int_{-\infty}^{+\infty} \mathrm{d}\omega' \, I(\omega, \Omega, \omega') \, A_\nu(\mathbf{k}', \omega') \quad . \end{aligned} \tag{C.1}$$

For $\alpha^2 F_i(\mathbf{q}, \Omega)$, we employ a Lorentzian in the frequency Ω around $\Omega_0 \approx \omega_D$ (Debye frequency), and a normalized form factor $F_i(\mathbf{q})$ peaked at $\mathbf{q} = \mathbf{q}_{\mathrm{pair}}$ as indicated in Fig. C.1. The spin fluctuations that dominate $V_{\mathrm{eff}}(\mathbf{q}, \omega_{sf})$ are peaked at $\mathbf{q} = \mathbf{Q}_{\mathrm{pair}}$.

It is instructive to write down the weak-coupling limit of the $\hat{\tau}_1$ component of (C.1), which reads (at $T = 0$)

$$\Delta(\mathbf{k}) = -\sum_{\mathbf{k}'} \frac{\left[V_{\mathrm{eff}}(\mathbf{q}) - \alpha^2 F_i(\mathbf{q})\right]}{2E_k} \Delta(\mathbf{k}) \quad , \tag{C.2}$$

where again $E_k = \sqrt{\Delta^2(\mathbf{k}) + \epsilon_k^2}$ is the dispersion of the quasiparticles in the superconducting state. Note that the contribution to the pairing potential is repulsive for spin fluctuations and attractive for phonons. In the case where no phonons contribute to the Cooper pairing ($\alpha^2 F_i(\mathbf{q}) = 0$), $V_{\mathrm{eff}}(\mathbf{q})$ bridges parts of the Fermi surface where the superconducting order parameter has opposite signs. This momentum dependence of the pairing interaction is required for solving (C.1) and is typical of unconventional superconductivity. Note that for a repulsive and momentum-independent pairing potential, $V_{\mathrm{eff}}(\mathbf{q}) = const$, no solution of (C.1) can be obtained (see sect. 1.4.3).

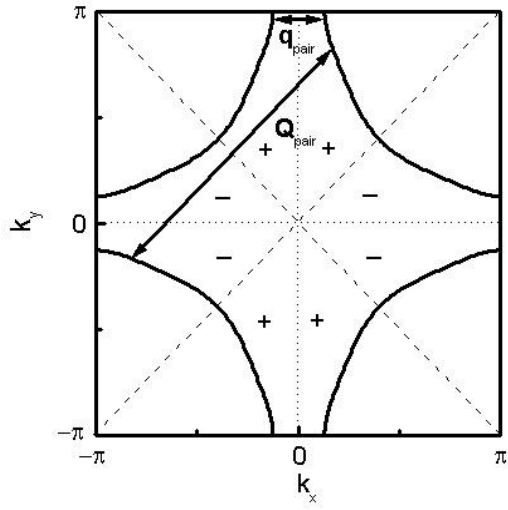

Fig. C.1. Illustration of $d_{x^2-y^2}$-wave Cooper pairing for a fixed frequency $\Omega = \Omega_0 \approx \omega_{sf} \approx \omega_D$ due to spin fluctuations peaked at momentum $\mathbf{k} - \mathbf{k}' = \mathbf{q} = \mathbf{Q}_{\rm pair}$ and phonons peaked at $\mathbf{q} = \mathbf{q}_{\rm pair}$. The *solid lines* denote the Fermi surface and the *dashed lines* the nodes of the $d_{x^2-y^2}$-wave order parameter. The corresponding sign of the order parameter is also displayed.

How is the kink related to the pairing mechanism? Physically speaking, the interdependence of the elementary excitations that dominate $V_{\rm eff}(\mathbf{q})$ leads to $d_{x^2-y^2}$-wave Cooper pairing, as well as to the kink structure observed by ARPES experiments. In other words, the quasiparticles around the hot spots couple strongly to spin fluctuations. This coupling leads to (a) a $d_{x^2-y^2}$-wave order parameter, and (b) a kink in the nodal direction that occurs *close to* the Fermi level where $\mathbf{Q}_{\rm pair} = (\pi, \pi)$, as indicated in Fig. 3.19.

It follows also from (C.1) that attractive phonons with a corresponding spectral function $\alpha^2 F(\mathbf{q})$ peaked at $\mathbf{q} = \mathbf{q}_{\rm pair}$ contribute *constructively* to $d_{x^2-y^2}$-wave pairing, as long as the main pairing interaction is provided by spin fluctuations. However, the kink close to the antinodal points occurs *only* below T_c and is a result of the fact that $\Delta(\omega)$ is maximal around $(0, \pi)$. Therefore, the kink structure in the antinodal direction is connected mainly to spin excitations peaked at $\mathbf{Q}_{\rm pair} = (\pi, \pi)$ and not to the phonon branch peaked at $\mathbf{q}_{\rm pair}$.

Note that in the case where no spin fluctuations were present, i.e. $V_{\rm eff}(\mathbf{q}) = 0$, the attractive phonon contribution would cancel the minus sign on the right-hand-side of (C.1), yielding an order parameter with s-wave symmetry. Thus we can safely conclude that $d_{x^2-y^2}$-wave Cooper pairing due to phonons and the anisotropy of the kink feature in the elementary excitations are hard to reconcile within the same physical picture.

Index